A MULTIMODAL APPROACH TO THE OSSEOINTEGRATION OF POROUS IMPLANTS

A MULTIMODAL APPROACH TO THE OSSEOINTEGRATION OF POROUS IMPLANTS

By JOSEPH DEERING, B.Eng.

A Thesis Submitted to the School of Graduate Studies in Partial Fulfilment of the Requirements for the Degree Doctor of Philosophy

McMaster University

Doctor of Philosophy (Materials Science & Engineering)

McMaster University (2022)

Hamilton, ON, Canada

TITLE: A Multimodal Approach to the Osseointegration of
                                Porous Implants

AUTHOR: Joseph Deering, B.Eng. (McMaster University)

SUPERVISOR: Prof. Dr. Kathryn Grandfield

NUMBER OF PAGES: xx, 170

Lay Abstract

Metallic implants are widely used in dental and orthopedic applications but can be prone to failure or incomplete integration with bone tissue due to a breakdown at the bone-implant interface as defined by clinical standards. In order to improve the ability of the implant to anchor itself into the surrounding bone tissue, it is possible to use novel three-dimensional (3D) printing approaches to produce porous metals with an increased area for direct bone-implant contact. This thesis examines strategies to design porous implants that better mimic the structure of human bone, possible coating materials to accelerate early bone growth at the implant interface, and the microscale-to-nanoscale origins of bone formation within the interior of porous materials.

Abstract

The field of implantology is centred around interfacial interactions with the surrounding bone tissue. Assessing the suitability of novel engineering materials as implants for clinical application follows a preliminary workflow that can be simplified into three main stages: *(i) implant design*, *(ii) in vitro compatibility*, and *(iii) in vivo compatibility.* This thesis is subdivided to mirror each of these three themes, with a specific focus on the multiscale features of the implant itself as well as appositional bone tissue. In Chapter 3, a biomimetic approach to generate porous metallic implants is presented, using preferential seeding in a 3D Voronoi tessellation to create struts within a porous scaffold that mirror the trabecular orientation in human bone tissue. In Chapter 4, cytocompatible succinate-alginate films are generated to promote the *in vitro* activity of osteoblast-like cells and endothelial cells using a methodology that could be replicated to coat the interior and exterior of porous metals. In Chapter 5, two types of porous implants with graded and uniform pore size are implanted into rabbit tibiae to characterize the biological process of osseointegration into porous scaffolds. In Chapter 6, these same scaffolds are probed with high-resolution 2D and 3D methods using scanning transmission electron microscopy (STEM) and the first-ever application of plasma focused ion beam (PFIB) serial sectioning to observe structural motifs in biomineralization at the implant interface in 3D. This thesis provides new knowledge, synthesis techniques, and development of characterization tools for bone-interfacing implants, specifically including a means to: *(i) provide novel biomaterial design strategies for additive manufacturing; (ii) synthesize coatings that are compatible with additively manufactured surfaces; (iii) improve our understanding of mineralization process in newly formed bone,* with the ultimate goal of improving the osseointegration of implants.

Acknowledgements

There are a great number of people I would like to thank for my success here at McMaster. First and foremost, I want to thank all of the technical and support staff that made my research possible and that truly make McMaster an academic leader in the world of biomaterials and electron microscopy. From the Canadian Centre for Electron Microscopy, I would like to extend warm thanks to Hui Yuan, Jhoynner Martinez, Chris Butcher, Natalie Hamada, Travis Casagrande, and Brian Langelier. From the Biointerfaces Institute, I would like to thank Marta Princz. From MSE: Mary-Anne Bechamp, Xiaogang Li, and Doug Culley. And from the Additive Manufacturing Group, Mostafa Yakout, Jan Boer, and Dalia Mahmoud.

Secondly, I'd like to take the opportunity to thank all of my family and friends for their support over the past few years, through thick and thin.

I have been fortunate enough in my time here to have collaborated on a number of projects with researchers around the world. A big thank you to Wolfram Bosbach & Alex Presas, Amanda Clifford & Igor Zhitomirsky, Dawn Lin & Boyang Zhang, Sanaz Hashemi & Thomas Willett, Derk Joester, Bosco Yu, Roberta Okamoto, and many others who I may have missed.

For all the constructive comments and assistance throughout my PhD, I would like to extend appreciation to my supervisory committee members: Greg Wohl & Andre Phillion.

I am proud to have been a part of a research group as tight-knit as the Grandfield Research Group. Between trivia nights, card games, potlucks, videography, and a wealth of other adventures, I've come to realize the importance of how great friends can make a workplace so much more enjoyable. Xiaoyue Wang, Dakota Binkley, Ivan Strakhov, Chiara Micheletti, Liza DiCecco, Alyssa Williams, Jeromy Williams, Alessandra Merlo, Pedro Henrique Silva Gomes Ferreira, Toni Teng, and all of our undergraduate researchers – thank you for making GRG so great. I'd like to especially thank Bryan Lee, GRG alumnus, for taking the time to teach me so much about leadership and shape the way I approach research.

Above all, I'd like to express my gratitude to Kathryn Grandfield. Thank you for allowing me the opportunity to pursue my own creative freedoms in the field of bone and biomaterial science, and all your support throughout my journey.

There have been so many people who have had an impact on my life in the past four years. To anyone who I may have overlooked and those that took the time to read this thesis, thank you!

Table of Contents

List of Figures

closely with tissue in the H&E section at twelve weeks. (E-H) Calcein fluorochrome and H&E stain showing correlative bone apposition at two and four weeks in (E-F) G300 and (G-H) FG600 implants. Fluorescent signals are bright throughout the implant interior where bone matrix is present, indicating that mineral transport is consistently occurring within the scaffold interior within the first two weeks and corresponds with regions of connective tissue in the H&E micrographs. Scale bars 1 mm.

List of Tables

List of All Abbreviations and Symbols

2D	Two-dimensional or two-dimensions
3D	Three-dimensional or three-dimensions
3N/4N/5N	Node geometry denoting number of intersecting trabeculae
ALG	Alginate
ANOVA	Analysis of variance
AM	Additive manufacturing or additively manufactured
BA	Bone area
BCA	Bicinchoninic acid assay
BIC	Bone-implant contact
BREP	Boundary representation
BSE	Backscattered electron
BV/TV	Fraction of bone volume per total volume
CAD	Computer-aided drawing
CNN	Convolutional neural network
CSD	Critical-sized defects
CT	Computed tomography
DED	Directed energy deposition
ELISA	Enzyme-linked immunosorbent assay
FIB	Focused ion beam
FG	Functionally-graded
FG600	Gyroid with pores of 600 μm (at exterior) to 300 μm (at interior)
G300	Gyroid with uniform pores of 300 μm throughout
G600	Gyroid with unform pores of 600 μm throughout
HAADF	High-angle annular dark-field
H&E	Hematoxylin and eosin
HC	Haversian canal
HIF-1α	Hypoxia-inducible factor 1α
HRE	Hypoxia-responsive element
HUVEC	Human umbilical vein endothelial cell
ITA	Inter-trabecular angle
LCN	Lacuno-canalicular network
L-PBF	Laser powder bed fusion
Micro-CT	X-Ray microcomputed tomography
MIL	Mean intercept length
OPN	Osteopontin
PBF	Powder bed fusion
PDGF	Platelet-derived growth factor
PFIB	Plasma focused ion beam
ROI	Region of interest
RTIL	Room-temperature ionic liquid

RUNX2	Runt-related transcription factor 2
SE	Secondary electron
SEM	Scanning electron microscopy
SLM	Selective laser melting
SPP	Seeds per plane
STEM	Scanning transmission electron microscopy
SUC	Disodium succinate
SVD	Star volume distribution anisotropy measurement
Tb.Th	Trabecular thickness
TEM	Transmission electron microscopy
Ti6Al4V	Titanium alloy with 6 wt% aluminum and 4 wt% vanadium
TPMS	Triply periodic minimal surface
VEGF	Vascular endothelial growth factor

Declaration of Academic Achievement

The *four major components* of my doctoral thesis are published, submitted, or in manuscript form with the intent to publish in scholarly peer-reviewed journals, and are listed in sequence as follows:

(Ch. 3)   **Deering, J.***, Dowling, K.I.*, DiCecco, L.-A., McLean, G.D., Yu, B., and Grandfield, K. (2021). Selective Voronoi tessellation as a method to design anisotropic and biomimetic implants. *Journal of the Mechanical Behaviour of Biomedical Materials*, *116*.

Contributions: I conducted the design of experiments for the work in Chapter 3, in addition to establishing the initial workflow for isotropic scaffold generation via Voronoi tessellation. Kierdra Dowling made modifications to the Voronoi workflow with suggestions from myself, Kathryn Grandfield, and Bosco Yu to incorporate the preferential seeding for generating anisotropy. Liza-Anastasia assisted with troubleshooting mesh exports, and I conducted the geometric evaluation in ORS Dragonfly with subsequent data processing and analysis. The manuscript was predominantly drafted by myself and Kierdra Dowling, with editing from Liza-Anastasia DiCecco, Bosco Yu, Griffin McLean, and Kathryn Grandfield. This manuscript has been published in the *Journal of the Mechanical Behaviour of Biomedical Materials.*

(Ch. 4)   **Deering, J.**, Lin, D.S.Y., D'Elia, A., Zhang, B., and Grandfield, K. Fabrication of succinate-alginate xerogel films for in vitro coupling of osteogenesis and neovascularization. *Biomaterials Advances, Submission No. BIOADV-D-22-01116.*

Contributions: I conducted the design of experiments for the work in Chapter 4 along with Andrew D'Elia. I synthesized the xerogel coatings with some early assistance from Andrew D'Elia, conducted the ionic liquid treatments, performed scanning electron microscopy, performed *in vitro* metabolic measurements, and performed image processing for the bright-field optical microscopy. Dawn Lin performed the endothelial cell culture and acquired the raw optical micrographs. I conducted the data analysis and drafted most of the original manuscript, incorporating comments and edits from all authors. In its current state, this manuscript has been submitted for publication in *Biomaterials Advances*.

(Ch. 5)   **Deering, J.**, Mahmoud, D., Rier, E., Lin, Y., Fang, Q., Wohl, G.R., Deng, F., Grandfield, K., Elbestawi, M.A., and Chen, J.

Osseointegration of functionally-graded Ti6Al4V porous implants: Histology of the pore network. *In Draft.*

Contributions: Implants were designed by Jianyu Chen, Dalia Mahmoud, Gregory Wohl, and Mohamed Elbestawi. Surgical implantation/retrieval, including fluorochrome injection and preparation of histology slides, was performed by Jianyu Chen and Yujing Lin. I conducted *in vitro* assays on the implants, prepared the extracted tissue for 3D characterization, acquired the X-ray microcomputed tomography datasets, trained the neural network for image segmentation, performed scaffold design validation, imaged and interpreted slides for histology and fluorochrome analysis, and drafted the manuscript. Elyse Rier conducted histomorphometric analysis from the resulting neural network output. All authors will provide edits for the final version of the manuscript prior to its submission for publication in a peer-reviewed journal.

(Ch. 6)   **Deering, J.**, Chen, J., Mahmoud, D., Tang, T., Fang, Q., Wohl, G.R., Elbestawi, M.A., and Grandfield, K. Characterizing mineral ellipsoids in new bone formation at the interface of Ti6Al4V porous implants. *In Draft.*

Contributions: The same implants from Chapter 5 were used for the study in Chapter 6. Again, Jianyu Chen, Dalia Mahmoud, Gregory Wohl, and Mohamed Elbestawi designed the gyroid structure, Jianyu Chen and YuJing Lin performed the pre-clinical work. I prepared the specimens for electron microscopy and conducted both focused ion beam tomography experiments and associated image processing/segmentation. Technical assistance was received from Travis Casagrande for the transmission electron microscopy lamella preparation. I performed the scanning transmission electron microscopy of the bone-implant interface with technical assistance from Natalie Hamada for electron energy loss spectroscopy and mapping. Methods for plasma focused ion beam microscopy were developed by myself with support from Tengteng Tang. I drafted the manuscript for this work, incorporating feedback and edits from all authors. The current version of this manuscript is to be submitted for publication in a peer-reviewed journal.

Among my published works, I have *other authorship contributions* that link the techniques and themes within the main body of this thesis; some of these articles are referenced throughout this thesis and are included as appendices:

(App. 1)   **Deering, J.** and Grandfield, K. (2021). Current interpretations on the in vivo response of bone to additively manufactured porous scaffolds: A review. *Biomaterials and Biosystems, 2.*

This review provides a complementary biological perspective on bone ingrowth into porous materials, reviewing the literature to highlight patterns in bone apposition and narrow the scope of scaffold design parameters. I conducted the literature review and drafting of this manuscript with input and direction from Kathryn Grandfield. This work has been published in *Biomaterials and Biosystems* and is drawn on for some content in Chapters 1 and 2.

(App. 2)   **Deering, J.**, Clifford, A., D'Elia, A., Zhitomirsky, I., and Grandfield, K. (2020). Composite dip coating improves biocompatibility of porous metallic scaffolds. *Materials Letters, 274.*

I designed and additively manufactured porous stainless steel specimens to assess the compatibility of dip coating methods as a means to functionalize biomolecules within the interior of a porous structure. Andrew D'Elia, Amanda Clifford, and Igor Zhitomirsky devised and conducted the dip-coating protocol, and I conducted the electron microscopy to confirm coating coverage. I drafted this letter with all authors editing the final version. This work is published in *Materials Letters*.

(App. 3)   Binkley, D.M., **Deering, J.**, Yuan, H., Gourrier, A., and Grandfield, K. (2020). Ellipsoidal mesoscale mineralization pattern in human cortical bone revealed in 3D by plasma focused ion beam serial sectioning. *Journal of Structural Biology, 212.*

Focused ion beam datasets in this work were acquired by Dakota Binkley and Hui Yuan following tissue preparation by Dakota Binkley. I assisted in the creation of a neural network for machine-learning segmentation of canaliculi in the dataset and applied image filtering techniques to highlight the mesoscale mineral ellipsoids. The final manuscript was written by Kathryn Grandfield and Aurélien Gourrier with significant draft contributions from Dakota Binkley and edits by myself. This work is published in the *Journal of Structural Biology.*

Chapter 1: Introduction

1.1 Research Motivation

The development of a structural and functional connection between bone and an implant is known as *osseointegration* [1,2]. Titanium and its alloys are among the most commonly employed materials for osseointegration in dental and orthopaedic applications. Recently, additive manufacturing has enabled the production of porous titanium geometries for bone integration. The general biocompatibility of implants is characterized using *in vitro* methods (with simulated body environments [3] or cells) while osseointegration is assessed *in vivo* using pre-clinical animal models to observe the regenerative capabilities of bone [4] around implants. Both of these approaches have their limitations with respect to predicting osseointegration in humans but provide important information about how novel engineering materials could clinically translate. Broadly speaking, osseointegration within the period immediately following surgery is associated with favourable long-term outcomes and implant survival [5,6]. However, unfavourable interaction with the host may necessitate revision surgeries, which account for a high percentage of all hip replacements in the 10 years following initial implantation of the prosthesis [7] as an example. This places an unnecessary burden on healthcare systems worldwide, including in Canada.

Understanding how material design, especially in the case of porous metals, can encourage osseointegration is pivotal for reducing the incidence of revision surgery. Related to this, suitable methods to functionalize implant surfaces and characterization tools for porous implants are needed to evaluate or improve their potential clinical success. The work in this thesis presents three themes: a sequence of *design*, *modification*, and microscale-to-nanoscale *characterization* to better control and understand the osseointegration of porous metallic implants.

1.1.1 Designing Bioinspired Porous Implant Structures

The size and shape of a metallic implant can be designed to follow the geometry of the bone itself. As an example, small screws are often used for dental prostheses in the jaw while larger hip replacements are designed to mimic the shape of the acetabulum or femur. The substructure of these materials is often inspired by naturally occurring materials themselves [8]. Trabecular bone, for instance, is composed of an architecturally-complex network of rods and plates [9] and its porous nature can be replicated with several new materials processing techniques. One problem is that the overall architecture of cancellous bone varies greatly depending on its sampling location within the body [10], e.g., trabecular bone patterns within the femoral head and vertebral body are substantially different. Loading regimes within the tissue tend to govern these large structural changes within the bone tissue itself [11], and also dictate the service environment of an endosseous implant. When considering the design of porous metallic implants (as summarized in my review in

Appendix 1), most implant geometries are designed with a uniform pore and strut architecture. As a result, there is renewed interest in developing easily-modifiable design protocols for implants that can be modified to account for the natural anisotropy within the existing tissue. The work presented in Chapter 3 develops a method to introduce tunable forms of isotropy using a selectively-seeded 3D Voronoi tessellation approach.

1.1.2 Modifying Metallic Implants with Coatings

The physical and chemical properties of the implant surface govern the dynamic response of osseointegration. Surface modification strategies such as coating application can also follow the principles of biomimetics, where biologically-derived materials can improve adhesion to the implant surface [12]. These coatings can integrate molecules that alter the host response to improve bioactivity [13] or antibacterial response [14]. Physical modification of the implant surface to add texture at the nanoscale and microscale can also improve the host response by increasing the amount of direct bone-implant contact area [15]. Techniques such as acid-etching, grit-blasting, or laser surface modification can induce roughness at the microscale or nanoscale [16]. While the current literature depicts these methods as highly-suitable for conventional implant materials, their extension to intricate pore networks, including those inside additively manufactured (AM) materials is of great interest. The work presented in Chapter 4 details one such material development strategy that may be applicable to pore networks for encouraging vascular ingrowth and osteogenesis within the interior of porous AM metals. Where my previous work has shown that dip coating techniques can permeate the interior of porous metals (Appendix 2), the films in Chapter 4 elute disodium succinate from surface-bound alginate in a way that can modify the peri-implant environment of porous metallic implant materials using a coating-based approach.

1.1.3 Characterizing Osseointegration in Porous Implants at the Microscale

With the discovery of a new structural feature in bone – the mineral ellipsoid – there is potentially a gap in our understanding of osseointegration near an implant. Since these clusters of mineral form at intermediate length scales between the microscale and nanoscale [17], plasma focused ion beam (PFIB) microscopy has been shown to be able to analyze their structure in 3D over large volumes at high resolution as in Appendix 3 [18], but has not yet been applied at the bone-implant interface. Similarly, the sequential biological response in porous implants has not yet been fully characterized to see how osseointegration and bone ingrowth differs inside and outside the pore network. The works in Chapters 5 and 6 highlight classical histological and histomorphometric observations at the macroscale and microscale, and develop a method to observe mineral packing across the multiscale continuum using optical, X-ray, and electron microscopy techniques to better understand the process of osseointegration in porous titanium.

1.2 Research Objectives

This thesis aims to improve our understanding of osseointegration within the context of additively manufactured porous implants as a long-term goal. The broad research objectives are focused on three themes: strategies for *designing* porous materials, *modifying* porous materials, and *characterizing* the response to porous materials. The specific objectives are:

(i) To develop biomimetic implants with anisotropic pores. One technique for matching the anisotropic nature of bone is presented in Chapter 3.

(ii) To develop surface modification strategies that can influence biological response inside a pore network. A solvent casting technique for adding biofunctionalized molecules to a surface film is presented in Chapter 4.

(iii) To characterize the biological performance of porous implants at the microscale. A myriad of 2D and 3D characterization techniques are presented in Chapter 5 to thoroughly analyze osseointegration.

(iv) To characterize the structure of newly formed bone in porous implants in 3D. Electron microscopy techniques, including plasma focused ion beam protocols, are used to assess ultrastructural features in newly formed bone in Chapter 6.

1.3 Thesis Chapter Summary

The research objectives presented in Section 1.2 are summarized within the following chapters of the thesis:

Chapter 2: Background and Literature Review. This chapter contextualizes later work in the thesis based on existing literature, with specific focus on implant design considerations, additive manufacturing technology, hierarchical bone structure, osseointegration, and multiscale imaging modalities.

Chapter 3: Selective Voronoi Tessellation as a Method to Design Anisotropic and Biomimetic Implants. This chapter presents a workflow to create porous metals using a 3D form of Voronoi tessellation with an asymmetric seeding approach to mimic the natural anisotropy within the human femur. This showcases an opportunity for anisotropy-graded porous structures by modifying the distribution of seeds within a subregion of the porous volume.

Chapter 4: Fabrication of Succinate-Alginate Xerogel Films for In Vitro Coupling of Osteogenesis and Neovascularization. This chapter presents a coating strategy for implant materials to encourage early endothelial cell activity by rapidly releasing disodium succinate in the local environment of the implant. This *in vitro* work highlights the

importance of a holistic approach to osseointegration, as bone apposition only occurs following other forms of biological response such as vascularization.

Chapter 5: Osseointegration of Functionally-Graded Ti6Al4V Porous Implants: Histology of the Pore Network. This chapter presents microscale histological and histomorphometric observations of both functionally-graded and uniform pore structures implanted into rabbit tibiae. This *in vivo* work is among the first to highlight trends occurring over time in the two types of triply-periodic minimal surface scaffolds.

Chapter 6: Characterizing Mineral Ellipsoids in New Bone Formation at the Interface of Ti6Al4V Porous Implants. This chapter presents the first application of PFIB-SEM tomography to the bone-implant interface. STEM and PFIB-SEM are used to gain an understanding of how mineral ellipsoids self-assemble near an implant during osseointegration.

Chapter 7: Conclusions. This chapter presents the links, commonalities, and conclusions for each of the preceding works to emphasize the key findings and present avenues for follow-up study.

Chapter 2: Background and Literature Review

This thesis is centred on the biomimetic design, modification, and characterization of bone-interfacing porous biomaterials to improve early outcomes of osseointegration. Additive manufacturing technology serves as a useful tool to produce intricate designs that are often not possible with conventional subtractive techniques. These parts can be further modified with a number of post-processing techniques to optimize the host response. To understand how the implant fabrication and subsequent modification affect the formation of new bone tissue, it is also important to understand the biological processes by which bone forms and the inherent multiscale structure of bone itself. Lastly, it is important to understand that a combination of characterization techniques is often required to probe each level in bone's hierarchical structure. This chapter provides relevant background for the research presented in this thesis, explaining themes in additive manufacturing technology, implant surface modification, bone structure and formation, and multiscale imaging modalities – with some adaptation from my first-author review paper in Appendix 1.

2.1 Bone-Interfacing Implants

The number of hip, knee, and dental implants placed into Canadians has seen a staggering rise in recent years (Table 2-1), in part due to an aging population. Roughly one in every twelve arthroplasty procedures is to replace an existing implant, highlighting the necessity for innovation in design to improve implant lifespans. Some of the common implant failure modes include aseptic loosening, implant instability, peri-prosthetic bone fracture, implant wear, and implant fracture among others [19]. In part, these all share a common theme – a breakdown at the bone-implant interface caused by complications in the material.

Table 2-1: *Incidence of hip and knee replacement surgeries in Canada across a five year period. Data obtained from the Canadian Joint Replacement Registry* [19].

Year	Number of Hip Replacements	Number of Knee Replacements
2015 – 2016	53,244	64,118
2016 – 2017	55,981	67,169
2017 – 2018	58,492	70,502
2018 – 2019	62,016	75,345
2019 – 2020	63,496	75,073

Many of these failure modes can be attributed, at least in part, to the material properties of the implant itself. Aseptic loosening, for instance, is often attributed to the accumulation of debris from wear that can result in osteolysis or resorption of the tissue [20]. Accelerated

by the amount of micro-mechanical motion, the loss of implant fixation over time can exacerbate this loosening phenomenon [20]. Similarly, primary implant stability is derived from the initial post-operative mechanical interaction with the bone, while secondary implant stability further anchors the implant in place through regeneration of the tissue [21]. Generally speaking, if neither of these stabilizing mechanisms occurs, the implant is at risk of failure. Fracture of the bone tissue adjacent to the implant (peri-prosthetic) is also prone to occur with low-energy trauma (e.g., falls), but stress amplification or osteolysis can arise from the implant design itself [22]. In rare instances of high-energy trauma, it is also possible for the implant itself to be damaged or become loosened where factors such as implant location, load distribution, size, and material selection can influence the likelihood of fracture [23].

What some of these failure modes have in common is a lack of osseointegration between the implant and surrounding bone. As a result, there is a need to improve the overall design of implants using novel engineering strategies to modify the mechanical properties of the implant and promote long-term osseointegration.

2.1.1 Low-Stiffness Implants

When it comes to the design of implant materials, special consideration should be given to the stiffness of the implant, which is governed by both material-specific and geometry-specific factors. When a metallic implant is used for arthroplasty, the resulting loading state in the joint is shared between both the remaining bone and the newly inserted implant. A stiffness mismatch between the low-stiffness bone and high-stiffness implant decreases the amount of physiological load exerted on the bone tissue in a phenomenon known as stress-shielding. Stress-shielding can serve as a mechanism for bone resorption near the implant [24] and persists over longer-term follow-up studies [25]. Reducing the intensity of the stiffness mismatch between the metal and bone is possible using two techniques: modifying the composition of the implant material to change its elastic modulus (which governs the stress-to-strain relationship for a specific material) or modifying the overall geometry of the implant design (i.e., porosity and pore size). Comparison of the elastic moduli offers one approach to examine stiffness in the bone-implant system. Cortical bone, for instance, has an elastic modulus on the order of $5 - 20$ GPa [26], depending on sampling location and patient-specific factors. Implant materials such as commercially pure titanium (103 GPa) [27], Ti-6Al-4V alloy (114 GPa) [27], and cobalt-chromium (200 GPa) [28] naturally have higher elastic moduli than bone tissue in their unmodified state

Recent advances in material design have lowered the elastic modulus of several biomedical alloys where high-zirconium, high-niobium, and other alloys of β-phase titanium [29,30] have achieved elastic moduli that approach the range of cortical bone. However, advances in implant geometry offer a higher degree of customization to the implant – especially considering that variations in stress fields may occur depending on location and local

anisotropy. In particular, the development of porous implant materials [31–33] enables a geometry-derived global stiffness reduction [34,35] for known biocompatible alloys such as Ti-6Al-4V although the local stress transfer is likely more complex and may change depending on the extent to which bone has formed. Generally, the porosity-stiffness relationship does not necessarily follow a 'rule-of-mixtures' approach, where many models use power or exponential relationships to describe this mechanical response [36].
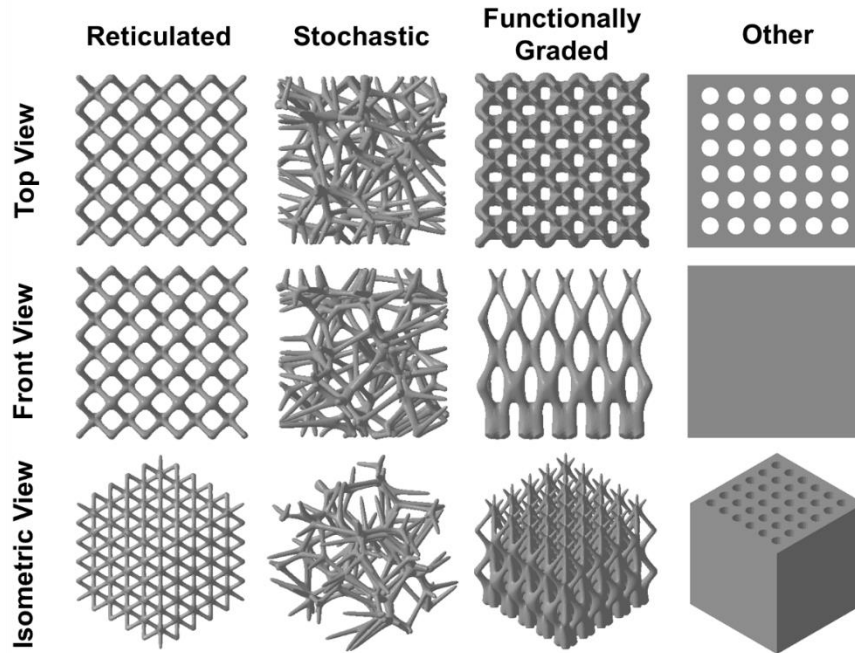
Figure 2-1: *Examples of varying types of porous geometries that can be applied to implant materials. Reproduced from* [37] *with permission.*

The pore structure in a porous implant material can be classified based on its repeating geometry (Figure 2-1). Reticulated forms of porous scaffold have a unit cell that repeats evenly in three-dimensional space. Stochastic or trabecular-like scaffolds do not contain a repeating topology, and instead have quasi-random strut orientation through the porous interior. Functionally-graded materials are a subset of porous materials that have some spatial variation in property along one of their principal axes (in Cartesian, cylindrical, or spherical coordinate systems). In porous materials, it is common to alter the size of the struts in the scaffold thereby changing the diameter and porosity of the implant along a specified gradient [38] while maintaining the same general architecture or topology of the unit cell. Recent works have also investigated functionally-graded (FG) chemical composition along the length of the implant [39]. By changing the implant geometry to include fully porous or partially porous regions, it may indeed be possible to improve the host response to the implant material.

<u>2.1.2 Additive Manufacturing Technologies</u>

As the material chemistry and the material geometry becomes more complex, so too must the manufacturing method. The intricate strut architecture within porous materials does not lend itself well to subtractive materials forming processes. Instead, the best approach is to leverage metallic AM processes to construct porous materials. Powder bed fusion (PBF) and directed energy deposition (DED) are the two main additive manufacturing processes for metals [40].

PBF processes use a layer-by-layer approach [41] under inert gas to build input parts from a computer-aided drawing (CAD) file with either an electron beam or laser as an energy source [42]. Selective laser melting (SLM) – one form of PBF – works by spreading a thin layer of powder (20-100 μm) onto the target build platform within the chamber. A laser then scans a pre-programmed pattern to melt along its track in a single layer of the 3D object, where the molten pool then solidifies to form the part [43]. The build platform then lowers to accommodate subsequent powder deposition to fabricate the next layer in the 3D geometry. Throughout the build, the unmelted powder provides a stable supporting structure to hold any overhanging portions in the future layers [44] – a characteristic that is not possible in DED. SLM also affords better fabrication of complex parts compared to current DED processes [45].

DED processes work by instantaneously guiding the feedstock material directly under the pathing of the energy source to build layer-by-layer without the use of a powder bed. In DED processing, metallic powder is blown towards the substrate, or a metal wire feedstock is fed directly underneath the laser spot as it scans [46], where the material melts and resolidifies into a solid layer. By linking the Cartesian coordinates of the feedstock deposition and laser pathing, complex implant geometries can be fabricated on the build platform [47]. DED techniques typically have faster deposition times than SLM [45] and also typically produce little waste [48].

Due to implant sizing constraints, there are appropriate restrictions that must be considered for the AM of porous implant materials. The interplay between net pore size and implant porosity can be tuned by adjusting the corresponding size of the unit cell and scaffold struts (Figure 2-2). An increase in strut diameter with a constant unit cell size or a decrease in unit cell size with constant strut diameter will both result in smaller pore diameter. With respect to the osseointegration of implants, the resulting pore size is an important consideration. Bone ingrowth can occur in pores as small as 50 μm in diameter [49], but further description of pore size in implants is complicated and highlighted in both Section 2.1.5 and Appendix 1. For AM processes, the minimum strut size possible in the porous material is dependent on the feedstock characteristics and optics of the energy source [50]. Often, the smallest fabricable strut size in SLM processes is on the order of 200 μm [51] and melt pools in DED tend to be larger than those in SLM [52]. After PBF, the resulting surface morphology of the part has a characteristic micro-rough texture with partially-

melted powder fused to the surface [53]. This native surface can be modified through a variety of post-processing techniques to add topography at other length scales or introduce macromolecules for local release at the site of the implant. Other forms of post-processing can be applied to additively manufactured components to compensate for poorer mechanical properties and any increased fracture risk of the material. For instance, additively manufactured parts can be more prone to fatigue failure than wrought counterparts in the scope of current AM technology [54]. Post-process hot isostatic pressing can reduce the number of internal defects in AM parts and help increase their overall fatigue strength [55].
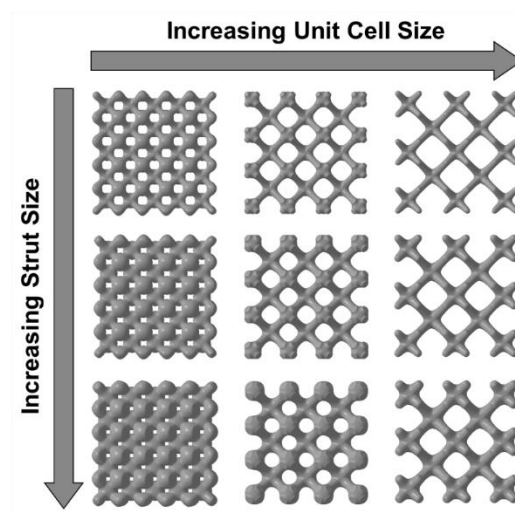
Figure 2-2: *Effect of altering design parameters on the resulting scaffold design in porous materials. Reproduced from* [37] *with permission.*

2.1.3 Surface Modification Strategies

Surface modification strategies are often used to improve host response and offer the potential to alter both surface chemistry and surface topography. Titanium substrates generated through additive manufacturing can be further improved to promote osseointegration through these post-processing techniques.

The surface chemistry directly influences the innate host response with both short-term and long-term consequences. The mitigation of ion release in certain metals, as an example, can aid in preventing corrosion and toxicity within the local implant environment [56]. In addition to creating non-toxic implants, modifications to the surface chemistry directly relate to the hydrophilicity of the implant [57]. With respect to the surface composition, various forms of bioactive glass and calcium phosphate bioceramics can form apatite at their surface [58]. On the surface of metallic implants, organic-inorganic composite materials can be integrated using bioceramic nanoparticles with the addition of a binder or within a polymeric matrix material [59]. Similarly, other physiologically-relevant materials

including antibacterial materials [60], proteins [61], or other macromolecules can also be integrated via chemical modification of the implant surface.

However, assuming the use of a biocompatible material, adding topographical features to the surface can prove more beneficial than minor changes in surface chemistry [62]. As some AM techniques rely on the fusion of molten powder particles, their native surface after fabrication contains an array of partially-fused powder, with sizes on the order of 30-45 μm [63]. It has often been shown that implant materials with multiscale roughness result in better osseointegration [64–66] due to the increase in net area available for deposition of mineralized tissue and migratory-enabling characteristics of adsorbed biological entities on the implant surface. In particular, the collective combination of sub-micron (< 1 μm), microscale (< 10 μm), and coarse-microscale (> 10 μm) features improve the overall integrity of the bone-implant interface [15,67] compared to surface structures that are missing topography at any of these length scales [68]. The post-processing steps to induce this form of multiscale topography are essential for any fabrication procedure to improve both the short-term and long-term performance of the implant, and several surface modification techniques can be applied to conventionally manufactured titanium [60].

In an ideal situation, modifying both the surface chemistry and surface topography is possible to expedite bone growth in porous scaffolds [69]. However, performing these simultaneously in porous materials proves to be a challenge. Some processing techniques such as grit blasting [70,71], laser modification [72,73], or plasma spraying [74,75] rely on line-of-sight application to modify the implant surface. While these techniques are suitable for altering the exterior of an implant, any porous interior remains predominantly unmodified. Acid etching techniques [76,77] provide a method of altering the surface topography within the interior of a porous implant material but lack the combinatory effect of substantial chemical modification. Micro-arc oxidation offers a means to modify both the chemistry and topography of the surface but is restricted to deposition of only oxides of the base metal, calcium, and phosphorus [78,79].

Coating techniques are highly suited to the surface modification of porous materials due to their ability to introduce organic-inorganic composite materials [80] and alter the surface structure to achieve dual-scale topography in the interior of the pores [81]. The development of novel composite materials, such as the succinate-alginate gel-based films presented in Chapter 4, offers a way to locally introduce relevant biomolecules to any potential sites of new bone growth.

2.1.4 *In Vitro* Characterization of Materials

The first step in assessing the potential for osseointegration of implant materials often uses *in vitro* characterization with simulated body fluids or cell culture. Work from Davies highlights some of the key benefits to *in vitro* modeling of the bone-implant interface, including aspects of organic matrix secretion and mineralization [3] but cytocompatibility

assays also offer benefits to quantitatively assess the biocompatibility of implant surfaces. To assess the compatibility with osteoblasts, many cell lines are available to characterize cell-material response. Primary cells extracted from human or animal tissue and immortalized cell lines (including Saos-2, MG-63, or MC3T3-E1 cells) are all widely used to characterize the interaction of osteoblasts and biomaterials, where Czekanska et al. outline the various advantages and disadvantages of each cell type [82]. The Saos-2 cell line, used in Chapters 4 and 5 of this thesis, is derived from human osteosarcoma cells but possesses many osteoblastic properties and has the added benefit of rapid growth [83]. Despite being smaller than human osteoblasts (both adherent and in suspension), the Saos-2 line is similar to human osteoblasts in that alkaline phosphatase is produced [84]. The alamarBlue assay, based on the reversible conversion from resazurin to fluorescent resorufin, is compatible with the Saos-2 cell line, acting as an intermediate electron acceptor in the electron transport chain during aerobic respiration and thereby a marker of metabolic activity and cell proliferation [85]. Another measurement of cell activity, the bicinchoninic acid (BCA) assay relies on amino acids and the biuret reaction to convert Cu^{2+} ions to Cu^+. BCA has a high affinity for the free Cu^+ ions, producing a colorimetric change upon reaction that is detectable via absorption measurement between 550-570 nm [86]. Other cells, including human umbilical vein endothelial cells (HUVECs), can model relevant vascular development processes *in vitro*. When seeded on extracellular matrix or its synthetic counterpart (as in Chapter 4), these cells form capillary-like tubes with neighbouring cells to rapidly build a provisional vascular network, which is often used to assess the angiogenic activity of various macromolecules [87].

These forms of *in vitro* assay are important to minimize the number of animals required for the assessment of implant materials and have been extensively applied to porous scaffolds of varying material composition in the form of 3D cell culture [88]. Ultimately, while these types of tests serve as an excellent first step in the characterization of porous metals or surface coatings, *in vivo* trials provide the most accurate environment to assess biomaterials since they can examine the simultaneous interaction of all relevant cell types and macromolecules at once. As a result, *in vivo* studies are the only true way to assess osseointegration.

2.1.5 *In Vivo* Characterization of Porous Scaffolds

The pre-clinical performance of porous materials is best characterized using animal models, with implantation often occurring in the long bones or calvaria of animals. The respective size of the bone, physiological loading conditions, rates of bone formation, and even multiscale structure can differ between animal models, often making it difficult to select a meaningful site for implantation [4]. Some of the most common models for *in vivo* biomaterial assessment include murine (rodent), leporine (rabbit), canine (dog), ovine (sheep), porcine (pig), and caprine (goat) [89]. Each of these has its benefits and drawbacks as it relates to modeling human bone regeneration. Leporine bone, as one of the most

common *in vivo* models for bone regeneration [90], is conveniently used due to ease of handling and relatively young age of skeletal maturity (where growth plate closure occurs at roughly six months, on average) [91,92]. Rabbits, much like humans but unlike some smaller mammals, also undergo a phenomenon called 'secondary remodeling' where populations of osteoclasts and osteoblasts work to sequentially resorb existing bone tissue and redeposit new bone in its place [93]. However, the small size of rabbit bones, physiological loading conditions [94], and comparatively fast rates of bone turnover or apposition [95] limit its direct extrapolation to bone regeneration in humans.

Within the rabbit, there are several anatomical locations (tibia, femur, calvaria, ulna) [89] that can be used to assess bone growth. When sizing implants for each of these locations, the guidelines typically follow that of critical-sized defects (CSDs). A CSD is often defined as the smallest size of a bone defect that will not spontaneously heal over the lifetime of the animal [96], although its efficacy is somewhat disputed [97]. Based on the anatomy and physiology of the leporine skeleton, the CSD for the long bones of the New Zealand White Rabbit tibia is roughly 1.4 cm in diameter [98]. When designing implants for pre-clinical implantation, this represents the minimum diameter of the implant that can be used to reliably assess the kinetics and quality of bone regeneration.

Looking at the timeline for leporine bone formation in porous materials, it is necessary to pick relevant time points to assess bone formation within the porous interior. For meaningful investigation of leporine bone evolution inside porous titanium, early endpoints often examine bone structure at four weeks of implantation [99–101] although regions of bone can begin to form after only two weeks of recovery [99,101]. Later stages of bone growth in this implant model are commonly assessed up to twelve weeks following implantation [100].

Concerning porous materials in particular, it is important to understand the interaction between any design parameters and potential influences on bone regeneration. Two factors of interest are the pore size of the implant and net porosity of the implant interior [102]. For stochastic and trabecular-like scaffold structures, the pore size can vary slightly throughout depending on design parameters [103]. Due to the design constraints imposed by additive manufacturing technologies, pore sizes for leporine implants are often between 100-1000 μm in diameter with net porous volumes ranging from 30-90% [37]. While still widely disputed, metallic implants with pore diameters between 300-500 μm have shown improved outcomes when characterizing bone regeneration in leporine [104] or canine models [105] but no definitive observations have been agreed upon in the literature. The net porosity of the implant has been less thoroughly investigated, but several histomorphometric measurements tend to be improved when the interior porosity ranges from 50-70%, indicating greater implant stability [37].

2.2 Bone Structure

The multiscale hierarchy of bone structure governs its robust mechanical properties. Ubiquitous structural entities, each with their own characteristic arrangement, exist within each layer of the hierarchy to assemble the unique framework of organic, water, and mineral components in the tissue [106]. When designing bone-interfacing materials, it is necessary to consider how each structural entity within the hierarchy is influenced by the implant to develop a structural and functional connection during osseointegration [107]. An overview of the hierarchical levels, ranging from millimeter to nanometer length scales, can be found in Figure 2-3.
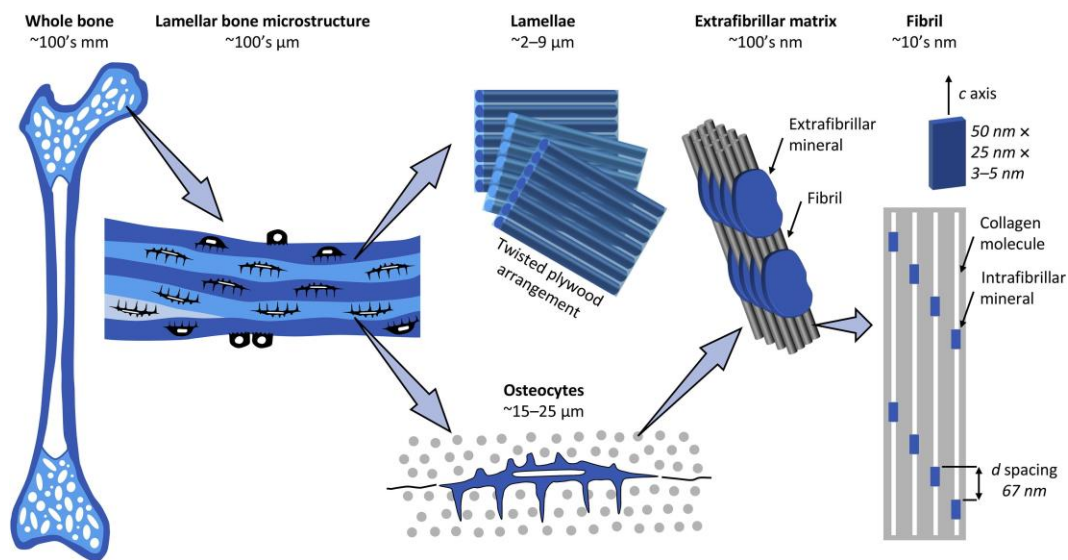
Figure 2-3: *Overview of the hierarchical structure in lamellar bone, spanning from macroscale to nanoscale. Reproduced from* [106] *with permission.*

2.2.1 Bone Structure at the Macroscale

At the macroscale, the long bones can be subdivided into their *cortical* and *cancellous/trabecular* components. As a whole, the human skeleton is composed of 80% cortical bone and 20% trabecular bone [108]. The cortical fraction is highly dense by nature and surrounds the internal marrow cavities of the bone. In contrast, the trabecular fraction occupies the marrow space in a highly porous rod-plate network. The porous nature of trabecular bone has led to the development of bioinspired metallic implant materials [109] for the next generation of implants in the orthopaedic and prosthodontic sectors.

However, a closer examination of trabecular bone shows distinct variation and anisotropy depending on the location in the body [110]. Dividing the femur into epiphyseal (proximal/distal ends of the whole bone), diaphyseal (shaft in the midsection), and metaphysis (intermediate region between epiphysis and diaphysis) can offer insight into the

trabecular organization in these regions. Specifically, looking at the transition from the femoral head into the femoral neck shows distinct patterns in trabecular organization in computed tomography (CT) datasets (Figure 2-4).
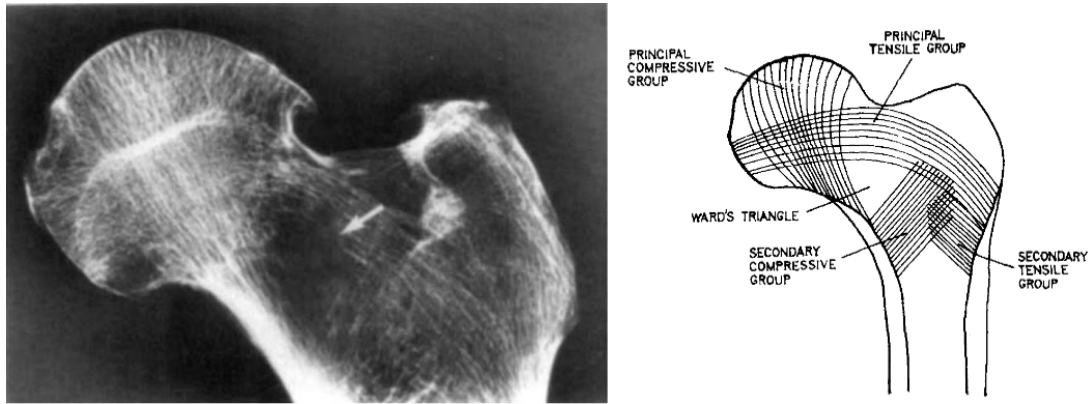
Figure 2-4: *(Left) Computed tomography section along the frontal plane of the femoral head displaying osteopenia. (Right) Regions of distinct trabecular co-alignment are seen in varying locations within the bone. Figures adapted from* [111] *with permission.*

Patterns in trabecular alignment were first explained by Julius Wolff, who surmised that trabecular bone adapts over time based on its mechanical loading regime [112]. In particular, this can manifest in the angular arrangement of trabecular bone under prolonged exposure to changes in directional strain [11]. These local variations in strain directionality create an inherently anisotropic organization within the femur, where mechanical properties vary depending on specific location and age [26]. Physiological markers used as mechanical axes in the lower extremity, such as the Mikulicz line [113] or femoral mechanical axis [114], can be used for realignment in arthroplasty to improve implant durability and reduce the likelihood of problematic conditions such as aseptic loosening [114]. The complexity of contouring porous materials to better adapt to local mechanical cues in bone tissue can extend beyond looking at the global axis of the long bone, taking into account the aforementioned patterns in trabecular bone orientation. Unidirectional functional-grading or reinforcement of porous implant materials does not take into account the dynamic and complex local strain fields within the tissue, and as a result, is unable to adaptively model trabecular orientation along the femur. Novel methods to design porous implants, much like the asymmetrical Voronoi tessellation illustrated in this thesis, are required to accurately model the strain-derived physiological patterns from the resected bone tissue.

2.2.2 Bone Structure Below the Macroscale

Within human cortical bone lies a Haversian substructure, where the repeating fundamental unit is the osteon. As illustrated in Figure 2-3, the osteon consists of concentric lamellae arranged around a central Haversian canal (HC). Each lamella within the osteon is offset

by neighbouring lamellae in a periodicity of 5-7 μm, and the constituent microfibrils in a lamella are angularly offset by 5-25° in a 'twisted plywood' arrangement [115]. The interconnected network of Haversian and Volkmann canals in cortical bone [116] contains both blood vessels and nerve fibres, aiding in nutrient delivery, oxygen transport, and as a signal transduction pathway through the existing tissue.

At the lower end of the microscale, extending into the mesoscale, lies the interconnected network of resident osteocyte cells that serve as a mechanotransduction pathway to report any changes within the local environment of the tissue [117]. The osteocytes reside within cavities known as lacunae, with a diameter of 5-20 μm [118] and are known to change their shape depending on the maturity of the bone tissue [119] and loading conditions [120]. Extensions from the main body of the osteocyte lacuna radiate outward to form an interconnected network of canaliculi within the tissue with a diameter of roughly 350 nm. The combination of lacunae and canaliculi join to compose a connected system known as the lacuno-canalicular network (LCN), responsible for the strain-driven transport of fluid and biochemical stimuli throughout surrounding tissue [121].

Mineralized collagen fibrils self-organize themselves into a distinct bundled form [122,123]. Mineralization can occur within these collagenous bundles, nucleating as small mineral crystallites [124] or calcospherulites [125] and growing along the collagen fibrils into ellipsoidal forms of mineral [18,122]. Below the level of the microfibril or fibril bundle lies the single mineralized collagen fibril. The characteristic banding pattern commonly observed in transmission electron microscopy (TEM) is composed of overlap zones (27 nm) and gap zones (40 nm) [126]. The exact spatial location and nucleation kinetics of mineral at this length scale is still often disputed, where evidence exists to support both intrafibrillar [127] and extrafibrillar [128] mineralization patterns. Based on its rapid deposition during bone apposition, the earliest form of bone tends to have a disorganized collagen structure [129]. The constituent mineralized collagen fibrils have minimal co-alignment to each other or any of the structural features (including lacunae and vascular spaces) in this form of bone termed 'woven bone' [130] and the tissue is mechanically weaker in comparison to mature bone tissue. This woven bone undergoes remodelling over time and the collagen fibrils begin to show periodicity in their alignment, gradually altering by as much as 90° across osteonal lamellae as an example [115,131,132]. This ordered form of bone, termed 'lamellar bone', is robust in nature, giving bone its inherent mechanical properties.

Each of these hierarchical features has been summarized in the literature with respect to their appearance in mature bone tissue and even at simple implant interfaces, but what remains to be determined is if structural changes occur in mineral ellipsoids – an often overlooked feature of bone composed of several fibril bundles – when interfacial bone growth inside and outside of the porous metallic substrate is characterized using modern electron microscopy.

2.3 Osseointegration at the Implant Interface
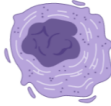
The initial deposition and development of new bone tissue around an implant consists of key transitional and formative processes before reaching its most mature form. Holistically, these processes determine when, where, and what type of bone will interface with a metallic implant. The spatial and temporal characteristics of each process are important for the timeline of osseointegration, where short-term implant success is often correlated to long-term implant success.

2.3.1 Cells in the Peri-Implant Environment

Much of the process of osseointegration depends on the recruitment, migration, and secretome of specific cells in the peri-implant environment. Analysis of the cell and extracellular matrix components during osseointegration is often conducted through histology, where specific staining procedures can be used in conjunction with microscopy methods to evaluate the process of bone formation at the implant surface [133]. A list of cells with high abundance in the peri-implant environment, some of which are seen in histology sections in Chapter 5, can be found in Table 2-2 with a brief description of their primary function.

Table 2-2: *List of select cell types in the peri-implant environment. Images generated in BioRender.*

Cell		Primary Function	Reference
Bone and Progenitor Cells			
Osteoblast		Depositing of collagen-rich osteoid during matrix formation, which later becomes mineralized.	[134]
Osteocyte		Mechanosensation and homeostasis of the mineralized bone tissue.	[134]
Osteoclast		Resorbing mineralized bone tissue, critical for repair of damaged or old tissue.	[134]
Mesenchymal Stem Cell		Non-specialized cells that are a precursor to osteoblasts, adipocytes, or other specialized cells.	[135]
Immune Cells (Granulocytes/Agranulocytes)			
Lymphocyte		Regulation and recruitment during the immune response; antibody production.	[136]

Neutrophil		Phagocytosis, degranulation, and trapping of microbes during the immune response.	[137]
Vascular-Associated Cells			
Endothelial Cell		Innermost lining cells of capillaries and blood vessels; facilitating mass transport through the tissue.	[138]
Pericyte		Facilitating transport and leakage at the vascular wall; governance of endothelial proliferation.	[139]
Erythrocyte		Delivery of oxygen throughout a biological tissue to maintain homeostasis.	[140]
Marrow-Associated Cells			
Adipocyte		Passive component within marrow stroma; possible energy storage or mediator of lipid metabolism.	[141]
Megakaryocyte		Platelet production in the bone marrow.	[142]

2.3.2 Osteoinduction, Osteogenesis, and Osseointegration

With respect to new bone formation at defective sites, the two predominant forms of bone formation at an implant surface can be divided into competing processes of *distance* and *contact osteogenesis* [65,143]. In the process of distance osteogenesis, new bone forms by nucleating on the surface of pre-existing bone and propagating inward to fill a defect site with mineralized tissue [62]. During contact osteogenesis, however, apposition of *de novo* bone tissue occurs directly on the implant surface by differentiating cells and propagates outward to span the bone defect [62]. The process by which osteogenesis is initiated, termed *osteoinduction* [107], encompasses the transition of mesenchymal stem cells to that of an osteoblast lineage for bone formation and is tightly intertwined with physical [144,145] and molecular stimuli [146,147] at the implant surface. The recruitment of osteoblasts and tissue formation along the implant surface continues via *osteoconduction* after the osteoinductive process has taken place [107], leading to tissue apposition that self-propagates along the implant surface. In the context of porous scaffolds, the osteoconductive process includes the guided penetration of bone growth into the pores along the struts of the scaffold [148]. While all of these biological processes have importance in developing a means for implant survival, expedited recovery is chiefly dependent on the ability for load transmission at the bone-implant interface, making early and complete osseointegration one of the all-important metrics for implant success.

In general, distance osteogenesis is not viewed as favourably as contact osteogenesis, although both can occur simultaneously at sites of new bone growth [149]. In cases where distance osteogenesis is predominant, direct contact between the bone matrix and the implant is less prevalent due to an intervening layer of cells [62]. As a result, sites of distance osteogenesis encapsulate the implant with bone but tend to lack a primary bone-implant connection. However, in instances of contact osteogenesis, the deposition of bone matrix occurs directly onto the implant [62], developing a stronger functional connection as the bone matrix and implant can integrate more intimately. The development of the structural and functional connection, or osseointegration, of an implant should consist of immobilization of the implant under loading, the apposition of new bone adjacent to the implant without fibrous tissue, the absence of motion between the tissue and the implant, and normal bone/marrow zones at the microscopic level [106]. While each of these has been previously shown to occur in the centre of porous Ti6Al4V scaffolds [149,150], topological designs have not yet been optimized and the best geometry may indeed differ depending on the animal model.

In the timeline of peri-implant healing, Dondossola and Friedl summarize the general wound healing process into three distinct stages [151], drawing some similarities to the fracture healing cascade [152]. First, in the initial period of wound healing, local trauma caused by the insertion of the implant results in bleeding at the implant site and the rapid deposition of fibrin on the implant surface. This stage also includes an acute inflammatory response, with recruitment of neutrophils and macrophages to the implant site. The second period of wound healing is primarily centred around the sprouting of neovessels in the peri-implant environment based on the secretion of growth factors in the first phase, providing a template for tissue homeostasis. Lastly, the inflammatory response begins to subside as osteoblasts are derived from their mesenchymal progenitors and bone matrix is deposited, with osteoblast migration enhanced by the properties of the initial fibrin layer [62]. This cascade is known to apply at the bone-implant interface of traditional metallic implant materials, but what remains to be seen is whether this sequential process occurs at both the exterior and interior of complex porous geometries, like those produced via additive manufacturing in Chapter 5 of this thesis.

2.3.3 Implant Neovascularization

The distribution of macromolecules in the peri-implant environment is dictated in part by how new blood vessels form networks near the implant surface during the neovascularization stage in implant wound healing. Most biological processes in the body depend on the transport of growth factors, proteins, or other macromolecules through these blood vessels. One possible mechanism for recruiting pre-osteoblast or mesenchymal progenitors at the implant interface is from the perivascular cells that line the wall of this newly-formed vessel network [153]. Examining tagged locations of Runt-related transcription factor 2 (RUNX2), a key protein involved in osteoblast differentiation, has

additionally shown some early evidence of localization in close proximity to the vascular network [154]. Implant surface design has a profound effect on how these new vessels branch within the peri-implant environment. Examination of implants with nanoscale surface topography has shown higher vessel densities through longitudinal imaging of the implant compared to surfaces with lower nanoscale roughness, with the largest changes tending to occur within the first 15 days [155].

Pro-angiogenic proteins are essential for helping build this provisional vascular network to aid in the process of osseointegration. Vascular endothelial growth factor (VEGF), and the VEGF-A isoform in particular, is one such protein involved in angiogenesis. VEGF is known as a mitogen for endothelial cells, regulating both cellular migration via chemoattraction and proliferation through kinase activation [156]. The migratory behaviour of osteoblasts has also been shown to be induced by elevated VEGF levels [157]. Platelet-derived growth factor (PDGF) also has direct applications with respect to the angiogenic-osteogenic environment. PDGF, and the PDGF-BB isoform in particular, is known to play a role in vascular development by increasing early vascular area [158] and can aid in the recruitment of mural cells (including pericytes) to stabilize the vascular wall after development [159]. One possible mechanism has also been proposed that outlines the pathway from perivascular cell to mesenchymal stem cell to pre-osteoblast using elevated PDGF levels as a driving force [160]. Both of these pro-angiogenic factors can be upregulated in hypoxic environments, where a lack of oxygen causes rapid vascular development [161]. Prolonged exposure to these ischemic conditions is problematic, as major disruptions to blood flow to the tissue can lead to necrosis [162]. As a result, there is a need to develop novel materials, like the alginate-succinate implant coating presented in this thesis, to safely induce neovascularization at the implant surface.

2.4 Multiscale 3D Imaging Techniques

The relatively large size of the implant and small size of some sequential biological processes makes 2D and 3D characterization of the bone-implant interface a challenge. Due to the hierarchical nature of the bone tissue itself and limitations in resolution or sample size, there is truly no 'one-size-fits-all' imaging modality to simultaneously view the structural features in bone or at implant interfaces with sufficient resolution for feature detection. As a result, correlative strategies using multiple imaging techniques are required to achieve a complete picture of bone and bone-implant interactions in three dimensions. An overview schematic detailing the structural levels in bone and imaging modalities is shown in Figure 2-5, and some techniques (X-ray microcomputed tomography, Xe FIB-SEM, and Ga FIB-SEM) are described further in this section.
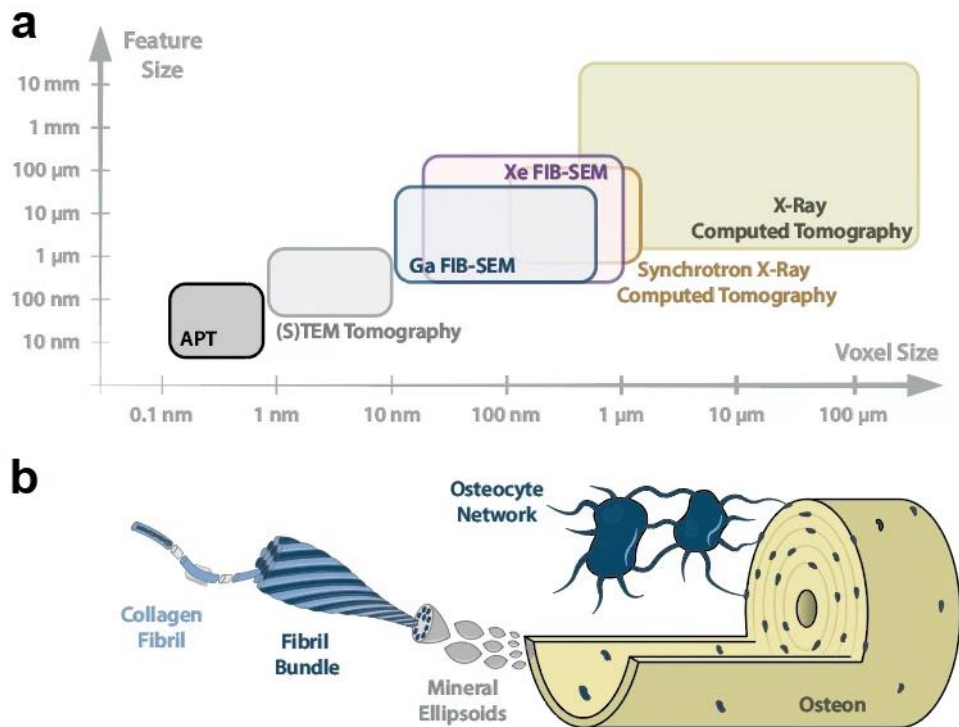
Figure 2-5: *(A) Multiscale imaging modalities for bone with associated feature and voxel sizes for each. (B) Hierarchical structure of bone between the level of a single collagen fibril and the osteon. FIB-SEM: Focused ion beam – scanning electron microscopy; APT: Atom probe tomography; (S)TEM: Scanning transmission electron microscopy. Reproduced from* [163].

2.4.1 X-Ray Microcomputed Tomography

X-ray imaging techniques are at the forefront of bone characterization for assessing skeletal regeneration in both clinical and research settings. X-ray microcomputed tomography (Micro-CT) is one of the more common laboratory methods for quantitatively assessing bone architecture and histomorphometry.

Working with a polychromatic beam from a fixed source, the sample of interest rotates with a fixed angular step. Based on the absorbance of X-rays within the sample, a 2D projection is obtained at a given angle where regions of high intensity correspond to high X-ray transmittance through the sample. The process is repeated over a 180° or 360° rotation of the sample to achieve a complete rotation series, where the angular projections can later be reconstructed to form a 3D image [164].

With respect to bone histomorphometry, three common imaging indicators for osseointegration are percent bone area (BA), percent of bone-implant contact (BIC), and

bone volume fraction (BV/TV). These metrics can all be obtained from micro-CT reconstructions or other means to quantify the secondary stability of the implant following osseointegration. BV/TV measurements are usually performed by taking the number of voxels attributed to bone and dividing by the total number of voxels available for bone growth within the defect [165]. Similarly, BA measurements measure the fraction of bone-like pixels in the 2D image series as a fraction of the area available for bony ingrowth [166]. BIC measurements are concerned with the immediate vicinity of the implant and are measured as the total surface fraction of the implant that is in direct contact with bone tissue [167] – albeit with some dependence on the resolution of the specific imaging technique. Within a porous implant, histomorphometric assessment is critically associated with the porous interior. Regions of abundant bone apposition appear immediately outside the implant and within the exterior pores, while more sparse bone apposition occurs deep within the implant interior [150]. For purposes of characterizing histomorphometry in porous materials, the segmentation workflow often benefits from subcategorizing the porous region into interior and exterior regions.

Micro-CT measurements are excellent as a first, non-destructive step in characterizing the osseointegration potential of regenerative treatments and implant materials. Computational techniques exist for the reduction of micro-CT artifacts such as beam hardening phenomena [168] and ring artifacts [169] to produce high-quality 3D images of the bone-implant interface. With the addition of statistical analyses, morphometric data relating to bone apposition can be used to assess the efficacy of various porous implants or treatment strategies. However, without the use of synchrotron facilities, micro-CT can be restricted by limitations in resolution. To obtain higher-resolution maps of the bone-implant interface and assess osseointegration across the multiscale, other forms of 3D imaging are required.

2.4.2 Focused Ion Beam Serial Sectioning

Focused ion beam (FIB) technology offers a higher-resolution, complementary 3D imaging technique to micro-CT via serial sectioning and subsequent imaging with scanning electron microscopy (SEM) [170]. In FIB-SEM systems, the microscope is equipped with both an ion source for directed milling of user-specified areas and an electron beam for backscatter (BSE) and secondary (SE) electron imaging modes. Similar to most methods of electron microscopy, the process takes place under vacuum meaning that specific sample preparation protocols are required prior to data collection. As examples, bone samples are both naturally hydrated and non-conductive [171]. Serial dehydration and proper sputter coating of the material can mitigate problems attributed to these respective effects in the SEM chamber [172].

In FIB applications, incident ions interact with the target material to create a sputtering effect, where a single ion will knock several target atoms out of their respective locations to remove a small amount of material (Figure 2-6) [173]. Over several minutes of exposure

to the ion beam, the amount of removed material can be on the order of several microns. This is sufficient to prepare and thin electron-transparent lamellae for transmission electron microscopy or tomography acquisition [174]. Among the most common ion sources for milling is the gallium liquid metal ion source [175], but recent advances have developed ion sources that utilize xenon plasma in a form of microscopy known as PFIB microscopy. The use of Xe ions as an inductively coupled plasma source can achieve much higher beam currents (up to 10 μA) than the average Ga liquid metal ion source (up to 50 nA) when holding the accelerating voltage constant [176]. On a per coulomb basis, PFIB is able to remove more material than traditional Ga FIB due to the higher collision energy of the incident ion [177]. The combinatory effect of these phenomena means that PFIB-SEM tomography acquisition can probe significantly larger volumes and has an overall higher milling efficiency than the typical Ga FIB-SEM process with equal milling times (Figure 2-7A).
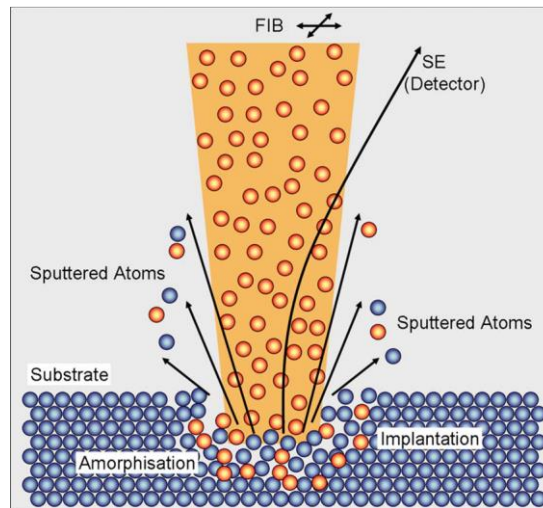
Figure 2-6: *Sputtering behaviour under the ion beam during milling. Incident Xe ions in the PFIB result in higher sputter yields than Ga in FIB. Reproduced from* [178] *with permission.*

The workflow for most FIB-SEM and PFIB-SEM tomography procedures generally follows a similar format, albeit with some flexibility in the order of operations (Figure 2-7B):

(i) Deposit a protective capping layer on the top surface of the region of interest (ROI) via ion-assisted or electron-assisted deposition to prevent excess ion damage to the cross-section;

(ii) Create fiducial markers for image alignment and spatial tracking during tomography acquisition;

(iii) Mill trenches on either side of the ROI to accommodate milled material during 3D data acquisition;

(iv) Use low-current milling protocols to prepare the cross-sectional face;

(v) Iteratively mill and image the cross-section to produce a stack of 2D images.
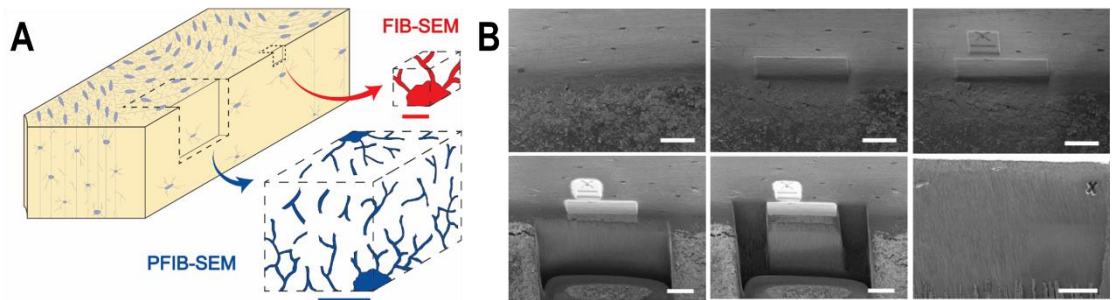
Figure 2-7: (A) Comparative sizing of Ga FIB tomography volumes and PFIB tomography volumes with respect to the LCN in cortical bone. (B) Stages of FIB-SEM tomography preparation including deposition of capping layer and fiducial, with subsequent milling to isolate the region of interest. Reproduced from [18] *with permission.*

While FIB-SEM and PFIB-SEM tomography is usually successful in homogenous materials, including seminal work in bone tissue [179] and at the bone-implant interface [180], any mismatch in milling rates in heterogeneous materials can cause complications. Milling across composite materials can often produce a curtain structure on the cross-section of interest [181], which can be mitigated by periodically changing the angle of orientation of incident ions with respect to the sample or through image post-processing. Specifically, studies of the bone-implant interface with FIB-SEM or PFIB-SEM, like the study in Chapter 6, have not been extensively conducted, possibly due to the added challenge of mismatched rates in milling of the interfacial titanium and mineralized bone tissue. Furthermore, the microscale mineral packing arrangement in the interfacial tissue inside porous scaffolds has not been fully described. 3D imaging modalities offer an additional means of describing the osseointegration process using these multiscale characterization modalities.

2.4.3 Deep Learning Segmentation Workflows

In the realm of 3D image acquisition using electron and X-ray techniques, it is often important to render specific features in 3D for both qualitative and quantitative analysis. Depending on the dataset, it may be useful to employ semantic or instance segmentation techniques. In semantic segmentation approaches, all items of the same class (e.g. osteocyte lacunae) are broadly combined into the same voxel/pixel cloud [182] irrespective of their number or independence. Instance segmentation techniques go a step further in specificity,

segmenting multiple items of the same class into objects with discrete boundaries from one another [182]. This allows for the application of a unique identifier to objects of the same type (e.g. Lacuna #1, Lacuna #2, etc.) while still recognizing their commonalities. The development of deep learning workflows for image classification has been productive in the field of biomineralization research, with successful segmentation strategies applied to mineral clusters [18,122], the LCN [18], and the osseointegration of porous materials [182,183].

The most common deep learning framework in medical imaging is UNet [184], named aptly after the shape of its encoding and decoding branches. Training a UNet classifier to segment datasets first requires the input of a ground truth, a manually segmented series of images in most cases, as training material to identify common semantic features within the image series. The classifier contains multiple layers to downsample the image in the encoding branch and upsample the image in the decoding branch. Contained within each layer of the framework is a series of filter matrices, with random values upon initialization that are iteratively changed to minimize the value of a loss function. The application of these filter matrices to the image serves as a convolution, to look for specific patterns within the dataset with respect to individual weighting factors in the matrix. Deeper layers within the neural network are able to look for more complex patterns within the data as the image becomes pooled, and the results from each layer in UNet are concatenated to form a single-channel image in the ascending branch. Overall, the application of deep learning classifiers to 3D datasets, like the micro-CT dataset in Chapter 5, provides an efficient and accurate way to render the complex and hierarchical nature of bone mineral apposition at the implant interface.

Linking the *design*, *modification*, and multiscale *characterization* of porous implants lies at the intersection of biological science and materials science. This thesis builds on the known literature presented in this section to provide further insight into the development of materials, with the end goal of improving and understanding the osseointegration of porous metals.

References

1. Brånemark PI, Breine U, Adell R, Hansson BO, Lindström J, Ohlsson Å. Intra-Osseous Anchorage of Dental Prostheses:I. Experimental Studies. Scand J Plast Recon. 1969;3(2):81–100.

2. Adell R, Lekholm U, Rockler B, Brånemark PI. A 15-year study of osseointegrated implants in the treatment of the edentulous jaw. Int J Oral Maxillof. 1981;10(6):387–416.

3. Davies JE. In vitro modeling of the bone/implant interface. Anatomical Rec. 1996;245(2):426–45.

4. Pearce A, Richards R, Milz S, Schneider E, Pearce S. Animal models for implant biomaterial research in bone: A review. European Cells Mater. 2007;13:1–10.

5. Yang Y, Hu H, Zeng M, Chu H, Gan Z, Duan J, Rong M. The survival rates and risk factors of implants in the early stage: a retrospective study. Bmc Oral Health. 2021;21(1):293.

6. Goiato MC, Santos DM dos, Santiago JFJr, Moreno A, Pellizzer EP. Longevity of dental implants in type IV bone: a systematic review. Int J Oral Max Surg. 2014;43(9):1108–16.

7. Hughes RE, Batra A, Hallstrom BR. Arthroplasty registries around the world: valuable sources of hip implant revision risk data. Curr Rev Musculoskelet Medicine. 2017;10(2):240–52.

8. Plessis A du, Broeckhoven C, Yadroitsava I, Yadroitsev I, Hands CH, Kunju R, Bhate D. Beautiful and Functional: A Review of Biomimetic Design in Additive Manufacturing. Addit Manuf. 2019;27:408–27.

9. Chappard D, Baslé MF, Legrand E, Audran M. Trabecular bone microarchitecture: A review. Morphol. 2008;92(299):162–70.

10. Singh I. The architecture of cancellous bone. J Anat. 1978;127(Pt 2):305–10.

11. Barak MM, Lieberman DE, Hublin JJ. A Wolff in sheep's clothing: Trabecular bone adaptation in response to changes in joint loading orientation. Bone. 2011;49(6):1141–51.

12. Lee BP, Messersmith PB, Israelachvili JN, Waite JH. Mussel-Inspired Adhesives and Coatings. Annu Rev Mater Res. 2011;41(1):99–132.

13. Hanawa T. A comprehensive review of techniques for biofunctionalization of titanium. J Periodontal Implant Sci. 2011;41(6):263–72.

14. Zhao L, Chu PK, Zhang Y, Wu Z. Antibacterial coatings on titanium implants. J Biomed Mater Res Part B Appl Biomaterials. 2009;91B(1):470–80.

15. Brånemark R, Emanuelsson L, Palmquist A, Thomsen P. Bone response to laser-induced micro- and nano-size titanium surface features. Nanomed Nanotechnol Biology Medicine. 2011;7(2):220–7.

16. Jemat A, Ghazali MJ, Razali M, Otsuka Y. Surface Modifications and Their Effects on Titanium Dental Implants. Biomed Res Int. 2015;2015:791725.

17. Micheletti C, Hurley A, Gourrier A, Palmquist A, Tang T, Shah FA, Grandfield K. Bone Mineral Organization at the Mesoscale: A Review of Mineral Ellipsoids in Bone and at Bone Interfaces. Acta Biomater. 2022;142:1–13.

18. Binkley DM, Deering J, Yuan H, Gourrier A, Grandfield K. Ellipsoidal mesoscale mineralization pattern in human cortical bone revealed in 3D by plasma focused ion beam serial sectioning. J Struct Biol. 2020;107615.

19. Hip and Knee Replacements in Canada: CJRR Quick Stats, 2019–2020. CIHI; 2021.

20. Abu-Amer Y, Darwech I, Clohisy JC. Aseptic loosening of total joint replacements: mechanisms underlying osteolysis and potential therapies. Arthritis Res Ther. 2007;9(Suppl 1):S6.

21. Meredith N. Assessment of implant stability as a prognostic determinant. Int J Prosthodont. 1998;11(5):491–501.

22. Franklin J, Malchau H. Risk factors for periprosthetic femoral fracture. Inj. 2007;38(6):655–60.

23. Tabrizi R, Behnia H, Taherian S, Hesami N. What Are the Incidence and Factors Associated With Implant Fracture? J Oral Maxil Surg. 2017;75(9):1866–72.

24. Huiskes R, Weinans H, Rietbergen B van. The Relationship Between Stress Shielding and Bone Resorption Around Total Hip Stems and the Effects of Flexible Materials. Clin Orthop Relat R. 1992;274(NA;):124–34.

25. Nagels J, Stokdijk M, Rozing PM. Stress shielding and bone resorption in shoulder arthroplasty. J Shoulder Elb Surg. 2003;12(1):35–9.

26. Murphy W, Black J, Hastings G. Handbook of Biomaterial Properties. New York, NY: Springer; 2016.

27. Wauthle R, Ahmadi SM, Yavari SA, Mulier M, Zadpoor AA, Weinans H, Humbeeck JV, Kruth JP, Schrooten J. Revival of pure titanium for dynamically loaded porous implants using additive manufacturing. Mater Sci Eng C. 2015;54:94–100.

28. Hazlehurst K, Wang CJ, Stanford M. Evaluation of the stiffness characteristics of square pore CoCrMo cellular structures manufactured using laser melting technology for potential orthopaedic applications. Mater Design. 2013;51:949–55.

29. Niinomi M, Liu Y, Nakai M, Liu H, Li H. Biomedical titanium alloys with Young's moduli close to that of cortical bone. Regen Biomaterials. 2016;3(3):173–85.

30. Niinomi M, Nakai M, Hieda J. Development of new metallic alloys for biomedical applications. Acta Biomater. 2012;8(11):3888–903.

31. Li Y, Jahr H, Zhou J, Zadpoor AA. Additively manufactured biodegradable porous metals. Acta Biomater. 2020;115:29–50.

32. Wang Z, Wang C, Li C, Qin Y, Zhong L, Chen B, Li Z, Liu H, Chang F, Wang J. Analysis of factors influencing bone ingrowth into three-dimensional printed porous metal scaffolds: A review. J Alloy Compd. 2017;717:271–85.

33. Wang X, Xu S, Zhou S, Xu W, Leary M, Choong P, Qian M, Brandt M, Xie YM. Topological design and additive manufacturing of porous metals for bone scaffolds and orthopaedic implants: A review. Biomaterials. 2016;83:127–41.

34. Ashby MF, Medalist RFM. The mechanical properties of cellular solids. Metallurgical Transactions. 1983;14(9):1755–69.

35. Al-Ketan O, Rowshan R, Al-Rub RKA. Topology-mechanical property relationship of 3D printed strut, skeletal, and sheet based periodic metallic cellular materials. Addit Manuf. 2018;19:167–83.

36. Choren JA, Heinrich SM, Silver-Thorn MB. Young's modulus and volume porosity relationships for additive manufacturing applications. J Mater Sci. 2013;48(15):5103–12.

37. Deering J, Grandfield K. Current interpretations on the in vivo response of bone to additively manufactured metallic porous scaffolds: A review. Biomaterials Biosyst. 2021;2:100013.

38. Mahmoud D, Elbestawi MA. Selective laser melting of porosity graded lattice structures for bone implants. Int J Adv Manuf Technology. 2019;100(9–12):2915–27.

39. Bandyopadhyay A, Krishna BV, Xue W, Bose S. Application of Laser Engineered Net Shaping (LENS) to manufacture porous and functionally graded structures for load bearing implants. J Mater Sci Mater Medicine. 2008;20(Suppl 1):29.

40. Frazier WE. Metal Additive Manufacturing: A Review. J Mater Eng Perform. 2014;23(6):1917–28.

41. Yap CY, Chua CK, Dong ZL, Liu ZH, Zhang DQ, Loh LE, Sing SL. Review of selective laser melting: Materials and applications. Appl Phys Rev. 2015;2(4):041101.

42. Zhao X, Li S, Zhang M, Liu Y, Sercombe TB, Wang S, Hao Y, Yang R, Murr LE. Comparison of the microstructures and mechanical properties of Ti–6Al–4V fabricated by selective laser melting and electron beam melting. Mater Design. 2016;95:21–31.

43. Gong H, Gu H, Zeng K, Dilip J, Pal D, Stucker B, Christiansen D, Beuth J, Lewandowski JJ. Melt Pool Characterization for Selective Laser Melting of Ti-6Al-4V Pre-alloyed Powder. In: Proceedings of the 25th Annual International Solid Freeform Fabrication Symposium. 2014.

44. Gibson I, Rosen D, Stucker B. Additive Manufacturing Technologies, 3D Printing, Rapid Prototyping, and Direct Digital Manufacturing. 2015;

45. Ngo TD, Kashani A, Imbalzano G, Nguyen KTQ, Hui D. Additive manufacturing (3D printing): A review of materials, methods, applications and challenges. Compos Part B Eng. 2018;143:172–96.

46. Dass A, Moridi A. State of the Art in Directed Energy Deposition: From Additive Manufacturing to Materials Design. Coatings. 2019;9(7):418.

47. Saboori A, Aversa A, Marchese G, Biamino S, Lombardi M, Fino P. Application of Directed Energy Deposition-Based Additive Manufacturing in Repair. Appl Sci. 2019;9(16):3316.

48. Liu S, Shin YC. Additive manufacturing of Ti6Al4V alloy: A review. Mater Design. 2019;164:107552.

49. Itälä AI, Ylänen HO, Ekholm C, Karlsson KH, Aro HT. Pore diameter of more than 100 μm is not requisite for bone ingrowth in rabbits. J Biomed Mater Res. 2001;58(6):679–83.

50. Shi W, Liu Y, Shi X, Hou Y, Wang P, Song G. Beam Diameter Dependence of Performance in Thick-Layer and High-Power Selective Laser Melting of Ti-6Al-4V. Materials. 2018;11(7):1237.

51. Arabnejad S, Johnston RB, Pura JA, Singh B, Tanzer M, Pasini D. High-strength porous biomaterials for bone replacement: A strategy to assess the interplay between cell morphology, mechanical properties, bone ingrowth and manufacturing constraints. Acta Biomater. 2016;30:345–56.

52. Wang C, Tan XP, Du Z, Chandra S, Sun Z, Lim CWJ, Tor SB, Lim CS, Wong CH. Additive manufacturing of NiTi shape memory alloys using pre-mixed powders. J Mater Process Tech. 2019;271:152–61.

53. Pyka G, Burakowski A, Kerckhofs G, Moesen M, Bael SV, Schrooten J, Wevers M. Surface Modification of Ti6Al4V Open Porous Structures Produced by Additive Manufacturing. Adv Eng Mater. 2012;14(6):363–70.

54. Sterling A, Shamsaei N, Torries B, Thompson SM. Fatigue Behaviour of Additively Manufactured Ti-6Al-4V. Procedia Engineer. 2015;133:576–89.

55. Tammas-Williams S, Withers PJ, Todd I, Prangnell PB. The Effectiveness of Hot Isostatic Pressing for Closing Porosity in Titanium Parts Manufactured by Selective Electron Beam Melting. Metallurgical Mater Transactions. 2016;47(5):1939–46.

56. Hanawa T. Metal ion release from metal implants. Mater Sci Eng C. 2004;24(6–8):745–52.

57. Schwarz F, Ferrari D, Herten M, Mihatovic I, Wieland M, Sager M, Becker J. Effects of Surface Hydrophilicity and Microtopography on Early Stages of Soft and Hard Tissue Integration at Non-Submerged Titanium Implants: An Immunohistochemical Study in Dogs. J Periodontol. 2007;78(11):2171–84.

58. Kokubo T. Design of bioactive bone substitutes based on biomineralization process. Mater Sci Eng C. 2005;25(2):97–104.

59. Haider A, Haider S, Han SS, Kang IK. Recent advances in the synthesis, functionalization and biomedical applications of hydroxyapatite: a review. Rsc Adv. 2017;7(13):7442–58.

60. Chouirfa H, Bouloussa H, Migonney V, Falentin-Daudré C. Review of titanium surface modification techniques and coatings for antibacterial applications. Acta Biomater. 2018;83:37–54.

61. Stewart C, Akhavan B, Wise SG, Bilek MMM. A review of biomimetic surface functionalization for bone-integrating orthopedic implants: Mechanisms, current approaches, and future directions. Prog Mater Sci. 2019;106:100588.

62. Davies JE. Understanding Peri-Implant Endosseous Healing. J Dent Educ. 2003;67(8):932–49.

63. Micheletti C, Lee BEJ, Deering J, Binkley DM, Coulson S, Hussanain A, Zurob H, Grandfield K. Ti5Al5Mo5V3Cr bone implants with dual-scale topography: a promising alternative to Ti6Al4V. Nanotechnology. 2020;31(23):235101.

64. Palmquist A, Lindberg F, Emanuelsson L, Brånemark R, Engqvist H, Thomsen P. Biomechanical, histological, and ultrastructural analyses of laser micro- and nano-

structured titanium alloy implants: A study in rabbit. J Biomed Mater Res A. 2010;92A(4):1476–86.

65. Davies JE. Mechanisms of endosseous integration. Int J Prosthodont. 1998;11(5):391–401.

66. Gittens RA, Olivares-Navarrete R, Schwartz Z, Boyan BD. Implant osseointegration and the role of microroughness and nanostructures: Lessons for spine implants. Acta Biomater. 2014;10(8):3363–71.

67. Wennerberg A, Albrektsson T. Effects of titanium surface topography on bone integration: a systematic review. Clin Oral Implan Res. 2009;20(s4):172–84.

68. Davies JE, Ajami E, Moineddin R, Mendes VC. The roles of different scale ranges of surface implant topography on the stability of the bone/implant interface. Biomaterials. 2013;34(14):3535–46.

69. Wild M de, Schumacher R, Mayer K, Schkommodau E, Thoma D, Bredell M, Gujer AK, Grätz KW, Weber FE. Bone Regeneration by the Osteoconductivity of Porous Titanium Implants Manufactured by Selective Laser Melting: A Histological and Micro Computed Tomography Study in the Rabbit. Tissue Eng Pt A. 2013;19(23–24):2645–54.

70. Feighan JE, Goldberg VM, Davy D, Parr JA, Stevenson S. The influence of surface-blasting on the incorporation of titanium-alloy implants in a rabbit intramedullary model. J Bone Jt Surg. 1995;77(9):1380–95.

71. Wennerberg A, Albrektsson T, Johansson C, Andersson B. Experimental study of turned and grit-blasted screw-shaped implants with special emphasis on effects of blasting material and surface topography. Biomaterials. 1996;17(1):15–22.

72. Guillemot F, Prima F, Tokarev VN, Belin C, Porté-Durrieu MC, Gloriant T, Baquey C, Lazare S. Single-pulse KrF laser ablation and nanopatterning in vacuum of β-titanium alloys used in biomedical applications. Appl Phys. 2004;79(4–6):811–3.

73. Lee BEJ, Exir H, Weck A, Grandfield K. Characterization and Evaluation of Femtosecond Laser-Induced Sub-micron Periodic Structures Generated on Titanium to Improve Osseointegration of Implants. Appl Surf Sci. 2018;441(Biomaterials 17 2 1996):1034–42.

74. Morks MF. Fabrication and characterization of plasma-sprayed HA / SiO2 coatings for biomedical application. J Mech Behav Biomed. 2008;1(1):105–11.

75. Quek CH, Khor KA, Cheang P. Influence of processing parameters in the plasma spraying of hydroxyapatite/Ti–6Al–4V composite coatings. J Mater Process Tech. 1999;89:550–5.

76. Klokkevold PR, Johnson P, Dadgostari S, Davies JE, Caputo A, Nishimura RD. Early endosseous integration enhanced by dual acid etching of titanium: a torque removal study in the rabbit. Clin Oral Implan Res. 2001;12(4):350–7.

77. Jr ABN, Souza SLS de, Barros RRM de, Pereira KKY, Iezzi G, Piattelli A. Influence of implant surfaces on osseointegration. Braz Dent J. 2010;21(6):471–81.

78. Xiu P, Jia Z, Lv J, Yin C, Cheng Y, Zhang K, Song C, Leng H, Zheng Y, Cai H, Liu Z. Tailored Surface Treatment of 3D Printed Porous Ti6Al4V by Microarc Oxidation for Enhanced Osseointegration via Optimized Bone In-Growth Patterns and Interlocked Bone/Implant Interface. Acs Appl Mater Inter. 2016;8(28):17964–75.

79. Chen Z, Yan X, Chang Y, Xie S, Ma W, Zhao G, Liao H, Fang H, Liu M, Cai D. Effect of polarization voltage on the surface componentization and biocompatibility of micro-arc oxidation modified selective laser melted Ti6Al4V. Mater Res Express. 2019;6(8):086425.

80. Jonge LT de, Leeuwenburgh SCG, Wolke JGC, Jansen JA. Organic–Inorganic Surface Modifications for Titanium Implant Surfaces. Pharmaceut Res. 2008;25(10):2357–69.

81. Deering J, Clifford A, D'Elia A, Zhitomirsky I, Grandfield K. Composite Dip Coating Improves Biocompatibility of Porous Metallic Scaffolds. Mater Lett. 2020;274:128057.

82. Czekanska E, Stoddart M, Richards R, Hayes J. In search of an osteoblast cell model for in vitro research. European Cells Mater. 2012;24:1–17.

83. Rodan SB, Imai Y, Thiede MA, Wesolowski G, Thompson D, Bar-Shavit Z, Shull S, Mann K, Rodan GA. Characterization of a human osteosarcoma cell line (Saos-2) with osteoblastic properties. Cancer Res. 1987;47(18):4961–6.

84. Pautke C, Schieker M, Tischer T, Kolk A, Neth P, Mutschler W, Milz S. Characterization of osteosarcoma cell lines MG-63, Saos-2 and U-2 OS in comparison to human osteoblasts. Anticancer Res. 2004;24(6):3743–8.

85. Rampersad SN. Multiple Applications of Alamar Blue as an Indicator of Metabolic Function and Cellular Health in Cell Viability Bioassays. Sensors Basel Switz. 2012;12(9):12347–60.

86. Walker JM. Basic Protein and Peptide Protocols. Methods Mol Biology Clifton N J. 1994;32:5–8.

87. Arnaoutova I, George J, Kleinman HK, Benton G. The endothelial cell tube formation assay on basement membrane turns 20: state of the science and the art. Angiogenesis. 2009;12(3):267–74.

88. Ravi M, Paramesh V, Kaviya SR, Anuradha E, Solomon FDP. 3D Cell Culture Systems: Advantages and Applications. J Cell Physiol. 2015;230(1):16–26.

89. Li Y, Chen SK, Li L, Qin L, Wang XL, Lai YX. Bone defect animal models for testing efficacy of bone substitute biomaterials. J Orthop Transl. 2015;3(3):95–104.

90. Spece H, Basgul C, Andrews CE, MacDonald DW, Taheri ML, Kurtz SM. A systematic review of preclinical in vivo testing of 3D printed porous Ti6Al4V for orthopedic applications, part I: Animal models and bone ingrowth outcome measures. J Biomed Mater Res Part B Appl Biomaterials. 2021;109(10):1436–54.

91. Gilsanz V, Roe TF, Gibbens DT, Schulz EE, Carlson ME, Gonzalez O, Boechat MI. Effect of sex steroids on peak bone density of growing rabbits. Am J Physiol-endoc M. 1988;255(4):E416–21.

92. Cacchioli A, Ravanetti F, Soliani L, Borghetti P. Preliminary Study on the Mineral Apposition Rate in distal femoral epiphysis of New Zealand White Rabbit at Skeletal Maturity. Anatomia Histologia Embryologia. 2012;41(3):163–9.

93. McFarlin SC, Terranova CarlJ, Zihlman AL, Enlow DH, Bromage TG. Regional variability in secondary remodeling within long bone cortices of catarrhine primates: the influence of bone growth history. J Anat. 2008;213(3):308–24.

94. Reifenrath J, Gottschalk D, Angrisani N, Besdo S, Meyer-Lindenberg A. Axial forces and bending moments in the loaded rabbit tibia in vivo. Acta Vet Scand. 2012;54(1):21–21.

95. Tam CS, Harrison JE, Reed R, Cruickshank B. Bone apposition rate as an index of bone metabolism. Metabolis. 1978;27(2):143–50.

96. Schmitz JP, Hollinger JO. The Critical Size Defect as an Experimental Model for Craniomandibulofacial Nonunions. Clin Orthop Relat R. 1986;NA;(205):299???308.

97. Vajgel A, Mardas N, Farias BC, Petrie A, Cimões R, Donos N. A systematic review on the critical size defect model. Clin Oral Implan Res. 2014;25(8):879–93.

98. Zhao MD, Huang JS, Zhang XC, Gui KK, Xiong M, Yin WP, Yuan FL, Cai GP. Construction of Radial Defect Models in Rabbits to Determine the Critical Size Defects. Plos One. 2016;11(1):e0146301.

99. Wang H, Su K, Su L, Liang P, Ji P, Wang C. The effect of 3D-printed Ti6Al4V scaffolds with various macropore structures on osteointegration and osteogenesis: A biomechanical evaluation. J Mech Behav Biomed. 2018;88(J. Mech. Behav. Biomed. Mater. 34 2014):488–96.

100. Ran Q, Yang W, Hu Y, Shen X, Yu Y, Xiang Y, Cai K. Osteogenesis of 3D printed porous Ti6Al4V implants with different pore sizes. J Mech Behav Biomed. 2018;84(Crit. Rev. Biomed. Eng. 40 2012):1–11.

101. Taniguchi N, Fujibayashi S, Takemoto M, Sasaki K, Otsuki B, Nakamura T, Matsushita T, Kokubo T, Matsuda S. Effect of pore size on bone ingrowth into porous titanium implants fabricated by additive manufacturing: An in vivo experiment. Mater Sci Eng C. 2016;59:690–701.

102. Bobyn JD, Pilliar RM, Cameron HU, Weatherly GC. The optimum pore size for the fixation of porous-surfaced metal implants by the ingrowth of bone. Clin Orthop Relat R. 1980;(150):263–70.

103. Li F, Li J, Xu G, Liu G, Kou H, Zhou L. Fabrication, pore structure and compressive behavior of anisotropic porous titanium for human trabecular bone implant applications. J Mech Behav Biomed. 2015;46:104–14.

104. Vasconcellos LMR de, Leite DO, Oliveira FN de, Carvalho YR, Cairo CAA. Evaluation of bone ingrowth into porous titanium implant: histomorphometric analysis in rabbits. Braz Oral Res. 2010;24(4):399–405.

105. Fukuda A, Takemoto M, Saito T, Fujibayashi S, Neo M, Pattanayak DK, Matsushita T, Sasaki K, Nishida N, Kokubo T, Nakamura T. Osteoinduction of porous Ti implants with a channel structure fabricated by selective laser melting. Acta Biomater. 2011;7(5):2327–36.

106. Shah FA, Thomsen P, Palmquist A. Osseointegration and current interpretations of the bone-implant interface. Acta Biomater. 2018;84:1–15.

107. Albrektsson T, Johansson C. Osteoinduction, osteoconduction and osseointegration. Eur Spine J. 2001;10(Suppl 2):S96–101.

108. Clarke B. Normal Bone Anatomy and Physiology. Clin J Am Soc Nephro. 2008;3(Supplement 3):S131–9.

109. Bencharit S, Byrd WC, Altarawneh S, Hosseini B, Leong A, Reside G, Morelli T, Offenbacher S. Development and Applications of Porous Tantalum Trabecular Metal-Enhanced Titanium Dental Implants. Clin Implant Dent R. 2014;16:817–26.

110. Augat P, Link T, Lang TF, Lin JC, Majumdar S, Genant HK. Anisotropy of the elastic modulus of trabecular bone specimens from different anatomical locations. Med Eng Phys. 1998;20(2):124–31.

111. Kerr R, Resnick D, Sartoris DJ, Kursunoglu S, Pineda C, Haghighi P, Greenway G, Guerra J. Computerized tomography of proximal femoral trabecular patterns. J Orthopaed Res. 1986;4(1):45–56.

112. Ruff C, Holt B, Trinkaus E. Who's afraid of the big bad Wolff?: "Wolff's law" and bone functional adaptation. Am J Phys Anthropol. 2006;129(4):484–98.

113. Diederichs G, Köhlitz T, Kornaropoulos E, Heller MO, Vollnberg B, Scheffler S. Magnetic Resonance Imaging Analysis of Rotational Alignment in Patients With Patellar Dislocations. Am J Sports Medicine. 2013;41(1):51–7.

114. Cherian JJ, Kapadia BH, Banerjee S, Jauregui JJ, Issa K, Mont MA. Mechanical, Anatomical, and Kinematic Axis in TKA: Concepts and Practical Applications. Curr Rev Musculoskelet Medicine. 2014;7(2):89–95.

115. Wagermaier W, Gupta HS, Gourrier A, Burghammer M, Roschger P, Fratzl P. Spiral twisting of fiber orientation inside bone lamellae. Biointerphases. 2006;1(1):1–5.

116. Jaffe HL. The Vessel Canals in Normal and Pathological Bone. Am J Pathology. 1929;5(3):323-332.5.

117. Hinton PV, Rackard SM, Kennedy OD. In Vivo Osteocyte Mechanotransduction: Recent Developments and Future Directions. Curr Osteoporos Rep. 2018;16(6):746–53.

118. McCreadie BR, Hollister SJ, Schaffler MB, Goldstein SA. Osteocyte lacuna size and shape in women with and without osteoporotic fracture. J Biomech. 2004;37(4):563–72.

119. Kerschnitzki M, Wagermaier W, Roschger P, Seto J, Shahar R, Duda GN, Mundlos S, Fratzl P. The organization of the osteocyte network mirrors the extracellular matrix orientation in bone. J Struct Biol. 2011;173(2):303–11.

120. Sugawara Y, Kamioka H, Ishihara Y, Fujisawa N, Kawanabe N, Yamashiro T. The early mouse 3D osteocyte network in the presence and absence of mechanical loading. Bone. 2013;52(1):189–96.

121. Yu B, Pacureanu A, Olivier C, Cloetens P, Peyrin F. Assessment of the human bone lacuno-canalicular network at the nanoscale and impact of spatial resolution. Sci Rep-uk. 2020;10(1):4567.

122. Buss DJ, Reznikov N, McKee MD. Crossfibrillar mineral tessellation in normal and Hyp mouse bone as revealed by 3D FIB-SEM microscopy. J Struct Biol. 2020;212(2):107603.

123. Reznikov N, Shahar R, Weiner S. Bone hierarchical structure in three dimensions. Acta Biomater. 2014;10(9):3815–26.

124. Ascenzi A, Bonucci E, Bocciarelli DS. An electron microscope study of osteon calcification. J Ultra Mol Struct R. 1965;12(3):287–303.

125. Boyde A, Sela J. Scanning electron microscope study of separated calcospherites from the matrices of different mineralizing systems. Calc Tiss Res. 1978;26(1):47–9.

126. Landis WJ, Song MJ, Leith A, McEwen L, McEwen BF. Mineral and Organic Matrix Interaction in Normally Calcifying Tendon Visualized in Three Dimensions by High-Voltage Electron Microscopic Tomography and Graphic Image Reconstruction. J Struct Biol. 1993;110(1):39–54.

127. Landis WJ, Song MJ. Early mineral deposition in calcifying tendon characterized by high voltage electron microscopy and three-dimensional graphic imaging. J Struct Biol. 1991;107(2):116–27.

128. McNally EA, Schwarcz HP, Botton GA, Arsenault AL. A Model for the Ultrastructure of Bone Based on Electron Microscopy of Ion-Milled Sections. Plos One. 2012;7(1):e29258.

129. Kini U, Nandeesh BN. Physiology of Bone Formation, Remodeling, and Metabolism. In: Fogelman I, Gnanasegaran G, Wall H van der, editors. Radionuclide and Hybrid Bone Imaging. Springer-Verlag Berlin Heidelberg; 2012. p. 29–57.

130. Smith JW. Collagen fibre patterns in mammalian bone. J Anat. 1960;94(Pt 3):329–44.

131. Giraud-Guille MM. Twisted plywood architecture of collagen fibrils in human compact bone osteons. Calcified Tissue Int. 1988;42(3):167–80.

132. Su X, Sun K, Cui FZ, Landis WJ. Organization of apatite crystals in human woven bone. Bone. 2003;32(2):150–62.

133. Masuda T, Yliheikkilä PK, Felton DA, Cooper LF. Generalizations regarding the process and phenomenon of osseointegration. Part I. In vivo studies. Int J Oral Maxillofac Implant. 1998;13(1):17–29.

134. Marks SC, Popoff SN. Bone cell biology: The regulation of development, structure, and function in the skeleton. Am J Anat. 1988;183(1):1–44.

135. Caplan AI, Bruder SP. Mesenchymal stem cells: building blocks for molecular medicine in the 21st century. Trends Mol Med. 2001;7(6):259–64.

136. Chaplin DD. Overview of the immune response. J Allergy Clin Immun. 2010;125(2):S3–23.

137. Amulic B, Cazalet C, Hayes GL, Metzler KD, Zychlinsky A. Neutrophil Function: From Mechanisms to Disease. Annu Rev Immunol. 2012;30(1):459–89.

138. Risau W. Differentiation of endothelium. Faseb J. 1995;9(10):926–33.

139. Shepro D, Morel NML. Pericyte physiology. Faseb J. 1993;7(11):1031–8.

140. Hamasaki N, Yamamoto M. Red Blood Cell Function and Blood Storage. Vox Sang. 2000;79(4):191–7.

141. Gimble JM, Robinson CE, Wu X, Kelly KA. The function of adipocytes in the bone marrow stroma: an update. Bone. 1996;19(5):421–8.

142. Beaulieu LM, Freedman JE. The role of inflammation in regulating platelet production and function: Toll-like receptors in platelets and megakaryocytes. Thromb Res. 2010;125(3):205–9.

143. Kuzyk PRT, Schemitsch EH. The basic science of peri-implant bone healing. Indian J Orthop. 2011;45(2):108–15.

144. Olivares-Navarrete R, Lee EM, Smith K, Hyzy SL, Doroudi M, Williams JK, Gall K, Boyan BD, Schwartz Z. Substrate Stiffness Controls Osteoblastic and Chondrocytic Differentiation of Mesenchymal Stem Cells without Exogenous Stimuli. Plos One. 2017;12(1):e0170312.

145. Winer JP, Janmey PA, McCormick ME, Funaki M. Bone Marrow-Derived Human Mesenchymal Stem Cells Become Quiescent on Soft Substrates but Remain Responsive to Chemical or Mechanical Stimuli. Tissue Eng Pt A. 2009;15(1):147–54.

146. Fakhry M, Hamade E, Badran B, Buchet R, Magne D. Molecular mechanisms of mesenchymal stem cell differentiation towards osteoblasts. World J Stem Cells. 2013;5(4):136.

147. Long F. Building strong bones: molecular regulation of the osteoblast lineage. Nat Rev Mol Cell Bio. 2012;13(1):27–38.

148. Weber FE. Reconsidering Osteoconduction in the Era of Additive Manufacturing. Tissue Eng Part B Rev. 2019;25(5):375–86.

149. Wang H, Su K, Su L, Liang P, Ji P, Wang C. Comparison of 3D-printed porous tantalum and titanium scaffolds on osteointegration and osteogenesis. Mater Sci Eng C. 2019;104:109908.

150. Shah FA, Omar O, Suska F, Snis A, Matic A, Emanuelsson L, Norlindh B, Lausmaa J, Thomsen P, Palmquist A. Long-term osseointegration of 3D printed CoCr constructs with an interconnected open-pore architecture prepared by electron beam melting. Acta Biomater. 2016;36:296–309.

151. Dondossola E, Friedl P. Host responses to implants revealed by intravital microscopy. Nat Rev Mater. 2022;7(1):6–22.

152. Marsell R, Einhorn TA. The biology of fracture healing. Inj. 2011;42(6):551–5.

153. Crisan M, Chen C, Corselli M, Andriolo G, Lazzari L, Péault B. Perivascular Multipotent Progenitor Cells in Human Organs. Ann Ny Acad Sci. 2009;1176(1):118–23.

154. Redenski I, Guo S, Machour M, Szklanny A, Landau S, Kaplan B, Lock RI, Gabet Y, Egozi D, Vunjak-Novakovic G, Levenberg S. Engineered Vascularized Flaps, Composed of Polymeric Soft Tissue and Live Bone, Repair Complex Tibial Defects. Adv Funct Mater. 2021;31(44):2008687.

155. Khosravi N, Maeda A, DaCosta RS, Davies JE. Nanosurfaces modulate the mechanism of peri-implant endosseous healing by regulating neovascular morphogenesis. Commun Biology. 2018;1(1).

156. Byrne AM, Bouchier-Hayes DJ, Harmey JH. Angiogenic and cell survival functions of Vascular Endothelial Growth Factor (VEGF). J Cell Mol Med. 2005;9(4):777–94.

157. Midy V, Plouet J. Vasculotropin/Vascular Endothelial Growth Factor Induces Differentiation in Cultured Osteoblasts. Biochem Bioph Res Co. 1994;199(1):380–6.

158. Cao R, Bråkenhielm E, Pawliuk R, Wariaro D, Post MJ, Wahlberg E, Leboulch P, Cao Y. Angiogenic synergism, vascular stability and improvement of hind-limb ischemia by a combination of PDGF-BB and FGF-2. Nat Med. 2003;9(5):604–13.

159. Lindahl P, Johansson BR, Levéen P, Betsholtz C. Pericyte Loss and Microaneurysm Formation in PDGF-B-Deficient Mice. Science. 1997;277(5323):242–5.

160. Caplan AI, Correa D. PDGF in bone formation and regeneration: New insights into a novel mechanism involving MSCs. J Orthopaed Res. 2011;29(12):1795–803.

161. Krock BL, Skuli N, Simon MC. Hypoxia-Induced Angiogenesis. Genes Cancer. 2011;2(12):1117–33.

162. Kim HKW, Bian H, Aya-ay J, Garces A, Morgan EF, Gilbert SR. Hypoxia and HIF-1α expression in the epiphyseal cartilage following ischemic injury to the immature femoral head. Bone. 2009;45(2):280–8.

163. Grandfield K, Micheletti C, Deering J, Arcuri G, Tang T, Langelier B. Atom Probe Tomography for Biomaterials and Biomineralization. Acta Biomaterialia. 2022.

164. Holdsworth DW, Thornton MM. Micro-CT in small animal and specimen imaging. Trends Biotechnol. 2002;20(8):S34–9.

165. Chappard D, Retailleau-Gaborit N, Legrand E, Baslé MF, Audran M. Comparison Insight Bone Measurements by Histomorphometry and μCT. J Bone Miner Res. 2005;20(7):1177–84.

166. Parfitt AM, Drezner MK, Glorieux FH, Kanis JA, Malluche H, Meunier PJ, Ott SM, Recker RR. Bone Histomorphometry: Standardization of Nomenclature, Symbols and Units. Journal of Bone and Mineral Research. 1988;6(2).

167. Buser D, Schenk RK, Steinemann S, Fiorellini JP, Fox CH, Stich H. Influence of surface characteristics on bone integration of titanium implants. A histomorphometric study in miniature pigs. J Biomed Mater Res. 1991;25(7):889–902.

168. Herman GT. Correction for beam hardening in computed tomography. Med Phys. 1978;5(3):209–14.

169. Sijbers J, Postnov A. Reduction of ring artefacts in high resolution micro-CT reconstructions. Phys Med Biol. 2004;49(14):N247–53.

170. Burnett TL, Kelley R, Winiarski B, Contreras L, Daly M, Gholinia A, Burke MG, Withers PJ. Large volume serial section tomography by Xe Plasma FIB dual beam microscopy. Ultramicroscopy. 2016;161:119–29.

171. Boyde A, Jones SJ. Scanning electron microscopy of bone: Instrument, specimen, and issues. Microsc Res Techniq. 1996;33(2):92–120.

172. Boyde A, Wood C. Preparation of animal tissues for surface-scanning electron microscopy. J Microsc-oxford. 1969;90(3):221–49.

173. Ali MY, Hung W, Yongqi F. A review of focused ion beam sputtering. Int J Precis Eng Man. 2010;11(1):157–70.

174. Binkley DM, Grandfield K. Advances in Multiscale Characterization Techniques of Bone and Biomaterials Interfaces. Acs Biomater Sci Eng. 2017;4(11):3678–90.

175. Swanson LW. Use of the liquid metal ion source for focused beam applications. Appl Surf Sci. 1994;76:80–8.

176. Smith NS, Notte JA, Steele AV. Advances in source technology for focused ion beam instruments. Mrs Bull. 2014;39(4):329–35.

177. Liu J, Niu R, Gu J, Cabral M, Song M, Liao X. Effect of Ion Irradiation Introduced by Focused Ion-Beam Milling on the Mechanical Behaviour of Sub-Micron-Sized Samples. Sci Rep-uk. 2020;10(1):10324.

178. Utke I, Hoffmann P, Melngailis J. Gas-assisted focused electron beam and ion beam processing and fabrication. J Vac Sci Technology B Microelectron Nanometer Struct Process Meas Phenom. 2008;26(4):1197–276.

179. Schneider P, Meier M, Wepf R, Müller R. Serial FIB/SEM imaging for quantitative 3D assessment of the osteocyte lacuno-canicular network. Bone. 2011;49(2):304–11.

180. Giannuzzi LA, Phifer D, Giannuzzi NJ, Capuano MJ. Two-Dimensional and 3-Dimensional Analysis of Bone/Dental Implant Interfaces With the Use of Focused Ion Beam and Electron Microscopy. J Oral Maxil Surg. 2007;65(4):737–47.

181. Ishitani T, Umemura K, Ohnishi T, Yaguchi T, Kamino T. Improvements in performance of focused ion beam cross-sectioning: aspects of ion-sample interaction. J Electron Microsc. 2004;53(5):443–9.

182. Reznikov N, Buss DJ, Provencher B, McKee MD, Piché N. Deep learning for 3D imaging and image analysis in biomineralization research. J Struct Biol. 2020;212(1):107598.

183. Reznikov N, Boughton OR, Ghouse S, Weston AE, Collinson L, Blunn GW, Jeffers J, Cobb JP, Stevens MM. Individual response variations in scaffold-guided bone

regeneration are determined by independent strain- and injury-induced mechanisms. Biomaterials. 2018;194(J. Bone Joint Surg. Am. 89 Suppl 3 2007):183–94.

184. Ronneberger O, Fischer P, Brox T. U-Net: Convolutional Networks for Biomedical Image Segmentation. In: International Conference on Medical Image Computing and Computer-Assisted Intervention. 2015.

Chapter 3: Selective Voronoi Tessellation as a Method to Design Anisotropic and Biomimetic Implants

Summary:

Trabecular bone within the femur varies greatly in its directionality along the length of the bone, but implant design strategies lag in accounting for this anisotropy. In this chapter, an approach to design anisotropy-graded porous implant materials is introduced. Partial asymmetrical re-seeding of a Voronoi tessellation followed by polyhedral edge conversion to scaffold beams was used to generate varying degrees of anisotropy within the porous material and the resulting inter-trabecular angle was compared to an isotropic form of Voronoi tessellation. The selectively re-seeded Voronoi tessellations had inter-trabecular angles similar to native trabecular bone and to isotropic Voronoi tessellations, where the mean intertrabecular angle is instead dependent on the number of intersecting trabeculae. Controlling scaling factors for the beam size enabled the generation of implant structures within the tolerance of metal additive manufacturing processes and near the upper threshold of what is seen in trabecular bone. This work contributes to the field by developing an algorithm to rapidly prototype porous implants with multidirectional and transient anisotropy gradients in the material using only moderate computational resources.

Citation:

Deering, J.*, Dowling, K.I.*, DiCecco, L.-A., McLean, G.D., Yu, B., and Grandfield, K. (2021). Selective Voronoi tessellation as a method to design anisotropic and biomimetic implants. *Journal of the Mechanical Behaviour of Biomedical Materials, 116*. https://doi.org/10.1016/j.jmbbm.2021.104361.

Permissions:

Permission for reprint has been provided by Elsevier, with the full article available at https://doi.org/10.1016/j.jmbbm.2021.104361.

Selective Voronoi tessellation as a method to design anisotropic and biomimetic implants

Joseph Deering [a,1], Kierdra I. Dowling [a,1], Liza-Anastasia DiCecco [a], Griffin D. McLean [b], Bosco Yu [a], Kathryn Grandfield [a,c,*]

[a] *Department of Materials Science and Engineering, McMaster University, Hamilton, ON, Canada*
[b] *Department of Mechanical Engineering, McMaster University, Hamilton, ON, Canada*
[c] *School of Biomedical Engineering, McMaster University, Hamilton, ON, Canada*

ARTICLE INFO

ABSTRACT

The geometry of a metallic scaffold is important for the success of bone implants, where the introduction of porosity can reduce stress shielding effects and allow for bone tissue integration. In this work, porous scaffolds were designed to closely mimic the natural structure of trabecular bone using selective Voronoi tessellation with preferential seeding. A workflow to generate these structures is introduced, where voided regions of seeds in the starting volume create preferential texture during polyhedral expansion, resulting in modified strut orientation in the implant. Anisotropy was digitally characterized by mean-intercept length and star volume distribution measurements to determine similarity to trabecular orientation. This work demonstrates that selective Voronoi tessellation is an effective method to generate biomimetic porous scaffolds with increased anisotropy and tunable strut architecture in three dimensions as a suitable alternative to patient-derived bone geometries.

1. Introduction

Stress shielding is a phenomenon that occurs when a high-stiffness implant in the human body results in bone loss. Decreased physiological loading occurs in the bone due to a stiffness mismatch between the implant and the surrounding bone, causing a reduction in bone density (Engh et al., 1987) and higher likelihood of periprosthetic fracture (Wik et al., 2010). Stiffness reduction by material selection (Heinl et al., 2008; Karre et al., 2015) or by intentional introduction of porosity into the implant structure (Harrysson et al., 2008; Choren et al., 2013; Bandyopadhyay et al., 2010) are two possible strategies to mitigate this effect. Introducing porosity into the structure not only reduces stress shielding effects, but also facilitates tissue ingrowth (de Vasconcellos et al., 2010). Geometric factors of a porous metallic implant such as pore size (Itälä et al., 2001) and pore geometry (Li et al., 2016) have been found to influence osseointegration. To date, there is no well-defined set of geometric parameters for optimal osseointegration in porous metallic implants, but it is believed that biomimetic pore structures may outperform other implant geometries.

Trabecular bone is a naturally anisotropic network of struts and plates (Reznikov et al., 2016). The inter-trabecular angle (ITA) measures the angle at trabecular junctions and has been shown to be based on the trabecular geometry (Reznikov et al., 2016). The ITA distribution of nodes with 3 connecting trabeculae (3N junctions) have a mean close to $120°$, nodes with 4 connecting trabeculae (4N junctions) have a mean close to $109°$ and nodes of higher connectivity (5N, 6N, or higher junctions) have mean ITA values around $100°$ (Reznikov et al., 2016). These trabecular struts reflect loading conditions and are found to be co-oriented or offset by a fixed amount from the mechanical axis of the bone (Sampath et al., 2015). The bulk of traditional implants do not take anisotropy into account, where fully dense materials or porous isotropic implants are predominant (Rajpura et al., 2014). Some biomimetic approaches use voxel-based finite element modelling of human trabeculae as observed by X-ray micro-computed tomography (Chevalier et al., 2007) to exactly mimic human trabeculae (Helguero et al., 2017). This is often limited by high cost or intensive computation. Since the global trabecular orientation lines up with the major axis of mechanical loading in the bone (Oftadeh et al., 2015), it is desirable to produce scaffolds that have struts elongated in this direction. Scaffolds like these can be translated to implants in a clinical setting for total hip joint

---

replacements or arthroplasty which involves replacement of femoral bone, for example, where the cortical bone displays overall orthotropy and increased anisotropy close to the epiphyses (Rudy et al., 2011) and the trabeculae have preferred orientation along several tension/compression lines in the proximal femur (Enns-Bray et al., 2014).

It is well-known that there is a significant correlation between the mechanical axis of bone and the trabecular orientation, especially in the long bones (Sampath et al., 2015), where the direction of force transmitted through the bone varies along the mechanical axis (Sampath et al., 2015). The mechanical axis of the lower extremity typically refers to the line drawn from the center of the femoral head down to the center of the ankle joint (Lin et al., 2018). On average, this is found to have a global 3° offset from the vertical axis (Cherian et al., 2014). The mechanical axis can then be separated into two separate subdivisions, the femoral mechanical axis and the tibial mechanical axis (Lin et al., 2018). The femoral mechanical axis extends from the head of the femur to the intercondylar notch of the distal femur, whereas the tibial mechanical axis runs from the center of the proximal tibia to the center of the ankle (Cherian et al., 2014). In the average healthy human, the mechanical tibiofemoral angle is slightly higher than 180°, however this can range case by case. One study found that the average mechanical tibiofemoral angle ranged from 183 to 186° (Hernigou et al., 1987), varying widely based on the patient's height, pelvic width, sex, and age (Sikorski, 2008). These linear approximations of the mechanical axis are somewhat limited in scope, especially considering how local regions of the bone can vary within these axes. Due to the offset loading condition associated with a local mechanical axis and inherent curvature around the femoral metaphysis, considerations with respect to implant design are complex. Global alignment of porous implant struts to the mechanical axis can be achieved with unidirectionally oriented repeating structures but a closer look at the anisotropy of the native bone proves this to be unsuitable.

Voronoi tessellation has been previously used to develop metallic scaffolds with a randomized pore architecture (Fantini et al., 2016). A Voronoi tessellation is generated as shown in Fig. 1. First, seeds are placed in a finite space from which a polygon or polyhedron grows outward, expanding at a constant rate to fill a space. Growth finishes when neighbouring polyhedra impinge on one another (Fantini et al.,

2016). In a three-dimensional space, these boundaries consist of planes rather than lines. By forming solid struts out of the polyhedral junctions, scaffolds can be created with a trabecular appearance at the microscale (Ying et al., 2015) but an isotropic mechanical behaviour at the macroscale, as has been shown in 2D Voronoi tessellations (Silva et al., 1995). The mechanical benefits of cellular Voronoi structures have been investigated previously, where change to the isotropy of the cellular structure can affect the deformation mode and stiffness of the structure (Alkhader and Vural, 2008). Two-dimensional Voronoi honeycombs with a high degree of regularity have been shown to behave isotropically in mechanical deformation, where introducing disorder to the structure can result in a change of the Young's modulus (Zhu et al., 2001). Similarly, random strut defects have been observed to affect the elastic moduli (Seiler et al., 2019), displaying particular dependence on the main deformation mode of the unit cell (Latture et al., 2019). Introduction of crystal-inspired randomness to the macroscale hierarchy of an otherwise repeating strut configuration offers the potential for refinement of mechanical properties (Pham et al., 2019). To produce biomimetic implants with tunable mechanical properties, adjustment to the conventional modelling of cellular Voronoi structures is required to generate structural anisotropy and control the mechanical response of the implant, thereby modulating bone regeneration.

Producing implants with such complex geometries is often unachievable by traditional manufacturing techniques. However additive manufacturing (AM) can produce complex and intricate implants with limited post-processing steps (Maconachie et al., 2019). This technique deposits material layer-by-layer, allowing the formation of complex structures with internal pore architectures that cannot be replicated in traditional subtractive technologies (Maconachie et al., 2019). By using an additive, layer-by-layer approach to selectively deposit material (Gebhardt, 2011), AM is not burdened by the same limitations concerning internal pore architecture that govern traditional subtractive technologies (Wang et al., 2016). For example, selective laser melting (SLM) is able to produce structures with thin walls and hidden voids or channels (Kruth et al., 2005). Complex structures, such as rhombic dodecahedral honeycomb lattices (Zheng et al., 2014), weighted planar stochastic lattices (Zheng et al., 2014), and implants based off patient geometry (Sikorski, 2008) have also been fabricated
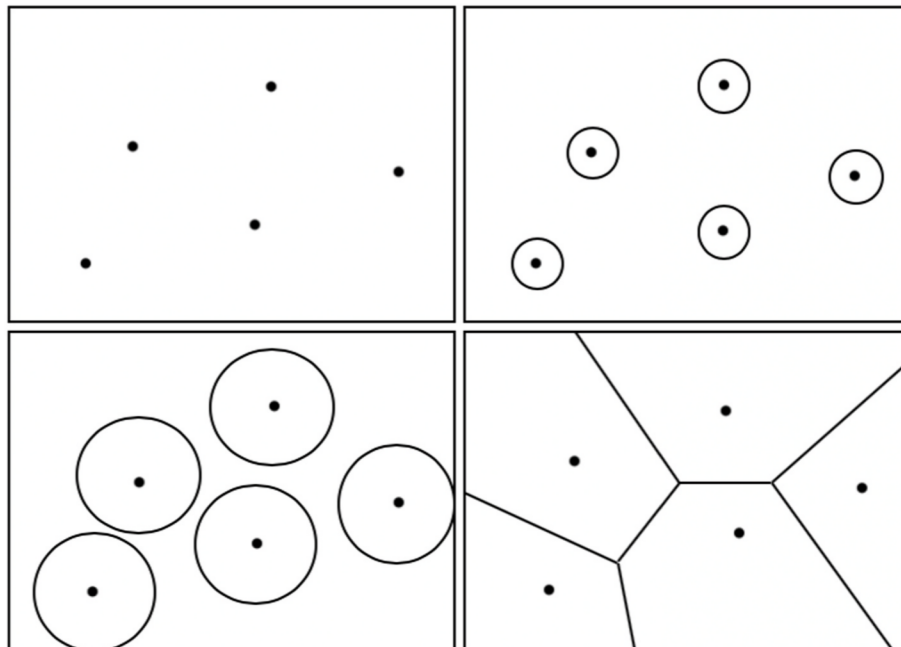
Fig. 1. Graphical representation showing the formation of a Voronoi diagram in 2D. Seeds are randomly distributed through a region, grow outward until they impinge on one another, and form distinct polygons.

with SLM. The *in vitro* performance of SLM scaffolds designed with a standard Voronoi tessellation show that the trabecular-like porous structure exhibit enhanced cell proliferation and osteoblast differentiation compared to structures with fewer irregularities and repeating patterns (Liang et al., 2019). This suggests that SLM is a suitable manufacturing process for production of porous lattices designed by any form of Voronoi tessellation in the future, and that these structures may also perform favorably in *in vitro* and *in vivo* environments.

In this study, we report the development of biomimetic and anisotropic porous scaffolds by a new method, selective Voronoi tessellation, and quantify the anisotropy and select histomorphometry of the resulting structures. This new method of designing porous trabecular structures has implications with regards to both osseointegration and mechanical load distribution in the design of porous anisotropic implants for joint replacement, in particular, for the application of total hip arthroplasty.

2. Methods

2.1. Voronoi tessellation

Rhinoceros3D 6 (Robert McNeel & Associates) with the Grasshopper graphical programming add-on was used to model both simple isotropic and anisotropic implant models by Voronoi tessellation, as described in work from Fantini and Curto (2018). Four bounding points and the associated curves were lofted to create a cubic geometry of 6 mm × 6 mm × 6 mm for both the isotropic and anisotropic structures. The

complete Grasshopper scripts can be found in supplemental information, where the workflows for each are documented in Fig. 2 and additional steps for selective seeding are highlighted in purple.

For the isotropic implant, dynamic seed population control was added using a numerical slider. One hundred and twenty-three seeds were randomly distributed through the volume and converted to boundary representations (BREPs) containing locations of vertices, edges, and faces for each volume. The BREPs were simultaneously transformed into bound volumes and scaled down to fit within the bounding cube, effectively creating a polyhedron from each seed. Volume endpoints for each polyhedron were extracted from both BREPs and volumes to get spatial coordinates for vertices in each polyhedron in one continuous object. Scaffold struts were formed along volume edges connecting these vertices and converted to independent meshes for each strut. Repetitive or overlapping mesh elements were culled before all meshes were welded to a single mesh to compose the penultimate Voronoi tessellation in 3D. The relative size of struts in the tessellation was assessed qualitatively to iteratively select an appropriate scaling factor for the constituent BREPs and volumes. A recursive Catmull-Clark subdivision algorithm was used to smooth the final mesh after scaling and remove any mesh errors.

The three anisotropic implants used selective Voronoi tessellation by a controlled redistribution of seeds to form strut directionality. Anisotropic implants were generated by controlled partial redistribution of seeds into periodic planes in the upper and lower third of the cube. For this, five equally spaced cross-sectional planes with an interplanar spacing of 0.5 mm were bound at the top as well as at the bottom of the
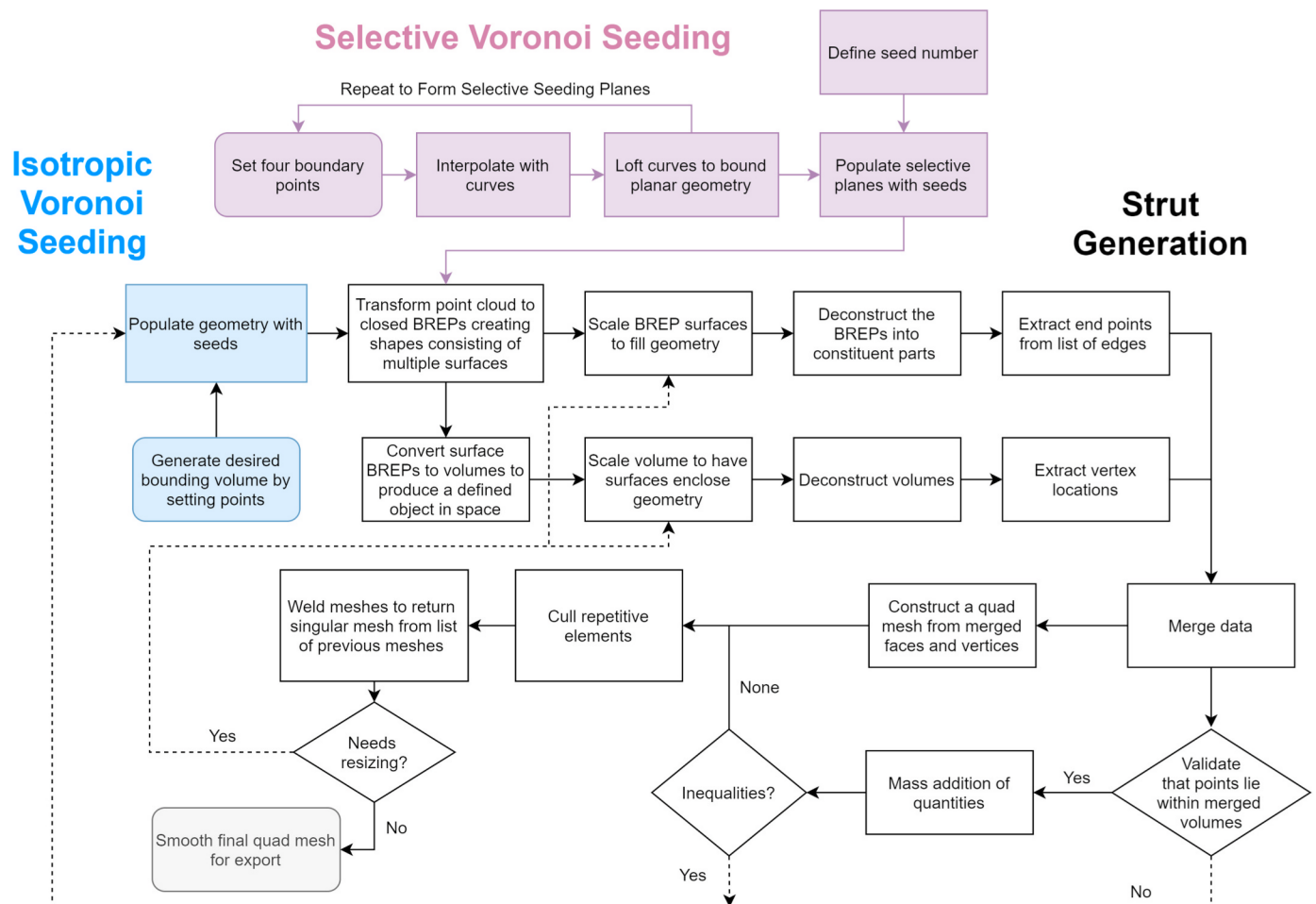
Fig. 2. Flow chart detailing the generation of standard Voronoi tessellations and selective Voronoi tessellations (purple extension) in Grasshopper to make implant structures. The selective seeding algorithm creates biomimetic anisotropy in the final structure.

cube. For the three models, ranges of 3–5, 5–7, and 8–10 seeds per plane (SPP) were considered for each, respectively. To have the same amount of seeds per volume considered (totalling to 123), the total number of SPP in a model was subtracted from 123 and these remaining non-planar seeds were evenly distributed throughout the 6 mm × 6 mm × 6 mm volume and the workflow was resumed in the described manner for the isotropic implant.

2.2. Strut analysis

Isotropic and anisotropic mesh files were exported to 500 voxel × 500 voxel × 500 voxel volumes in Autodesk Netfabb (2019) before being imported to Dragonfly 4.1 (Object Research Systems) as an image stack for analysis. Dragonfly's Bone Analysis tool was used to generate global measurements of mean-intercept length (MIL) and star volume distribution (SVD) (Smit et al., 1998; Whitehouse, 1974) as a form of measuring anisotropy in all structures using 5000 orientations and 10, 000 iterations.

The MIL technique calculates the fabric tensor using the average distance between collinear points that lie on the periphery of segmented struts (L_{avg}), where varying angular orientations (ω) and a defined number of lines (m) are used to assign a final anisotropy value according to some scalar value as outlined in Equation (1) (Reznikov et al., 2020; Odgaard, 1997).

$$MIL(\omega) = f\left(\frac{\sum_{i=1}^{m} L_{i,\,avg}(\omega)}{m}\right) \qquad (1)$$

The SVD technique also uses a fabric tensor, but the intercept length across a single strut (D) is instead found in several orientations for a single bounded point within the scaffold, where intercepts are then weighted in cubic fashion and averaged across a number of bounded points (n) as described in Equation (2). For further descriptions of the MIL and SVD techniques, we refer the reader elsewhere (Odgaard,

1997). In cases of MIL and SVD measurements in this study, a higher value of MIL or SVD refers to a greater degree of anisotropy in the trabecular structure. Therefore, when MIL or SVD = 0, this refers to an isotropic structure, and when MIL or SVD approaches 1, the degree of anisotropy increases.

$$SVD(\omega) = f\left(\frac{\sum_{i=i}^{n} D_i(\omega)^3}{n}\right) \qquad (2)$$

The bone volume fraction (BV/TV) and mean trabecular thickness (Tb.Th) for each structure were also assessed using the Bone Analysis tool in Dragonfly. Representative vector fields were also generated as colorimetric descriptors of strut orientation using the surface-normal algorithm for each implant using the projection tool in Dragonfly with sample spacing of 94 μm. Vectors parallel to the defined X-axis appear red, vectors parallel to the Y-axis appear green, vectors parallel to the Z-axis appear blue, and intermediate vectors are assigned a corresponding colour based on their misorientation with respect to the coordinate axes.

Image stacks were also imported into ImageJ (NIH) for ITA pre-processing. Image stacks were skeletonized across the 3D volume and branch information, including vector endpoints, was exported. A list of unique vector endpoints was filtered from the branch information and the number of vectors sharing a particular endpoint was used to define the junction type (3N, 4N, 5N, or other). Vectors were loaded into a custom script in R 3.6.1 for the measurement of ITAs in each junction type.

3. Results

3.1. Voronoi tessellation

The seed distribution for isotropic and anisotropic structures is shown in Fig. 3. As anticipated, the anisotropic structures contain regions with higher seed density near the planar additions and regions
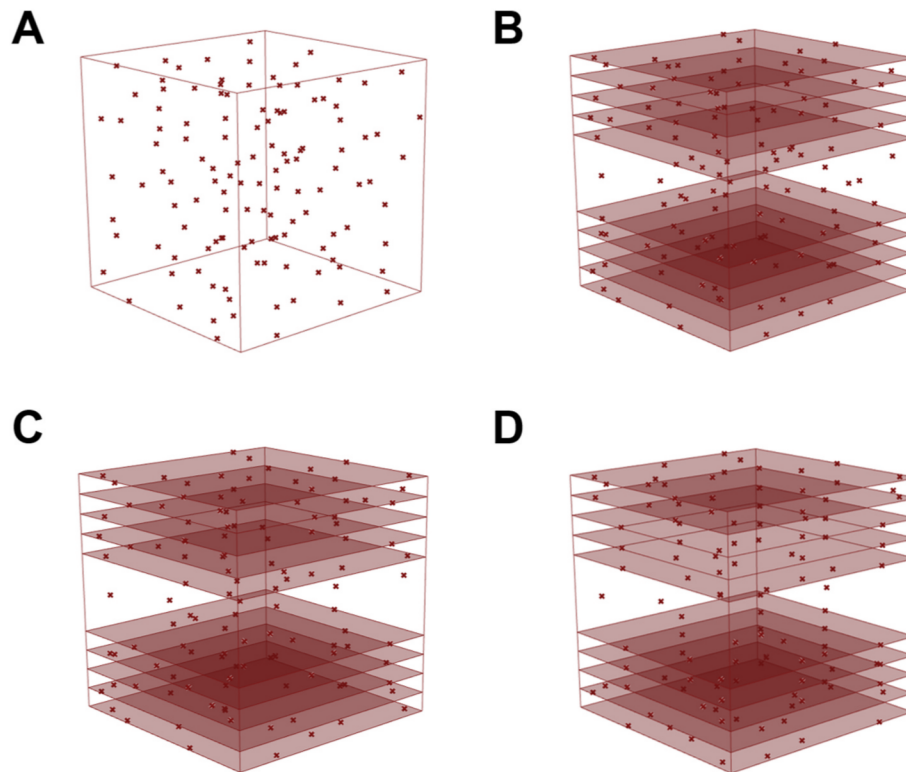
Fig. 3. Selective Voronoi seeding in 6 mm × 6 mm x 6 mm cubic volumes. Anisotropic implants have seeds redistributed preferentially to the upper and lower thirds of the cube, but each cube contains 123 seeds. (A) Isotropic implant where seeding is entirely uniform. (B) Anisotropic implant with 3–5 seeds redistributed in each plane. (C) Anisotropic implant with 5–7 seeds redistributed in each plane. (D) Anisotropic implant with 8–10 seeds redistributed in each plane.

with lower seed density in the voided regions. Seeding in the isotropic structure appears random, but uniform in comparison to the anisotropic structures. Upon polyhedral expansion (Fig. 4), preferential orientation was observed in the polyhedra of the anisotropic implants as a result of the heterogeneous seeding. Boundary conversion to lattice struts (Fig. 5) visually confirms directionality in the anisotropic implants, where the meshed structures all have the appearance of naturally-occurring trabecular bone.

3.2. Strut analysis

Normalized global anisotropy values by MIL and SVD measurements are shown in Table 1 for the isotropic and anisotropic implants. Adding the preferential seeding to form an anisotropic structure increased the MIL measurement in all cases relative to the isotropic structure. Increasing the number of seeds on each redistribution plane in the anisotropic structure also resulted in higher MIL, indicating a greater tendency for scaffold struts to be co-aligned in any anisotropic implant than the isotropic implant. A similar trend was observed for SVD measurements of anisotropy, where the anisotropic geometry with 8–10 seeds per plane had a substantially higher star volume distribution than any of the other implant models.

Histomorphometry of each of the four structures is also shown in Table 1. For all four structures, the bone volume fraction was measured to be constant at 0.16. No appreciable deviation was observed in the trabecular thickness of struts generated using the isotropic or selective seeding techniques. For the isotropic structure and each of the preferentially seeded structures, the mean trabecular thickness ranged from 249 μm to 259 μm.

The ITA measurements for each implant structure are shown in Fig. 6, with average values and standard deviations reported in Table 2 alongside literature values from a human femur. For 3N junctions, the isotropic implant behaves very similarly to the anisotropic implants, where high-angle inter-trabecular angles in the range of 130–170° are
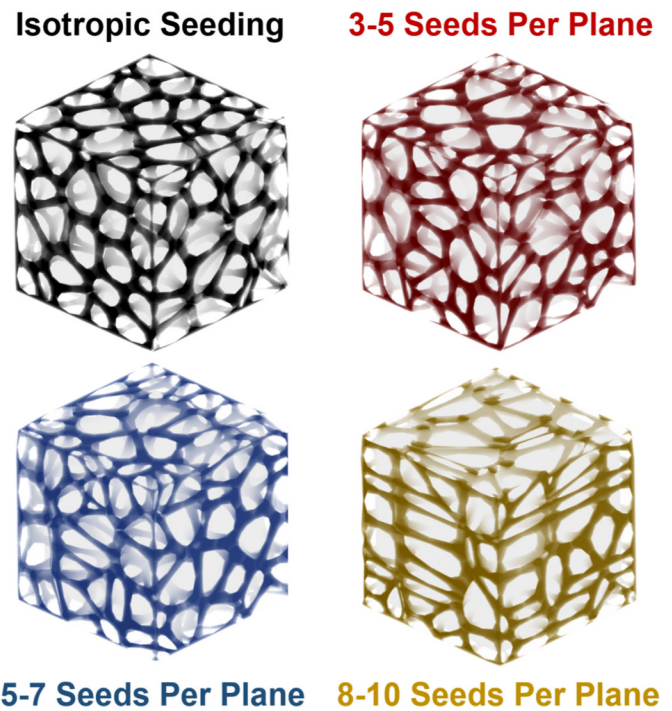
Fig. 5. Resulting strut architecture of the isotropic implant (black), 3–5 SPP anisotropic implant (red), 5–7 SPP anisotropic implant (blue), and 8–10 SPP anisotropic implant (gold). As the number of seeds per plane increases, strut distortion is visible along two preferential axes.

most abundant. Compared to tomography data averaged across a human femur (Reznikov et al., 2016), the deviation in mean 3N angle is within 5° for any of the implants investigated in this study.
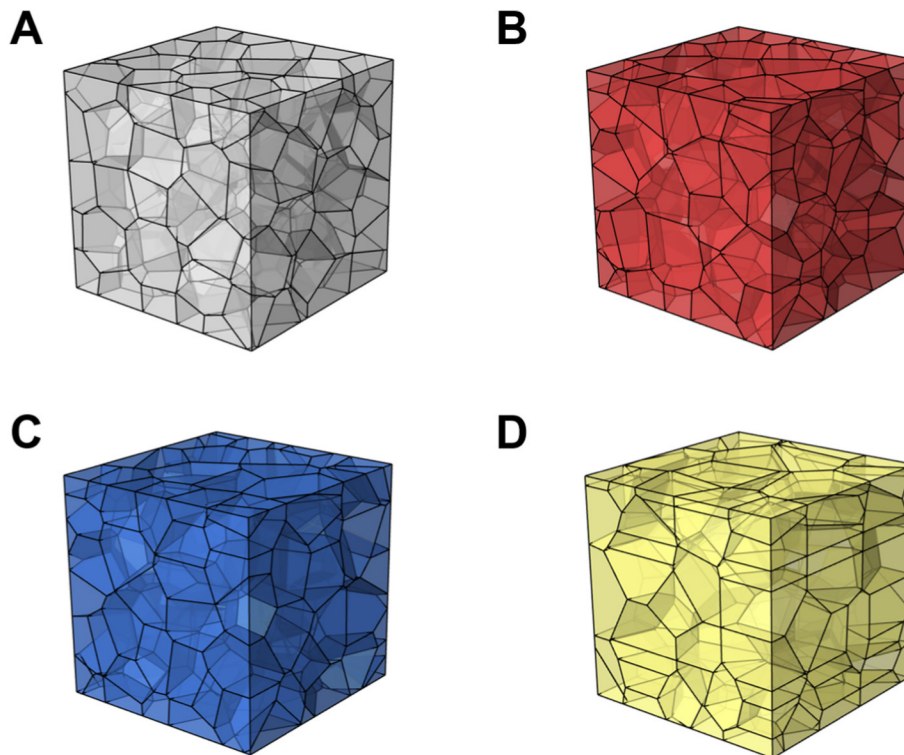
Fig. 4. Polyhedral expansion in the isotropic and anisotropic implants. Polyhedral morphology appears uniform when using traditional Voronoi seeding and distorted when using selective Voronoi seeding. (A) Isotropic implant with uniform seeding. (B) Anisotropic implant with 3–5 seeds redistributed in each plane. (C) Anisotropic implant with 5–7 seeds redistributed in each plane. (D) Anisotropic implant with 8–10 seeds redistributed in each plane.

Table 1

Normalized degree of anisotropy for each implant. Nonuniform Voronoi seeding resulted in higher normalized values of anisotropy in the implant, which increased with increasing seed redistribution.

	Isotropic	3-5 SPP	5-7 SPP	8-10 SPP
Anisotropy (MIL)	0.06	0.11	0.21	0.38
Anisotropy (SVD)	0.16	0.14	0.18	0.34
Bone Volume Fraction (BV/TV)	0.16	0.16	0.16	0.16
Trabecular Thickness (Tb.Th)	258.7 μm	250.9 μm	251.2 μm	249.1 μm
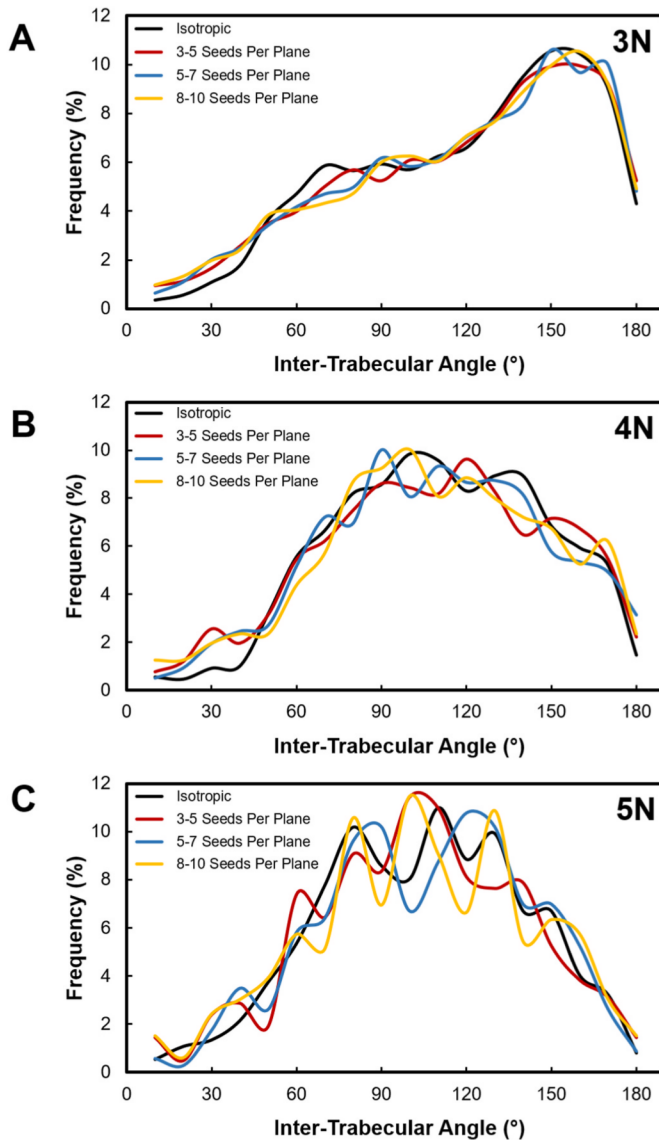
Fig. 6. ITA measurements for isotropic, 3–5 SPP anisotropic, 5–7 SPP anisotropic, and 8–10 SPP anisotropic implants. (A) 3N junctions. High-angle ITAs (130–170°) are most frequent for this junction type. (B) 4N junctions. ITAs in the range of 90–130° are more common in 4N junctions, where this range lies below that of the 3N junction type. (C) 5N junctions. ITAs are elevated in a somewhat similar range to that of 4N junctions (80–130°).

4N junctions for the isotropic and anisotropic implants were also similar. Angles between 90 and 130° were most common for the Voronoi implant structures, which is lower than the values observed for the 3N junctions. While the mean 4N angle for the implants is slightly below that of an averaged human femur, the deviation is reduced to within 2–4° of human femoral tissue.

5N junctions were less common in the implants than 3N or 4N junctions, resulting in greater variation in the ITA plots. Similar to the 4N junctions, angles were commonly found in the range of 80–130°. No substantial difference was observed between the isotropic and anisotropic implant structures, where the deviation from human femoral tissue ranged from 2 to 3°.

Field vector diagrams (Fig. 7) of the cube interior affirm these results. Vectors in this diagram are assigned a colour depending on co-alignment to a coordinate axis. In the isotropic implant, field vectors are distributed evenly between the three coordinate axes and their intermediate directions. In the anisotropic implants, especially in the 8–10 SPP implant, vectors are more likely to be co-oriented with the defined X-axis or Y-axis. Z-oriented vectors become less common as the seed redistribution is increased in an anisotropic Voronoi tessellation.

4. Discussion

This work highlights a method of selective Voronoi tessellation as an effective means of creating a biomimetic anisotropic scaffold. By placing a higher density of Voronoi seeds in specific regions of the implant geometry, pores can be elongated in a desired direction. This elongation introduces anisotropy into the scaffold versus the traditional form of Voronoi tessellation, as measured by MIL and SVD.

The MIL anisotropy of the isotropic structure was found to be 0.06. This value is atypical of what is found in human femoral and humeral bone, which have been measured to average 0.641 and 0.207, respectively (Doershuk et al., 2019). By introducing the redistributed seeding planes and adjusting their seed density, selective Voronoi tessellation was able to increase anisotropy to a range of 0.11–0.38 by MIL measurement, or up to 0.34 from 0.16 in the case of SVD measurement. The selective form of Voronoi tessellation for implant design is therefore able to better mimic human trabecular bone with regards to anisotropy by creating a customizable design environment. By adjusting the seed distribution in the implant geometry, implants can be designed with a target level of anisotropy that best matches the anatomy of the defect site. Similarly, bone volume fractions and trabecular thickness from isotropic and anisotropic Voronoi models were measured to be 0.16 and roughly 250 μm, respectively. These are both consistent with values from dual energy X-ray absorption scans of femoral trabecular bone in humans, where bone volume fractions are roughly 0.11 to 0.18 (Parkinson and Fazzalari, 2003; Greenwood et al., 2015) and trabecular thickness can extend up to 250 μm (Greenwood et al., 2015). The design of implants for joint replacement can make use of these biomimetic principles, where scaffold struts can be fabricated in an equivalent size to natural trabeculae in the defect site.

Trabecular bone geometry has also been stated to follow prescribed angles. Investigation of 5N/6N junctions in human femoral tissue shows angles most commonly between 80° and 115° (Reznikov et al., 2016). This model is fairly consistent with an ideal trigonal bipyramidal structure, which contains six 90° angles and three 120° angles, for a mean ITA of 100°. A similar ITA distribution for 5N junctions was observed in the generation of the isotropic and anisotropic implants in this work, where the highest frequency of angles was in the range of 80–130° and mean 5N ITAs ranged from 98.1 to 100.5°. Similar observations can be made with the 4N junctions in the isotropic and anisotropic Voronoi implants, where the mean angle of 103.3–105.3° is comparable to a tetrahedral trabecular arrangement. In 3N junctions, the mean angle of 113.4–114.6° in the Voronoi tessellations suggests a possible similarity to a trigonal planar trabecular arrangement.

Here, our results were presented solely on the basis of a cubic volume. The cubic volume used for selective Voronoi tessellation is a model for a simplistic implant geometry, but the technique can certainly be expanded to other, more complex implant geometries. For example, future applications of this work could apply this selective tessellation to the design of complex geometrical implants. In one such potential extension of this work, looking at the femoral component of a typical

Table 2

Inter-trabecular angle measurements from the isotropic implant structure, anisotropic implant structure, and literature value for human femur. Values between test groups are similar for any given junction type.

	Isotropic	3-5 SPP	5-7 SPP	8-10 SPP	Human Femur
5N Junction	$99.3° \pm 35.9°$	$98.1° \pm 37.3°$	$100.5° \pm 36.3°$	$98.9° \pm 38.6°$	$103.1° \pm 33.0°$ (Reznikov et al., 2016)
4N Junction	$105.3° \pm 36.3°$	$103.5° \pm 39.7°$	$103.5° \pm 38.6°$	$103.3° \pm 39.7°$	$107.6° \pm 31.8°$ (Reznikov et al., 2016)
3N Junction	$114.6° \pm 40.7°$	$113.5° \pm 42.9°$	$113.9° \pm 42.7°$	$113.4° \pm 43.2°$	$116.3° \pm 29.1°$ (Reznikov et al., 2016)
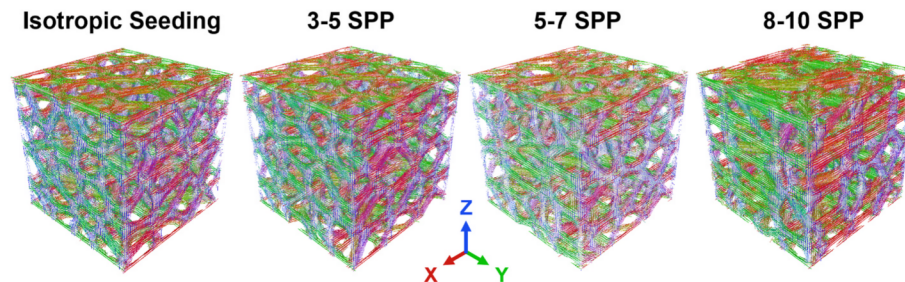
Fig. 7. Field vector diagrams of the implant interior showing even distribution of field vectors in the isotropic implant versus the predominant alignment of field vectors in the X and Y axes for the anisotropic implants. Red vectors are aligned with the X-direction, green vectors are aligned with the Y-direction, and blue vectors are aligned with the Z-direction. Intermediate colours represent spatial orientation with respect to each coordinate axis. Blue vectors are notably less abundant in the 8–10 SPP implant.

total hip arthroplasty, the transition through the epiphyseal and metaphyseal regions typically follows the inherent curvature of the bone. The average angle between the femoral head and femur shaft in a healthy adult is approximately 130° (Clohisy et al., 2009). While the global mechanical axis of the lower extremity runs at 3° (Cherian et al., 2014), the average orientation of trabeculae in the epiphyseal region and femoral head tends to be closer to 40° when measured from the center of the femoral head in primates (Ryan and Ketcham, 2005). Selective Voronoi tessellation of more complex geometries, such as this hypothetical example, would offer the potential to contour pore structures to follow trabecular orientation through the epiphyseal, metaphyseal, and diaphyseal portions of the long bones, providing a promising approach for generating femoral implants that mimic the natural femur. The vector field diagrams in this work show that preferential planes with a high seed density result in a co-oriented representative vector field within the implant struts. By controlling the rotation angle and spacing of adjacent seeding planes, the selective seeding approach introduced here offers an interesting alternative to contour local strut orientation along a complex mechanical axis while maintaining co-alignment with neighbouring struts and overall contiguity. As an example, Fig. 8A shows the traditional implant geometry of a total hip joint replacement. Using conventionally repeated patterning (Fig. 8B) fails to introduce local directionality into a curved implant geometry. Traditional Voronoi tessellation (Fig. 8C) introduces a seemingly biomimetic structure but again lacks this degree of local trabecular alignment. However, selective Voronoi tessellation (Fig. 8D) produces struts that are able to follow local contours of the implant while maintaining global anisotropy. Where this work demonstrates the relationship between seed density within the added seeding planes and resulting anisotropy, it is also possible to extend the method of selective Voronoi tessellation to produce isotropy-graded implants to best mimic the properties of existing human bone tissue in future work.

5. Conclusions

This study demonstrates that selective Voronoi tessellation is an effective way to introduce global and local anisotropy into a biomimetic porous scaffold. Selective seed placement in the geometry results in preferential strut elongation. MIL measurements confirm that anisotropy increases when directionality is introduced into the scaffold compared to a standard Voronoi tessellation. Selective Voronoi tessellation also offers a way of elongating the struts along the mechanical axis in complex geometries without compromising the randomization of the structure. By introducing redistributed seeding planes, the anisotropy
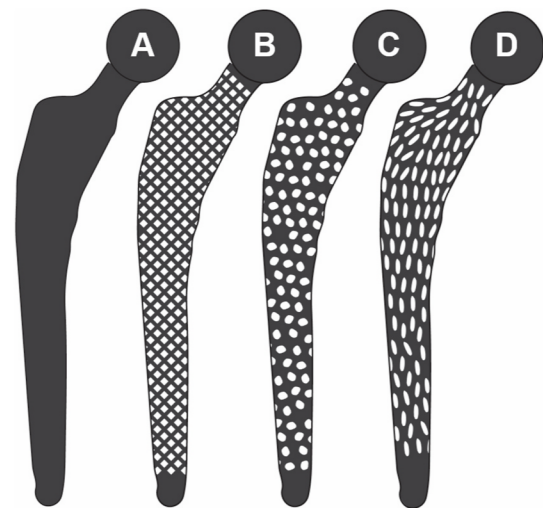
Fig. 8. The use of porous structures in curved geometries such as the femoral component of hip implants. (A) The geometry of a traditional full-density implant. (B) The use of a reticulated porous geometry, where the use of a repeating pattern fails to follow contours anisotropy, (C) The use of standard Voronoi tessellation, where the implant geometry has a trabecular-like appearance, but struts do not follow the contoured geometry of the implant. (D) The use of selective Voronoi tessellation to form a biomimetic geometry, where struts are trabecular in appearance and follow the local contours of the implant.

was increased to within the range of human trabecular bone without substantial compromise to the biomimetic inter-trabecular angle for 3N, 4N, and 5N junction types. 3N, 4N, and 5N angular distributions in all Voronoi implants were also observed to mimic trigonal planar, tetrahedral, and trigonal bipyramidal trabecular arrangements, respectively. This work paves a path towards the fabrication of customizable biomimetic implants using additive manufacturing with tunable mechanical properties based on the inherent bone geometry of a specific anatomical site in a patient. For example, this work shows that selective Voronoi tessellation can be used as an implant fabrication method for total hip arthroplasty to take into account the local anisotropic regions along the mechanical axis, where tunable degrees of seed density along preferred planes can add or subtract the desired quantity of anisotropy. For complex regions of bone associated with the replacement of the hip, such as the femoral metaphysis, selective Voronoi tessellation improves

upon standard non-trabecular porous geometries. Future research should focus on modifying the selective Voronoi method to better match strut thickness in human trabeculae, characterizing the mechanical performance of these scaffolds, and investigating the *in vitro* and *in vivo* osseointegration potential of these geometries as biomimetic implants.

Credit authorship statement

J. Deering: Conceptualization, Methodology, Software, Formal Analysis, Writing – Original Draft, Writing - Review & Editing.

K.I. Dowling: Conceptualization, Methodology, Software, Formal Analysis, Writing – Original Draft, Writing – Review & Editing.

L.A. DiCecco: Conceptualization, Software, Visualization, Writing - Review & Editing.

G.D. McLean: Conceptualization, Investigation, Writing – Review and Editing.

B. Yu: Conceptualization, Methodology, Writing – Review and Editing.

K. Grandfield: Conceptualization, Supervision, Funding Acquisition, Writing – Review & Editing.

Declaration of competing interest

The authors declare that they have no known competing financial interests or personal relationships that could have appeared to influence the work reported in this paper.

Acknowledgements

Appendix A. Supplementary data

Supplementary data to this article can be found online at https://doi.org/10.1016/j.jmbbm.2021.104361.

References

Alkhader, M., Vural, M., 2008. Mechanical response of cellular solids: role of cellular topology and microstructural irregularity. Int. J. Eng. Sci. 46 (10), 1035–1051.

Bandyopadhyay, A., Espana, F., Balla, V.K., Bose, S., Ohgami, Y., Davies, N.M., 2010. Influence of porosity on mechanical properties and in vivo response of Ti6Al4V implants. Acta Biomater. 6 (4), 1640–1648.

Cherian, J.J., Kapadia, B.H., Banerjee, S., Jauregui, J.J., Issa, K., Mont, M.A., 2014. Mechanical, anatomical and kinematic Axis in TKA: concepts and practical applications. Curr Rev Musculoskelet Medicine 7 (2), 89–95.

Chevalier, Y., Pahr, D., Allmer, H., Charlebois, M., Zysset, P., 2007. Validation of a voxel-based FE method for prediction of the uniaxial apparent modulus of human trabecular bone using macroscopic mechanical tests and nanoindentation. J. Biomech. 40 (15), 3333–3340.

Choren, J.A., Heinrich, S.M., Silver-Thorn, M.B., 2013. Young's modulus and volume porosity relationships for additive manufacturing applications. J. Mater. Sci. 48 (15), 5103–5112.

Clohisy, J.C., Nunley, R.M., Carlisle, J.C., Schoenecker, P.L., 2009. Incidence and characteristics of femoral deformities in the dysplastic hip. Clin. Orthop. Relat. Res. 467 (1), 128–134.

de Vasconcellos, L.M.R., Leite, D.O., de Oliveira, F.N., Carvalho, Y.R., Cairo, C.A.A., 2010. Evaluation of bone ingrowth into porous titanium implant: histomorphometric analysis in rabbits. Braz. Oral Res. 24 (4), 399–405.

Doershuk, L.J., Saers, J.P.P., Shaw, C.N., Jashashvili, T., Carlson, K.J., Stock, J.T., Ryan, T.M., 2019. Complex variation of trabecular bone structure in the proximal humerus and femur of five modern human populations. Am. J. Phys. Anthropol. 168 (1), 104–118.

Engh, C., Bobyn, J., Glassman, A., 1987. Porous-coated hip replacement. The factors governing bone ingrowth, stress shielding, and clinical results. J. Bone Jt. Surg. Br. Vol. 69-B (1), 45–55.

Enns-Bray, W.S., Owoc, J.S., Nishiyama, K.K., Boyd, S.K., 2014. Mapping anisotropy of the proximal femur for enhanced image based finite element analysis. J. Biomech. 47 (13), 3272–3278.

Fantini, M., Curto, M., 2018. Interactive design and manufacturing of a Voronoi-based biomimetic bone scaffold for morphological characterization. Int J Interact Des Manuf Ijidem 12 (2), 585–596.

Fantini, M., Curto, M., Crescenzio, F.D., 2016. A method to design biomimetic scaffolds for bone tissue engineering based on Voronoi lattices. Virtual Phys. Prototyp. 11 (2), 77–90.

Gebhardt, A., 2011. Understanding Additive Manufacturing. Carl Hanser Verlag, Munich.

Greenwood, C., Clement, J.G., Dicken, A.J., Evans, J.P.O., Lyburn, I.D., Martin, R.M., Rogers, K.D., Stone, N., Adams, G., Zioupos, P., 2015. The micro-architecture of human cancellous bone from fracture neck of femur patients in relation to the structural integrity and fracture toughness of the tissue. BoneKEy Rep. 3, 67–75.

Harrysson, O.L.A., Cansizoglu, O., Marcellin-Little, D.J., Cormier, D.R., West, H.A., 2008. Direct metal fabrication of titanium implants with tailored materials and mechanical properties using electron beam melting technology. Mater. Sci. Eng. C 28 (3), 366–373.

Heinl, P., Müller, L., Körner, C., Singer, R.F., Müller, F.A., 2008. Cellular Ti-6Al-4V structures with interconnected macro porosity for bone implants fabricated by selective electron beam melting. Acta Biomater. 4 (5), 1536–1544.

Helguero, C.G., Amaya, J.L., Komatsu, D.E., Pentyala, S., Mustahsan, V., Ramirez, E.A., Kao, I., 2017. Trabecular Scaffolds' mechanical properties of bone reconstruction using biomimetic implants. Proc Cirp. 65, 121–126.

Hernigou, P., Medevielle, D., Debeyre, J., Goutallier, D., 1987. Proximal tibial osteotomy for osteoarthritis with varus deformity. A ten to thirteen-year follow-up study. J Bone Jt Surg 69 (3), 332–354.

Itälä, A.I., Ylänen, H.O., Ekholm, C., Karlsson, K.H., Aro, H.T., 2001. Pore diameter of more than 100 Ï¼m is not requisite for bone ingrowth in rabbits. J. Biomed. Mater. Res. 58 (6), 679–683.

Karre, R., Niranjan, M.K., Dey, S.R., 2015. First principles theoretical investigations of low Young's modulus beta Ti-Nb and Ti-Nb-Zr alloys compositions for biomedical applications. Mater. Sci. Eng. C 50, 52–58.

Kruth, J., Mercelis, P., Vaerenbergh, J.V., Froyen, L., Rombouts, M., 2005. Binding mechanisms in selective laser sintering and selective laser melting. Rapid Prototyp. J. 11 (Issue 1), 26–36.

Latture, R.M., Begley, M.R., Zok, F.W., 2019. Defect sensitivity of truss strength. J. Mech. Phys. Solid. 124, 489–504.

Li, G., Wang, L., Pan, W., Yang, F., Jiang, W., Wu, X., Kong, X., Dai, K., Hao, Y., 2016. In vitro and in vivo study of additive manufactured porous Ti6Al4V scaffolds for repairing bone defects. Sci Rep-uk 6 (1), 34072.

Liang, H., Yang, Y., Xie, D., Li, L., Mao, N., Wang, C., Tian, Z., Jiang, Q., Shen, L., 2019. Trabecular-like Ti-6Al-4V scaffolds for orthopedic: fabrication by selective laser melting and in vitro biocompatibility. J. Mater. Sci. Technol. 35, 1284–1297. Der Unfallchirurg 109 2006.

Lin, Y.-H., Chang, F.-S., Chen, K.-H., Huang, K.-C., Su, K.-C., 2018. Mismatch between femur and tibia coronal alignment in the knee joint: classification of five lower limb types according to femoral and tibial mechanical alignment. Bmc Musculoskelet Di 19 (1), 411.

Maconachie, T., Leary, M., Lozanovski, B., Zhang, X., Qian, M., Faruque, O., Brandt, M., 2019. SLM lattice structures: properties, performance, applications and challenges. Mater. Des. 183, 108137.

Odgaard, A., 1997. Three-dimensional methods for quantification of cancellous bone architecture. Bone 20 (4), 315–328.

Oftadeh, R., Perez-Viloria, M., Villa-Camacho, J.C., Vaziri, A., Nazarian, A., 2015. Biomechanics and mechanobiology of trabecular bone: a review. J. Biomech. Eng. 137 (1), 010802.

Parkinson, I.H., Fazzalari, N.L., 2003. Interrelationships between structural parameters of cancellous bone reveal accelerated structural change at low bone volume. J. Bone Miner. Res. 18 (12), 2200–2205.

Pham, M.-S., Liu, C., Todd, I., Lertthanasarn, J., 2019. Damage-tolerant architected materials inspired by crystal microstructure. Nature 565 (7739), 305–311.

Rajpura, A., Kendoff, D., Board, T.N., 2014. The current state of bearing surfaces in total hip replacement. Bone Jt J 96-B (2), 147–156.

Reznikov, N., Chase, H., Zvi, Y.B., Tarle, V., Singer, M., Brumfeld, V., Shahar, R., Weiner, S., 2016. Inter-trabecular angle: a parameter of trabecular bone architecture in the human proximal femur that reveals underlying topological motifs. Acta Biomater. 44, 65–72.

Reznikov, N., Alsheghri, A.A., Piché, N., Gendron, M., Desrosiers, C., Morozova, I., Siles, J.M.S., Gonzalez-Quevedo, D., Tamimi, I., Song, J., Tamimi, F., 2020. Altered topological blueprint of trabecular bone associates with skeletal pathology in humans. BoneKEy Rep. 12, 100264.

Rudy, D.J., Deuerling, J.M., Orías, A.A.E., Roeder, R.K., 2011. Anatomic variation in the elastic inhomogeneity and anisotropy of human femoral cortical bone tissue is consistent across multiple donors. J. Biomech. 44 (9), 1817–1820.

Ryan, T.M., Ketcham, R.A., 2005. Angular orientation of trabecular bone in the femoral head and its relationship to hip joint loads in leaping primates. J. Morphol. 265 (3), 249–263.

Sampath, S.A., Lewis, S., Fosco, M., Tigani, D., 2015. Trabecular orientation in the human femur and tibia and the relationship with lower-limb alignment for patients with osteoarthritis of the knee. J. Biomech. 48 (6), 1214–1218.

Seiler, P.E., Tankasala, H.C., Fleck, N.A., 2019. The role of defects in dictating the strength of brittle honeycombs made by rapid prototyping. Acta Mater. 171, 190–200.

Sikorski, J.M., 2008. Alignment in total knee replacement. Bone Joint Lett. J 90-B (9), 1121–1127.

Silva, M.J., Hayes, W.C., Gibson, L.J., 1995. The effects of non-periodic microstructure on the elastic properties of two-dimensional cellular solids. Int. J. Mech. Sci. 37 (11), 1161–1177.

Smit, T.H., Schneider, E., Odgaard, A., 1998. Star length distribution: a volume-based concept for the characterization of structural anisotropy. J Microsc-oxford 191 (3), 249–257.

Wang, X., Xu, S., Zhou, S., Xu, W., Leary, M., Choong, P., Qian, M., Brandt, M., Xie, Y.M., 2016. Topological design and additive manufacturing of porous metals for bone scaffolds and orthopaedic implants: a review. Biomaterials 83, 127–141.

Whitehouse, W.J., 1974. The quantitative morphology of anisotropic trabecular bone. J Microsc-oxford. 101 (2), 153–168.

Wik, T.S., Foss, O.A., Havik, S., Persen, L., Aamodt, A., Witsø, E., 2010. Periprosthetic fracture caused by stress shielding after implantation of a femoral condyle endoprosthesis in a transfemoral amputee - a case report. Acta Orthop. 81 (6), 765–767.

Ying, S., Xu, G., Li, C., Mao, Z., 2015. Point cluster Analysis using a 3D Voronoi diagram with applications in point cloud segmentation. Isprs Int Geo-inf 4 (3), 1480–1499.

Zheng, Q., Ju, S., Jiang, D., 2014. Anisotropic mechanical properties of diamond lattice composites structures. Compos. Struct. 109, 23–30.

Zhu, H.X., Hobdell, J.R., Windle, A.H., 2001. Effects of cell irregularity on the elastic properties of 2D Voronoi honeycombs. J. Mech. Phys. Solid. 49 (4), 857–870.

Selective Voronoi Tessellation as a Method to Design Anisotropic and Biomimetic Implants

Joseph Deering [a, †], Kierdra I. Dowling [a, †], Liza-Anastasia DiCecco [a], Griffin D. McLean [b], Bosco Yu [a], Kathryn Grandfield [a,c,*]

[†] *These authors contributed equally.*

[a] *Department of Materials Science and Engineering, McMaster University, Hamilton, ON, Canada*

[b] *Department of Mechanical Engineering, McMaster University, Hamilton, ON, Canada*

[c] *School of Biomedical Engineering, McMaster University, Hamilton, ON, Canada*

The link to Grasshopper scripts and STL files for the isotropic, 3-5 SPP, 5-7 SPP, and 8-10 SPP implant structures can be found below. The Grasshopper plug-in for Rhino 6 modelling software is required to run the scripts, but STL files can be opened with any modelling software.

https://github.com/j-deering/Anisotropic-Implants-by-Voronoi-Tessellation

Chapter 4: Fabrication of Succinate-Alginate Xerogel Films for *In Vitro* Coupling of Osteogenesis and Neovascularization

Summary:

Part of the peri-implant healing response in bone involves the early formation of a vascular network near the implant surface before substantial bone apposition. Much of the innovation for bone-interfacing implant surface modification focuses on the osteoblast-implant interaction rather than any preceding biological response. This chapter explains the development of surface films to promote the activity of endothelial cells in addition to osteoblast-like cells using an alginate matrix to release varying concentrations of disodium succinate. The release rate was characterized via pH measurement to find that elution of the succinate occurs within the first few hours. *In vitro* exposure of endothelial cells to succinate-conditioned media resulted in a coarser tube network and higher baseline protein production, without significant depletion or production of two vascular growth markers. In xerogel form, the films produce a micro-rough cobblestone-like morphology that transitions to an intermittently wrinkled surface after rehydration. This work relates to the themes of the thesis by developing surface modification strategies for future application to porous additively manufactured materials.

Citation:

Deering, J., Lin, D.S.Y., D'Elia, A., Zhang, B., and Grandfield, K. (2022). Fabrication of succinate-alginate xerogel films for in vitro coupling of osteogenesis and neovascularization. *Biomaterials Advances, Submission No. BIOADV-D-22-01116.*

Permissions:

This work is currently in submission in *Biomaterials Advances* (Submission No. BIOADV-D-22-01116). As the author of this article, I retain the right to include the work within this thesis, provided there is no commercial benefit.

Fabrication of succinate-alginate xerogel films for in vitro coupling of osteogenesis and neovascularization

Joseph Deering[1], Dawn S. Y. Lin[2], Andrew D'Elia[1], Boyang Zhang[2,3], Kathryn Grandfield[1,3,4]

[1] Department of Materials Science and Engineering, McMaster University, Hamilton, ON, Canada

[2] Department of Chemical Engineering, McMaster University, Hamilton, ON, Canada

[3] School of Biomedical Engineering, McMaster University, Hamilton, ON, Canada

[4] Brockhouse Institute for Materials Research, McMaster University, Hamilton, ON, Canada

Abstract

The osseointegration of metallic implants relies on a cascade of molecular interactions and the delivery of macromolecules to the implant environment that occurs before substantial bone formation. Early blood vessel formation is a requisite first step in the healing timeline for osteoid formation, where vascular development can be accelerated as a result of controlled hypoxic conditioning. In this study, alginate-derived xerogel films containing varied concentrations of disodium succinate salt which has been shown to induce pseudohypoxia (short-term hypoxic effects while maintaining an oxygenated environment) were developed. Xerogels were characterized for their morphology, succinate release over time, and cellular response with osteoblast-mimicking Saos-2 and human umbilical vein endothelial cells (HUVEC). Scanning electron microscopy revealed a multiscale topography that may favour osseointegration and alamarBlue assays indicated no cytotoxic effects during *in vitro* proliferation of Saos-2 cells. pH measurements of eluted succinate reach 95% of peak value after 7 hr of immersion for all gels containing 10 mM of succinate or less, and 60% within the first 40 min. *In vitro* exposure of HUVECs to succinate-conditioned media increased the net concentration of total proteins measured by bicinchoninic acid (BCA) assay and maintains stable vascular endothelial growth factor (VEGF) and extracellular platelet-derived growth factor (PDGF) for vessel formation through comparison of enzyme-linked immunosorbent assays (ELISAs) of the culture media and cell lysate. Tube formation assays also showed a sustained increase in tube diameter across the first 48 hr of HUVEC culture when succinate concentrations of 1 and 10 μM in the xerogel. Overall, the succinate-alginate films serve as a prospective organic coating for bone-interfacing implant materials which may induce temporary pseudohypoxic conditions favourable for early angiogenesis and bone regeneration *in vivo* at succinate concentrations of 1 or 10 μM.

4.1 Introduction

At the core of total joint replacement and dental procedures, success is contingent on the integration of implant materials with existing bone and connective tissue in a process termed 'osseointegration' [1]. Failure of classical implants has sparked the development of biomaterials and bioactive agents that mimic and support the growth of bone tissue while addressing root causes of implant failure, especially where improvement in short-term bone ingrowth and direct bone-implant contact has been correlated to long-term implant success [2]. Coating deposition offers a means to improve the bioactivity of the native implant surface and techniques including electrodeposition [3,4], dip coating [5,6], plasma spraying [7,8], or vapour deposition [9,10] are available to apply organic, ceramic, or composite films to a metallic prosthesis. In particular, immersion-based strategies can be better than line-of-sight techniques for coating the entirety of materials with complex or porous geometries. Matrix materials such as chitosan [11,12], alginate [13,14], and hyaluronic acid [15,16] exhibit the capacity to deliver biomolecules directly to the bone-implant interface while simultaneously mimicking the structure of the natural extracellular matrix in hydrogel form [17]. Integration of nanoceramics, therapeutic drugs and growth factors, and/or antimicrobial agents into these gel-based coatings may improve long-term outcomes of the implant. However, the early osteoinductive pathway begins long before any form of bone mineral apposition with the formation of a blood vessel network.

Neovascularization within the surgically resected volume is one step within the osteoinduction process, where the development of new blood vessels is pivotal for driving local cell recruitment and potentiating macromolecular transport [18]. Aside from facilitating waste transport and oxygen delivery, the formation of new blood vessels allows for direct migration of osteogenic progenitor cells and relevant growth factors [19], where angiogenic growth factors such as vascular endothelial growth factor (VEGF) or platelet-derived growth factor (PDGF) can serve as osteoblastic and osteoclastic chemoattractants on the surface of implant materials [20,21]. The exogenous addition of these compounds has resulted in favourable vascular development in general tissue engineering [22] and cardiac-specific [23] applications. Tumour angiogenesis can also be attributed to these factors [24]. Elution of angiogenic growth factors in the peri-implant environment has been shown to increase proliferation and differentiation of cells during the development and remodelling of blood vessels in a generalized manner [25–27]. Specifically, the presence of VEGF influences cell fates in a complex, time-dependent manner. Early in the angiogenic cascade, VEGF can encourage survival of cells with an endothelial origin [28] but prolonged exposure can cause leakage in more mature vascular networks [29]. Angiogenic agents have been incorporated into materials in various studies to facilitate formation of new blood vessels both *in vivo* and *in vitro* [30–33], but the recombinant form of growth factors can be sensitive to handling/storage [34] and their efficacy depends highly on structural preservation of subunits [35] making them difficult agents to incorporate into biomaterial coatings.

The family of hypoxia-related genes, which are stimulated in oxygen-starved environments, is regulated by the transcription factor hypoxia-inducible factor 1-alpha

(HIF-1α) [36]. Upstream stabilization of HIF-1α has been shown to have direct consequences on activating hypoxia-responsive elements (HREs) in the nucleus and can result in further endogenous upregulation of angiogenic growth factors (PDGF and VEGF) and angiogenesis as a whole [37]. Within normoxic environments (Figure 4-1i), existing HIF-1α within the cellular domain is tagged with a hydroxyl group by prolyl hydroxylase 2 [38] and HIF-1α is subsequently subjected to proteasomal degradation after its ubiquitination with von Hippel Lindau [39]. In hypoxic environments (Figure 4-1ii), the absence of oxygen allows the HIF-1α complex to bypass the hydroxylation step of the typical degradation process and translate to activate nuclear HREs, resulting in increased levels of angiogenic proteins [40]. Extending to an *in vivo* setting, prolonged hypoxia and ischemia can have more far-reaching negative consequences. In bone especially, ischemic mechanisms are commonly the final stage in avascular necrosis of the tissue [41]. However, it is possible to alter the HIF-1α pathway without disrupting oxygen levels in the tissue. The stabilization of HIF-1α with precise administration of cobalt chloride is something that has been recently investigated for angiogenic applications and has resulted in upregulation of VEGF and activation of vascular cell progenitors [42–44], although its long-term health effects are still being observed. Due to its potentially hazardous nature [45], it is important to establish viable alternatives for controlled coupling of angiogenesis and osteogenesis at the implant surface. Succinate, a naturally-derived metabolite, offers the capability to produce a similar pseudohypoxic response (Figure 4-1iii) within the cell where it serves as both a competitive inhibitor and product of prolyl hydroxylases [46]. With respect to cellular transport, a local abundance of extracellular succinate can be uptaken into mammalian cells to create intracellular pseudohypoxia using sodium-dependent SLC13 transporters [47]. In theory, tuning the local release profile of succinate within the implant environment can temporarily control how much HIF-1α bypasses the hydroxylation stage and translocates to activate HREs.

In this work, we assess the viability and *in vitro* response of alginate – a known biocompatible material [48] – with added succinate as a coating material for implants. By isolating cell studies to assess osteocompatibility and endothelial activity, we aim to characterize the *in vitro* influence of succinate-stabilized HIF-1α as a tool for fabricating tunable implant surfaces and implicate corresponding responses for bone mineral apposition rates.
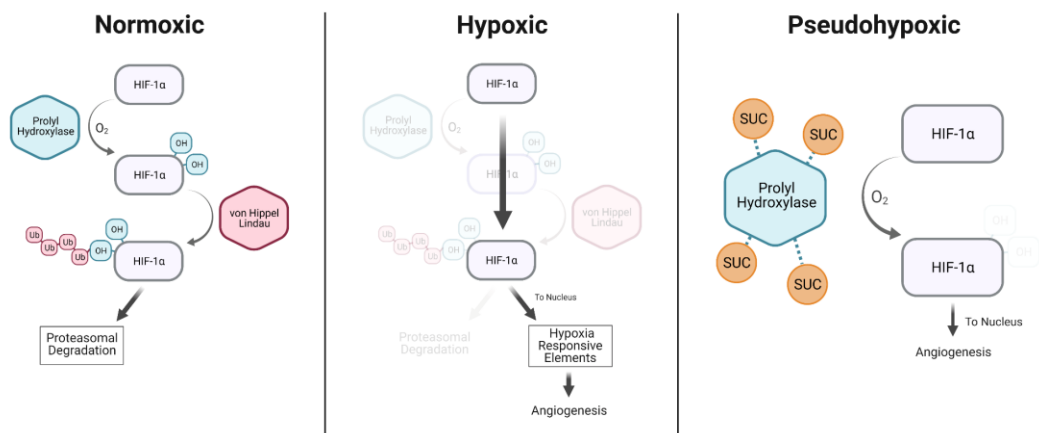
Figure 4-1: *Pathways for HIF-1α under: (i) Normoxic conditions, where prolyl hydroxylase tags HIF-1α with a hydroxyl group for subsequent ubiquitination, and there is no corresponding activation of hypoxia responsive elements. (ii) Hypoxic conditions, where the absence of oxygen allows high amounts of stable HIF-1α to be translated to the nucleus and upregulate the production of angiogenic factors. (iii) Pseudohypoxic conditions, where the addition of succinate serves as a competitive inhibitor for prolyl hydroxylase and partial translation of HIF-1α to the nucleus occurs as a result.*

4.2 Methods

4.2.1 Xerogel Synthesis

Stock solution of 3 wt% alginic acid sodium salt (1.56 mannuronate-to-guluronate ratio, MilliporeSigma) in deionized water was prepared by mixing at 800 RPM for 20 min until a notable viscosity change was observed and the solution appeared homogenous. For each following experimental protocol, the corresponding mass of succinic acid disodium salt (162.05 g/mol, MilliporeSigma) was added to aliquots of the alginate stock solution to produce solutions with succinate concentrations of 100 mM, 10 mM, 1 mM, 100 μM, 10 μM, and 1 μM, pipetting up and down at least fifteen times to mix thoroughly. Xerogels were formed by solvent casting the mixture onto the substrate and drying in air at room temperature for 48-72 hr, until no visible liquid remained.

4.2.2 Scanning Electron Microscopy

Alginate-succinate coatings were cast directly onto aluminum stubs wrapped in aluminum tape to form a bowl shape for containment (300 μL of casting solution for each 12.7 mm diameter stub). Substrates were left to dry in air for 48 hr prior to imaging. Xerogels were imaged without sputter coating at an accelerating voltage of 5 kV with a JSM-6610LV microscope (JEOL). Gels were rehydrated with 100 μL of 4 vol% choline lactate (SigmaMillipore) in deionized water to add conductivity to the gels in addition to maintaining hydration under microscope vacuum. Imaging of the hydrated gels was performed at an accelerating voltage of 20 kV.

4.2.3 Succinate Release Profiles

2 mL of each alginate-succinate solution (100, 10, 1, 0.1, 0.01, and 0.001 mM succinic acid disodium salt) was cast into 20 mL borosilicate scintillation vials and allowed to dry completely in air (typically 7 days). 18 mL of deionized water was added to the vials and pH measurements were recorded at 5 min intervals over a span of 36 hours using a pH of 7.00 as a starting point – ensuring the pH probe was left in solution for the entire duration. As succinic acid is classified as a weak acid, the complementary sodium salt produces a minor pH increase upon solubilization. Two replicates were run for release studies in each succinate concentration and the average profile was reported.

4.2.4 In Vitro Osteoblast Culture

1 mL of each alginate-succinate gel (100, 10, 1, 0.1, 0.01, 0.001, and 0 mM succinate) was pipetted into individual wells of a 24-well tissue culture polystyrene plate, with six replicates for each test condition, and left to dry for 48 hr. Saos-2 (HTB-85, ATCC) osteoblast-mimicking cells were seeded onto each gel and uncoated wells at a density of 10,000 cells/cm^2 in McCoy's modified 5A media supplemented with fetal bovine serum and penicillin-streptomycin as described elsewhere [49]. Plates were incubated at 37°C and 5% CO_2 for metabolic measurement at 1 and 4 days. At these time points, metabolic activity was assessed by incubating in a 5% mixture of alamarBlue™ dye (Life Technologies Inc.) in culture media for 60 min and corresponding fluorescence readings at an excitation-emission wavelength of 540-580 nm. Following the 1-day measurements, culture media was restored to the wells, and the same culture was assessed at the 4-day endpoint, with subsequent statistical analysis using a two-way ANOVA and $p < 0.05$.

4.2.5 In Vitro Endothelial Culture

Green Fluorescent Protein-tagged Human Umbilical Vein Endothelial Cells (GFP-HUVECs, Angio-Proteomie) were cultured in a 0.2% w/v gelatin (Sigma Aldrich) coated flask with a mixture of Endothelial Cell Growth Media (ECGM2, PromoCell) and disodium succinate. To observe vascularization at the implant interface, a 96-well plate was filled with 30 μL of growth-factor reduced Matrigel (Corning) into each well. Immediately after adding Matrigel, the plate was incubated at 37°C and 5% CO_2 for 30 minutes to allow gelation. After gelation, 200 μL of the cell suspension (30,000 cells/cm^2 for ELISAs and 10,000 cells/cm^2 for other analyses) was added on top of the Matrigel in each well. Vascularization was imaged using an image cytometer (BioTek Instruments Inc.).

Bright-field images were processed in Dragonfly 2020.1 (Object Research Systems) by application of a Sobel filter for edge detection of the tube network and a high-pass grayscale filter for segmentation of the vascular network. Thickness maps were generated from the segmentation for each biological replicate and timepoint in Dragonfly. Maps were overlaid onto the Sobel-filtered images for visualization and raw data was exported for quantitative measurements of the tube network. Coarsening of the tube network for each succinate concentration was assessed using a one-way ANOVA with a significance value of 0.05. Branching behaviour was operationalized by creating a skeletonization of the tube network

in Dragonfly, examining the total number of branching locations, and normalizing with respect to other culture conditions.

After 48 hr of culture and succinate exposure, endothelial cells were lysed with 250 µL of 0.1% Triton X-100 in phosphate-buffered saline for 10 min to permeabilize the cell membrane and release intracellular proteins. Three technical replicates containing 25 µL of lysis solution from each well were mixed with 200 µL of bicinchoninic acid reagent and incubated for 30 min. Absorbance readings were measured at an incident wavelength of 562 nm and converted to total protein content via a standard calibration curve generated from known concentrations of bovine serum albumin.

HUVEC cells were cultured at a density of 3×10^5 cells/cm^2 in endothelial growth medium-2 with 100 µM, 10 µM, and 1 µM of added disodium succinic acid salt for VEGF-A and PDGF-BB enzyme-linked immunosorbent assays. Cultures were conducted with four replicates and two samples were extracted from each well for ELISAs. ELISAs were conducted according to manufacturer instructions using 20 µL of culture media for intracellular PDGF-BB determination, 20 µL of lysate solution for extracellular PDGF-BB determination, 50 µL of culture media for intracellular VEGF-A determination, and 50 µL of lysate solution for extracellular VEGF-A measurement. Absorbance measurements were converted to concentrations using standard calibration curves and compared using a one-way ANOVA with significance defined as *p < 0.05*.

4.3 Results and Discussion

4.3.1 Scanning Electron Microscopy

Dehydrated alginate films with and without exogenous succinate addition were solvent cast to assess their morphology using secondary electron imaging in the scanning electron microscope (SEM). In Figure 4-2A, the dehydrated film of alginate alone shows a layered, fibre-like structure on the surface of the organic coating, with a series of nanoscale wrinkles that propagate across the entirety of the surface. The optimal surface for osseointegration is described to contain dual-scale topography with both microscale and nanoscale features aiding in the recruitment of osteoblasts and osteoblast progenitors [50], consistent with the topography shown in the dehydrated alginate gels. The wrinkled nature of the alginate xerogel is similar to what has been seen before from dehydrated forms of alginate [51] or other xerogels [52], which appear to contain a continuous network of fibres at their exterior and fulfil the intermediate length scale between nano- and microscale topographies. In the xerogel form, the alginate coatings appear to have a cobblestone-like appearance with consistent long-order patterning (Figure 4-2A) and a fragmented morphology with intermittent cavities at slightly higher magnification (Figure 4-2B). Additions of succinate across the millimolar and micromolar range (Figure 4-2C-H) to the gel casting solution retain this level of multiscale topography, with similar spacing between filaments in the fibrous backbone and similar size of 'fragments' in the xerogel. In all of the alginate-based xerogels, there appear to be circular-appearing regions that are consistent with shrinkage cavities. These are surrounded by concentric fragments within the xerogel and could be

regions of step-wise solidification within the alginate gel. Additions of succinate do not appear to significantly alter the surface morphology of the xerogel, and the lack of visible succinate aggregates indicates relatively uniform dispersion throughout the coating material.

Inducing vascular development at an implant site has also been shown to be sensitive to the surface topography of the implant. Metallic surface modification techniques such as acid etching or grit-blasting with roughness values on the order of a few microns have been shown to increase the amount of *in vitro* VEGF and PDGF being expressed at a wound site via increased platelet adhesion [53]. Similarly, the introduction of nanoscale features on an implant surface has shown stark increases in vascular regeneration after only seven days of *in vivo* growth [54]. Independent of any pseudohypoxic response, the topography of the alginate gels has a similar magnitude to that of a grit-blasted or acid-etched metallic surface. The cobblestone-like morphology of the films provides elements favourable for prospective aid in both osteogenesis and angiogenesis.
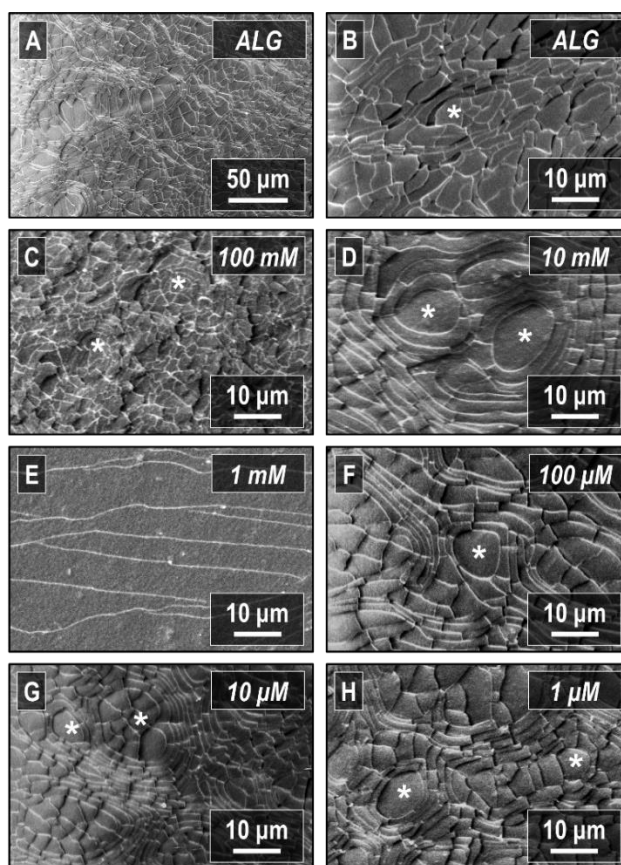
Figure 4-2: SEM of dehydrated succinate xerogels on metallic substrates with the following concentrations of succinate: (A-B) Alginate (ALG) only; (C) 100 mM; (D) 10 mM; (E) 1 mM; (F) 100 µM; (G) 100 µM; (H) 1 µM. Xerogels display a complex, fragmented surface topography favourable for cellular adhesion with a common concentric pattern centred at the marked regions.

SEM of hydrated materials is often challenging due to the high-vacuum environment within the microscope. Treatment with room-temperature ionic liquids has previously been shown to enable imaging of hydrated biological materials in a manner that preserves delicate microscale structures [55,56] where choline lactate pre-treatments cause minimal surface damage to hydrated polymeric structures [57,58]. While the surface topography of the succinate-alginate gels is favourable in dehydrated xerogel form, *in vitro* testing environments and *in vivo* applications of succinate-based gels are necessarily hydrated. To assess the effect of gel swelling on surface topography, the xerogels were rehydrated with a solution of room temperature choline lactate solution for additional SEM. A markedly different surface structure was seen in the hydrated gels compared to their xerogel state. A micrograph of the rehydrated alginate-only gel is seen in Figure 4-3A, where surface patterning on the microscale is equally abundant to the dehydrated state but there is a loss in mesoscale roughness. Here, the micro-wrinkled architecture of the dehydrated xerogel is evident in isolated regions, where wrinkles are seemingly more evident in gels with succinate content under 10 μM. In both the rehydrated alginate-only and rehydrated succinate-alginate gels, the multiscale features should be both angiogenic and osteogenic in nature. The transition from fragmented to micro-wrinkled is something that warrants further study during *in vivo* swelling after exposure to blood or other biological fluids and could posit interesting conclusions on the kinetics and adaptive response of early cell adhesion.
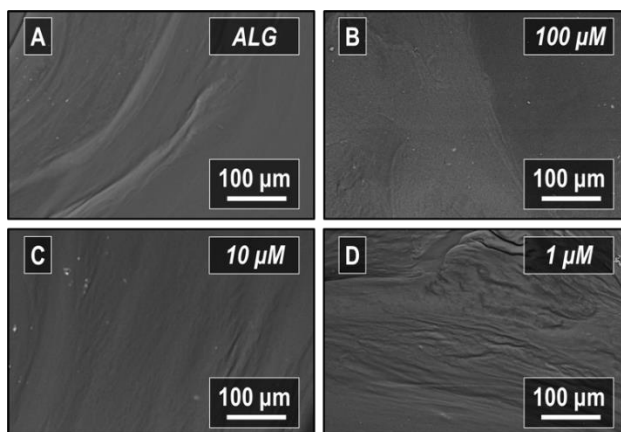
Figure 4-3: SEM of hydrated succinate gels using choline lactate ionic liquid, showing films with concentrations of succinate:(A) Alginate (ALG) only; (B) 100 μM; (C) 10 μM; (D) 1 μM. Imaging in the hydrated state eliminates the fragmented topography and instead introduces a micro-wrinkled surface texture. The persisting features in the rehydrated state show promise for improving cellular activity on an alginate-coated metallic surface.

4.3.2 Succinate Release Profiles

Since the aim of the films is for driving neovascularization to an implant interface, it is important to establish release profiles of succinate during rehydration and measure the cellular response in a succinate-enriched environment. Neovascularization at the implant interface occurs very early in the osteogenic cascade, where partial vascular ingrowth into

a murine defect is visible after only three days [18] and a vascular network can span the entirety of a defect after one week [59]. It is important that the pseudohypoxic gels are eluting succinate in a rapid-release format to help build this early provisional vascular network after implantation. As a conjugate base for succinic acid, disodium succinate release from the gel results in a pH increase in the absence of buffer solution. pH measurements were recorded during alginate-succinate gel release studies at succinate concentrations between 100 mM and 1 μM. Short-term succinate release profiles across the first 100 min of rehydration can be seen in Figure 4-4 and longer-term release profiles over 36 hr can be found in Figure S4-1. All gels showed an increase in average pH over alginate films as a result of succinate addition, with higher concentrations of disodium succinate resulting in higher solution pH. It is also important to note that the observed pH changes are associated with the 18 mL rehydration volume; their magnitude is expected to change if other rehydration volumes or solvents are used.

Trends in pH release can be found in succinate concentrations of 10 mM or below. At 10 mM, the maximum pH of disodium succinate in the deionized water was measured at 9.8. At lower succinate concentrations (1 mM, 100 μM, 10 μM, and 1 μM), the peak pH was measured at 9.0 ± 0.1, 8.1 ± 0.1, 7.8 ± 1.2, and 7.3 ± 0.9 respectively. For every tenfold reduction in succinate concentration within the xerogel, the resulting peak hydroxyl concentration in the solution diminished by less than tenfold. Where the pH shift in these experiments is appreciable, natural buffering effects in an *in vivo* setting should help maintain a physiological pH. Gels loaded with 100 mM of succinate showed lower peak pH than that of the 10 mM concentrations and a similar magnitude to the 1 mM gels (Figure S4-1), where a decline was also observed after the early spike in solution pH. This could suggest that high succinate content within the xerogel induces some structural change that is not visible in SEM.
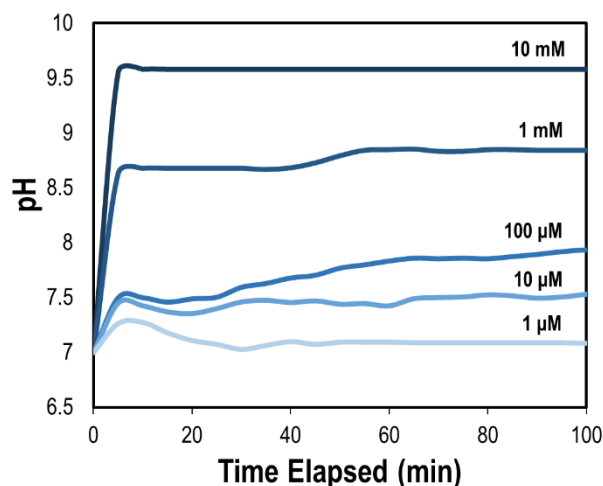
Figure 4-4: *Short-term release profiles for alginate gels containing succinate concentrations of 10 mM, 1 mM, 100 μM, 10 μM, and 1 μM. Independent of concentration, succinate has a rapid release profile due to its small molecular size and weak binding within the gel. Gels with higher succinate content elevate solution pH by a greater amount.*

For the 10 mM, 1 mM, and 0.1 mM gels, peak solution pH was typically observed after roughly 10 hr of immersion in deionized water, although the bulk of the disodium succinate escapes the gel within the first several minutes as all gels reached 60% of peak solution pH after only 40 min of immersion. For gels containing 10 mM of succinate or less, 95% of peak solution pH was also achieved within the first 7 hr. The rapid release profile of the succinate-laden xerogel films could facilitate early changes in the implant's local environment to affect the fracture healing cascade and signal recruitment for progenitors of both osteogenesis and angiogenesis, assuming that intracellular succinate concentrations are elevated in coordination with extracellular succinate concentrations. Where prolific vascular growth on a metallic implant material is present after only seven days of implantation and evidence of vascular branching is evident as early as three days after implantation [54], fast-releasing materials may be favourable to promote early assembly of the provisional vascular network and angiogenesis. Platelets, as an example, are known to release inflammatory mediators (including PDGF and VEGF) and are active within seconds during the wound healing process, while neutrophils can aid in increasing vascular permeability with peak activity occurring at 24 hr [60]. It may be beneficial in the future to attempt cross-linking within the alginate gel or tune succinate release profiles with other organic binders to create slow-releasing forms of temporally-relevant pseudohypoxic environments at the implant exterior with the addition of antibacterial agents or other forms of functional biomolecules.

4.3.3 In Vitro Saos-2 Culture

The development of early capillaries within the bone defect is directly related to osteogenic differentiation near the implant, where clustering of RUNX2-positive mesenchymal cells or pericytes can occur around the capillary wall [61]. As succinate is released into the peri-implant space, there is potential for interaction with pre-existing bone tissue or with newly differentiated osteoblastic progenitors. As such, it is important to understand how a near-bolus release of succinate can interact with osteoblasts near an implant surface. We used the Saos-2 cell line here to quantify the *in vitro* metabolic activity of cells with osteoblastic behaviour as they interact with the succinate-loaded xerogels after one and four days of culture.
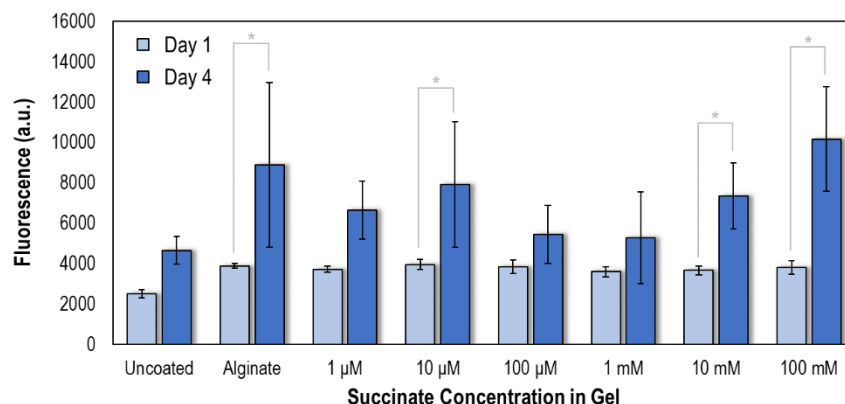
Figure 4-5: *Cytocompatibility of alginate-succinate gels as measured by metabolic activity of Saos-2 cells. Alginate-succinate gels are able to sustain in vitro growth of osteoblast-mimicking cells and statistically outperform uncoated polystyrene control substrates after one day. Significance defined as p < 0.05.*

Measurements of metabolic activity for osteoblast-mimicking cells grown on alginate-succinate xerogel films and polystyrene control surfaces are shown in Figure 4-5. All coatings showed statistically significant increases in metabolic activity compared to the uncoated polystyrene after only one day of culture, which is consistent with the fast-acting release mechanism of the gels. After one day of culture, alginate coatings with and without succinate addition produced statistically similar results. The 100 mM succinate, 10 mM succinate, 10 μM succinate, and succinate-deficient rehydrated gels all showed increases in cellular metabolism from day one to day four of *in vitro* culture, suggesting that succinate inclusion within the gels does not compromise the cytocompatibility of the material with respect to newly derived osteoblasts or pre-existing bone tissue, and can instead promote cellular proliferation of osteoblasts. This is important as it suggests minimal damage to surrounding tissue should succinate induce a pseudohypoxic environment and further promotes osteogenesis on an implant surface. Despite the common influence of pH on fluorescence intensity [62] and the recommended assay pH of 7.4, the optical characteristics of resazurin-based assays have been observed to change more drastically in acidic conditions rather than basic conditions [63]. The presence of sodium bicarbonate (2.2 g/L) as a buffering agent in the culture media should help prevent pH-dependent fluorescence shifts, especially in the cultures conducted on gels with a succinate concentration in the micromolar range. It is important to note that no colour change was observed in the culture media, which uses phenol red as a pH indicator, after succinate addition. The osteoblast lineage appears to be resilient in the presence of exogenous succinate at or below 100 mM, with no cytotoxic effects observed in the pseudohypoxic environment.

4.3.4 In Vitro Endothelial Culture

In light of their potentially suitable surface structure and osteocompatibility, it is necessary to quantify the vascular development and endogenous protein production occurring as a

result of endothelial exposure to the succinate. Human umbilical vein endothelial cells (HUVECs) were cultured in the presence of succinate-conditioned media to assess the effects of locally elevated succinate on neovascularization potential. Since the rapid release profile of the alginate-succinate gels enables elevated succinate levels within the first 7 hr, early characterization of endothelial cell behaviour offers insight as to how vascular development can occur at the implant interface.

Total protein content after 48 hours was assessed using a bicinchoninic acid (BCA) protein assay, as shown in Figure 4-6. Disodium succinate concentrations of 0, 1, 10, and 100 µM in endothelial growth culture medium were used to evaluate the potency of succinate in eliciting hypoxia-mediated HUVEC activity. Culture environments containing 1 µM or 10 µM of succinate exhibited significantly increased levels of total protein expression. An insignificant difference in protein levels between treatment and control environments is observed when the concentration is increased to 100 µM of succinate. Stabilized HIF-1α from pseudohypoxia can result in different cell fates depending on hypoxic severity and protein concentrations, ranging from enhanced cell survival to the initiation of apoptosis [64]. Hypoxia-induced cellular fates could change following succinate exposure, with differences in protein expression arising from the added succinate. Where the 10 µM succinate concentration resulted in an increase of Saos-2 cell metabolism between one and four days, it is also possible that the increase in total protein content at this concentration in the HUVEC culture can be attributed in part to proliferative effects.
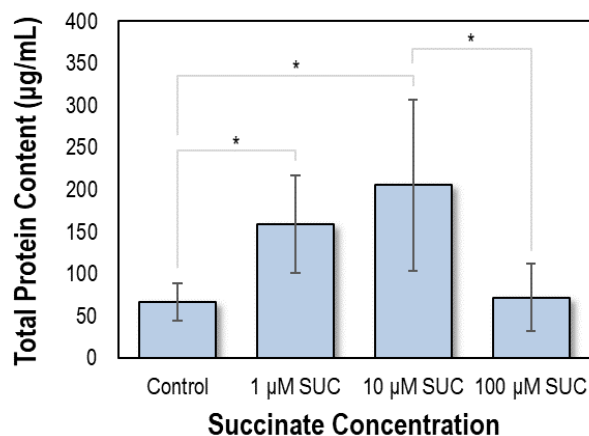
Figure 4-6: *Total protein content from BCA assay of HUVECs treated with succinate-added media after 48 hr. Succinate concentrations of 10 µM and 1 µM in the culture media promote early endogenous protein production in the cells. Significance defined as $p < 0.05$.*

Tube thickness maps overlaid onto bright-field optical micrographs of HUVEC cells (Figure 4-7A) further demonstrate trends observed in Figure 4-6. The tube-forming behaviour of HUVEC cells is evidently modified by the presence of succinic acid salt in solution. Although cells treated with 1 and 10 µM show decreased vascular branching compared to succinate-free controls (Figure S4-2) along with lower vascularized areas (Figure 4-7B), there is circumstantial evidence to support earlier tube formation in both

cases. The reduced vascularized area in the 1 µM and 10 µM succinate concentrations after 48 hr is inversely correlated to the total protein content measured at this time point, suggesting that factors other than cell count are driving the difference in lysate protein content and that succinate-enhanced media in the low-micromolar range can alter molecular pathways. At 100 µM, the branching behaviour at 6 hr is comparable to succinate-free HUVECs but also declines at later time points. At 1 and 10 µM, it is possible that the reduced branching behaviour can be explained by an early onset of cell anastomosis and stabilization of the endothelial-to-endothelial junctions at 6 hr, 24 hr, and 48 hr timepoints investigated here. The quiescent layer of endothelial cells is known to maintain a more dormant phenotype unless acted on by pro-angiogenic macromolecules, which activates only select cells in the local microenvironment and encourage outward branching from parental vessels [65]. Where total protein content is highest at 1 and 10 µM, it is assumed that any corresponding degree of HIF-1α stabilization should lead to earlier shifts in phenotypic behaviour, cell anastomosis, and a more mature form of vascularization at these time points in an *in vitro* setting. Where relevant concentrations of cobalt chloride as a known pseudohypoxic agent are often within the micromolar range to induce angiogenic behaviour [66], we show that similar concentrations of succinate can induce protein production.

Moreover, improving vascular permeability in the healing cascade holds promise for increasing macromolecular transport of growth factors, stem cells, and oxygen-rich blood to the implant site. Upregulation of pro-angiogenic factors in the VEGF family has been associated with both increased vascular permeability and vascular diameter [67]. In the work presented here, the HUVEC tube network is observed as a spindly vascular plexus at the 6 hr time point and expands as the process of tubulogenesis continues (Table 4-1 and Figure S4-3). Sustained growth in vessel diameter is only observed at the 48 hr time point in the test groups of 1 and 10 µM, where the control and 100 µM test groups both display a regression in vascular diameter at the later endpoint. The succinate-free media increased the vessel diameter after only 24 hr but regressed at the 48 hr mark. As cord-hollowing mechanisms during lumen formation in tubulogenesis can result in thickening of the primitive single-celled vascular network to two or more cells in diameter [68], the sustained expansion at 48 hr may be evidence of post-angiogenic perfusability in the pseudohypoxic environment.
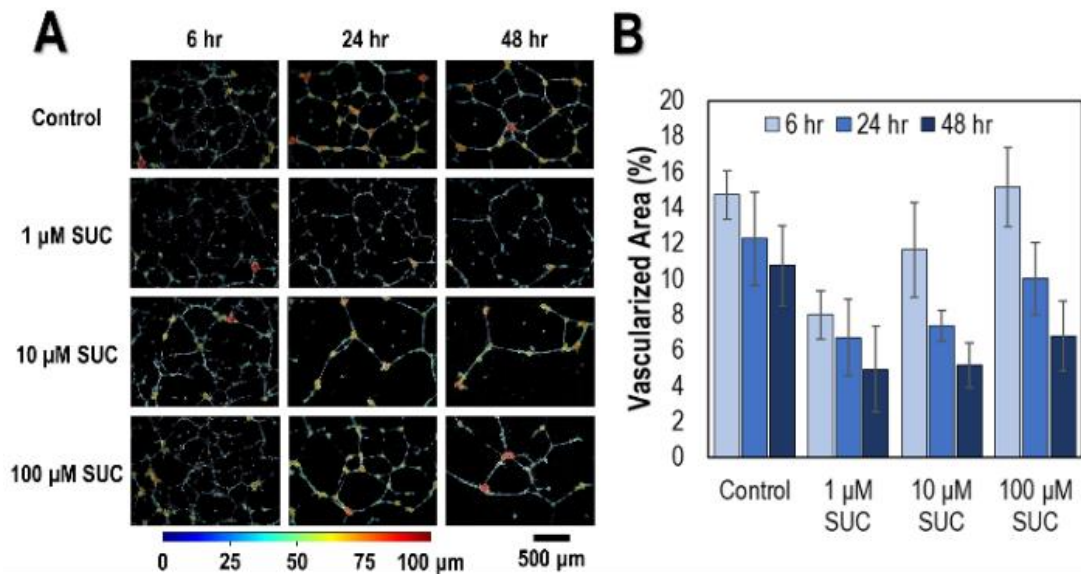
Figure 4-7: *(A) Thickness maps of HUVEC tube formation following 6, 24, and 48 hr of culture in succinate-supplemented culture media. Tubes are narrow and tortuous at early timepoints but coarsen over time as a result of lumen formation and anastomosis. Evolution from the provisional network at 6 hr into a coarser network at 24 hr is more evident in the 100 μM and 10 μM succinate concentrations, while many nodes appear similar in the control and 1 μM groups. (B) A net decrease in vascularized area is seen in all cases, with lower initial vascularized areas at succinate concentrations of 1 μM and 10 μM.*

Table 4-1: *Average HUVEC tube width and evolution across 6, 24, 48 hr study periods. Pseudohypoxic treatments corresponding to higher total protein content (1 and 10 µM) are consistent with sustained tube widening after 48 hr (n = 4). ** Statistical significance defined as p < 0.05.*

Culture Condition	Time (hr)	Tube Width (µm)	Change from 6 hr
Control	6	29.2 ± 1.9	–
	24	37.5 ± 2.1	+ 28.4%[*]
	48	32.5 ± 2.1	+ 11.3%
1 µM SUC	6	23.1 ± 1.4	–
	24	27.5 ± 1.4	+ 19.0%
	48	29.5 ± 1.7	+ 27.7%[*]
10 µM SUC	6	26.7 ± 1.5	–
	24	34.3 ± 1.9	+ 28.4%
	48	38.0 ± 2.4	+ 42.3%[*]
100 µM SUC	6	31.2 ± 1.8	–
	24	38.4 ± 2.1	+ 23.1%
	48	34.7 ± 2.5	+ 11.2%

Despite the longer-term benefit of adding the 1 and 10 µM of succinate to the culture media, undesirable vessel morphogenesis may occur at higher concentration. Cells treated with 100 µM succinic acid form early networks with large tube diameters (Table 1) but tubes decrease in size at later time points. It is possible that, in these highly pseudohypoxic environments, vessels are becoming hyperpermeable or 'leaky' in nature [69] in part by disassembling endothelial adherens junctions [70]. It is also possible that the induction of apoptotic signalling takes place in environments where more severe hypoxia is present [64]. In either case, exposure to 100 µM of succinate appears less beneficial than 1 or 10 µM, leading to reduced intracellular protein content and possibly less permeable vessels in the first 48 hours.

The lack of longer-term vascular stability in the 100 µM and control groups may also be attributed to the complexity of vascular morphogenesis and limitations of *in vitro* modelling. Specifically, the importance of mural cells and pericyte recruitment in tubulogenesis cannot be observed in endothelial-only systems. Endothelial-pericyte co-cultures have previously shown that the recruitment of pericytes to the site of tube formation results in enhanced secretion and deposition of basement membrane matrix, which is integral to vessel maturation. Further, the absence of pericytes reportedly leads to tube instability and regression [71]. An added benefit of introducing pericytes is a potential osteogenic progenitor source, where an abundance of PDGF-BB is one mechanism for

improved osseointegration [72] via potential pericyte recruitment, maturation, and detachment [73].

Examining the levels of PDGF-BB in both the culture media and cell lysate solution during HUVEC culture (Figure 4-8A) shows high levels of PDGF-BB within the extracellular domain in both control media and succinate-conditioned media. In its role as an osteoblast mitogen and chemoattractant, PDGF-BB can aid in the recruitment of early osteoblasts at a defect site. However, cytokines such as PDGF have known complications in osteopontin (OPN) production [74], where OPN can be more abundant in certain osteoblastic phenotypes and the resulting OPN influences extracellular matrix mineralization patterns in the bone tissue [75]. Levels of VEGF-A content in the intracellular and extracellular domains appear to be consistent with HUVEC cells cultured in the control media (Figure 4-8B). After 48 hr, some intracellular VEGF may have been degraded as a part of the early response necessary for cell survival. Since the culture media formulation contains both VEGF and PDGF, HUVECs exposed to the succinate in vitro may be sustained by the media as an exogenous source rather than endogenously producing the proliferative growth factors. Follow-up studies using Medium-199 or other media formulations without growth factor addition could help decouple the endogenous and exogenous sources. Potential exogenous sources *in vivo* include mesenchymal stem cells [76], platelets [77], and neutrophils [78] which all secrete angiogenic factors and are present early in the fracture healing cascade. Ultimately, a complete characterization of succinate addition cannot be feasibly made *in vitro* using HUVEC cells alone.
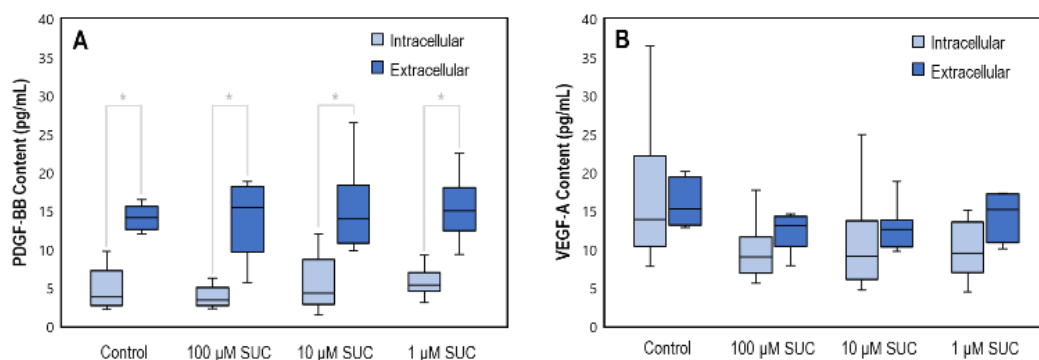
Figure 4-8: *Growth factor content in the succinate conditioned media (extracellular) and the cell lysate solution (intracellular) components following HUVEC culture for (A) PDGF-BB and (B) VEGF-A.*

An important confounding factor to these results is the aspect of time. Tube formation can begin to occur *in vitro* between 2-6 hr with peak tube formation occurring in the wide range of 3-12 hr depending on the presence of angiogenic stimuli [79]. At 6 hours, vessel diameter distributions are consistent across succinate treatment groups, while at later time points, the distribution shifts toward larger tube diameters. Figure S4-3 shows that different treatment groups showed differing vessel diameter distributions over the first 48 hours following succinate addition. The rapid changes in the cellular environment shown in Figure 4-7 suggest that neovascularization demands timely availability of vessel-forming resources to

develop from a thin, lumen-free network into a more mature network. Further to this claim is the possibility that succinate-induced hypoxia influences the time at which these resources are needed to form viable vasculature before regression ensues.

4.4 Conclusions

Alginate-based xerogels produced a surface film capable of rapid release of disodium succinate which may create a local pseudohypoxic environment for faster neovascularization in the vicinity of implants. By adding succinate to the gel on the order of 1 or 10 µM, an increase in the amount of stabilized protein and branching behaviour in HUVEC cells occurred. Succinate concentrations in the low-µM range encouraged the expansion of the provisional vascular network formed *in vitro* by HUVECs without risk of hyperpermeability or cytotoxic effects. Moreover, the rapid dosing of succinate below 100 mM did not inhibit the proliferation of osteoblast-like Saos-2 cells. Therefore, based on the response of HUVEC and Saos-2 cells, the succinate release showed promise for providing short-term angiogenic benefits during early timepoints for vessel formation at an implant surface. Future work could assess the co-functionalization of other macromolecules to improve early implant stability, while *in vitro* experiments should explore co-culture environments to better replicate vessel formation, and ultimately the investigation of *in vivo* vessel development and downstream implications on early osteogenesis is needed.

4.5 Supplemental Figures
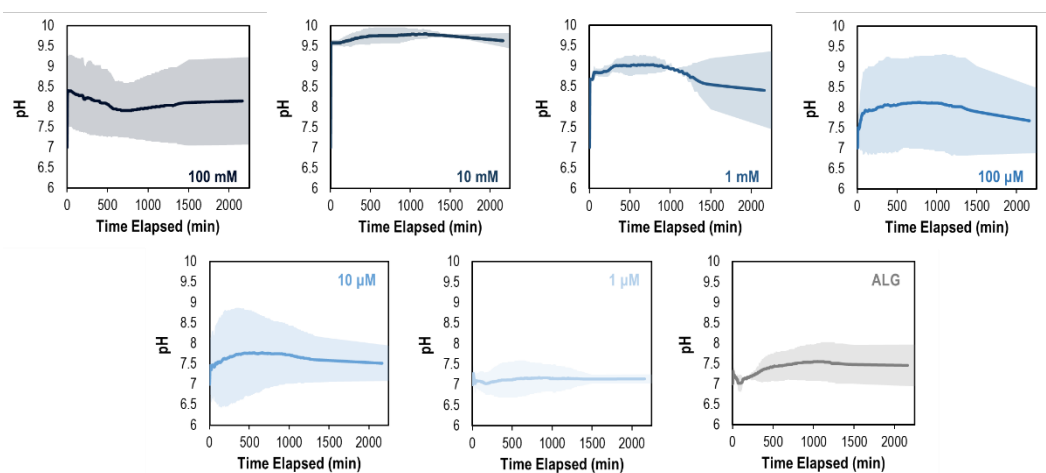
Figure S4-1: *Long-term pH release profiles of succinate-alginate gels. Release plateaus after the initial burst release of the encapsulated succinate. Shaded regions represent ± one standard deviation.*
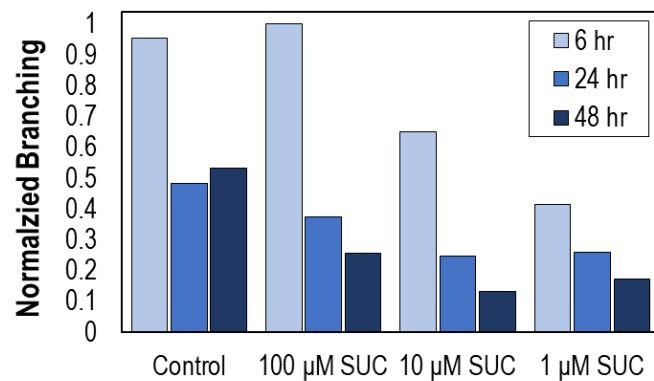
Figure S4-2: *Branching behaviour of endothelial cells cultured in succinate-media mixtures, as measured by relative number of junctions in the tube formation assay.*
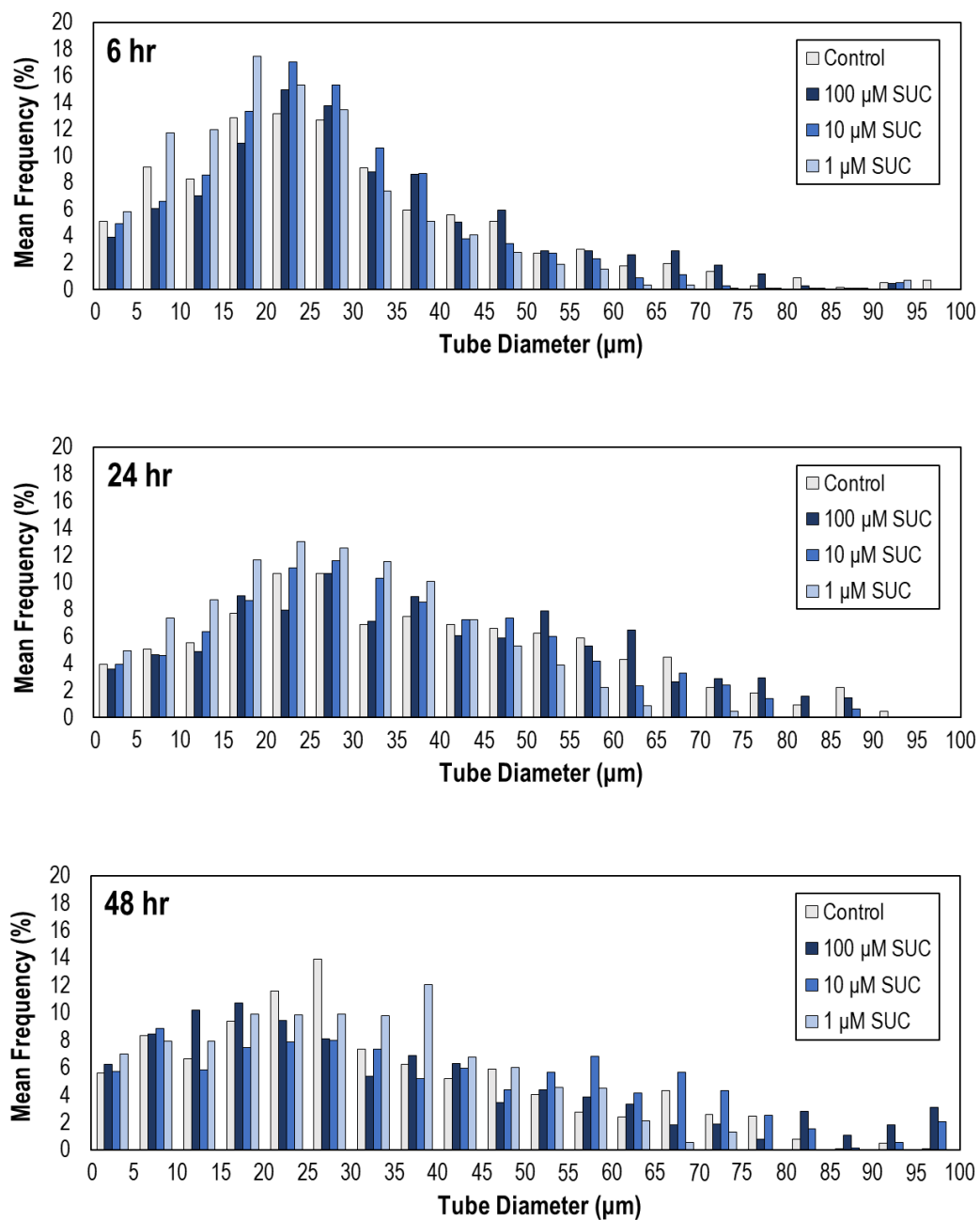
Figure S4-3: *HUVEC tube network diameters after 6/24/48 hr of culture based on measurements from optical micrographs. Distributions of early HUVEC tube width appears Gaussian in most early cases and positively skewed as the tube network matures. At 24/48 hr, larger tubes are more evident for the succinate-treated conditions.*

References

1. Albrektsson T, Johansson C. Osteoinduction, osteoconduction and osseointegration. Eur Spine J. 2001;10(Suppl 2):S96–101.

2. Albrektsson T, Brånemark PI, Hansson HA, Lindström J. Osseointegrated Titanium Implants: Requirements for Ensuring a Long-Lasting, Direct Bone-to-Implant Anchorage in Man. Acta Orthop Scand. 1981;52(2):155–70.

3. D'Elia A, Deering J, Clifford A, Lee BEJ, Grandfield K, Zhitomirsky I. Electrophoretic deposition of polymethylmethacrylate and composites for biomedical applications. Colloids Surfaces B Biointerfaces. 2019;188:110763.

4. Clifford A, D'Elia A, Deering J, Lee BEJ, Grandfield K, Zhitomirsky I. Electrochemical Fabrication and Characterization of Pectin Hydrogel Composite Materials for Bone Tissue Repair. Acs Appl Polym Mater. 2020;2(8):3390–6.

5. Deering J, Clifford A, D'Elia A, Zhitomirsky I, Grandfield K. Composite Dip Coating Improves Biocompatibility of Porous Metallic Scaffolds. Mater Lett. 2020;274:128057.

6. Catauro M, Bollino F, Giovanardi R, Veronesi P. Modification of Ti6Al4V implant surfaces by biocompatible TiO2/PCL hybrid layers prepared via sol-gel dip coating: Structural characterization, mechanical and corrosion behavior. Mater Sci Eng C. 2017;74:501–7.

7. Cao L, Ullah I, Li N, Niu S, Sun R, Xia D, Yang R, Zhang X. Plasma spray of biofunctional (Mg, Sr)-substituted hydroxyapatite coatings for titanium alloy implants. J Mater Sci Technol. 2019;35(5):719–26.

8. Vercaigne S, Wolke JGC, Naert I, Jansen JA. Histomorphometrical and mechanical evaluation of titanium plasma-spray-coated implants placed in the cortical bone of goats. J Biomed Mater Res. 1998;41(1):41–8.

9. Giavaresi G, Ambrosio L, Battiston GA, Casellato U, Gerbasi R, Finia M, Aldini NN, Martini L, Rimondini L, Giardino R. Histomorphometric, ultrastructural and microhardness evaluation of the osseointegration of a nanostructured titanium oxide coating by metal-organic chemical vapour deposition: an in vivo study. Biomaterials. 2004;25(25):5583–91.

10. Cabañas MV, Vallet-Regí M. Calcium phosphate coatings deposited by aerosol chemical vapour deposition. J Mater Chem. 2003;13(5):1104–7.

11. Bumgardner JD, Wiser R, Gerard PD, Bergin P, Chestnutt B, Marini M, Ramsey V, Elder SH, Gilbert JA. Chitosan: potential use as a bioactive coating for orthopaedic and craniofacial/dental implants. J Biomaterials Sci Polym Ed. 2003;14(5):423–38.

12. Leedy MR, Martin HJ, Norowski PA, Jennings JA, Haggard WO, Bumgardner JD. Use of Chitosan as a Bioactive Implant Coating for Bone-Implant Applications. Adv Polym Sci. 2011;129–65.

13. Yin X, Yang C, Wang Z, Zhang Y, Li Y, Weng J, Feng B. Alginate/chitosan modified immunomodulatory titanium implants for promoting osteogenesis in vitro and in vivo. Mater Sci Eng C. 2021;124:112087.

14. Lv H, Chen Z, Yang X, Cen L, Zhang X, Gao P. Layer-by-layer self-assembly of minocycline-loaded chitosan/alginate multilayer on titanium substrates to inhibit biofilm formation. J Dent. 2014;42(11):1464–72.

15. Chua PH, Neoh KG, Kang ET, Wang W. Surface functionalization of titanium with hyaluronic acid/chitosan polyelectrolyte multilayers and RGD for promoting osteoblast functions and inhibiting bacterial adhesion. Biomaterials. 2008;29(10):1412–21.

16. Valverde A, Pérez-Álvarez L, Ruiz-Rubio L, Olivenza MAP, Blanco MBG, Díaz-Fuentes M, Vilas-Vilela JL. Antibacterial hyaluronic acid/chitosan multilayers onto smooth and micropatterned titanium surfaces. Carbohyd Polym. 2019;207:824–33.

17. Tibbitt MW, Anseth KS. Hydrogels as extracellular matrix mimics for 3D cell culture. Biotechnol Bioeng. 2009;103(4):655–63.

18. Khosravi N, Maeda A, DaCosta RS, Davies JE. Nanosurfaces modulate the mechanism of peri-implant endosseous healing by regulating neovascular morphogenesis. Commun Biology. 2018;1(1).

19. Kanczler J, Oreffo R. Osteogenesis and angiogenesis: The potential for engineering bone. European Cells Mater. 2008;15:100–14.

20. Street J, Bao M, deGuzman L, Bunting S, Peale FV, Ferrara N, Steinmetz H, Hoeffel J, Cleland JL, Daugherty A, Bruggen N van, Redmond HP, Carano RAD, Filvaroff EH. Vascular endothelial growth factor stimulates bone repair by promoting angiogenesis and bone turnover. Proc National Acad Sci. 2002;99(15):9656–61.

21. Mayr-Wohlfart U, Waltenberger J, Hausser H, Kessler S, Günther KP, Dehio C, Puhl W, Brenner RE. Vascular endothelial growth factor stimulates chemotactic migration of primary human osteoblasts. Bone. 2002;30(3):472–7.

22. Parajó Y, d'Angelo I, Welle A, Garcia-Fuentes M, Alonso MJ. Hyaluronic acid/Chitosan nanoparticles as delivery vehicles for VEGF and PDGF-BB. Drug Deliv. 2010;17(8):596–604.

23. Chung HJ, Kim JT, Kim HJ, Kyung HW, Katila P, Lee JH, Yang TH, Yang YI, Lee SJ. Epicardial delivery of VEGF and cardiac stem cells guided by 3-dimensional PLLA mat enhancing cardiac regeneration and angiogenesis in acute myocardial infarction. J Control Release. 2015;205:218–30.

24. Ferrara N. VEGF and the quest for tumour angiogenesis factors. Nat Rev Cancer. 2002;2(10):795–803.

25. Ehrbar M, Djonov VG, Schnell C, Tschanz SA, Martiny-Baron G, Schenk U, Wood J, Burri PH, Hubbell JA, Zisch AH. Cell-Demanded Liberation of VEGF121 From Fibrin Implants Induces Local and Controlled Blood Vessel Growth. Circ Res. 2004;94(8):1124–32.

26. Zisch AH, Schenk U, Schense JC, Sakiyama-Elbert SE, Hubbell JA. Covalently conjugated VEGF–fibrin matrices for endothelialization. J Control Release. 2001;72(1–3):101–13.

27. Silva EA, Mooney DJ. Effects of VEGF temporal and spatial presentation on angiogenesis. Biomaterials. 2010;31(6):1235–41.

28. Pidgeon GP, Barr MP, Harmey JH, Foley DA, Bouchier-Hayes DJ. Vascular endothelial growth factor (VEGF) upregulates BCL-2 and inhibits apoptosis in human and murine mammary adenocarcinoma cells. Brit J Cancer. 2001;85(2):273–8.

29. Sano H, Hosokawa K, Kidoya H, Takakura N. Negative Regulation of VEGF-Induced Vascular Leakage by Blockade of Angiotensin II Type 1 Receptor. Arteriosclerosis Thrombosis Vasc Biology. 2006;26(12):2673–80.

30. Lee KY, Peters MC, Mooney DJ. Comparison of vascular endothelial growth factor and basic fibroblast growth factor on angiogenesis in SCID mice. J Control Release. 2003;87(1–3):49–56.

31. Poh CK, Shi Z, Lim TY, Neoh KG, Wang W. The effect of VEGF functionalization of titanium on endothelial cells in vitro. Biomaterials. 2010;31(7):1578–85.

32. Cleland JL, Duenas ET, Park A, Daugherty A, Kahn J, Kowalski J, Cuthbertson A. Development of poly-(d,l-lactide–coglycolide) microsphere formulations containing recombinant human vascular endothelial growth factor to promote local angiogenesis. J Control Release. 2001;72(1–3):13–24.

33. Wu J, Zeng F, Huang XP, Chung JCY, Konecny F, Weisel RD, Li RK. Infarct stabilization and cardiac repair with a VEGF-conjugated, injectable hydrogel. Biomaterials. 2011;32(2):579–86.

34. Schellekens H. Immunogenicity of therapeutic proteins: Clinical implications and future prospects. Clin Ther. 2002;24(11):1720–40.

35. Fairbrother WJ, Champe MA, Christinger HW, Keyt BA, Starovasnik MA. Solution structure of the heparin-binding domain of vascular endothelial growth factor. Structure. 1998;6(5):637–48.

36. Wang W, Huang X, Lin W, Qiu Y, He Y, Yu J, Xi Y, Ye X. Hypoxic preconditioned bone mesenchymal stem cells ameliorate spinal cord injury in rats via improved survival and migration. Int J Mol Med. 2018;42(5):2538–50.

37. Shweiki D, Itin A, Soffer D, Keshet E. Vascular endothelial growth factor induced by hypoxia may mediate hypoxia-initiated angiogenesis. Nature. 1992;359(6398):843–5.

38. Berra E, Benizri E, Ginouvès A, Volmat V, Roux D, Pouysségur J. HIF prolyl-hydroxylase 2 is the key oxygen sensor setting low steady-state levels of HIF-1α in normoxia. Embo J. 2003;22(16):4082–90.

39. Tanimoto K, Makino Y, Pereira T, Poellinger L. Mechanism of regulation of the hypoxia-inducible factor-1α by the von Hippel-Lindau tumor suppressor protein. Embo J. 2000;19(16):4298–309.

40. Tsuzuki Y, Fukumura D, Oosthuyse B, Koike C, Carmeliet P, Jain RK. Vascular endothelial growth factor (VEGF) modulation by targeting hypoxia-inducible factor-1alpha--> hypoxia response element--> VEGF cascade differentially regulates vascular response and growth rate in tumors. Cancer Res. 2000;60(22):6248–52.

41. Lafforgue P. Pathophysiology and natural history of avascular necrosis of bone. Joint Bone Spine. 2006;73(5):500–7.

42. Tanaka T, Kojima I, Ohse T, Ingelfinger JR, Adler S, Fujita T, Nangaku M. Cobalt promotes angiogenesis via hypoxia-inducible factor and protects tubulointerstitium in the remnant kidney model. Lab Invest. 2005;85(10):1292–307.

43. Yuan Y, Hilliard G, Ferguson T, Millhorn DE. Cobalt Inhibits the Interaction between Hypoxia-inducible Factor-α and von Hippel-Lindau Protein by Direct Binding to Hypoxia-inducible Factor-α*. J Biol Chem. 2003;278(18):15911–6.

44. Fan W, Crawford R, Xiao Y. Enhancing in vivo vascularized bone formation by cobalt chloride-treated bone marrow stromal cells in a tissue engineered periosteum model. Biomaterials. 2010;31(13):3580–9.

45. Lison D, Boeck MD, Verougstraete V, Kirsch-Volders M. Update on the genotoxicity and carcinogenicity of cobalt compounds. Occup Environ Med. 2001;58(10):619.

46. King A, Selak MA, Gottlieb E. Succinate dehydrogenase and fumarate hydratase: linking mitochondrial dysfunction and cancer. Oncogene. 2006;25(34):4675–82.

47. Fremder M, Kim SW, Khamaysi A, Shimshilashvili L, Eini-Rider H, Park IS, Hadad U, Cheon JH, Ohana E. A transepithelial pathway delivers succinate to macrophages, thus perpetuating their pro-inflammatory metabolic state. Cell Reports. 2021;36(6):109521.

48. Lee KY, Mooney DJ. Alginate: Properties and biomedical applications. Prog Polym Sci. 2012;37(1):106–26.

49. Deering J, Presas A, Lee BEJ, Valentin D, Yu B, Heiss C, Grandfield K, Bosbach WA. Response of Saos-2 osteoblast-like cells to kilohertz-resonance excitation in porous metallic scaffolds. J Mech Behav Biomed. 2020;106:103726.

50. Davies JE. Understanding Peri-Implant Endosseous Healing. J Dent Educ. 2003;67(8):932–49.

51. Pupa P, Apiwatsiri P, Sirichokchatchawan W, Pirarat N, Muangsin N, Shah AA, Prapasarakul N. The efficacy of three double-microencapsulation methods for preservation of probiotic bacteria. Sci Rep-uk. 2021;11(1):13753.

52. Bera S, Haldar D. A rechargeable self-healing safety fuel gel. J Mater Chem A. 2015;4(18):6933–9.

53. Kämmerer PW, Gabriel M, Al-Nawas B, Scholz T, Kirchmaier CM, Klein MO. Early implant healing: promotion of platelet activation and cytokine release by topographical, chemical and biomimetical titanium surface modifications in vitro. Clin Oral Implan Res. 2012;23(4):504–10.

54. Khosravi N, DaCosta RS, Davies JE. New insights into spatio-temporal dynamics of mesenchymal progenitor cell ingress during peri-implant wound healing: Provided by intravital imaging. Biomaterials. 2021;273:120837.

55. DiCecco L, D'Elia A, Miller C, Sask KN, Soleymani L, Grandfield K. Electron Microscopy Imaging Applications of Room Temperature Ionic Liquids in the Biological Field: A Review. Chembiochem. 2021;22(15):2488–506.

56. Lee BEJ, DiCecco L, Exir H, Weck A, Sask KN, Grandfield K. Simultaneous Visualization of Wet Cells and Nanostructured Biomaterials in SEM using Ionic Liquids. Chembiochem. 2021;22(3):571–6.

57. Tsuda T, Mochizuki E, Kishida S, Iwasaki K, Tsunashima K, Kuwabata S. SEM Observation of Hydrous Superabsorbent Polymer Pretreated with Room-Temperature Ionic Liquids. Plos One. 2014;9(3):e91193.

58. DiCecco LA, D'Elia A, Quenneville C, Soleymani L, Grandfield K. Ionic Liquid Treatment for Efficient Sample Preparation of Hydrated Bone for Scanning Electron Microscopy. Micron. 2021;103192.

59. Huang C, Ness VP, Yang X, Chen H, Luo J, Brown EB, Zhang X. Spatiotemporal Analyses of Osteogenesis and Angiogenesis via Intravital Imaging in Cranial Bone Defect Repair. J Bone Miner Res. 2015;30(7):1217–30.

60. Young A, McNaught CE. The physiology of wound healing. Surg Oxf. 2011;29(10):475–9.

61. Redenski I, Guo S, Machour M, Szklanny A, Landau S, Kaplan B, Lock RI, Gabet Y, Egozi D, Vunjak-Novakovic G, Levenberg S. Engineered Vascularized Flaps, Composed of Polymeric Soft Tissue and Live Bone, Repair Complex Tibial Defects. Adv Funct Mater. 2021;31(44):2008687.

62. Williams RT, Bridges JW. Fluorescence of solutions: A review. J Clin Pathol. 1964;17(4):371.

63. Zare M, Amin MM, Nikaeen M, Bina B, Pourzamani H, Fatehizadeh A, Taheri E. Resazurin reduction assay, a useful tool for assessment of heavy metal toxicity in acidic conditions. Environ Monit Assess. 2015;187(5):276.

64. Greijer AE, Wall E van der. The role of hypoxia inducible factor 1 (HIF-1) in hypoxia induced apoptosis. J Clin Pathol. 2004;57(10):1009.

65. Herbert SP, Stainier DYR. Molecular control of endothelial cell behaviour during blood vessel morphogenesis. Nat Rev Mol Cell Bio. 2011;12(9):551–64.

66. Zan T, Du Z, Li H, Li Q, Gu B. Cobalt chloride improves angiogenic potential of CD133+ cells. Front Biosci. 2012;17(7):2247.

67. Jain RK. Molecular regulation of vessel maturation. Nat Med. 2003;9(6):685–93.

68. Tung JJ, Tattersall IW, Kitajewski J. Tips, Stalks, Tubes: Notch-Mediated Cell Fate Determination and Mechanisms of Tubulogenesis during Angiogenesis. Csh Perspect Med. 2012;2(2):a006601.

69. Oakley R, Tharakan B. Vascular Hyperpermeability and Aging. Aging Dis. 2014;5(2):114–25.

70. Kumar P, Shen Q, Pivetti CD, Lee ES, Wu MH, Yuan SY. Molecular mechanisms of endothelial hyperpermeability: implications in inflammation. Expert Rev Mol Med. 2009;11:e19.

71. Stratman AN, Malotte KM, Mahan RD, Davis MJ, Davis GE. Pericyte recruitment during vasculogenic tube assembly stimulates endothelial basement membrane matrix formation. Blood. 2009;114(24):5091–101.

72. Chang PC, Seol YJ, Cirelli JA, Pellegrini GR, Jin Q, Franco LM, Goldstein SA, Chandler LA, Sosnowski B, Giannobile WV. PDGF-B Gene Therapy Accelerates Bone Engineering and Oral Implant Osseointegration. Gene Ther. 2010;17(1):95–104.

73. Caplan AI, Correa D. PDGF in bone formation and regeneration: New insights into a novel mechanism involving MSCs. J Orthopaed Res. 2011;29(12):1795–803.

74. Sodek J, Chen J, NAGATA T, KASUGAI S, Todescan R, Li IWS, Kim RH. Regulation of Osteopontin Expression in Osteoblasts. Ann Ny Acad Sci. 1995;760(1):223–41.

75. McKee MD, Buss DJ, Reznikov N. Mineral tessellation in bone and the stenciling principle for extracellular matrix mineralization. J Struct Biol. 2022;214(1):107823.

76. Kagiwada H, Yashiki T, Ohshima A, Tadokoro M, Nagaya N, Ohgushi H. Human mesenchymal stem cells as a stable source of VEGF-producing cells. J Tissue Eng Regen M. 2008;2(4):184–9.

77. Webb NJA, Bottomley MJ, Watson CJ, Brenchley PEC. Vascular Endothelial Growth Factor (VEGF) is Released from Platelets during Blood Clotting: Implications for Measurement of Circulating VEGF Levels in Clinical Disease. Clin Sci. 1998;94(4):395–404.

78. Koehne P, Willam C, Strauss E, Schindler R, Eckardt KU, Bührer C. Lack of hypoxic stimulation of VEGF secretion from neutrophils and platelets. Am J Physiol-heart C. 2000;279(2):H817–24.

79. DeCicco-Skinner KL, Henry GH, Cataisson C, Tabib T, Gwilliam JC, Watson NJ, Bullwinkle EM, Falkenburg L, O'Neill RC, Morin A, Wiest JS. Endothelial Cell Tube

Formation Assay for the In Vitro Study of Angiogenesis. J Vis Exp. 2014;(91):e51312.

Chapter 5: Osseointegration of Functionally-Graded Ti6Al4V Porous Implants: Histology of the Pore Network

Summary:

The topological design of porous scaffolds is strongly correlated to their mechanical properties. While this mechanical interrelation is well-described in the literature, the resulting timeline of osseointegration inside additively manufactured implants with varying pore structure has not been described extensively at the cellular level and functional grading of pore size is only recently emerging for *in vivo* assessment of osseointegration. In this chapter, the histomorphometric properties of bone around a functionally-graded porous implant (with pore size ranging from 600 µm at the exterior to 300 µm at the midpoint) and a porous implant with uniform pore size (constant at 300 µm) are assessed. BV/TV and BIC measurements also show that bone-implant interaction is more favourable in the gyroid structure with a pore size of 300 µm. Histological sections at four weeks show evidence of osteogenesis within the scaffold interior, extensive vascular infiltration into the pore network, and residual inflammatory markers at the defect site. The fraction of adipocyte-rich myeloid tissue within the scaffold interior is greater at twelve weeks and appears higher in the functionally-graded implant. Examination of fluorochrome signals at two weeks and twelve weeks provides evidence of bone mineralization at both timepoints. This work fits the themes of the thesis by providing a multimodal characterization of porous implant performance, with specific focus on microscale characterization techniques using optical, fluorescent, and X-ray techniques. The same functionally-graded specimens from Chapter 5 are also used in Chapter 6 for analysis with electron microscopy techniques.

Citation:

Deering, J., Mahmoud, D., Rier, E., Lin, Y., Fang, Q., Wohl, G.R., Deng, F., Grandfield, K., Elbestawi, M.A., and Chen, J. (2022). Osseointegration of Functionally-Graded Ti6Al4V Porous Implants: Histology of the Pore Network. *Manuscript in draft.*

Permissions:

This work is intended for submission to a peer-reviewed journal following minor adaptations to the body of the text and approval from all authors. As the author of this article, I retain the right to include the work within this thesis, provided there is no commercial benefit.

Osseointegration of functionally-graded Ti6Al4V porous implants: Histology of the pore network

Joseph Deering[1], Dalia Mahmoud[2], Elyse Rier[3], Yujing Lin[4], Qiyin Fang[5], Gregory R. Wohl[2,3,6], Feilong Deng[4], Kathryn Grandfield[1,3,6], Mohamed A. Elbestawi[2], Jianyu Chen[4]

[1] Department of Materials Science and Engineering, McMaster University, Hamilton, ON, Canada

[2] Department of Mechanical Engineering, McMaster University, Hamilton, ON, Canada

[3] School of Biomedical Engineering, McMaster University, Hamilton, ON, Canada

[4] Guanghua School of Stomatology, Hospital of Stomatology, Guangdong Provincial Key Laboratory of Stomatology, Sun Yat-sen University, Guangzhou, China

[5] Department of Engineering Physics, McMaster University, Hamilton, ON, Canada

[6] Brockhouse Institute for Materials Research, McMaster University, Hamilton, ON, Canada

Abstract

The additive manufacturing of titanium into porous geometries offers a means to generate low-stiffness endosseous implants with a greater surface area to improve osseointegration. To optimize pore size in the scaffolds, it is important to first understand the timeline of osseointegration in pre-clinical models. In this work, selective laser melting was used to produce gyroid-based scaffolds with a uniform pore size of 300 μm or functionally-graded pore size from 600 μm to 300 μm before implantation in New Zealand white rabbit tibiae for 4 and 12 weeks. Initial *in vitro* assessment with Saos-2 cells showed favourable cell proliferation at pore sizes of 300 and 600 μm. At four weeks, histological observations indicated some residual inflammation alongside neovessel infiltration into the scaffold interior and some early apposition of mineralized bone tissue. At twelve weeks, both scaffolds were filled with a mixture of adipocyte-rich marrow, micro-capillaries, and mineralized bone tissue. X-ray microcomputed tomography showed a higher bone volume fraction (BV/TV) and percentage of bone-implant contact (BIC) in the implants with 300 μm pores than in the functionally-graded specimens, indicating that these smaller pore sizes may be favourable for osseointegration in leporine bone.

5.1 Introduction

Central to the success of dental and orthopaedic implants is the development of a structural and functional connection at the bone-implant interface [1]. Careful control over material biocompatibility, surgical technique, and macroscale implant design are among the core parameters for governing the early stages of osseointegration – especially important as failure is most common within the first year of implantation [2]. These design strategies [3,4] have been developed to include elements of isotropy [5,6] and biomimetics to tune the mechanical characteristics [7,8] of tissue scaffolds, with renewed interest in optimizing scaffolds for osseointegration. In particular, the advancement in laser powder bed fusion (L-PBF) has allowed for the fabrication and geometric control of metallic lattice structures for use in bone tissue engineering applications [9–11]. These lattice structures utilize interconnected pore structures to provide additional surface area for bone ingrowth [12] and their use aims to improve the secondary stability of dental and orthopaedic prostheses. Moreover, stiffness reduction in the implant helps to mitigate long-term bone resorption from stress shielding phenomena [13] – a phenomenon that can be produced with a change in the material properties or the addition of engineered porosity.

In general, additively manufactured lattice structures may be categorized by their repeating topology into a dichotomy of computer-aided drawings (strut-based) or triply periodic minimal surfaces (TPMS) [14,15]. Gyroid is one subset of the TPMS lattice family, with the possibility to mimic the mechanical properties of bone by tuning the relative density of the scaffold [16]. The main advantage of gyroid structures is that their architecture facilitates cell migration, in part due to their infinitely smooth architecture and relatively high fluid permeability [17]. TPMS structures also demonstrate high surface area to volume ratio, high energy absorption [18], and high specific strength/stiffness [19]. Recent research has been directed to investigate the capability of functionally-graded (FG) TPMS designs in terms of pore volume fraction and morphology [20–22]. While the optimal pore size for each pre-clinical animal model is still disputed, a benchmark for adequate pore size ranges between 300-500 μm for osseointegration to occur and porosity values in the implant ranging from 50-70% appear to be most abundant for porous implants [11]. Numerous experimental and numerical studies of functionally-graded TPMS scaffolds have shown they are suitable for bone tissue engineering with respect to their mechanical properties [23–25], but only few studies have investigated the osseointegration of implants with a changing pore size throughout their interior [26].

Despite the design and *in vitro* characteristics of TPMS structures having been reviewed elsewhere [27], these forms of experimentation are generally limited compared to *in vivo* studies [28]. In general, the *in vivo* wound healing response in the peri-implant environment follows distinct stages of clotting and inflammatory response, sprouting of new blood vessels and extracellular matrix deposition, and formation of mineralized bone tissue around classical implants [29]. However, there is a distinct lack of in-depth histological

probes describing whether these biological processes occur through the interior of porous metals during the healing timeline – especially in implants with TPMS geometries.

In this work, we assess the *in vitro* cytocompatibility and *in vivo* osseointegration within the interior of uniform and functionally-graded Ti6Al4V gyroid structures. Using Saos-2 metabolic activity measurements, X-ray microcomputed tomography of newly formed tissue in the rabbit tibia, and hematoxylin/eosin staining of histological sections, we describe common themes in bone tissue nucleation and adaptation over twelve weeks within the sheltered porous interior of metallic implant materials.

5.2 Methods

5.2.1 Scaffold Design and Fabrication

A Renishaw machine was used to fabricate skeletal TPMS Ti6Al4V gyroid parts with selective laser melting. The machine was equipped with a 200 W pulsed laser, creating a series of overlapping exposures to assemble parts one layer at a time using an exposure time of 40 μs, point distance of 60 μm, layer thickness of 30 μm, and hatch spacing of 65 μm [30]. The surface of gyroids was modelled using Equation 5-1, where *a* defines the unit cell size, *t* defines the volume fraction (relative density) of the gyroids, and *x/y/z* represent the spatial coordinates within the scaffold interior.

(Eqn. 5-1) $\quad G: \sin\left(\frac{2\pi x}{a}\right)\cos\left(\frac{2\pi y}{a}\right) + \sin\left(\frac{2\pi y}{a}\right)\cos\left(\frac{2\pi z}{a}\right) + \sin\left(\frac{2\pi z}{a}\right)\cos\left(\frac{2\pi x}{a}\right) - t = 0$

A MATLAB® code was used to generate the surface of the gyroids, both with and without functional grading of the pore structure. Uniform gyroid structures with an approximate pore size of 300 μm (herein denoted as G300), uniform pore size of 600 μm (G600), or functionally-graded gyroid structures (FG600) were fabricated as illustrated in Figure 5-1. FG600 implants were created with a radially-varying pore size using a change in unit cell size to create a pore size distribution between 600 μm at the scaffold exterior and 300 μm at the scaffold midpoint. The porous fraction of all implants was designed with a height of 6 mm and merged to a slotted crown with a height of 1 mm to form a single mesh prior to PBF, with a total height of 7 mm and implant diameter of 6 mm. The relative porosity of the G300 scaffold was estimated at 50% while the net porosity of the FG600 was estimated at 60%.
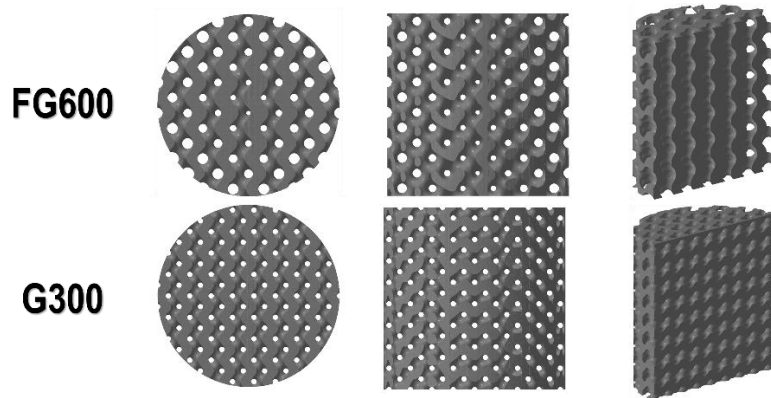
Figure 5-1: Overview of porous regions within the gyroid implants. *The FG600 implant contains pores that decrease in size from 600 µm to 300 µm as a function of implant radius in the gyroid. The G300 implant contains a uniform array of 300 µm pores through the gyroid.*

5.2.2 In Vitro Saos-2 Culture

Saos-2 cells (ATCC HTB-85) were seeded on uniform titanium gyroids to mimic osteoblast proliferation *in vitro* as described elsewhere [31]. Briefly, cells were seeded onto six replicates of G300 and G600 scaffolds using a seeding density of 10,000 cells/cm^2. Culture was conducted in McCoy's modified 5A media (Life Technologies Inc.), using incubation at 37°C and 5% CO_2. After one, three, and seven days of culture, cell metabolism was measured by incubating samples with a mixture of 5% alamarBlue dye (Life Technologies Inc.) in culture media for 60 min and extracting the dye for fluorescence readings at excitation-emission wavelengths of 540/580 nm. A two-way analysis of variance (ANOVA) was conducted to determine statistical significance for each test group using R 3.6.1 *(α = 0.05)*. Following metabolic measurement at seven days, cells on a gyroid specimen were fixed by immersion in 0.25% glutaraldehyde in cacodylate buffer for 2 hr and stained with osmium tetroxide. Samples were dehydrated in a graded ethanol series (50%, 70%, 70%, 95%, 95%, 100%, 100%) in roughly 1 hr intervals before critical point drying in ethanol. Scanning electron microscopy (SEM) was conducted on the gyroid specimen following the application of a 5 nm platinum coating using a TESCAN VP microscope at an accelerating voltage of 10 kV to examine cellular interaction with the titanium.

5.2.3 Surgical Implantation

20 adult male New Zealand white rabbits, weighing about 3 kg, were used in this study under the approval of the Animal Care Committee of Sun Yat-sen University (Approval No. SYSU-IACUC-2020-000198) – using a tibial defect due to its size and load-bearing behaviour. Under general anesthesia and routine disinfection, a FG600 and a G300 implant were alternately placed in the left and right tibial epiphyses of each rabbit to avoid bias

from strong and weak responders [32], at the level of the cortical bone surface before suturing the surgical sites. Antibiotics were administered for three consecutive days after surgery. In order to trace and quantify new bone growth, calcein (C0875 Sigma-Aldrich) and alizarin red (A3882 Sigma-Aldrich) fluorochrome labels were injected into all rabbits in the 2nd and 6th week of implantation respectively. The concentrations of calcein and alizarin red were 5 mg/ml and 30 mg/ml respectively.

At each end-point (4 and 12 weeks after surgery), 10 rabbits were sacrificed and the tibia-implant blocks were retrieved and fixed in 10% neutral buffered formalin solution. Five of the blocks were taken for X-ray microcomputed tomography (Micro-CT) and the remaining five were used for the histological evaluation at each time point.

5.2.4 X-ray Microcomputed Tomography

Following tissue fixation, tibia-implant samples were subjected to an ethanol dehydration series (70%, 80%, 90%, 95%, 95%, 100%, 100%) in 48 hr intervals and gradually infiltrated with Embed812 resin (Electron Microscopy Sciences) in sequential ratios of 1:3, 1:1, and 3:1 with either acetone or propylene oxide. Resin was cured for 48 hr at 65°C. X-ray microcomputed tomography (micro-CT) was conducted using a Bruker Skyscan 1172 system using a 100 kV beam and 100 μA current with a 0.5 mm Al filter. Voxel size during acquisition was set to 3.55 μm with a 0.25° rotation step. NRecon software (Bruker) was used to create an image stack from the projections using misalignment compensation, moderate ring-artifact reduction, and beam-hardening correction of 67%.

Image processing was conducted in Dragonfly 2022.1 (Object Research Systems) where all micro-CT datasets were subjected to a Gaussian smoothing operation with a kernel size of 9 and σ = 3.0. A 5-layered convolutional neural network (CNN) was created to semantically segment four classes within the micro-CT datasets (Figure S5-1), designated as implant material, bone residing within the implant, bone residing outside the implant, and resin/void space. The CNN was trained using augmented training data from 19 periodically sampled images across two separate datasets, where 80% of the data was used for training and 20% was used for validation. Training was conducted using a patch size of 64, stride ratio of 0.5, batch size of 32, learning rate of 0.30, and was stopped early after 10 consecutive epochs without decrease in the validation loss to avoid overfitting.

Scaffold pore size validation and strut size variation was found by fitting a cylindrical sub-volume to the porous interior of the scaffold and masking regions attributed to implant and non-implant. Island removal was conducted to remove connected components with a voxel count of 1,000,000 or fewer and each region was assigned to a thickness mesh using a downsampling factor of three. Bone volume fraction (BV/TV), measured here as the percent of available pore space in the implant filled with tissue, was measured by applying a cylindrical mask to the segmentation at the boundaries of the porous midsection and calculating the number of bone-classified voxels divided by the sum of total voxels (pore

and bone). Percentage of bone-implant contact (BIC) was measured by performing a 3D cubic dilation with a kernel size of 15 on the region of interest (ROI) labelled as implant within the previously defined cylinder to create a zone within 25 μm of implant struts. The Boolean difference between the dilated ROI and original implant ROI was taken. BIC was then calculated as the ratio of the number of bone-labelled voxels within the Boolean subtraction divided by the total volume of the Boolean subtraction. BIC and BV/TV measurements were compared using a two-way ANOVA and Tukey's HSD test using a significance value of $\alpha = 0.05$.

5.2.5 Histology

The tibia-implant specimens for histology were dehydrated using increasing concentrations of alcohol (70%, 80%, 90%, 95%, 95%, 100%, 100%) and then embedded in methylmethacrylate for sectioning. Cutting of 100-μm-thick sections, parallel to the long axis of the implants, was performed by using a EXAKT E300CP (EXAKT, Germany). The sections were then ground by EXAKT 400CS (EXAKT, Germany) and stained with hematoxylin and eosin (H&E).

H&E-stained histological sections were observed using an EVOS inverted microscope (Life Technologies Inc.) to view cell and bone matrix deposition at ROIs defined on the interior and exterior of the scaffolds. Fluorescent signals from calcein and alizarin red on the same sections were observed using an A1R HD25 inverted confocal microscope (Nikon) to assess locations of calcification in the new tissue after 2 weeks and 6 weeks post-implantation. Fluorescent images were overlaid in Dragonfly 2022.1 with gamma correction and implant boundaries were found using a grayscale-derived segmentation of the implant volume.

5.3 Results and Discussion

5.3.1 In Vitro Scaffold Characterization

In vitro characterization of the gyroid scaffolds (G300 and G600) was conducted using the Saos-2 cell line as a rapidly-proliferating approximation of the behaviour of osteoblasts on the scaffolds [33]. By measuring the metabolic activity of Saos-2 cells on the scaffolds at one, three, and seven days of culture (Figure 5-2A), statistically significant growth was observed between each time point regardless of scaffold geometry. At each unique time point in the seven-day study, gyroid scaffolds in the G300 and G600 groups showed similar potential for osteoblast proliferation via metabolic measurement. SEM of cellular interactions with the additively manufactured titanium shows that Saos-2 cells adhere to the Ti6Al4V substrates and can co-locate to bridge gaps between partially-fused titanium powder particles on the surface (Figure 5-2B).
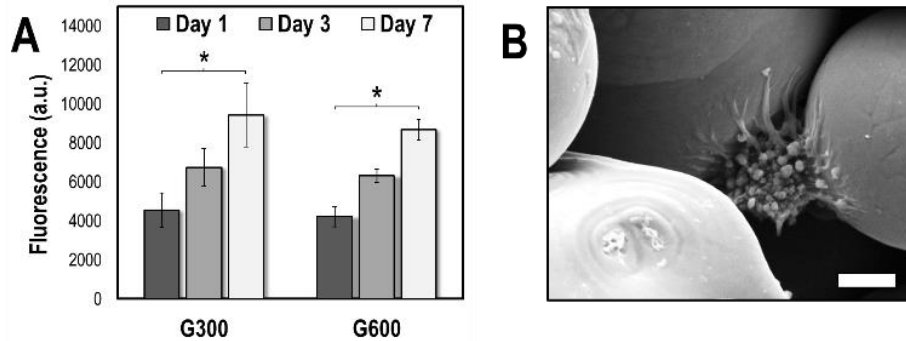
Figure 5-2: In vitro assessment of uniform gyroid Ti6Al4V scaffolds. (A) Saos-2 metabolic activity increases for each type of scaffold at three and seven days of culture (p < 0.05). Scaffolds showed comparable behaviour with pore sizes of 300 μm and 600 μm at each time point. (B) Adherent Saos-2 cell on the surface of an additively manufactured Ti6Al4V gyroid specimen, showing interaction with the cleft between two sintered powder particles on the surface. Scale bar: 5 μm.

In the absence of post-processing surface modification strategies such as acid-etching [34,35] or grit-blasting [36,37], the packing behaviour of these surface-bound metallic particles is governed by characteristics of the feedstock powder and processing parameters defined during selective laser melting [38]. Where similar observations of *in vitro* cell-surface interaction have been observed on stainless steel powder particles [39], it seems as though the pore design of the scaffold may have less of a role than physical or chemical modification of the surface for *in vitro* proliferative effects. Similar fluorescence readings were obtained for the G300 scaffolds and G600 scaffolds, despite the increase in internal surface area in the G300 group. It appears the bulk of the metabolic activity can therefore be attributed to near-surface cells in the scaffold. Similar behaviour has been observed with 3D cell culture in porous microcarriers for other cell types, including chondrocytes [40] and adipose-derived stem cells [41], where cell proliferation to internal surfaces only starts to become evident around five or seven days of culture.

5.3.2 X-ray Microcomputed Tomography

5.3.2.1 Scaffold Feature Size Validation

To assess the deviation in pore and strut size in each *in vivo* scaffold type (G300 and FG600) from the design, measurements were extracted from micro-CT scans of the implants (Figure 5-3). Representative slices from the porous midsection (Figure 5-3A-B) show a distinguishable difference between the two scaffolds (uniform and functionally-graded) at a glance based on their relative pore size. Mapping the pore and strut size distributions for the G300 implant (Figure 5-3C and 5-3E) showed a similar distribution in each. The highest frequency of pore size for the G300 implant was measured to be between 300-310 μm, indicating that the build parameters utilized during additive manufacturing

result in parts with a relatively high tolerance. The median pore size for the G300 implants lies in the range of 250-260 μm, however the lower bound of the distribution is subject to image processing artifacts as pores at the edge of the scaffold can be partially truncated when performing the Boolean intersection with the bounding cylinder or some marginal pore occlusion by partially-fused powder particles. Similarly, the most frequent strut size in the G300 scaffold also ranges between 300-310 μm with a median between 250-260 μm. For uniform pore sizing, the gyroid topology appears to offer a consistent interconnected pore structure throughout the scaffold interior and avoids sharp self-intersections as is typical of TPMS geometries.
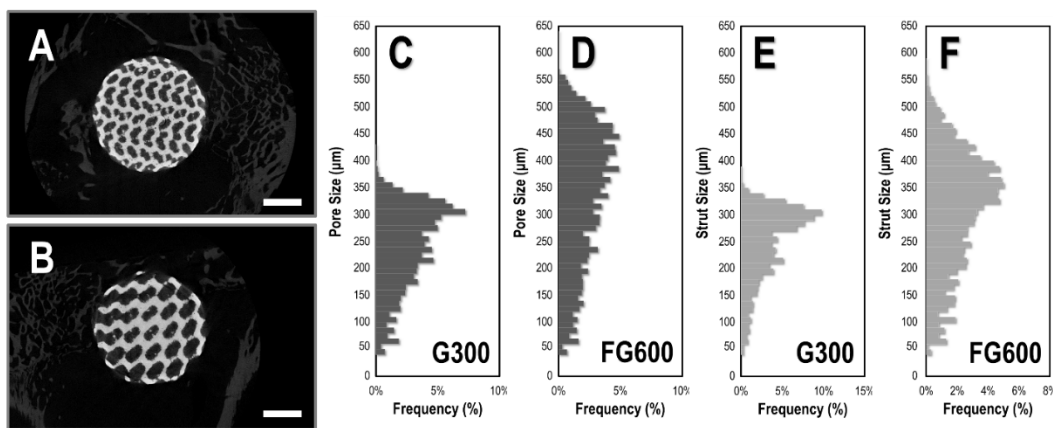
Figure 5-3: Micro-CT and gyroid topology validation. (A) Micro-CT slice showing cross-section of G300 scaffold after 12 wk of implantation in leporine tibia. (B) Micro-CT slice showing cross-section of FG600 scaffold after 12 wk of implantation in leporine tibia. (C) Pore size distribution (n = 10) within the G300 scaffold interior. (D) Pore size distribution (n = 10) within the FG600 scaffold interior. (E) Titanium strut size distribution (n = 10) in the G300 scaffolds. (F) Titanium strut size distribution (n = 10) in the FG600 scaffolds. FG600 scaffolds appear to have a wider distribution of both pore diameter and strut diameter as a result of the functionally-graded pore design. Scale bars: (A-B) 2 mm.

In contrast, it is clear from the pore and strut size distributions in the FG600 implant that the addition of functional grading widens the overall pore and strut size distribution in the implant. Here, larger pore sizes are more commonplace, with the highest frequency between 440-450 μm although the median lies between 350-360 μm. Due to the relative size of the implants, the functional grading from 600 μm to 300 μm occurs over a short radius of 3 mm in the scaffold. As a result, only the outermost surface of the scaffold is anticipated to have pores of 600 μm diameter before shrinking with radius and this is the portion that is most prone to edge effects during image processing. The titanium strut diameter has a slight shift towards smaller values in the FG600 scaffold, with a mode between 350-360 μm. The mismatch between pore size and strut size distributions in the FG600 implant can be attributed to the overall scaffold design. Since functional grading of

the scaffold is with respect to the entire unit cell, it is possible to tune topology without one-to-one inverse proportionality in the strut-pore relationship.

5.3.2.2 Bone Apposition

Bone apposition occurred within the pores and surrounding the exterior of both scaffolds at 4 and 12 weeks, as demonstrated in the micro-CT reconstructions in Figure 5-4. The BV/TV for the G300 implants at 4 and 12 wk was measured at 0.68 ± 0.10 and 0.74 ± 0.04, respectively. For the FG600 implants, the BV/TV values were measured at 0.58 ± 0.12 after 4 weeks and 0.47 ± 0.04 after 12 weeks. As illustrated in Figure 5-5, a significant difference *(p < 0.05)* was found between the two types of scaffolds after retrieval, with the functionally-graded scaffold (FG600) containing a lower bone volume fraction than the scaffold with uniformly-sized pores (G300).
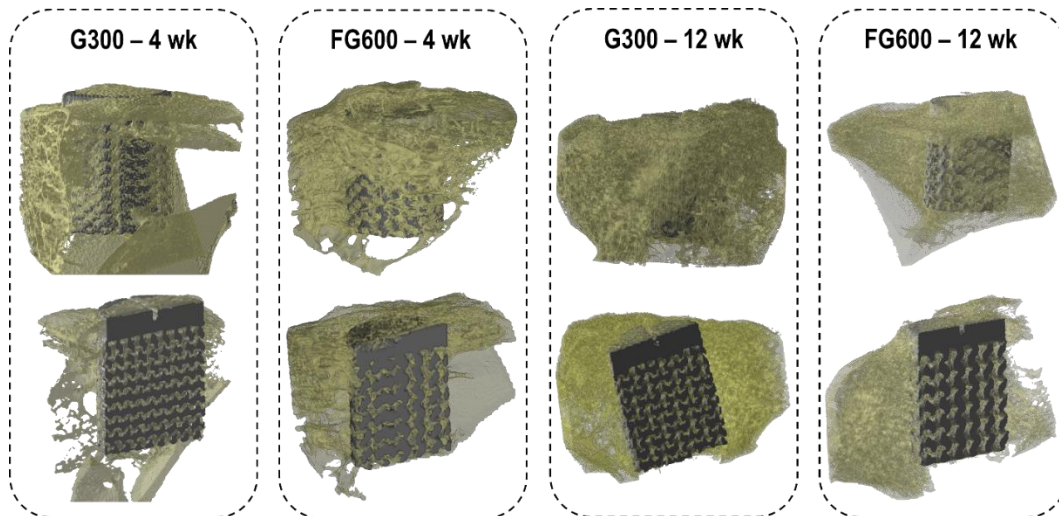
Figure 5-4: 3D Micro-CT reconstructions at 4 wk and 12 wk. *Formation of bone inside the defect area has occurred after four weeks and twelve weeks, resulting in implant fixation. The porous region of the implants is situated within the trabecular fraction of the epiphysis in the leporine tibia, while the full-density titanium in the crown lies in the cortex. Longitudinal cross-sections for all implants show evidence of bone apposition at both four weeks and twelve weeks.*

The measured BIC values for the G300 implants at the 4-week time point were 87.9% $\pm$ 2.7%, with a similar value after 12 weeks (89.1% $\pm$ 1.1%). Ranges in the FG600 implants were approximately the same magnitude, with 84.2% $\pm$ 4.1% BIC at four weeks and 82.0% $\pm$ 2.2% at twelve weeks. The G300 implant had significantly higher BIC at the twelve-week endpoint compared to the FG600 implant *(p < 0.05)*. BIC measurements in these porous scaffolds appear higher than what is in the literature for pore sizes of 800 and 1200 µm after 3 and 8 weeks in rabbit femora [42], but it is also important to note that the difference in imaging modality. Micro-CT of porous titanium, with a pore size range of 500-700 µm, placed into ovine femora yield BIC measurements of roughly 60% at 26

weeks [43]. Imaging artifacts can occur at the implant interface due to attenuation from the titanium [44]; using a threshold of 25 μm from the implant surface for BIC assessment may help reduce noise in these interfacial calculations, but the number of transitions from bone to implant along the path of a single X-ray is still expected to be greater in implants with more pores in the cross-section. Ultimately, correlative high-resolution 3D imaging techniques are best used as a complement to micro-CT to assess the intimacy of bone-implant at smaller length scales and improve the reliability of BIC measurements. Correlation to histological observation is important to confirm trends observed through micro-CT at the bone-implant interface.
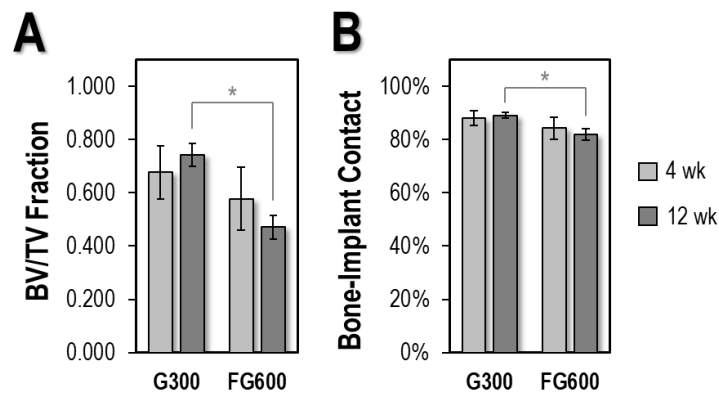
Figure 5-5: Histomorphometry of G300 and FG600 scaffolds at 4 wk and 12 wk. (A) Bone volume fractions for each scaffold. The uniform 300 μm pore size retains a higher bone volume fraction at 12 wk than the implant with functionally-graded pore size. (B) Percentage of bone-implant contact for each scaffold. BIC is higher at 12 wk in the implant with a uniform 300 μm pore size.

5.3.3 Histology of Scaffolds in Rabbit Tibiae

5.3.3.1 H&E Staining

Representative histological sections detailing interior and exterior sites of FG600 and G300 implants retrieved at 4 wk are shown in Figure 5-6. Additional H&E sections can be found in Figure S5-2 and S5-3.

At the outermost layer of the FG600 scaffold (Fig. 5-6B), there is evidence of the inflammatory response occurring in close proximity to the apex of the titanium scaffold. The inflammatory tissue that has formed varies widely in its composition across distances of 500 μm or less. In the inset shown in Figure 5-6C, dense clusters of dark-coloured basophilic cells or white blood cells tend to aggregate around dispersed lipids in the tissue. Due to their lack of eosinophilic cytoplasm in most cases and large nuclear fraction, these cells are consistent with lymphocytes [45]. At the FG600 apex, the white blood cells (black/purple) and erythrocyte-rich microvasculature (red) both infiltrate the space between

lipids (white) in the region. This region has direct line-of-sight access to the scaffold exterior, with no titanium struts obfuscating osteoblasts or other biological response. In the first interior layer of pores (Figure 5-6D), there is a much lower density of white blood cells present in the inflammatory tissue, with similar volumes of red blood cells in the titanium-bound microcapillaries and a comparable dispersion of lipids near the titanium surface. The immune cells here appear to have a higher cytoplasmic fraction than in the high-density region and are more consistent with granulocytes [45]. Figure 5-6E shows a neighbouring region, with a finer capillary structure in the tissue and a slightly higher granulocyte density compared to what is seen in Fig. 5-6D. With respect to the apposition of bone tissue at the implant surface, nearby regions have an 'interlocking' effect where new bone has formed to fully encapsulate an exterior scaffold strut (Figure 5-6F). Osteocyte lacunae are visible within the bone matrix as close as 20 μm from the implant surface, with an approximate concentric alignment around the contours of the strut surface. The extent of bone regeneration at this site and maturity of the tissue seems to indicate that bone at exterior sites is further along in the modelling cascade than bone nucleating at interior sites. This distinction is often made in porous implant materials, where quantitative histomorphometry can be subcategorized into interior and exterior moieties depending on whether near-surface pores are sampled [43].

While the *in vitro* results at early timepoints show a biological response that is predominantly occurring on the exterior of the scaffolds or within the first layer of pores, the *in vivo* results show the formation of bone in the scaffold interior after only four weeks of implantation. Figure 5-6G and 5-6I illustrate bone regeneration at interior sites within the scaffolds at this time point, where lower-magnification images show a disperse network of thin trabeculae that populate the scaffold interior in the G300 implant (Figure 5-6H-I) and residual inflammatory tissue mixed with bone matrix in the FG600 implant (Figure 5-6I). The apical portion of the G300 implant (Figure 5-6N) after four weeks has a characteristic appearance of bone marrow and is mostly filled with adipocytes and microcapillaries rather than white blood cells. At the crown of the G300 and FG600 implants, osteoconduction from cortical regrowth is beginning to occur, providing inward growth into the pores nearest the cortex.
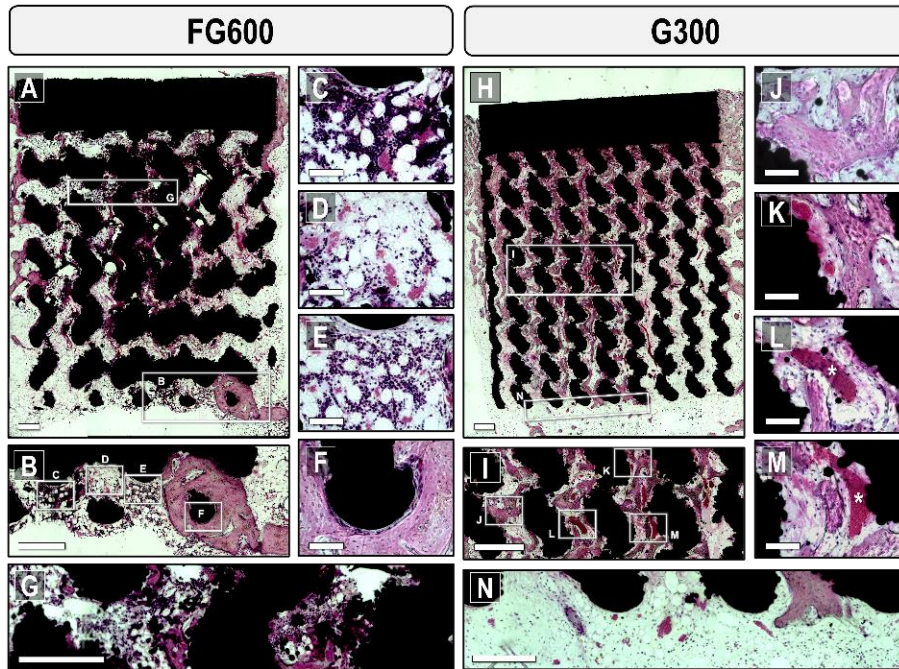
Figure 5-6: Histology of interior and exterior implant sites after four weeks. (A) Hallmarks of bone formation throughout the FG600 scaffold with H&E staining after four weeks of implantation in a rabbit tibia. (B) Inflammatory interactions occur at the FG600 exterior with a trabecular and marrow-like appearance around the initial clot, including the formation of: (C) Dark-appearing cells, likely lymphocytes, apparent among clusters of adipocytes and erythrocytes; (D) Erythrocyte-rich regions in the granulation tissue with fewer white blood cells present; (E) Inflammatory tissue without formation of a mineralized matrix at the implant interface and an intermediate fraction of white blood cells; (F) More extensive bone regeneration to create intimate bone-implant contact at the scaffold exterior. (G) Formation of bone matrix along with inflammatory tissue occurs within the FG600 interior. (H) Patterns in early osseointegration of the G300 implant. (I) Thin regions of appositional bone tend to span the implant interior with less inflammation than in the FG600 implants. (J) Bridging of the scaffold struts occurs with the formation of new trabecular bone. Trabeculae appear to integrate closely at the strut surface and partially contour around titanium particles. (K) Competition occurs at the strut surface between microvascular entities and osteocyte-rich bone. Trabecular orientation seems to be dominant in parallel with the pore wall. (L-M) Vascular structures, denoted by asterisks, are able to permeate deep into the scaffold interior with trabeculae forming around the vasculature. Microvasculature propagates through both the void volume in the scaffold and along the titanium surface. (N) G300 exterior with high content of adipocytes, a network of microvasculature, and low relative counts of white blood cells. Scale bars (A-B, G-I, N) 500 μm; (C-F, J-M) 100 μm.

Looking at pores at increasing radial depth into the G300 scaffold (Figure 5-6I) tends to illustrate a lack of depth-dependency for bone growth, with pores at the midpoint of the G300 scaffold containing similar amounts of bone to shallow pores near the implant surface in this instance. The location of the scaffold in the medullary canal also appears to affect bone tissue apposition, as osteogenesis appears more dominant in the leftmost and central regions of the image for the G300 implant. However, at sites within the scaffold interior, appositional bone tissue appears to bridge adjacent scaffold struts at the four-week endpoint with an appearance that is consistent with trabecular bone (Figure 5-6J-K). Osteocytes in these regions of new bone formation appear mostly disorganized, with high density and no clear direction of co-alignment as is typically seen in mature bone tissue [46], e.g., the apical regrowth in the FG600 implant. Tissue regeneration in the scaffold is not always unidirectional with respect to the scaffold struts, where bone formation can occur in a predominantly transverse direction (as in Figure 5-6J), or with longitudinal components (Figure 5-6K). There are also fewer lipids and granulocytes in and around the G300 scaffold compared to the FG600 implant in Figure 5-6, suggesting that bone repair and the fracture healing cascade may be slightly more advanced in the G300 implant compared to the FG600 implant.

In terms of biological interaction, a fine network of vasculature permeates throughout the entirety of the implant to aid in both tissue formation and homeostasis. These microcapillaries contain an abundance of erythrocytes, denoted by asterisks in Figure 5-6L and 5-6M, and appear to be sectioned obliquely based on their aspect ratio. This ability for this provisional capillary network to maintain carrying capacity is important for osseointegration as it mediates the delivery of oxygen, growth factors, and the removal of waste by-products at these interior scaffold sites during bone modelling and remodelling [47]. Concerning osseointegration, neovascularization has been documented to occur on the surface of solid titanium implants long before the formation of new bone tissue [48] with local expression of factors such as Runt-related transcription factor 2 [49] that control the pre-osteoblast to osteoblast transition. Here, we note that this newly formed vasculature can infiltrate a porous metallic scaffold in leporine defects in a similar manner to what has been seen for murine interfaces with solid titanium [48]. The newly formed vasculature has a tendency to interface and propagate along the porous titanium (as in Figure 5-6M and 5-6M) but also spans scaffold struts in a freeform manner (as in Figure 5-6L). At early time points, the capillary network is observed to periodically interact with the titanium as a self-supporting mechanism during trabecular modelling.
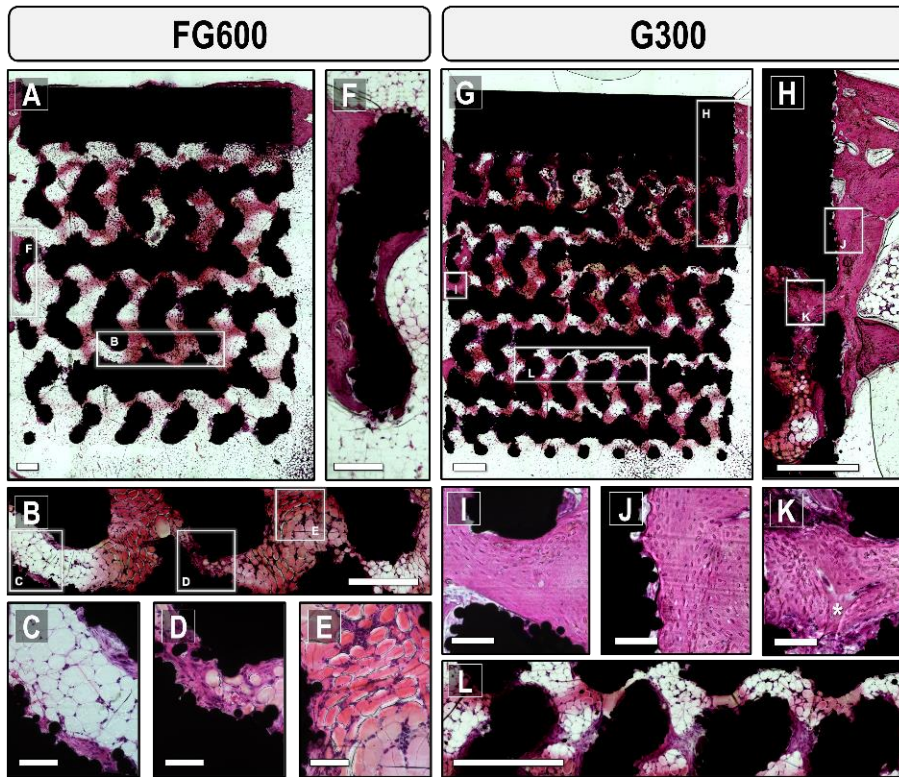
Figure 5-7: Histology of interior and exterior implant sites after twelve weeks. (A) Bone formation throughout the FG600 scaffold with H&E staining after twelve weeks of implantation in a rabbit tibia. Appositional bone has coarsened compared to the four-week endpoint and fully occupies the pore diameter in some instances. (B) Inset in the FG600 interior shows high lipid content, with: (C) Circular adipocytes in the centre of the pore, flanked by regions of bone matrix along the titanium; (D) Predominantly bone matrix where pores narrow; (E) Elliptically-shaped adipocytes in an eosinophilic matrix, with marginally higher white blood cell clustering compared to other myeloid regions. (F) Trabecular integration at the scaffold exterior, with bone fully encapsulating an outer strut. (G) Bone formation throughout the G300 scaffold with H&E staining after twelve weeks of implantation in a rabbit tibia, with seemingly higher bone area fraction than the FG600. (H) Inset at the crown of the implant shows cortical osteoconduction beyond to the first layer of pores within the scaffold. (I) Newly formed tissue in the trabecular region enters the implant, with mature osteocytes that concentrically align with the upper scaffold strut. (J) The tissue formation front at the crown tends to only interact with a single tangential region on each sintered powder particle. (K) New bone tissue completely surrounds a branching microcapillary, denoted by an asterisk, where the capillary is roughly located at the midplane of the two scaffold struts. Scale bars (A-B, G-H, L) 500 μm; (F) 250 μm; (C-E, I-K) 100 μm.

Examination of the FG600 (Figure 5-7A-F) and G300 (Figure 5-7G-L) scaffold geometries after twelve weeks show evidence of sustained osteogenesis between the four and twelve week endpoints. The interior pores of scaffolds retrieved after 12 wk tend to have much higher adiposity than those retrieved at 4 wk, where the bulk of the tissue inside the scaffold is consistent with that of myeloid tissue (Figure 5-7B and 5-7L) with radially-oriented eosinophilic regions characteristic of the bone matrix that bridge neighbouring struts in the gyroid topology. The consistent patterns in bone apposition within the scaffold interior mirror what is seen in the micro-CT reconstructions, confirming that the unit cell topology can, at least in part, govern the directionality of nascent tissue in the scaffold interior. At 12 wk, adaptation of the tissue is noted to maintain this pattern and preserve the functional connection of bone and implant throughout the scaffold interior. It is possible that the increase in adipocyte-rich myeloid tissue within the scaffold (Fig. 5-7C-E) can be attributed to a shift in stem cell differentiation, where osteoblast progenitors can ostensibly commit to an adipogenic pathway [50,51]. As bone marrow is formed inside the scaffold interior, hematopoiesis can occur to sustain red and white blood cell production. Figure S5-4 shows an interior pore channel, with a myeloid structure, including the presence of a suspected megakaryocyte along with white blood cells, red blood cells, connective tissue, and adipocytes – indicating that residual platelet production and clotting [52] are still occurring in the scaffold after 12 wk. Comparing the two types of scaffolds, bone matrix appears more densely distributed throughout the interior of the G300 implant due to the smaller pore size helping to facilitate bone formation that spans multiple scaffold struts.

There is generally less inflammatory tissue present near the implant exterior at twelve weeks for both scaffold types, although some persists near the apex of the implant and there are fewer white blood cells present. Similar to trabecular integration at four weeks, there are regions (Figure 5-7F) where mature trabeculae wrap around the entirety of the outermost scaffold struts. At twelve weeks, bone in the newly formed trabeculae and cortex tends to be coarser. Bone within the trabecular region is able to branch into the porous interior, spanning the entire diameter of the pore in some instances. Osteocytes within these inwardly-directed trabeculae have a mature phenotype according to their shape [53], with a flat lacunar morphology (Figure 5-7I). These osteocytes tend to align more closely with the upper scaffold strut in this pore, perhaps due to the higher number of sintered powder particles and therefore rougher nature of the lower strut. Tissue integration in this trabecular region follows the contours of surface-bound titanium particles but this is not ubiquitous on the implant surface. Cortical regeneration along the implant crown shows that the bone formation front can instead form tangential to the surface particles, with no tissue penetrating the crevices between powder particles (Figure 5-7J). Osteocyte lacunae in this region of the crown are also consistent with a mature morphology, with their flatter edge parallel to the implant surface. In some instances at four and twelve weeks, a clear path of osteoconduction can be observed where bone develops at the existing cortex and grows along the crown of the implant to merge with newly formed trabeculae. This bone then

breaches the porous layers adjacent to the cortex to enter the scaffold interior – a phenomenon observed in both the FG600 and the G300 scaffolds.

After twelve weeks, microvascular capillaries no longer appear to be interfacing with the titanium scaffold. Capillaries instead appear with a typical appearance in mature bone tissue, propagating through continuous vascular canals in the mineralized bone tissue, with one such example shown in Figure 5-7K. The vascular structure seems to follow the gyroid scaffold topology, bifurcating at a site where the pore network branches. The vascular entities also appear to be roughly centered at the midplane between neighbouring scaffold struts. Preservation of these capillaries throughout the scaffold is essential to allow for the survival of bone at the innermost scaffold locations by acting as a transport system for biological macromolecules and regulating tissue metabolism.

It may indeed be worthwhile in the future to assess the spatial distribution of factors such as Runt-related transcription factor 2 (RUNX2) or peroxisome proliferator-activated receptor-γ (PPARγ) [54] to validate the decline in osteogenic commitment inside the scaffolds and corresponding increase in adipocyte formation. This would provide information about the differentiation of mesenchymal stem cells over time inside the pore network of a scaffold and provide a basis for developing temporally-relevant physical and chemical surface modification strategies.

5.3.3.2 Fluorochrome Labels

To compare sites of calcification throughout the interior of the implant, fluorochrome signals were compared using calcein injection at two weeks and alizarin red at six weeks post-implantation. By comparing fluorochrome-labelled regions in these implants with H&E-stained sections (sampled at four weeks and twelve weeks), it is possible to localize regions of matrix mineralization within the tissue. For all implants in Figure 5-8, a fluorescent signal from calcein was evident within the scaffold interior after only two weeks, indicating that a framework for mineral transport into the scaffold was present in a very early period following implantation. The co-localization of calcein signal at two weeks and tissue present at four weeks (Figure 5-8E-H) indicates that similar quantities of mineralized tissue were present in the scaffold interior at early timepoints, despite the more extensive network of bone matrix in the G300 implant. The same trends persist for the implants retrieved at twelve weeks, where the bulk of the fluorescent signal is co-localized with stained regions in the H&E sections. These early mineral loci do not appear ubiquitously through the matrix material and do not yet span the full pore diameter in regions where they appear, instead nucleating as smaller clusters.

In both the H&E and fluorochrome images, periodicity is evident with respect to where new tissue forms. At similar radii through the implant, there are consistent patterns in appositional bone formation inside the implant. Bone that spans two neighbouring struts of titanium has a consistent and somewhat unidirectional appearance in all pores on the same

azimuth (i.e. along the same 'rows' of pores in Figures 5-7 and 5-8). For the FG600 implants, this appositional bone tends to orient itself in the radial direction of the implant, while the G300 implants tend to have a more oblique direction in the tissue. Pobloth et al describe a similar ability for bone to grow through axial, perpendicular, and oblique pore directions along the interior struts of titanium scaffolds, instead using collagen directionality to assess this form of tissue patterning [55]. Although the unidirectionality may be an artifact of sectioning orientation, commonalities in appositional bone orientation in the fluorochrome and H&E deserve further investigation. Where unit cell topology was shown to have only a minor role for *in vitro* scaffold assessment, the *in vivo* results suggest that topology can indeed play a larger role with respect to the directionality of osteogenesis in the scaffold interior.

The evolution of mineralization from two weeks to six weeks is more evident in the FG600 implants, where calcified regions appear to propagate outward from the original loci present at two weeks (Figure 5-8C). This is consistent with the use of fluorochrome labelling in other studies, where early endpoints tend to have smaller fluorochrome-labelled areas near the interface of a titanium implant [56]. Alizarin red fluorescence shows that mineralized tissue can span across entire pores, effectively linking two titanium struts. The G300 group of implants shows a similar trend where existing mineralized tissue coarsens, but there are also regions where new mineral apposition seems to occur at six weeks, connecting scaffold struts with no prior mineral adjacent to them.
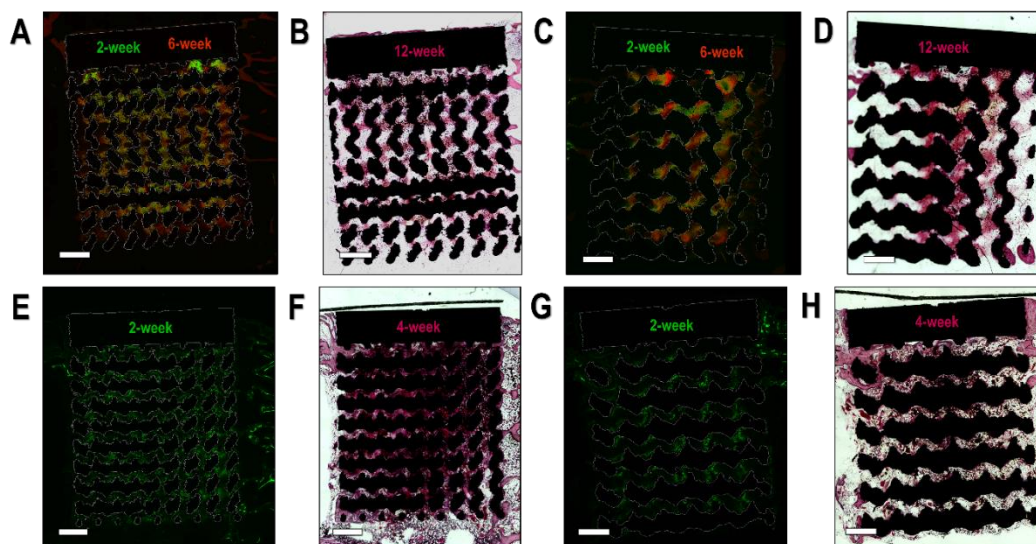
Figure 5-8: Fluorochrome labelling of calcification loci. *(A-D) Fluorochrome images of calcein injected two weeks post-implantation, alizarin red injected six weeks post-implantation, and correlative H&E-stained section after twelve weeks in the (A-B) G300 and (C-D) FG600 implants. Calcified regions expand between the two-week and six-week endpoints, correlating closely with tissue in the H&E section at twelve weeks. (E-H) Calcein fluorochrome and H&E stain showing correlative bone apposition at two and four weeks in (E-F) G300 and (G-H) FG600 implants. Fluorescent signals are bright throughout the implant interior where bone matrix is present, indicating that mineral transport is consistently occurring within the scaffold interior within the first two weeks and corresponds with regions of connective tissue in the H&E micrographs. Scale bars 1 mm.*

5.4 Conclusions

Additive manufacturing of titanium enables the production of complex scaffolds with an interconnected pore geometry to influence early osseointegration and short-term implant stability. Ti6Al4V gyroid structures display *in vitro* cytocompatibility with respect to Saos-2 metabolism. *In vivo* assessment of the uniform and functionally-graded gyroid structures in rabbit tibiae both show potential for improving early implant outcomes by encouraging osteogenesis to occur on the scaffold exterior and interior. In general, newly formed bone spans internal scaffold struts with a common directionality relative to neighbouring regions of bone apposition, governed at least in part by the strut orientation of the scaffold itself. BV/TV and BIC measurements from micro-CT reconstructions demonstrated that values were higher for G300 implants compared to FG600 implants at 12 wk, suggesting that the G300 implants have an increased ability to facilitate bone formation. A progression in the osteogenic cascade for implants spanning the medullary canal took place with residual inflammatory response, neovessel development along titanium struts, and some early

formation of bone occurring inside and outside of scaffold pores after four weeks. By twelve weeks of implantation, bone formed in a somewhat unidirectional manner to span scaffold struts, and infiltration of bone marrow occurred into the scaffold interior. Overall, the additively manufactured scaffolds both provide additional surface area for bone growth to occur inside the pores, a means to maintain the tissue through the vascular network, and a promising means for encouraging osseointegration at the implant interface.

5.5 Supplemental Figures
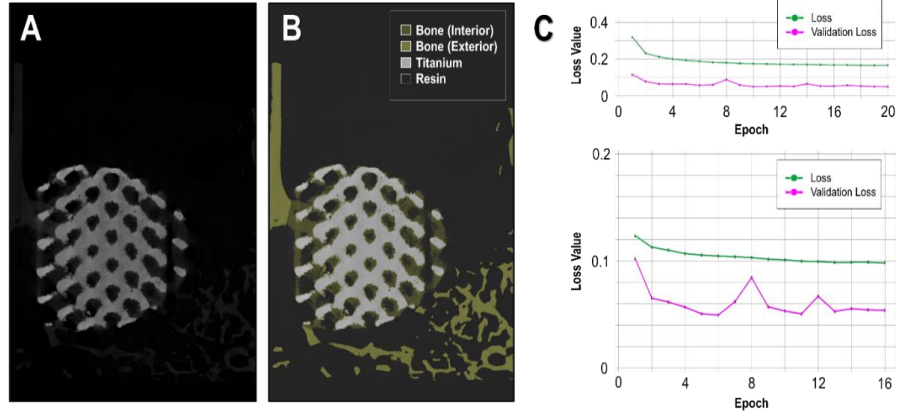
**Figure *S5-1: Convolutional neural network training on micro-CT data.* (A) *Training slice from FG600 implant retrieved after four weeks. (B) Grayscale-assisted manual classification of bone inside the scaffold, bone outside the scaffold, titanium implant, and resin/void space for the slice presented in (A). (C) Training iterations of the convolutional neural network from ten slices of a FG600 scaffold and ten slices of a G300 scaffold. Loss values and validation loss values both decrease through successive epochs of training.*
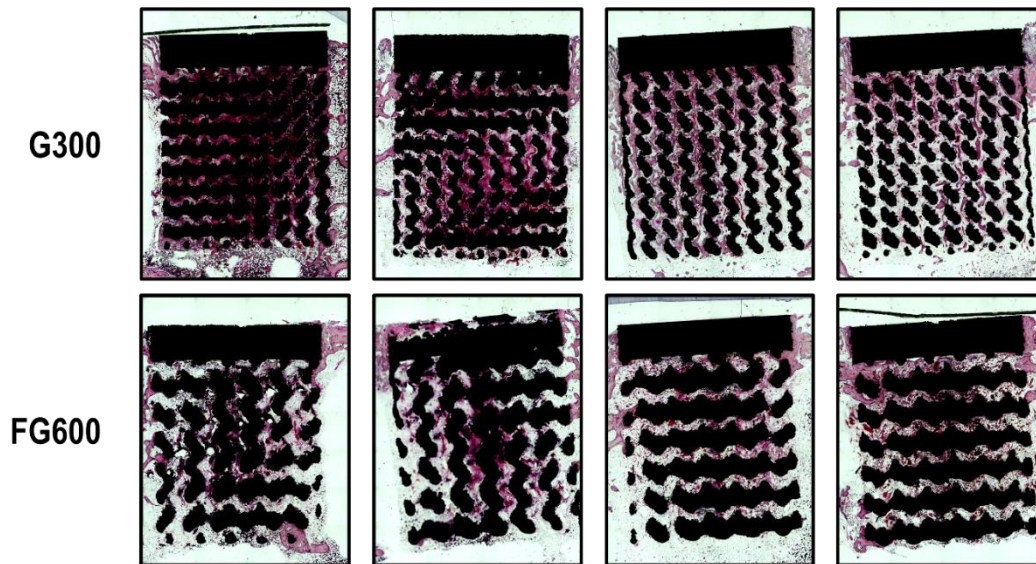
Figure S5-2: All H&E stained sections from the four-week endpoint. Implants in the same column were implanted bilaterally in the same rabbit, taking into account the effect of strong and weak responders. Common themes in all implants include inflammatory response occurring at the apex of the implant, cortical integration at the crown of the implant, and spindles of bone forming with microvasculature in the implant interior.
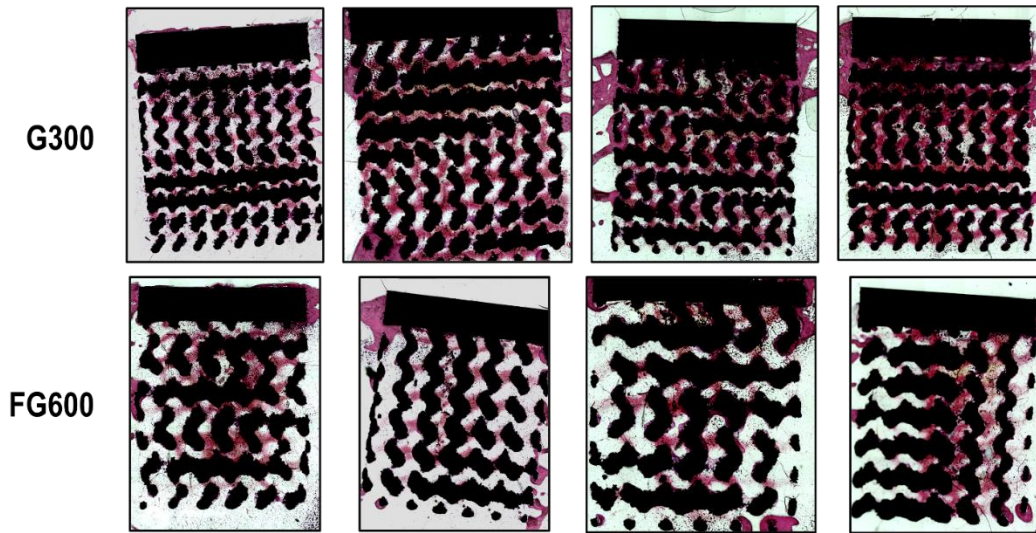
Figure S5-3: All H&E stained sections from the twelve-week endpoint. *Implants in the same column were implanted bilaterally in the same rabbit, taking into account the effect of strong and weak responders. Bone apposition after twelve weeks appears more prolific in the G300 implants, and much of the inflammatory response has subsided. Regions of connective tissue bridge scaffold struts in the interior, and often appear unidirectional with tissue in neighbouring pore channels. Cortical and trabecular integration at the scaffold exterior appears coarser.*
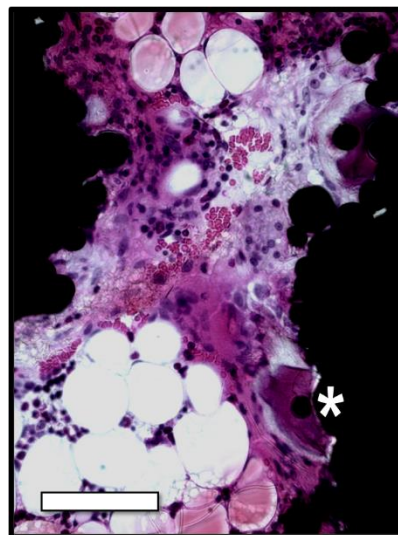
Figure S5-4: Interior pore of a H&E stained section from a G300 implant after twelve weeks. *Red blood cells propagate in vasculature along the centerline of the pore, while a suspected megakaryocyte (denoted with an asterisk) produces platelets to preserve vascular response inside the scaffold.*

References

1. Branemark PI. Osseointegration and its experimental background. J Prosthet Dent. 1983;50(3):399–410.

2. Albrektsson T, Albrektsson B. Osseointegration of bone implants: A review of an alternative mode of fixation. Acta Orthop Scand. 1987;58(5):567–77.

3. Gómez S, Vlad MD, López J, Fernández E. Design and properties of 3D scaffolds for bone tissue engineering. Acta Biomater. 2016;42:341–50.

4. Dias MR, Guedes JM, Flanagan CL, Hollister SJ, Fernandes PR. Optimization of scaffold design for bone tissue engineering: A computational and experimental study. Med Eng Phys. 2014;36(4):448–57.

5. Scaglione S, Giannoni P, Bianchini P, Sandri M, Marotta R, Firpo G, Valbusa U, Tampieri A, Diaspro A, Bianco P, Quarto R. Order versus Disorder: in vivo bone formation within osteoconductive scaffolds. Sci Rep-uk. 2012;2(1):274.

6. Deering J, Dowling KI, DiCecco LA, McLean GD, Yu B, Grandfield K. Selective Voronoi tessellation as a method to design anisotropic and biomimetic implants. J Mech Behav Biomed. 2021;116:104361.

7. Arabnejad S, Johnston RB, Pura JA, Singh B, Tanzer M, Pasini D. High-strength porous biomaterials for bone replacement: A strategy to assess the interplay between cell morphology, mechanical properties, bone ingrowth and manufacturing constraints. Acta Biomater. 2016;30:345–56.

8. Melancon D, Bagheri ZS, Johnston RB, Liu L, Tanzer M, Pasini D. Mechanical characterization of structurally porous biomaterials built via additive manufacturing: experiments, predictive models, and design maps for load-bearing bone replacement implants. Acta Biomater. 2017;63:350–68.

9. Wang Z, Wang C, Li C, Qin Y, Zhong L, Chen B, Li Z, Liu H, Chang F, Wang J. Analysis of factors influencing bone ingrowth into three-dimensional printed porous metal scaffolds: A review. J Alloy Compd. 2017;717:271–85.

10. Wang X, Xu S, Zhou S, Xu W, Leary M, Choong P, Qian M, Brandt M, Xie YM. Topological design and additive manufacturing of porous metals for bone scaffolds and orthopaedic implants: A review. Biomaterials. 2016;83:127–41.

11. Deering J, Grandfield K. Current interpretations on the in vivo response of bone to additively manufactured metallic porous scaffolds: A review. Biomaterials Biosyst. 2021;2:100013.

12. Stok JV der, Jagt OPV der, Yavari SA, Haas MFPD, Waarsing JH, Jahr H, Lieshout EMMV, Patka P, Verhaar JAN, Zadpoor AA, Weinans H. Selective laser melting-produced porous titanium scaffolds regenerate bone in critical size cortical bone defects. J Orthopaed Res. 2013;31(5):792–9.

13. Huiskes R, Weinans H, Rietbergen B van. The Relationship Between Stress Shielding and Bone Resorption Around Total Hip Stems and the Effects of Flexible Materials. Clin Orthop Relat R. 1992;274(NA;):124–34.

14. Mahmoud D, Elbestawi MA. Lattice Structures and Functionally Graded Materials Applications in Additive Manufacturing of Orthopedic Implants: A Review. J Manuf Mater Process. 2017;1(2):13.

15. Al-Ketan O, Rowshan R, Al-Rub RKA. Topology-mechanical property relationship of 3D printed strut, skeletal, and sheet based periodic metallic cellular materials. Addit Manuf. 2018;19(Acta Biomater. 4 2008):167–83.

16. Abueidda DW, Elhebeary M, Shiang CS (Andrew), Pang S, Al-Rub RKA, Jasiuk IM. Mechanical properties of 3D printed polymeric Gyroid cellular structures: Experimental and finite element study. Mater Design. 2019;165:107597.

17. Kapfer SC, Hyde ST, Mecke K, Arns CH, Schröder-Turk GE. Minimal surface scaffold designs for tissue engineering. Biomaterials. 2011;32(29):6875–82.

18. Zhang L, Feih S, Daynes S, Chang S, Wang MY, Wei J, Lu WF. Energy absorption characteristics of metallic triply periodic minimal surface sheet structures under compressive loading. Addit Manuf. 2018;23:505–15.

19. Plessis A du, Razavi SMJ, Benedetti M, Murchio S, Leary M, Watson M, Bhate D, Berto F. Properties and applications of additively manufactured metallic cellular materials: a review. Prog Mater Sci. 2021;125:100918.

20. Yu S, Sun J, Bai J. Investigation of functionally graded TPMS structures fabricated by additive manufacturing. Mater Design. 2019;182:108021.

21. Zhou H, Zhao M, Ma Z, Zhang DZ, Fu G. Sheet and network based functionally graded lattice structures manufactured by selective laser melting: Design, mechanical properties, and simulation. Int J Mech Sci. 2020;175:105480.

22. Bai L, Gong C, Chen X, Sun Y, Xin L, Pu H, Peng Y, Luo J. Mechanical properties and energy absorption capabilities of functionally graded lattice structures: Experiments and simulations. Int J Mech Sci. 2020;182:105735.

23. Zhang XY, Yan XC, Fang G, Liu M. Biomechanical influence of structural variation strategies on functionally graded scaffolds constructed with triply periodic minimal surface. Addit Manuf. 2020;32:101015.

24. Zhang XY, Fang G, Xing LL, Liu W, Zhou J. Effect of porosity variation strategy on the performance of functionally graded Ti-6Al-4V scaffolds for bone tissue engineering. Mater Design. 2018;157:523–38.

25. Liu F, Mao Z, Zhang P, Zhang DZ, Jiang J, Ma Z. Functionally graded porous scaffolds in multiple patterns: New design method, physical and mechanical properties. Mater Design. 2018;160(Biomaterials 23 2002):849–60.

26. Liao B, Xia RF, Li W, Lu D, Jin ZM. 3D-Printed Ti6Al4V Scaffolds with Graded Triply Periodic Minimal Surface Structure for Bone Tissue Engineering. J Mater Eng Perform. 2021;30(7):4993–5004.

27. Yuan L, Ding S, Wen C. Additive manufacturing technology for porous metal implant applications and triple minimal surface structures: A review. Bioact Mater. 2019;4(1):56–70.

28. Coelho PG, Granjeiro JM, Romanos GE, Suzuki M, Silva NRF, Cardaropoli G, Thompson VP, Lemons JE. Basic research methods and current trends of dental implant surfaces. J Biomed Mater Res Part B Appl Biomaterials. 2009;88B(2):579–96.

29. Dondossola E, Friedl P. Host responses to implants revealed by intravital microscopy. Nat Rev Mater. 2022;7(1):6–22.

30. Mahmoud D, Al-Rubaie KS, Elbestawi MA. The influence of selective laser melting defects on the fatigue properties of Ti6Al4V porosity graded gyroids for bone implants. Int J Mech Sci. 2021;193:106180.

31. D'Elia A, Deering J, Clifford A, Lee BEJ, Grandfield K, Zhitomirsky I. Electrophoretic deposition of polymethylmethacrylate and composites for biomedical applications. Colloids Surfaces B Biointerfaces. 2019;188:110763.

32. Reznikov N, Boughton OR, Ghouse S, Weston AE, Collinson L, Blunn GW, Jeffers J, Cobb JP, Stevens MM. Individual response variations in scaffold-guided bone regeneration are determined by independent strain- and injury-induced mechanisms. Biomaterials. 2018;194(J. Bone Joint Surg. Am. 89 Suppl 3 2007):183–94.

33. Rodan SB, Imai Y, Thiede MA, Wesolowski G, Thompson D, Bar-Shavit Z, Shull S, Mann K, Rodan GA. Characterization of a human osteosarcoma cell line (Saos-2) with osteoblastic properties. Cancer Res. 1987;47(18):4961–6.

34. Thenard T, Catapano A, Allena R, May ME, Saintier N, Mesnard M. Topography and wettability characterization of surfaces manufactured by SLM and treated by chemical etching. Mech Adv Mater Struc. 2020;29(12):1–18.

35. Xu J yun, Chen X shuai, Zhang C yu, Liu Y, Wang J, Deng F long. Improved bioactivity of selective laser melting titanium: Surface modification with micro-/nano-textured hierarchical topography and bone regeneration performance evaluation. Mater Sci Eng C. 2016;68:229–40.

36. Rønold HJ, Lyngstadaas SP, Ellingsen JE. Analysing the optimal value for titanium implant roughness in bone attachment using a tensile test. Biomaterials. 2003;24(25):4559–64.

37. Gotfredsen K, Berglundh T, Lindhe J. Anchorage of Titanium Implants with Different Surface Characteristics: An Experimental Study in Rabbits. Clin Implant Dent R. 2000;2(3):120–8.

38. Gockel J, Sheridan L, Koerper B, Whip B. The influence of additive manufacturing processing parameters on surface roughness and fatigue life. Int J Fatigue. 2019;124:380–8.

39. Deering J, Presas A, Lee BEJ, Valentin D, Yu B, Heiss C, Grandfield K, Bosbach WA. Response of Saos-2 osteoblast-like cells to kilohertz-resonance excitation in porous metallic scaffolds. J Mech Behav Biomed. 2020;106:103726.

40. Fang J, Zhang Y, Yan S, Liu Z, He S, Cui L, Yin J. Poly(l-glutamic acid)/chitosan polyelectrolyte complex porous microspheres as cell microcarriers for cartilage regeneration. Acta Biomater. 2014;10(1):276–88.

41. Yan S, Xia P, Xu S, Zhang K, Li G, Cui L, Yin J. Nanocomposite Porous Microcarriers Based on Strontium-Substituted HA-g-Poly(γ-benzyl-l-glutamate) for Bone Tissue Engineering. Acs Appl Mater Inter. 2018;10(19):16270–81.

42. Lopez-Heredia MA, Goyenvalle E, Aguado E, Pilet P, Leroux C, Dorget M, Weiss P, Layrolle P. Bone growth in rapid prototyped porous titanium implants. J Biomed Mater Res A. 2008;85A(3):664–73.

43. Palmquist A, Snis A, Emanuelsson L, Browne M, Thomsen P. Long-term biocompatibility and osseointegration of electron beam melted, free-form–fabricated solid and porous titanium alloy: Experimental studies in sheep. J Biomater Appl. 2013;27(8):1003–16.

44. Zhang X, Wang J, Xing L. Metal artifact reduction in x-ray computed tomography (CT) by constrained optimization. Med Phys. 2011;38(2):701–11.

45. Bolliger AP. Cytologic evaluation of bone marrow in rats: indications, methods, and normal morphology. Vet Clin Path. 2004;33(2):58–67.

46. Shah FA, Snis A, Matic A, Thomsen P, Palmquist A. 3D printed Ti6Al4V implant surface promotes bone maturation and retains a higher density of less aged osteocytes at the bone-implant interface. Acta Biomater. 2016;30(Biomaterials 27 2006):357–67.

47. Filipowska J, Tomaszewski KA, Niedźwiedzki Ł, Walocha JA, Niedźwiedzki T. The role of vasculature in bone development, regeneration and proper systemic functioning. Angiogenesis. 2017;20(3):291–302.

48. Khosravi N, Maeda A, DaCosta RS, Davies JE. Nanosurfaces modulate the mechanism of peri-implant endosseous healing by regulating neovascular morphogenesis. Commun Biology. 2018;1(1).

49. Redenski I, Guo S, Machour M, Szklanny A, Landau S, Kaplan B, Lock RI, Gabet Y, Egozi D, Vunjak-Novakovic G, Levenberg S. Engineered Vascularized Flaps, Composed of Polymeric Soft Tissue and Live Bone, Repair Complex Tibial Defects. Adv Funct Mater. 2021;31(44):2008687.

50. Augello A, Bari CD. The Regulation of Differentiation in Mesenchymal Stem Cells. Hum Gene Ther. 2010;21(10):1226–38.

51. Liu TM, Martina M, Hutmacher DW, Hui JHP, Lee EH, Lim B. Identification of Common Pathways Mediating Differentiation of Bone Marrow- and Adipose Tissue-Derived Human Mesenchymal Stem Cells into Three Mesenchymal Lineages. Stem Cells. 2007;25(3):750–60.

52. Rabellino EM, Levene RB, Leung LL, Nachman RL. Human megakaryocytes. II. Expression of platelet proteins in early marrow megakaryocytes. J Exp Medicine. 1981;154(1):88–100.

53. Shah FA, Thomsen P, Palmquist A. A Review of the Impact of Implant Biomaterials on Osteocytes. J Dent Res. 2018;97(9):977–86.

54. James AW. Review of Signaling Pathways Governing MSC Osteogenic and Adipogenic Differentiation. Sci. 2013;2013:684736.

55. Pobloth AM, Checa S, Razi H, Petersen A, Weaver JC, Schmidt-Bleek K, Windolf M, Tatai AÁ, Roth CP, Schaser KD, Duda GN, Schwabe P. Mechanobiologically optimized 3D titanium-mesh scaffolds enhance bone regeneration in critical segmental defects in sheep. Sci Transl Med. 2018;10(423).

56. Koo S, König B, Allegrini S, Yoshimoto M, Carbonari MJ, Mitri-Luiz FF. Titanium implant osseointegration with calcium pyrophosphate in rabbits. J Biomed Mater Res Part B Appl Biomaterials. 2006;76B(2):373–80.

Chapter 6: Characterizing Mineral Ellipsoids in New Bone Formation at the Interface of Ti6Al4V Porous Implants

Summary:

Interaction of biological features at the bone-implant interface can occur with characteristic patterns at multiple length scales. With the recent identification and 3D characterization of a new structural feature (the mineral ellipsoid) in mature bone tissue and at the mineralization front, questions have arisen about how these structures form and arrange themselves in new bone tissue. In this chapter, the interface of the porous implants from Chapter 5 are examined at two time points through high-resolution imaging with STEM and PFIB-SEM tomography. HAADF-STEM shows 2D motifs (elliptical and rosette) associated with varying section planes of mineral ellipsoids in close proximity to the implant interface, with the presence of a mineral-dense zone near the implant interface and orientation shifts in the neighbouring packets of mineral ellipsoids. PFIB-SEM allows for 3D imaging and shows the packing arrangement and heterogenous nature of these mineral ellipsoids within newly formed bone directly adjacent to the implant interface. This work fits the themes of the thesis by providing characterization of the bone-implant interface inside porous metallic implants using 2D and 3D methods.

Characterizing Mineral Ellipsoids in New Bone Formation at the Interface of Ti6Al4V Porous Implants

Joseph Deering[1], Jianyu Chen[2], Dalia Mahmoud[3], Tengteng Tang[1], Qiyin Fang[4], Gregory R. Wohl[3,5,6], Mohamed Elbestawi[3], Kathryn Grandfield[1,5,6]

[1] Department of Materials Science and Engineering, McMaster University, Hamilton, ON, Canada

[2] Guanghua School of Stomatology, Hospital of Stomatology, Guangdong Provincial Key Laboratory of Stomatology, Sun Yat-sen University, Guangzhou, China

[3] Department of Mechanical Engineering, McMaster University, Hamilton, ON, Canada

[4] Department of Engineering Physics, McMaster University, Hamilton, ON, Canada

[5] School of Biomedical Engineering, McMaster University, Hamilton, ON, Canada

[6] Brockhouse Institute for Materials Research, McMaster University, Hamilton, ON, Canada

Abstract

The intrinsic hierarchy of newly-formed bone contains elements of disorder within a naturally-ordered multiscale structure, spanning from the macroscale to below the nanoscale. With mineralized structures often presenting in the shape of ellipsoids in mature and mineralizing tissue, this work characterizes the heterogeneity in mineral ellipsoid packing at the interface of porous titanium implants. The 2D and 3D characterization of these mineral ellipsoids at the bone-implant interface prospectively offers insight into the osseointegration of titanium implants and should help govern the mechanical properties of the interfacial bone tissue. Using scanning transmission electron microscopy and plasma focused ion beam - scanning electron microscopy, mineral ellipsoids are characterized at the implant interface in both 2D and 3D. Heterogeneous in their size and shape within the newly formed bone tissue, the ellipsoids are observed with alternating orientations corresponding to unique lamellar packets within the nearest 2-3 μm to the titanium implant interface – although this motif is not universal, and a mineral-dense zone can also appear at the implant interface. The short-order ellipsoid orientation shifts are also present in the 3D probe of the implant interface, where an approximate 90° misorientation angle between neighbouring packets of mineral ellipsoid resolves with increasing distance from the titanium, possibly providing a strengthening mechanism to prevent crack propagation in the peri-implant bone.

6.1 Introduction

The natural structure of mineralized bone tissue spans the continuum between the macroscale and nanoscale, encompassing both organic and inorganic components to achieve robust mechanical properties. At smaller length scales, osteoblast-secreted type I collagen constitutes much of the organic assembly and provides a template for mineral ingress into the tissue [1]. As the tissue begins to mineralize, an ellipsoidal mineral packing arrangement is theorized to occur according to a stencilling principle based on inhibition of inhibitors [2], with resulting mineral clusters sized at roughly 0.4-1.5 µm along their major and minor axes [3]. When viewed in orthogonal directions with two-dimensional imaging such as transmission electron microscopy (TEM), these ellipsoids take on either an elliptical motif or a circular rosette motif. Based on large-scale 3D imaging, these mineral clusters appear to be ubiquitous throughout bone tissue (as noted in human femora [4] and murine tibiae [5]) and have been noted adjacent to implants of titanium, bioactive glass, and others in either of the elliptical or rosette motifs [3]. Yet, little is known about their shape, origin, or evolution in new bone tissue or their 3D organization at the interface of metallic biomaterials despite a wealth of literature about smaller features, such as collagen orientation [6,7].

Additive manufacturing offers a new way to produce implants with engineered porosity in the microscale range [8], with porous titanium and tantalum implants showing closer mechanical properties to cortical bone [9] and improved secondary stability in biomechanical evaluation [10]. The low mechanical stiffness [11,12] imparted by these implants offers one method to mitigate long-term bone resorption associated with stress-shielding [13] and the corresponding increase in surface area creates additional bone-to-implant contact [14]. Understanding bone mineral apposition and morphological transformations at implant interfaces and into these pores may therefore have major implications for early osseointegration, implant stability, and longevity of implants in the body.

Prior to the discovery of mineral ellipsoids, osseointegration at implant interfaces was identified by key markers and used techniques other than electron microscopy [15,16]. At the microscale, observations of cellular response [17] or woven-to-lamellar transition [18,19] are often used to qualitatively and quantitatively assess osseointegration. At the nanoscale, higher-resolution studies have shown the accumulation of non-collagenous proteins near the implant interface [20,21] or that of a calcified cement line [22], and generally denoted the orientation of collagen parallel to the implant surface [23,24]. While all of these observations give a strong understanding of bone growth near implants, a lack of widespread 3D imaging may be at the heart of why mineral ellipsoids have not been studied in detail at implant interfaces, with few examples of osseointegration studies by FIB-SEM over small volumes [25], and electron tomography with an even smaller field of view [26–30]. Moreover, microscale pores present a unique challenge for characterization,

with a simultaneous need for high-resolution and large-volume imaging. Plasma focused ion beam tomography provides a window to examine tissue apposition in the pore network over time.

Here, we report a high resolution and 3D study of the osseointegration of titanium implants with a graded pore size in rabbits at 4 and 12 weeks. We utilize scanning transmission electron microscopy and plasma focused ion beam to provide an innovative approach for assessing ellipsoidal mineral organization at implant interfaces – achieving both high-resolution and 3D structure – and offering insight into potential consequences in the mechanical properties of interfacial bone tissue.

6.2 Methods

6.2.1 Scaffold Design and Implantation

Porous implant scaffolds were designed according to the specifications described in Chapter 5. Briefly, implants were designed with a total height of 7 mm and total diameter of 6 mm. The porous midsection was designed to contain a gyroid unit cell, with radially-varying pore size from $\varnothing = 600$ μm at the scaffold exterior to $\varnothing = 300$ μm at the midpoint of the scaffold. Powder bed fusion of Ti6Al4V powder feedstock was used to create the implants.

Under general anesthesia, implants were placed into the tibial epiphyses of male New Zealand white rabbits (2.5-3 kg) with approval from the Animal Care Committee of Sun Yat-sen University. Antibiotics were administered for three days following animal surgery. Implants were retrieved after 4 and 12 wk to prepare for electron microscopy imaging.

6.2.2 Sample Preparation

Tibial tissue was defatted after animal sacrifice and implant retrieval using immersion in acetone for 12-24 hr. Samples were fixed in 10% neutral buffered formalin on a rocking table for 24 hr before rinsing steps (4 hr, 4 hr, and 12 hr) with deionized water to remove fixative and subsequent sectioning to the defect area. Serial dehydration was conducted using 48 hr intervals at 50%, 70%, 70%, 80%, 90%, 95%, 95%, 100%, 100% ethanol concentrations under vacuum (-80 kPag). Embed812 resin was gradually infiltrated into the tissue at ratios of 1:3, 1:1, and 3:1 using acetone as a solvent. Tibiae were transferred to 100% resin in embedding molds and cured at 60°C under vacuum (-90 kPag) for 48 hr. Embedded implants were roughly sectioned at their midplane using a slow-speed saw to reveal the porous interior for electron microscopy and the cross-section was ground with silicon carbide paper (400, 600, 800, and 1200 grit). Implants with exposed cross-sections were mounted to stubs using silver paint and were sputter-coated with 20 nm of gold before scanning electron microscopy at 20 kV (JEOL 6610LV) to view the interaction between the implant and undemineralized tissue.

6.2.3 Scanning Transmission Electron Microscopy

A site of bone-implant contact was identified near the crown of the implant following twelve weeks of implantation. A focused ion beam microscope (Zeiss NVision 40) was used to prepare a lamella [31] along the long axis of the implant for scanning transmission electron microscopy (STEM) by depositing a 4 µm layer of tungsten over the region of interest and milling trenches on all sides at 30 kV with currents ranging from 6.5 to 45 nA. The lift-out, containing bone flanked on either side by titanium, was attached to a copper grid, where the lamella was thinned to electron transparency (70-120 nm) using a series of decreasing ion beam currents from 300 pA to 40 pA at 30 kV, and a final low-voltage polish at 5 kV.

Scanning transmission electron microscopy was conducted in a Talos 200X (ThermoFisher Scientific) using a high-angle annular dark field (HAADF) detector and an accelerating voltage of 200 kV with eightfold frame averaging. Electron energy loss spectroscopy (EELS) was conducted using a dispersion of 0.3 eV/channel, acquisition time of 0.01s, and pixel size of 7 nm on a Continuum S imaging filter (Gatan). EELS elemental maps for carbon, calcium, and titanium were generated in Digital Micrograph software.

6.2.4 Plasma Focused Ion Beam-Scanning Electron Microscopy

The implants retrieved after four weeks and twelve weeks were polished further to allow for site selection during plasma focused ion beam - scanning electron microscopy (PFIB-SEM) tomography. Implants from each endpoint (4 and 12 weeks) were loaded into a Helios G4 UXE DualBeam (ThermoFisher Scientific) focused ion beam microscope with a xenon plasma source for serial sectioning. Sites were selected based on the schematic in Figure 6-1, sampling both cortical and trabecular bone-implant interfaces at a radial depth of roughly 150 µm into the implant interior (Figure S6-1 and S6-2).

A region of interest was selected at a site of trabecular ingrowth in an implant after four weeks of implantation and was coated with 13 µm of carbon using a 12 kV ion beam at 20 nA and 65 nA to protect the surface from ion damage and prevent curtaining artifacts. Excess material was subsequently removed around the volume using beam currents of 15-200 nA at 30 kV to create trenches, and fiducials were added to the top surface and the block-face onto small pads of tungsten deposition. Auto Slice and View (ThermoFisher Scientific) was used to automate the sequential milling and imaging processes for tomography acquisition. Specifically, milling was performed at 30 kV and 4 nA with the ion beam using a 4° rocking angle and slice thickness of 30 nm. Images in the series were acquired with a 1.2 kV, 400 pA electron beam in immersion mode using a 500 ns dwell time and pixel size of 14.5 nm x 14.5 nm, with fourfold line integration and averaging across two frames on the through-the-lens detector (6144 x 4096 pixels).

The region of interest in the implant retrieved after twelve weeks, near the cortex, was similarly coated with a 10 µm layer of carbon using a 12 kV ion beam and currents of 20

nA and 150 nA. Trenches at the side and front of the region of interest were milled at 30 kV and ion currents starting at 200 nA and decreasing to 60 nA to isolate the region of interest. A fiducial marker for ion beam tracking during tomography was milled into a 3 µm tungsten pad adjacent to the capping layer, and a fiducial marker was milled adjacent to the block-face for slice registration and drift correction. Tomography acquisition for this dataset was obtained through similar serial sectioning as the first dataset, with a 30 kV, 1 nA ion beam with a 300 ns dwell time, 4° rocking mill angle, and slice thickness of 29 nm. Backscattered electron images with a pixel size of 15.0 nm x 15.0 nm were recorded after each milling step using a 1.2 kV, 400 pA electron beam in immersion mode with a 500 ns dwell time, fourfold line integration, and averaging across two frames.
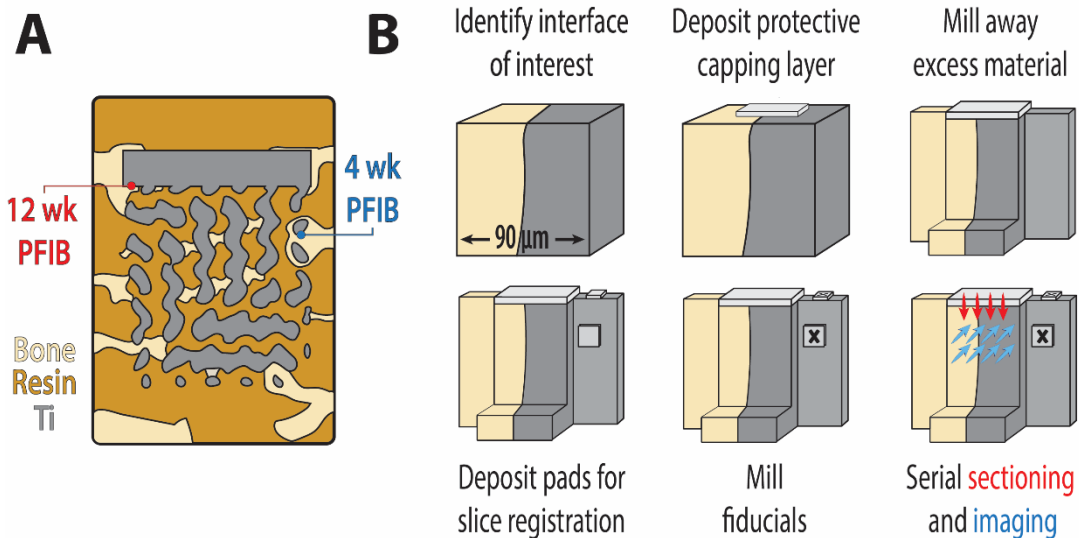
Figure 6-1: *Workflow of PFIB-SEM tomography workflow at the bone-implant interface. (A) Regions of interest were extracted at near-surface pores in the cortical region after 12 wk and at regions of trabecular ingrowth after 4 wk. (B) Serial sectioning takes place after the region of interest is carefully prepared to avoid excessive ion damage and provide a means for accurate post-process image stack alignment and feature detection.*

6.2.5 PFIB-SEM Data Processing

All image processing was conducted in Dragonfly 2022.1 (Object Research Systems). PFIB-SEM tomography datasets were aligned using mutual info from the block-face fiducial to translate slices with a 5.0% initial translation step in the imaging plane and smallest translation step of 0.05%. Datasets were subjected to a 3D Gaussian blur (kernel size = 5, σ = 1.0) without contrast correction before further processing.

6.2.5.1 Mineral Ellipsoid Morphology
Neighbouring regions of bone tissue at the mineralization front in the 4 wk PFIB-SEM dataset were extracted using grayscale-based segmentation, with a threshold value of 155

or greater in the 8-bit images. Clusters or aggregated clusters of mineral forming adjacent to the mineralization front were extracted using 6-connected component labelling to isolate their boundary from any adjacent mineralized entities. Mineral clusters with a size of 500 voxels or greater were used to assess the 3D aspect ratio and cluster volume distribution, while the shortest distance from each mineral cluster to the mineralization front was found by taking a distance map from the largest mineralized component (i.e., the bulk tissue) and using the minimum intensity in the overlap between said distance map and each isolated mineral cluster.

6.2.5.2 Lacunocanalicular Network

The lacunocanalicular network (LCN) within the mineralized tissue of the 4 wk PFIB-SEM datasets was segmented by further Gaussian smoothing (2D, kernel size = 15, σ = 4.0) and using application of grayscale-based thresholding (0-150) to extract the LCN and resin-filled features in 4 wk tomography dataset. Bone matrix (along with other high-contrast regions) was extracted in this PFIB-SEM dataset using a grayscale window of 150-256, with a subsequent fill operation in the Z-direction to infill the darker LCN components (including regions of charging). A Boolean intersection was taken between the matrix/titanium/LCN segmentation and resin/LCN segmentations for final extraction of the LCN components.

To account for contrast and brightness inhomogeneities during tomography acquisition of the 12 wk PFIB-SEM dataset, partitioning of the data into four regions was necessary. Mineralized matrix was extracted using grayscale ranges of 125-255, 90-255, 195-255, and 150-255 to account for brightness/contrast changes. In each partition, the LCN/resin fraction was extracted using grayscale ranges from zero to the lower end of the matrix segmentation (125, 90, 195, or 150 depending on region). The same infill and Boolean intersection operations were then used to isolate the LCN component of the tissue.

High-contrast areas with a cell-associated morphology beyond the mineralization front were enhanced using application of contrast-limited adaptive histogram equalization (Clip = 0.02, kernel size = 100), a Gaussian blur for noise reduction (3D kernel size = 15, σ = 2.5), a maximum smoothing operation (3D kernel size = 3), and further Gaussian smoothing (3D kernel size = 5, σ = 2.5) in cropped sub-volumes.

6.3 Results and Discussion

In Chapter 5, observations at the bone-implant interface were highlighted to illustrate the osseointegration of the implants in 3D and corresponding 2D cellular response at the microscale. Apposition of bone was observed to occur both inside and outside of the pore network in the scaffold alongside other forms of biological response, but the structural features in bone at the lower-end of the microscale and into the nanoscale could not be

resolved with optical and X-ray methods. The 2D and 3D organization of the bone-implant interface are explored further in this section with higher-resolution methods.

6.3.1 Scanning Transmission Electron Microscopy

Understanding the interaction of smaller features in the hierarchical structure of bone with implant surfaces can help provide insight into the macroscale mechanical stability of the implant. A FIB lift-out at the interface of new cortical bone and the porous implant was extracted after 12 wk of implantation and thinned to electron transparency to assess the sub-micron interplay between collagen, mineral, and the implant itself.

Within bone tissue, collagen fibril bundles contain distinct motifs of mineral packing, with 3D microscale mineral packing in the form of ellipsoidal entities [4]. Electron-transparent subregions in the FIB lift-out (Figure 6-2A-B) allow for observation of this form of mineral at the bone-implant interface. One such subregion is shown in Figure 6-2C-E, where mineral ellipsoids are packed into layers of alternating orientation with a thickness of roughly one or two ellipsoids. The layer closest to the implant has a dominant out-of-plane collagen fibril orientation, denoted as O_1, with the long axes of ellipsoids also extending out of the imaging plane. An adjacent region with the same collagen orientation is shown in Figure 6-2E. The intervening layer of mineral ellipsoids, highlighted in Figure 6-2D, is instead encapsulated within a more in-plane collagen fibrillar matrix (I_1), where collagen banding is visible due to gap and overlap zones in the collagen [32]. Lamellar packing of these alternating layers occurs in the next layers of mineral for a final structure of $O_1 \rightarrow I_1 \rightarrow O_2 \rightarrow I_2$ within the first 2 μm of the titanium interface. Within each of these first few layers, collagen fibrils still lie mostly parallel to the implant interface in either of the in-plane and out-of-plane orientations. Beyond 2 μm, however, a new motif (O_3/I_3) extends into the bulk of the tissue where the long axes of the mineral ellipsoids (and collagen fibril bundles) no longer lie parallel to the titanium surface and are instead oriented more obliquely. The introduction of a titanium implant appears to perturb the natural co-aligned ellipsoidal packing order in HAADF-STEM imaging of the implant retrieved after 12 wk in leporine tibia, with clear demarcations between zones of similar ellipsoidal orientation near the implant interface.
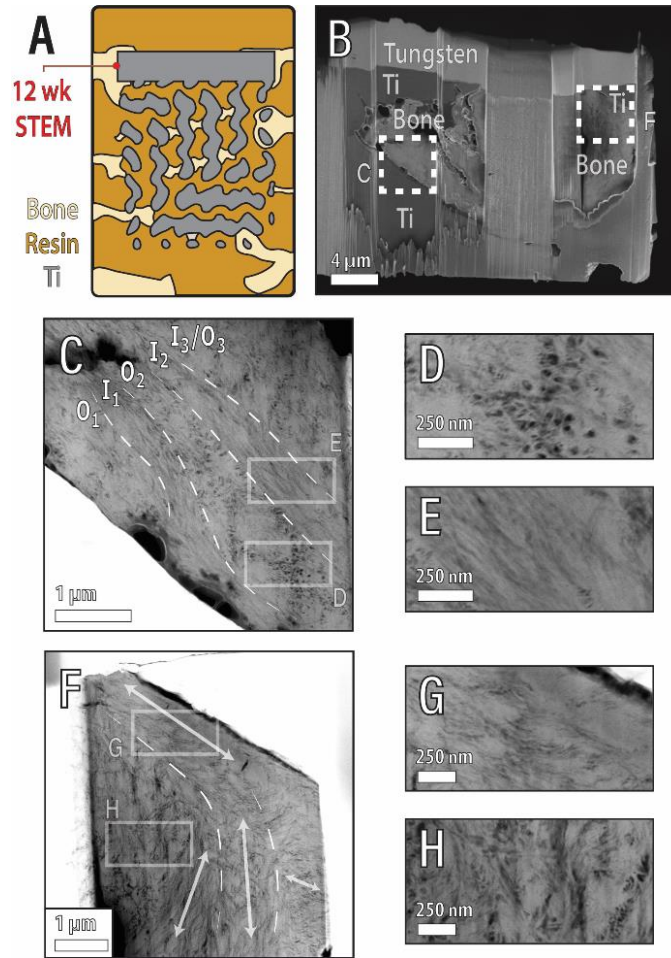
Figure 6-2: *HAADF-STEM imaging at the implant interface after 12 wk. (A) Specimen orientation and sampling location for FIB liftout. (B) Site overview in the FIB liftout showing a cross-section from the location in (A). Two windows with direct-bone contact were thinned to electron transparency. (C-E) HAADF-STEM image at the bone-implant interface. Mineral ellipsoids have an alternating orientation of their long axis, packing in (O) out-of-plane orientation and (I) in-plane arrays with noted collagen banding in (E). (F-H). HAADF-STEM image at the bone-implant interface, showing a second ellipsoidal motif. Mineral clusters near the titanium pack with their long axis parallel to the implant interface (G), while a rotational shift occurs as the distance from the implant interface increases (H).*

The second window for observing the bone-implant interface using HAADF-STEM (Figure 6-2F) shows a trend in ellipsoid orientation that is quite different in some aspects. Within the first 2-3 µm of the implant interface, collagen fibrils still lie parallel to the implant (Figure 6-2G). However, beyond this first zone of co-oriented collagen and mineral, there are no subsequent lamellae where collagen fibrils lie parallel to the implant interface. Instead, an abrupt shift occurs in collagen fibril orientation where collagen

becomes obliquely oriented to the implant interface (Figure 6-2H) and such orientation extends into the tissue with longer-range order than that of the alternating collagen/mineral orientation in the first window.

In most two-dimensional imaging techniques, the presentation of a singular mineral ellipsoid depends on its sectioning orientation through the cluster, with the formation of rosettes having been shown previously [33] along with early identification of 'filamentous', 'lacey', and rosette mineral motifs in the nanoscale structure of bone [34]. Longitudinal sections through an idealized cluster will produce the 'marquise' or elliptical shape shown in Figure 6-3A, and oblique sectioning orientation will produce ellipses with skewed proportions depending on the sectioning angle (Figure 6-3B), while transverse sections will appear as circular (Figure 6-3C). Generally speaking, the tip-to-tail orientation (along the long axis) of these mineralized clusters runs parallel to the collagen fibril bundles within the same domain to create the in-plane and out-of-plane motifs. The short-order periodicity, with mineral ellipsoid orientation shifts, has been observed in mineralization fronts by Buss et al. [5], but here we observed a similar phenomenon occurring at the implant interface, albeit not universally. Two-dimensional imaging with HAADF-STEM provides a snapshot of any order and disorder in collagen-mineral packing arrangements [35] but structural elements are often better visualized in 3D; we also confirm large-scale ellipsoidal packing heterogeneity in the bulk of the tissue and at the implant interface in 3D using PFIB-SEM tomography in Section 6.3.2.2.
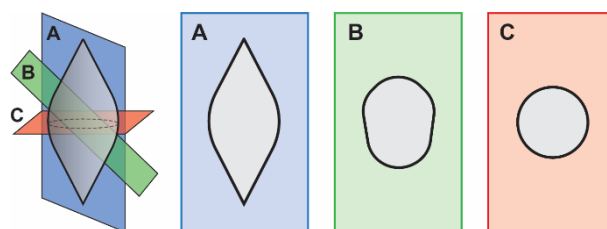
Figure 6-3: Sectioning planes in a 3D mineral ellipsoid. Sectioning planes of varying angular orientation in a mineral ellipsoid show different ellipsoidal motifs depending on the viewing angle. The elliptical motif in (A) and rosette motif in (C) are parallel and orthogonal to the long axis of the ellipsoid, respectively. Oblique sectioning planes tend to create egg-shaped projections as in (B).

Discrete regions are often seen within the first few nanometres of the implant interface with a seemingly afibrillar appearance [36] with attribution to two possible mechanisms. The first relies on the adhesion of early non-collagenous protein on the implant surface to promote mineralization, with the assembly of a collagenous layer shortly following [37]. The second posits the deposition of a dominant collagenous zone in the direct vicinity of the implant, with only a small fraction of granular or afibrillar material [24]. In either case, the structure and packing of mineral ellipsoids or clusters within this region could give indication of the mineral density at the bone-implant interface. HAADF-STEM imaging at

the interface of the porous titanium retrieved after 12 wk is shown in Figure 6-4, with EELS maps of calcium (Figure 6-4B and E), carbon (Figure 6-4C and F), and titanium (Figure 6-4D). An artifact of tissue preparation is present at the titanium interface, giving rise to inflated carbon content within the first 200 nm of the titanium. In the 300 nm beyond this preparation artifact, there is a zone of higher mineral density with slightly elevated calcium and slightly depleted carbon (Figure 6-4G). Distinct collagen fibril bundles can be observed outside of this mineral-dense band, where mineral is more loosely packed. While the mineral-dense band likely still contains collagen fibrils in some quantity, the size distribution or high packing density of mineral ellipsoids or mineral clusters within this band could be masking the collagen in HAADF-STEM imaging. It is also important to note that this mineral-dense band does not span the entire titanium surface, but instead appears sporadically across the bone-implant interface. In all regions, the interface between titanium and bone is directly juxtaposed without a gradient of bone and oxides/nitrides of titanium that is sometimes reported [23].
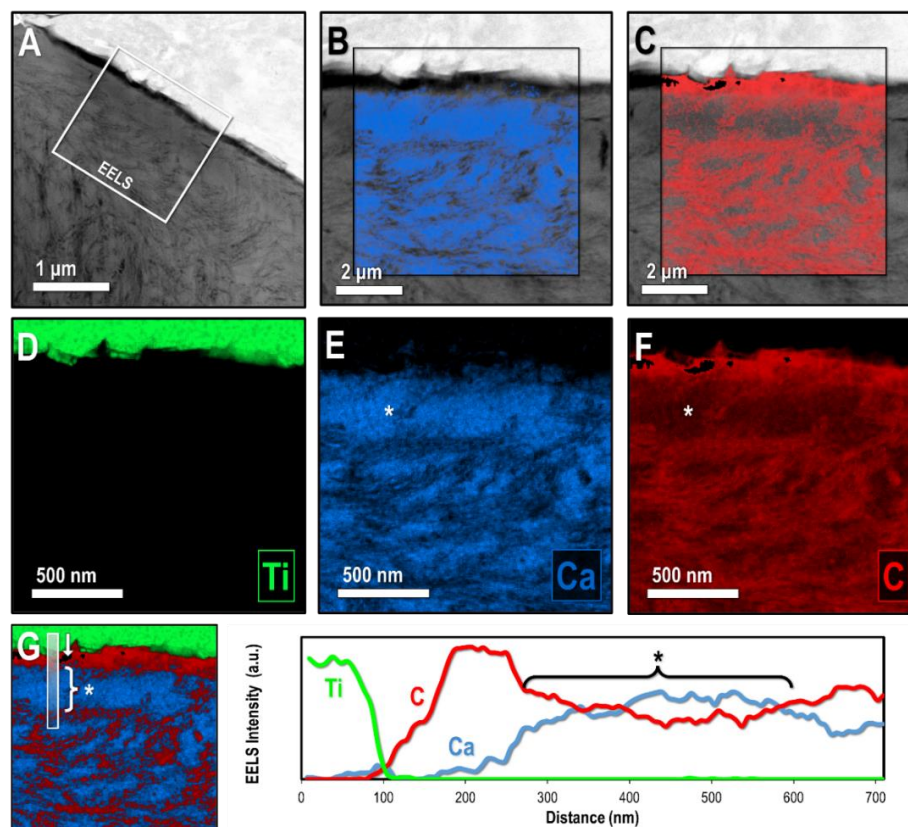
Figure 6-4: *STEM-EELS of de novo bone formation at the implant interface. (A) Site overview of bone-implant near cortical interaction with the crown of the implant after 12 wk. (B-C) Calcium and carbon EELS maps overlaid with the STEM image at the implant interface. (D-F) Titanium, calcium, and carbon EELS maps at the implant interface. Carbon-rich areas tend to overlap with calcium-deficient regions. A mineral-dense zone (*) is present in the tissue at the interface of the titanium. (G) EELS intensity profiles across the mineral-dense zone. Marginal carbon depletion occurs in this zone in addition to slight calcium elevation.*

6.3.2 Plasma Focused Ion Beam-Scanning Electron Microscopy

6.3.2.1 Spatial Characteristics of the LCN

PFIB-SEM tomography of the bone-implant interface provides a high-resolution 3D probe that can span microscale volumes of biological tissues, with faster milling rates using the xenon beam than conventional gallium-based ion beams [38]. Tomography of the bone-implant interface after four weeks of implantation in leporine tibia (Figure 6-5A) yielded a volume size of 56.2 μm × 57.0 μm × 14.0 μm after removal of the extraneous regions around each image. Some instrument instability occurred during acquisition, resulting in contrast and brightness changes throughout each dataset. A 3D volume of this size provides a useful snapshot of mineralizing tissue, covering regions of the implant itself (bright

regions), the mineralizing bone tissue (intermediate regions), and carbon-rich or void entities (dark regions). Despite the high roughness of the additively manufactured implants, it is possible to obtain FIB cross-sections that show the distribution of mineral at the titanium interface. Segmentation of each component (mineralized bone matrix, lacunocanalicular network, and titanium) is shown in Figure 6-5C. After 4 wk of implantation, bone in the shallow pores appeared to closely mirror the micro-rough surface of the implant, with points of bone-implant contact at each of the two titanium interfaces in the volume. Since preparation for electron microscopy can cause shrinkage artifacts in the tissue, some of the gaps between bone and implant may be attributed to sample preparation artifacts. The lacunocanalicular network at 4 wk had a dispersed network of canalicular channels, with the LCN occupying 3.7 vol% of the mineralized bone matrix in this dataset.

Bone adjacent to the implant interface after 12 wk of implantation is shown in Figure 6-5B and 6-5D, with a PFIB-SEM tomography volume of 68.9 μm × 59.1 μm × 11.4 μm. The lacunocanalicular network here is more densely distributed through the bone matrix, occupying 6.8 vol% of the bone in the tomography dataset. Baseline lacunocanalicular porosity levels in mature human femoral bone have been measured at 1.45 vol% utilizing a technique with similar voxel size in synchrotron computed tomography [39], which is a value considerably lower than what we observe in newly mineralizing tissue at the implant interface. A net increase in lacunocanalicular volume density at both 4 wk and 12 wk is expected based on prior work from Shah et al. [40], who reported high osteocyte counts adjacent to near-cortical implant interfaces in porous titanium (compared to similar locations in solid titanium and within the native bone). For each osteocyte, Shah et al. also reported a higher number of canaliculi per osteocyte at the implant interface than in the native bone, helping characterize tissue with high LCN fraction at the two bone-implant interfaces as newly formed.
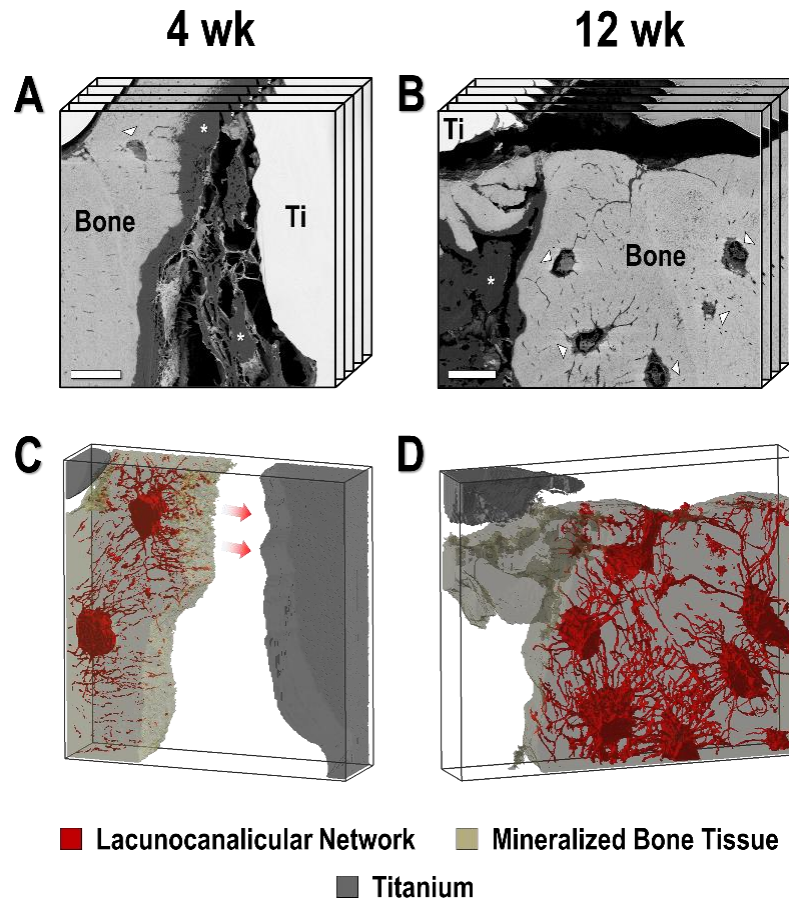
Figure 6-5: *Representative slices from PFIB-SEM tomography and data reconstructions. (A) 3D representation of the PFIB-SEM image stack of the implant interface retrieved after 4 wk. Bright regions are indicative of titanium, dark regions are indicative of carbon- or resin-rich material, and intermediate grayscale regions are mineralized bone matrix. Osteocyte lacunae are denoted with arrowheads and carbon-rich regions are denoted with asterisks. (B) 3D representation of the PFIB-SEM image stack at the implant interface acquired 12 wk after implantation. Segmentation of the bone matrix, implant volume, and LCN is achievable after 4 wk (C) and 12 wk (D). After 4 wk, canaliculi orient towards the mineralization front. Scale bars: 10 μm.*

As the tissue ages, one potential question raises the issue of deriving factors to help drive the transition from high LCN density to low LCN density in the mineralized bone tissue. The accumulation of microdamage, for instance, is one known aspect that is correlated with a decline in osteocyte lacunar density [41,42]. The high LCN fractions in each of the 4 wk and 12 wk PFIB datasets helps indicate that the bone is of new origin rather than a fragment introduced during surgical implantation or highly-damaged region of pre-existing bone.

In the 4 wk dataset, some preferential orientation of canaliculi towards the mineralization front is seen – an observation also associated with *de novo* bone formation. Hasegawa et al. examined the canalicular orientation of osteoblasts and osteocytes and found that osteoblast-associated cytoplasmic processes often have a 'looping' geometry extending from the secretory side of their membrane, while cell processes associated with osteocytes extend perpendicularly outward from the cell body to connect with osteoblasts at the mineralization front [43]. The directionality observed in the implant retrieved after 4 wk indicates that the resident osteocytes near the implant interface maintain a connection with some biological entities outside of the mineralized matrix to help maintain tissue homeostasis. In addition, osteocytes adjacent to implant surfaces with micro-rough or minimally-rough surfaces will extend cell processes perpendicularly towards the implant interface, eventually attaching to the implant itself [44]. In part, osteocyte-driven remodelling [45] may take place within the vicinity of the implant to restructure the provisional LCN seen at the interface of both of these implants. This process will rely on local shifts in pH and tartrate-resistant acid phosphatase production within the LCN to locally resorb mineral and reorganize cell processes. Lacunar remodelling has been seen to occur in bone after only 3 weeks of exercise in murine tibiae [46,47]. While the bone in the PFIB-SEM dataset is newly formed, it is unclear if extensive peri-canalicular remodelling has taken place at these 4 wk and 12 wk endpoints or if the bone is in its as-deposited state.

The possible presence of cells outside of the mineralized matrix can also be observed in the FIB-SEM volume retrieved after 12 wk (Figure 6-6), where high-contrast regions are observed in the shape of a membrane and sporadically through their interior. An opposing observation has been previously observed with secondary electron imaging of unstained cells using an in-column detector under cryogenic conditions, where lipid-rich regions and the cell membrane appear as darker than the cytoplasm rather than brighter [48]. Where small regions of mineral have been observed as mitochondrial granules or vesicle-bound deposits in the intracellular region of osteoblasts [49,50], and osteoblasts close to the mineralization front are known to be mineral-enriched [51], it is possible that these high-contrast regions in the filtered images are associated with either mineral- or phosphorus-rich regions that are common within plasma membranes or sub-cellular organelles [52]. Image processing operations (Figure 6-6A) may help reveal these cellular features without any form of heavy metal staining during sample preparation. The cavitation in the mineralized tissue surrounding the cell in panel *(i)* of Figure 6-6C is consistent with that of mineralizing osteocytes [53] or Type III osteocytes [54]. The transition of osteoblast to osteocyte involves a shift in the presence of several molecular markers as they become mechanosensory cells encapsulated within the mineralized matrix [53]. The two neighbouring cells in panel *(ii)* are separated by only 1 µm or less in some instances throughout the volume – proximity which is atypical of most osteocyte phenotypes. Instead, their flat morphology, size, and location with respect to mineralized tissue could be attributed to bone lining cells [55] or osteoblasts. Without additional staining via osmium

tetroxide [56] or other means, it is difficult to determine whether these are cells embedded within a matrix of osteoid, or if these features simply help demarcate the boundary of mineralized bone tissue.
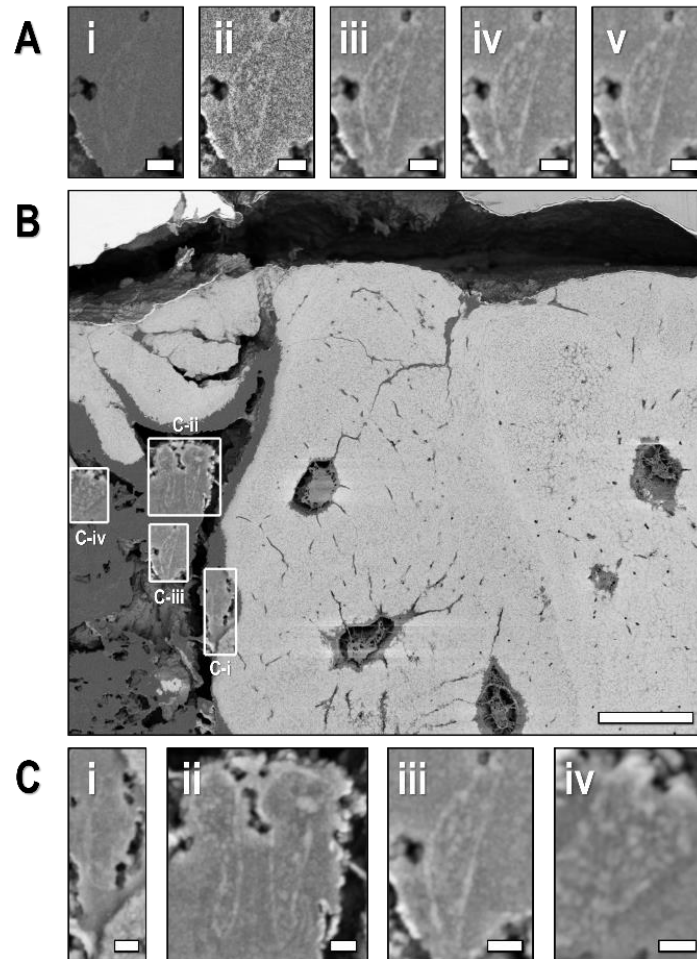
Figure 6-6: *High-contrast regions in the extracellular matrix beyond the mineralization front. (A) Sequential application of Gaussian smoothing, contrast-limited histogram equalization, Gaussian smoothing, maximum filtering, and Gaussian smoothing to highlight cell membranes beyond the mineralization front. (B) Location of possible cells outside of the mineralized matrix. (C) Insets showing the morphology of nearby cells in the osteoid or extracellular matrix. Scale bars: (A,C) 1 μm (B) 10 μm.*

6.3.2.2 Ellipsoid Organization at the Mineralized Boundary

Two topographies at the boundary of the newly formed are seen in the 3D view of the bone-implant interface after four weeks of implantation (Figure 6-7A-B). Subregions of the mineralizing bone tissue are shown using the 3D renderings in Figure 6-7C and 6-7D. One such subregion – flanked on either side by the titanium implant – presents with a rough and granular morphology in 3D. This first region contains cavities for cells to potentially

connect to near-surface osteocytes as the LCN is formed. The neighbouring subregion presents with an overall smoother morphology, with only small woven protrusions from the mineralized bone. The rough morphology is typical of actively mineralizing bone surfaces, where quasi-spherical calcium phosphate precipitates are observed in the form of calcospherites/calcospherulites [57], having a mean diameter of roughly 420 nm [58]. Isolation of mineralizing features using connected-component analysis in the implant retrieved after four weeks can identify individual mineral ellipsoids or aggregates of mineral ellipsoids that are close to, but not yet attached to the mineralized bone matrix (Figure 6-7E). 3D rendering of select clusters shows a great deal of heterogeneity with respect to their size and shape. Newly-evolving mineral sometimes appears to present in the ellipsoidal shape described in mature bone tissue [4], but other times present in abnormal clusters similar to that of hypophosphatemic bone [5]. Considering the leporine bone here is otherwise healthy apart from the bone defect, it appears as though these mineral ellipsoids nucleate or amalgamate to form an inconsistent architecture in newly formed tissue. Figure 6-7F-H shows the distribution of cluster volumes, distance from the boundary of the mineralized tissue, and aspect ratio from the isolation of the 3D mineral clusters. The mean cluster volume was measured at 0.0095 μm^3, or equivalent spherical diameter of roughly 262 nm, with an average distance of 290 nm from the bulk of the mineralized tissue. These clusters have a wide distribution with respect to their 3D aspect ratio, supporting what Shah presents in 2D relating to their isotropic growth during ongoing bone mineralization [59]. It is important to note that these isolated clusters perhaps can undergo further growth before connecting to the bulk of the bone tissue and that these morphometric parameters are not necessarily representative of mineral clusters within the bulk of the mineralized matrix.

The second subregion at the boundary of the mineralized bone, with the smoother topography and more mesh-like organization of mineral, is also characteristic of a mineralizing surface. Examination of sutures in murine calvaria show three stages of mineral shape evolution at these smoother mineralized surface of bone [60], presenting with either *(i)* repeating ellipsoid units; *(ii)* a continuous interwoven mesh of mineralized matrix; or *(iii)* some intermediate combination of mesh and ellipsoids. These mesh-like structures can be associated with earlier mineralization events as in the floor of osteocyte lacunae [60], meaning that the mineralized boundary in Figure 6-7D is perhaps associated with a more dormant mineralization front near the titanium implant due to its intermediate combination of protruding features and mesh structure.
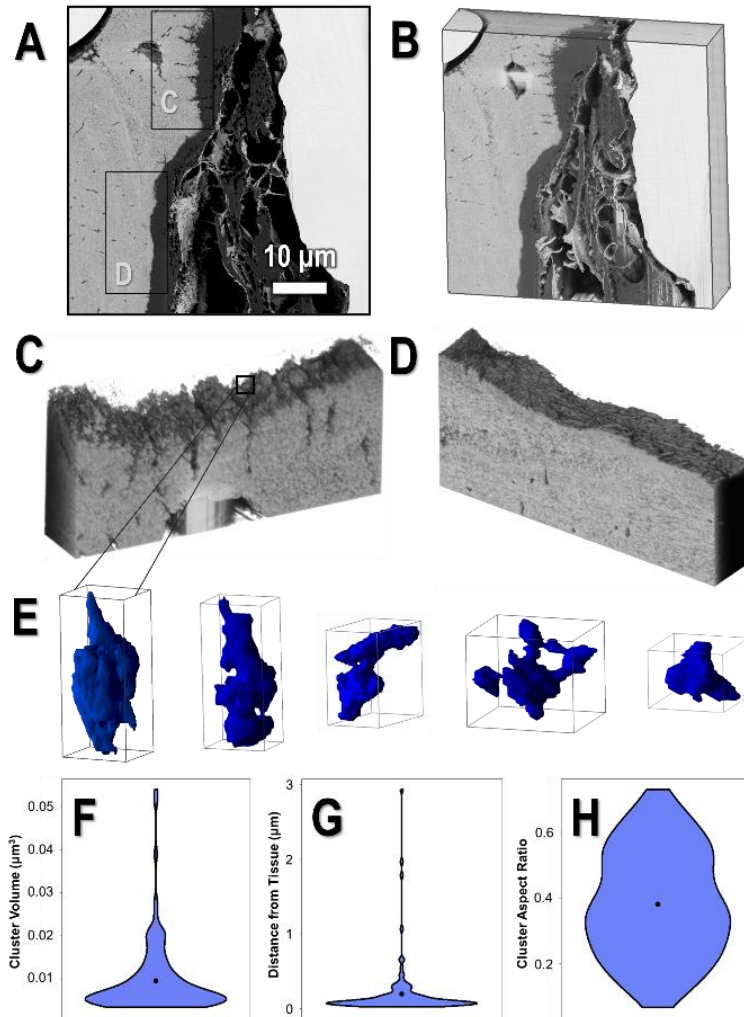
Figure 6-7: *Mineral evolution and topographies at the boundary of the mineralized tissue after 4 wk. (A) Two neighbouring regions at the periphery of the mineralized bone matrix. (B) 3D view of the bone-implant interface. (C) 3D topography of a granular or active mineralized surface adjacent to the implant interface, with distinct shapes attributed to evolving mineral clusters. (D) Smoother 3D topography, with only small protrusions, at a dormant mineralized surface near the implant interface. (E) 3D reconstruction of select mineral clusters at the active site of mineralization, detailing their heterogeneity in size and shape. (F-H) Size, distance to the bulk of mineralized tissue, and aspect ratio of these 3D mineral clusters (n = 116 ellipsoids).*

6.3.2.3 A Heterogeneous Distribution of Mineral Ellipsoids

A 3D reconstruction of fully-mineralized bone tissue at the interface of the implant after four weeks of implantation is shown in Figure 6-8. Spherical cropping to remove the titanium region reveals the underlying orientation of mineral ellipsoids directly at the

implant interface (Figure 6-8B-D) and slightly further into the tissue (Figure 6-8E-F). As illustrated in Figure 6-8C and Figure 6-8D, there is a clear demarcation between two neighbouring arrays of mineral ellipsoids, each with a unique orientation. The misorientation angle between these two separate mineral ellipsoid packets is approximately 90° when studying the ellipsoids at the immediate interface of the titanium. However, examination of 3D ellipsoids further into the tissue shows that the misorientation between these two neighbouring arrays is quickly resolved into that of a unidirectional orientation. Despite this, it is important to note that each of these two adjacent packing arrangements still has collagenous arrangement that lies parallel to the implant interface. Also of note is that ellipsoids within one packet appear to decrease in size as they approach the intersection of the neighbouring packet.

Near naturally-occurring biological interfaces, namely at the boundary of osteonal lamellae, collagen orientation shifts in the manner of twisted plywood [61] or Bouligand structure [62] – which is known to add toughness to composite materials [63]. In the bone retrieved from leporine tibiae, we observe a similar twisting effect in ellipsoid orientation that can occur near the interface of the titanium implant. Within the context of the alternating collagen orientation and ellipsoid packing observed in both the PFIB-SEM and HAADF-STEM, these shifts in mineral ellipsoid orientation likely provide some form of mechanical advantage during osseointegration. Here, we speculate that the collagen orientation shift occurring near the implant interface may improve the mechanical properties of the most interfacial bone tissue – preventing implant instability by stabilizing microcrack propagation in the tissue during osseointegration. Within the context of implant design, one important question for future research is to examine how implant surfaces can be modified or optimized to encourage the formation of these Bouligand ellipsoid structures within the interfacial bone tissue.
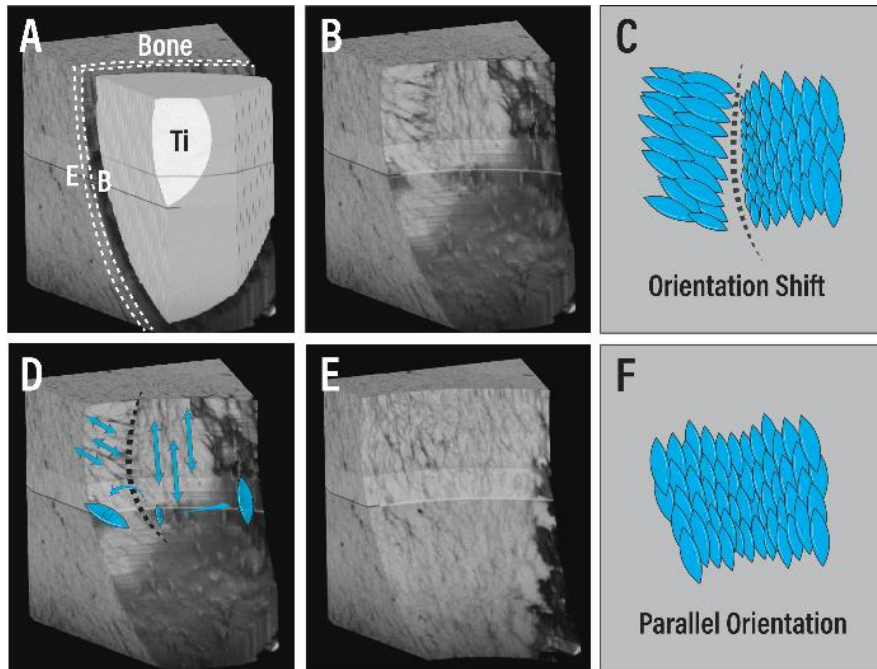
Figure 6-8: *Disordered packing arrays of mineral ellipsoids at the implant interface at 4 wk. (A) 3D view of bone appearing at the titanium interface. (B-D) Cropping to remove the titanium reveals two separate packing arrangements of mineral ellipsoids with a sharp orientation shift between, and a size gradient across one packet. (E-F) Cropping slightly further into the tissue shows that this misorientation is quickly resolved with increasing distance from the implant interface.*

Understanding the packing orientation of mineral ellipsoids further from the implant interface is much more convoluted in nature. Figure 6-9A shows the distribution of mineral ellipsoids near a band of high-contrast tissue in the form of a 2D cement line or a 3D cement sheath. On one side of the cement sheath, a dense region of low-contrast organic or void space is present next to sub-sized mineral ellipsoids, with the marquise motif showing in the imaging plane. Within the zone of the cement sheath itself, there does not appear to be any of the three defined ellipsoidal motifs presented in Figure 6-4, possibly due to high-density packing. These cement sheaths have been documented to contain three or more preferred fibril orientations using a fast Fourier transform in FIB-SEM data, but in general, they have more complex fibril orientations than in mature osteonal bone [64]. Elsewhere in the tissue at 4 wk (Figure 6-9B), the mineral is distributed in small clusters with both the rosette and marquise orientations in the imaging plane. After 12 wk of implantation (Figure 6-9C-F), there is much more size variance with respect to the mineral ellipsoid distribution. The highly disordered regions in Figure 6-9C-D contain relatively large ellipsoids, that rapidly decrease in size as the distance from this domain increases, until the ellipsoidal motifs are no longer visible. Canaliculi have been shown to propagate mainly through these

confined regions of disordered collagen [65], but there has been little discussion of whether canaliculi form and propagate through regions of disordered mineral clusters as well.
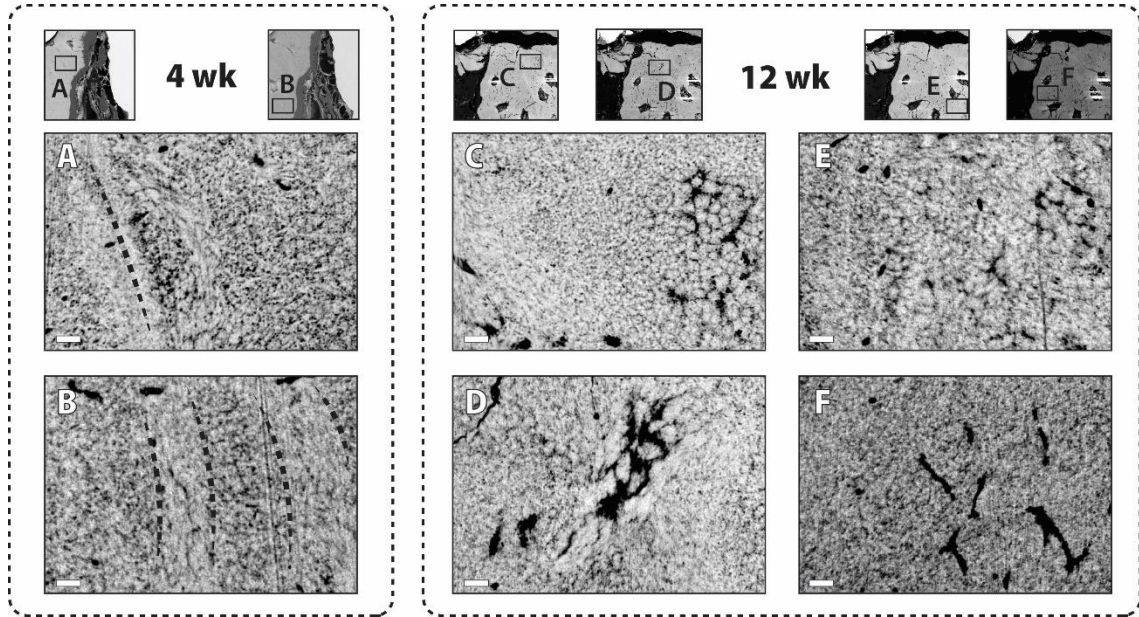
Figure 6-9: *Ellipsoidal heterogeneity near naturally-occurring interfaces and in new bone tissue. (A) Large clusters of void space or organic component are present adjacent to a hypermineralized band at 4 wk, disrupting the natural marquise or rosette patterns on either side. (B) Variation in ellipsoid orientation and organic/void distribution in the bulk of the tissue at 4 wk, separated into regions with common ellipsoid motifs. (C) The size of mineral rosettes varies widely across only a few microns and is small near where the collagen direction shifts after 12 wk. (D) Disorganized ellipsoids residing within a largely disordered organic matrix at 12 wk. (E-F) Further evidence of size variance in mineral ellipsoids within bone forming near the implant interface. Scale bars 1 µm.*

6.4 Conclusions

High-resolution 3D imaging, particularly with PFIB-SEM, affords the opportunity to image multiscale features spanning the nanoscale and microscale continuum. Mineral ellipsoids have recently been characterized in 3D but little is known about their formation and organization at the bone-implant interface. Here, PFIB-SEM tomography and HAADF-STEM are applied to newly formed leporine bone at the interface of a porous titanium implant to visualize mineral ellipsoids with heterogeneous size and orientation during osseointegration. Following retrieval of the porous titanium implants from rabbit tibiae after 12 wk, HAADF-STEM revealed a lamellar packing arrangement of mineral ellipsoids in the first few microns of the implant interface, with alternating orientation between each.

A mineral-dense band was also observed directly adjacent to the titanium in some instances. Using PFIB-SEM, a high lacunocanalicular volume fraction was observed in interfacial tissue – helping characterize the bone as newly formed. Two distinct topographies were observed at active and dormant sites in the boundary of the mineralized tissue, with a wide variety of shapes and sizes in mineral ellipsoids. In the 3D PFIB-SEM datasets, mineral is arranged into ellipsoidal shapes with a heterogeneous distribution of both size and shape throughout the newly mineralized tissue. In the bulk of the mineralized bone, this short-order heterogeneity in mineral ellipsoid morphology is also visible, with frequent changes in mineral ellipsoid orientation. These shifts in orientation could be a natural mechanism of increasing fracture toughness to prevent crack propagation and stabilize the implant during osseointegration.

Overall, the process of osseointegration occurs as a multiscale 3D process that is best characterized by 3D imaging techniques. Coupling FIB-SEM or PFIB-SEM with sample preparation techniques to highlight non-collagenous protein, organelles, or other organic components features will provide a further understanding of how osseointegration occurs and how mineral is distributed at the interface of both conventional and additively manufactured porous metallic implants.

6.5 Supplemental Figures
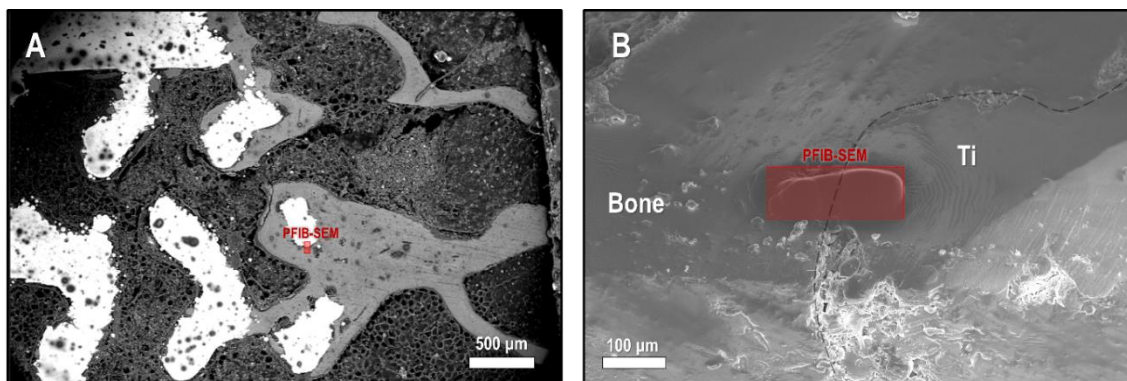
Figure S6-1: *Location of PFIB-SEM tomography in the implant retrieved after 4 wk. (A) Broad site overview. (B) Bone-implant interface with deposition of protective carbon layer for PFIB-SEM.*
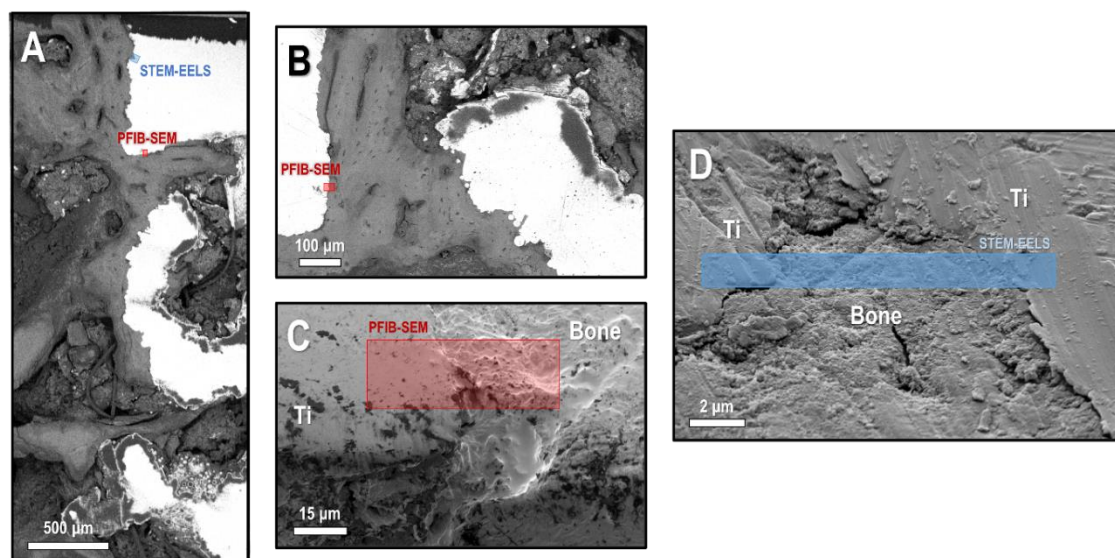
Figure S6-2: *Location of PFIB-SEM tomography and site of the FIB lift-out for STEM-EELS analysis in the implant retrieved after 12 wk. (A) Crown of the implant, showing sampling locations for STEM-EELS and PFIB-SEM. (B) Rotated inset showing bone-implant interface sampled for PFIB-SEM. (C) Higher magnification of the PFIB-SEM region. (D) Rotated inset in the crown of the implant showing location of the TEM lift-out.*

References

1. Clarke B. Normal Bone Anatomy and Physiology. Clin J Am Soc Nephro. 2008;3(Supplement 3):S131–9.

2. McKee MD, Buss DJ, Reznikov N. Mineral tessellation in bone and the stenciling principle for extracellular matrix mineralization. J Struct Biol. 2022;214(1):107823.

3. Micheletti C, Hurley A, Gourrier A, Palmquist A, Tang T, Shah FA, Grandfield K. Bone Mineral Organization at the Mesoscale: A Review of Mineral Ellipsoids in Bone and at Bone Interfaces. Acta Biomater. 2022;142:1–13.

4. Binkley DM, Deering J, Yuan H, Gourrier A, Grandfield K. Ellipsoidal mesoscale mineralization pattern in human cortical bone revealed in 3D by plasma focused ion beam serial sectioning. J Struct Biol. 2020;107615.

5. Buss DJ, Reznikov N, McKee MD. Crossfibrillar mineral tessellation in normal and Hyp mouse bone as revealed by 3D FIB-SEM microscopy. J Struct Biol. 2020;212(2):107603.

6. Steflik DE, Sisk AL, Parr GR, Gardner LK, Hanes PJ, Lake FT, Berkery DJ, Brewer P. Osteogenesis at the dental implant interface: High-voltage electron microscopic and conventional transmission electron microscopic observations. J Biomed Mater Res. 1993;27(6):791–800.

7. Linder L, Obrant K, Boivin G. Osseointegration of metallic implants: II. Transmission electron microscopy in the rabbit. Acta Orthop Scand. 1989;60(2):135–9.

8. Deering J, Grandfield K. Current interpretations on the in vivo response of bone to additively manufactured metallic porous scaffolds: A review. Biomaterials Biosyst. 2021;2:100013.

9. Han Q, Wang C, Chen H, Zhao X, Wang J. Porous Tantalum and Titanium in Orthopedics: A Review. Acs Biomater Sci Eng. 2019;5(11):5798–824.

10. Wang H, Su K, Su L, Liang P, Ji P, Wang C. The effect of 3D-printed Ti6Al4V scaffolds with various macropore structures on osteointegration and osteogenesis: A biomechanical evaluation. J Mech Behav Biomed. 2018;88(J. Mech. Behav. Biomed. Mater. 34 2014):488–96.

11. Wang X, Xu S, Zhou S, Xu W, Leary M, Choong P, Qian M, Brandt M, Xie YM. Topological design and additive manufacturing of porous metals for bone scaffolds and orthopaedic implants: A review. Biomaterials. 2016;83:127–41.

12. Choren JA, Heinrich SM, Silver-Thorn MB. Young's modulus and volume porosity relationships for additive manufacturing applications. J Mater Sci. 2013;48(15):5103–12.

13. Huiskes R, Weinans H, Rietbergen B van. The Relationship Between Stress Shielding and Bone Resorption Around Total Hip Stems and the Effects of Flexible Materials. Clin Orthop Relat R. 1992;274(NA;):124–34.

14. Bencharit S, Byrd WC, Altarawneh S, Hosseini B, Leong A, Reside G, Morelli T, Offenbacher S. Development and Applications of Porous Tantalum Trabecular Metal-Enhanced Titanium Dental Implants. Clin Implant Dent R. 2014;16:817–26.

15. Branemark PI. Osseointegration and its experimental background. J Prosthet Dent. 1983;50(3):399–410.

16. Chang P, Lang NP, Giannobile WV. Evaluation of functional dynamics during osseointegration and regeneration associated with oral implants. Clin Oral Implan Res. 2010;21(1):1–12.

17. Sennerby L, Thomsen P, Ericson LE. Early tissue response to titanium implants inserted in rabbit cortical bone. J Mater Sci Mater Medicine. 1993;4(3):240–50.

18. Bosshardt DD, Chappuis V, Buser D. Osseointegration of titanium, titanium alloy and zirconia dental implants: current knowledge and open questions. Periodontol 2000. 2017;73(1):22–40.

19. Shah FA, Thomsen P, Palmquist A. Osseointegration and current interpretations of the bone-implant interface. Acta Biomater. 2018;84:1–15.

20. Nanci A. Content and Distribution of Noncollagenous Matrix Proteins in Bone and Cementum: Relationship to Speed of Formation and Collagen Packing Density. J Struct Biol. 1999;126(3):256–69.

21. McKee MD, Nanci A. Osteopontin at mineralized tissue interfaces in bone, teeth, and osseointegrated implants: Ultrastructural distribution and implications for mineralized tissue formation, turnover, and repair. Microsc Res Techniq. 1996;33(2):141–64.

22. Davies JE, Baldan N. Scanning electron microscopy of the bone-bioactive implant interface. J Biomed Mater Res. 1997;36(4):429–40.

23. Wang X, Langelier B, Shah FA, Korinek A, Bugnet M, Hitchcock AP, Palmquist A, Grandfield K. Biomineralization at Titanium Revealed by Correlative 4D Tomographic and Spectroscopic Methods. Adv Mater Interfaces. 2018;5(14):1800262.

24. Steflik DE, Corpe RS, Lake FT, Young TR, Sisk AL, Parr GR, Hanes PJ, Berkery DJ. Ultrastructural analyses of the attachment (bonding) zone between bone and implanted biomaterials. J Biomed Mater Res. 1998;39(4):611–20.

25. Giannuzzi LA, Phifer D, Giannuzzi NJ, Capuano MJ. Two-Dimensional and 3-Dimensional Analysis of Bone/Dental Implant Interfaces With the Use of Focused Ion Beam and Electron Microscopy. J Oral Maxil Surg. 2007;65(4):737–47.

26. Palmquist A. A multiscale analytical approach to evaluate osseointegration. J Mater Sci Mater Medicine. 2018;29(5):60.

27. Grandfield K, McNally EA, Palmquist A, Botton GA, Thomsen P, Engqvist H. Visualizing biointerfaces in three dimensions: electron tomography of the bone–hydroxyapatite interface. J Roy Soc Interface. 2010;7(51):1497–501.

28. Grandfield K, Palmquist A, Engqvist H. High-resolution three-dimensional probes of biomaterials and their interfaces. Philosophical Transactions Royal Soc Math Phys Eng Sci. 2012;370(1963):1337–51.

29. Grandfield K, Palmquist A, Engqvist H. Three-dimensional structure of laser-modified Ti6Al4V and bone interface revealed with STEM tomography. Ultramicroscopy. 2013;127:48–52.

30. Wang X, Shah FA, Palmquist A, Grandfield K. 3D Characterization of Human Nano-osseointegration by On-Axis Electron Tomography without the Missing Wedge. Acs Biomater Sci Eng. 2017;3(1):49–55.

31. Micheletti C, Gomes-Ferreira PHS, Casagrande T, Lisboa-Filho PN, Okamoto R, Grandfield K. From tissue retrieval to electron tomography: nanoscale characterization of the interface between bone and bioactive glass. J Roy Soc Interface. 2021;18(182):20210181.

32. Landis WJ, Song MJ, Leith A, McEwen L, McEwen BF. Mineral and Organic Matrix Interaction in Normally Calcifying Tendon Visualized in Three Dimensions by High-Voltage Electron Microscopic Tomography and Graphic Image Reconstruction. J Struct Biol. 1993;110(1):39–54.

33. Grandfield K, Vuong V, Schwarcz HP. Ultrastructure of Bone: Hierarchical Features from Nanometer to Micrometer Scale Revealed in Focused Ion Beam Sections in the TEM. Calcified Tissue Int. 2018;103(6):606–16.

34. Reznikov N, Bilton M, Lari L, Stevens MM, Kröger R. Fractal-like hierarchical organization of bone begins at the nanoscale. Science. 2018;360(6388):eaao2189.

35. Reznikov N, Shahar R, Weiner S. Bone hierarchical structure in three dimensions. Acta Biomater. 2014;10(9):3815–26.

36. Puleo DA, Nanci A. Understanding and controlling the bone–implant interface. Biomaterials. 1999;20(23–24):2311–21.

37. Davies JE. Bone bonding at natural and biomaterial surfaces. Biomaterials. 2007;28(34):5058–67.

38. Burnett TL, Kelley R, Winiarski B, Contreras L, Daly M, Gholinia A, Burke MG, Withers PJ. Large volume serial section tomography by Xe Plasma FIB dual beam microscopy. Ultramicroscopy. 2016;161:119–29.

39. Yu B, Pacureanu A, Olivier C, Cloetens P, Peyrin F. Assessment of the human bone lacuno-canalicular network at the nanoscale and impact of spatial resolution. Sci Rep-uk. 2020;10(1):4567.

40. Shah FA, Snis A, Matic A, Thomsen P, Palmquist A. 3D printed Ti6Al4V implant surface promotes bone maturation and retains a higher density of less aged osteocytes at the bone-implant interface. Acta Biomater. 2016;30(Biomaterials 27 2006):357–67.

41. Mori S, Harruff R, Ambrosius W, Burr DB. Trabecular bone volume and microdamage accumulation in the femoral heads of women with and without femoral neck fractures. Bone. 1997;21(6):521–6.

42. Vashishth D, Verborgt O, Divine G, Schaffler MB, Fyhrie DP. Decline in osteocyte lacunar density in human cortical bone is associated with accumulation of microcracks with age. Bone. 2000;26(4):375–80.

43. Hasegawa T, Yamamoto T, Hongo H, Qiu Z, Abe M, Kanesaki T, Tanaka K, Endo T, Freitas PHL de, Li M, Amizuka N. Three-dimensional ultrastructure of osteocytes assessed by focused ion beam-scanning electron microscopy (FIB-SEM). Histochem Cell Biol. 2018;149(4):423–32.

44. Shah FA, Thomsen P, Palmquist A. A Review of the Impact of Implant Biomaterials on Osteocytes. J Dent Res. 2018;97(9):977–86.

45. Nango N, Kubota S, Hasegawa T, Yashiro W, Momose A, Matsuo K. Osteocyte-directed bone demineralization along canaliculi. Bone. 2016;84:279–88.

46. Gardinier JD, Al-Omaishi S, Morris MD, Kohn DH. PTH signaling mediates perilacunar remodeling during exercise. Matrix Biol. 2016;52:162–75.

47. Yee CS, Schurman CA, White CR, Alliston T. Investigating Osteocytic Perilacunar/Canalicular Remodeling. Curr Osteoporos Rep. 2019;17(4):157–68.

48. Schertel A, Snaidero N, Han HM, Ruhwedel T, Laue M, Grabenbauer M, Möbius W. Cryo FIB-SEM: Volume imaging of cellular ultrastructure in native frozen specimens. J Struct Biol. 2013;184(2):355–60.

49. Landis WJ, Glimcher MJ. Electron diffraction and electron probe microanalysis of the mineral phase of bone tissue prepared by anhydrous techniques. J Ultra Mol Struct R. 1978;63(2):188–223.

50. Boonrungsiman S, Gentleman E, Carzaniga R, Evans ND, McComb DW, Porter AE, Stevens MM. The role of intracellular calcium phosphate in osteoblast-mediated bone apatite formation. Proc National Acad Sci. 2012;109(35):14170–5.

51. Imai K, Neuman MW, Kawase T, Saito S. Calcium in osteoblast-enriched bone cells. Bone. 1992;13(3):217–23.

52. Horvath SE, Daum G. Lipids of mitochondria. Prog Lipid Res. 2013;52(4):590–614.

53. Dallas SL, Prideaux M, Bonewald LF. The Osteocyte: An Endocrine Cell … and More. Endocr Rev. 2013;34(5):658–90.

54. Franz-Odendaal TA, Hall BK, Witten PE. Buried alive: How osteoblasts become osteocytes. Dev Dynam. 2006;235(1):176–90.

55. Miller SC, Saint-Georges L de, Bowman BM, Jee WS. Bone lining cells: structure and function. Scanning Microscopy. 1989;3(3):953–60; discussion 960-1.

56. Chissoe WF, Vezey EL, Skvarla JJ. The Use of Osmium-Thiocarbohydrazide for Structural Stabilization and Enhancement of Secondary Electron Images in Scanning Electron Microscopy of Pollen. Grana. 1995;34(5):317–24.

57. Boyde A, Sela J. Scanning electron microscope study of separated calcospherites from the matrices of different mineralizing systems. Calc Tiss Res. 1978;26(1):47–9.

58. Midura RJ, Vasanji A, Su X, Wang A, Midura SB, Gorski JP. Calcospherulites isolated from the mineralization front of bone induce the mineralization of type I collagen. Bone. 2007;41(6):1005–16.

59. Shah FA, Jolic M, Micheletti C, Omar O, Norlindh B, Emanuelsson L, Engqvist H, Engstrand T, Palmquist A, Thomsen P. Bone without borders – Monetite-based calcium phosphate guides bone formation beyond the skeletal envelope. Bioact Mater. 2022;19:103–14.

60. Shah FA, Ruscsák K, Palmquist A. Transformation of bone mineral morphology: From discrete marquise-shaped motifs to a continuous interwoven mesh. Bone Reports. 2020;13:100283.

61. Giraud-Guille MM. Twisted plywood architecture of collagen fibrils in human compact bone osteons. Calcified Tissue Int. 1988;42(3):167–80.

62. Bouligand Y. Twisted fibrous arrangements in biological materials and cholesteric mesophases. Tissue Cell. 1972;4(2):189–217.

63. Suksangpanya N, Yaraghi NA, Kisailus D, Zavattieri P. Twisting cracks in Bouligand structures. J Mech Behav Biomed. 2017;76:38–57.

64. Raguin E, Rechav K, Shahar R, Weiner S. Focused ion beam-SEM 3D analysis of mineralized osteonal bone: lamellae and cement sheath structures. Acta Biomater. 2021;121:497–513.

65. Reznikov N, Shahar R, Weiner S. Three-dimensional structure of human lamellar bone: The presence of two different materials and new insights into the hierarchical organization. Bone. 2014;59:93–104.

Chapter 7: Conclusions and Future Work

Developing new implant designs with the aim to improve osseointegration encompasses a multi-step workflow to understand multiscale bone apposition. The sequential *design*, *modification*, and *characterization* workflows presented in this thesis are pivotal for characterizing osseointegration to further improve commercially available implant materials. As additive manufacturing technology is still being optimized for implant design and development, the main findings here present important considerations for their short-term and long-term success. In this thesis, I develop new methods to design implants, use both *in vitro* and *in vivo* methods to examine their performance, and image with optical and electron microscopies to examine bone structure during osseointegration.

Key Findings and Contributions

In this thesis, a diverse but complementary range of techniques is used to characterize strategies and outcomes relating to the use of porous implants. The workflow used here aids in the research and development of implant materials in many different stages of their production and post-processing. Our current understanding of porous implants and the bone-implant interface is improved based on the use of my bio-inspired modifications to a 3D Voronoi tessellation for implant design, succinate-based coatings for surface modification, and multimodal investigation of tissue, cellular, and mineral response at the implant interface.

(i) Use of Voronoi tessellation to tune isotropy in porous AM materials

In Chapter 3, I first present a new technique to mimic the naturally anisotropic structure of bone. The restriction of Voronoi seeding to user-defined planes within the bounding volume modifies the volume into which the polyhedra can expand. Adjusting seed density within these planes creates an interconnected strut architecture that can mimic trabecular bone in a number of anatomical sites by using similar distributions of the inter-trabecular angle. The seed density within the planes does not appear to greatly change the intertrabecular angle but instead elongates struts in a direction controlled by the user. This form of *implant design* creates structures compatible with metallic additive manufacturing and can be tailored for specialized cases where patient-specific implants are required.

With respect to next steps, the 3D asymmetrical Voronoi tessellation can be improved by finding methods to introduce concavity in the unit cells, as this pattern is sometimes observed in trabecular bone. Additionally, the current model can be extended to more complex geometries, following contoured paths of varying seed density or with further modification of the workflow to implement anisotropy-graded implants to truly mimic regions of trabecular bone.

(ii) Elution of succinate to promote biological activity at the implant interface

In Chapter 4, I present a synthesis technique to create biocompatible implant coatings. Encapsulating disodium succinate within an alginate matrix creates a rapidly-releasing surface film to interact with early progenitors at the implant interface. Based on the molecular size of the succinate and its transport properties through the alginate xerogel, rehydration releases 95% of the functionalized succinate within the first 7 hr and transforms the surface topography from a cobblestone appearance to an intermittently-wrinkled one. Compatible with osteoblasts and encouraging coarsening behaviour in endothelial tubes, this work provides proof of concept for *surface modification* that can be extended to additively manufactured implants.

While not explicitly reported in this thesis, pilot studies demonstrate that these films easily adhere to titanium surfaces but their ability to follow a complex pore network has yet to be shown. Further characterization of these films can measure the carrying capacity of the endothelial network to corroborate my observations of tube widening, *in vitro* stabilization of the tube network with mural cell co-culture, conversion rates of excess intracellular succinate to fumarate via the Krebs cycle, or *in vivo* application of the films on porous metallic scaffolds to expedite vascular ingrowth in the pores.

(iii) Similarities to the classical wound healing response inside the pore network

In Chapter 5, I show that the *in vivo* wound healing response can occur both inside and outside of additively manufactured porous implants through *characterization*, and that pore size is an important factor within porous gyroids when it comes to osseointegration. After four weeks, evidence of early bone formation occurs at the scaffold exterior, neovessels infiltrate the scaffold interior, and some residual inflammation remains at the defect site. After twelve weeks, myeloid and bone tissue infiltrates the scaffold interior alongside the vascular network and mineralization continues as noted via fluorochrome analysis. Functionally-graded implants with an exterior pore size of 600 μm and an interior pore size of 300 μm have lower bone-implant contact and lower bone volume fractions after twelve weeks in rabbit tibiae compared to implants with pores sized uniformly at 300 μm. Where functional grading of pore size in Chapter 5 did not necessarily improve outcomes with respect to bone apposition in this specific instance, this study helps define baseline metrics that can be used to assess other forms of functional grading (including anisotropy gradients as in Chapter 3, multi-material additive manufacturing, or other pore size distributions).

Possible avenues for future work include the inversion of functional grading, where smaller pores appear at the scaffold exterior and larger pores appear in the scaffold interior. It may also be worthwhile to reduce pore size further to determine if there is a pore size threshold where the combination of bone, vascular tissue, and myeloid tissue ceases to appear inside. It also remains to be seen if this trend persists in different pre-clinical animal models, as there are inherent differences in bone structure and bone apposition rate across species.

(iv) Microscopic heterogeneity of mineral ellipsoids at the implant interface

In Chapter 6, I use high-resolution imaging of the bone-implant interface to *characterize* mineral arrangement in 2D and 3D. This work is the first to use PFIB-SEM to examine the implant interface in 3D and offers insight into bone structure during the process of osseointegration. Mineral ellipsoids, nucleating at the mineralization front with a variety of morphologies, are dispersed throughout the tissue in a heterogeneous fashion with respect to their size and orientation. Misoriented packets of these mineral ellipsoids at the implant interface resolve with increasing distance from the implant itself, where a twisting morphology of collagen and mineral may provide strengthening as a Bouligand structure.

If this arrangement does indeed strengthen the tissue, we can potentially modify implant surfaces to encourage this form of twisted mineral structure by physical or chemical means. Finally, the development of intravital microscopy techniques is required to fully understand the nucleation, growth, and eventual packing arrangement of these mineral ellipsoids in newly formed bone tissue.

Appendix 1: Current Interpretations on the In Vivo Response of Bone to Additively Manufactured Metallic Porous Scaffolds: A Review

This paper is a summary of the current literature on the osseointegration and pre-clinical work relating to additively manufactured porous materials. The literature was surveyed to find common trends with respect to implant design including materials, pore size, and net porosity of the scaffold. Studies of osseointegration in leporine bone using additively manufactured titanium alloys tend to be most common. Pore sizes ranging from 300-500 μm and a porosity range of 50-70% often result in the most favourable form of bone regeneration, although it is important to note the dependency on pre-clinical model for bone formation and that these may not directly translate to human bone. These findings are complementary to the production of any porous metallic scaffold for bone-interfacing materials and help frame the study design for the pre-clinical studies spanning Chapter 5 and Chapter 6.

Permission for reprint has been provided by Elsevier, with the full article available at https://doi.org/10.1016/j.bbiosy.2021.100013.

Current interpretations on the *in vivo* response of bone to additively manufactured metallic porous scaffolds: A review

Joseph Deering [a], Kathryn Grandfield [a,b,*]

[a] *Department of Materials Science and Engineering, McMaster University, Hamilton, ON, Canada*
[b] *School of Biomedical Engineering, McMaster University, Hamilton, ON, Canada*

A R T I C L E   I N F O

A B S T R A C T

Recent advances in the field of metallic additive manufacturing have expanded production capabilities for bone implants to include porous lattice structures. While traditional models of *de novo* bone formation can be applied to fully dense implant materials, their applicability to the interior of porous materials has not been well-characterized. Unlike other reviews that focus on materials and mechanical properties of lattice structures, this review compiles biological performance from *in vivo* studies in pre-clinical models only. First, we introduce the most common lattice geometry designs employed *in vivo* and discuss some of their fabrication advantages and limitations. Then lattice geometry is correlated to quantitative (histomorphometric) and qualitative (histological) assessments of osseointegration. We group studies according to two common implant variables: pore size and percent porosity, and explore the extent of osseointegration using common measures, including bone-implant contact (BIC), bone area (BA), bone volume/total volume (BV/TV) and biomechanical stability, for various animal models and implantation times. Based on this, trends related to *in vivo* bone formation on the interior of lattice structures are presented. Common challenges with lattice structures are highlighted, including nonuniformity of bone growth through the entirety of the lattice structure due to occlusion effects and avascularity. This review paper identifies a lack of systematic *in vivo* studies on porous AM implants to target optimum geometric design, including pore shape, size, and percent porosity in controlled animal models and critical-sized defects. Further work focusing on surface modification strategies and systematic geometric studies to homogenize *in vivo* bone growth through the scaffold interior are recommended to increase implant stability in the early stages of osseointegration.

Scaffold Design and Fabrication

Introduction

Metallic additive manufacturing (AM) processes are beginning to see increased usage in the world of bone implants, especially for dental and orthopaedic implants, due to their ability to fabricate complex geometries, particularly porous lattice structures. The ability to produce porous implants presents two main advantages for this field. Firstly, it presents the potential for improvement in osseointegration – a long-term structural and functional connection between bone and implant – enabled by the complex pore system that provides superior mechanical interlocking effects. Early-stage osteoconduction – the process where bone conforms to a surface or biomaterial [1] – depends heavily on the design of the scaffold geometry, including pore size and shape. Secondly, where load-bearing implants may suffer from stress shielding, onset by increased bone resorption rates in the presence of high elastic modulus

metallic implants [2], porous metallic structures can lead to an effective stiffness reduction mechanism by intentionally introducing porosity to implant geometries. Generally, reduction in stiffness responds by an exponential or power relationship as porosity increases [3,4] due to a change in the second moment of area [3]. Towards the same effort, novel alloys with high niobium and zirconium content have been developed [5–9] to reduce the elastic moduli of titanium materials by changing the bonding structure and phase stability while maintaining biocompatibility and ease of processing with AM [10]. As the benchmark material for traditional implants, alloys of titanium often have elastic moduli in the range of 55–117 GPa, which can be reduced to the range of cortical bone (3–20 GPa) by intentional introduction of porosity [11]. Conventional biomaterial alloys with high elastic moduli, such as stainless steel or CoCr (both on the order of 200 GPa), can also make use of AM methodologies to create lattice structures to similarly reduce implant stiffness into the range of cortical bone without sacrificing their inherent biocompatibility [12,13].

Previous reviews on the usage and development of porous metallic materials have predominantly focused on broad development of these materials, including materials selection [14,15], design considerations

[16–18], surface modification [16,17], and mechanical properties [17], with only superficial investigation of the resulting bone structure from a biological perspective following implant retrieval. In a review from Weber, special consideration has been given to bone formation along porous structures to introduce the importance of design factors in relation to osteogenesis [19]. However, to optimize lattice conditions for bone ingrowth in humans, a comprehensive review of pre-clinical *in vivo* models is first needed to evaluate how these porous implants behave in various animals. In this evaluation, one must consider the effect of the lattice geometry on materials and mechanical properties, the limitations of particular printing methods, and most importantly their corresponding influence on osseointegration and osteoconduction. In the following sections we present a brief summary of printing methods prior to the ultimate focus of this work: understanding the biological effects of these implant geometries on bone tissue, as summarized using quantitative measures from histomorphometry and qualitative histological observations.

AM Fabrication Techniques for Porous Metallic Implants Studied In Vivo

Several AM methods exist for the production of porous metallic scaffolds in bone applications. Where comprehensive outlines of each AM process exist in the literature for metal fabrication [20–22], here we briefly describe the relevant scope and limitations for the most common types of AM processes.

The most common forms of powder bed processes include selective laser sintering (SLS), selective laser melting (SLM), direct metal laser sintering (DMLS), and electron beam melting (EBM). The minimum size for an SLM part is dependent on factors such as powder absorptivity [23], but the stability of the molten pool has been observed to decrease as the energy density increases [24]. This can result in material ejection from the melt pool [25] and a part that is susceptible to defects [26]. The production of porous materials also requires overhanging components. As the strut angle deviates further from the normal in powder bed processes, there is a marked decrease in geometric accuracy of the part [27]. An investigation of this phenomenon in EBM and SLM materials has shown that deviations up to 10% can occur and that this effect is more pronounced in EBM materials [28]. These factors along with the commercial availability of powders and energy source optics mean that the minimum size of stable struts in a porous material is restricted to roughly 200 μm.

Directed energy deposition alternatives to powder bed methods include laser engineered net shaping (LENS®), direct metal deposition (DMD), and laser metal deposition. Analysis of LENS parts has shown that substantial residual stresses can accumulate due to their thermal history [29,30]. Without further post-processing, these stresses can cause complications including premature part failure. Directed energy deposition methods are also classified to have lower resolution, low-quality surface finishes, and the inability to produce complex geometries compared to powder bed processes [31]. The lower accuracy of DED processes further restricts the minimum strut size and accessible geometries compared to what is available in powder bed techniques. Of the papers surveyed in this review, nearly 98% of porous implants for in vivo studies were produced by powder-bed techniques (78% SLM, 12% EBM, 5% SLS, 3% DMLS), while only 2% were produced by DED or laser engineered net shaping. The dominant reason for this likely pertains to ease of manufacturing and equipment abundance rather than *in vivo* response.

Most porous metallic structures for *in vivo* implantation focus on traditional implant materials. Commercially pure titanium and Ti-6Al-4V have extensively been used in the literature for animal studies due to their well-defined processing parameters in SLM, but novel biocompatible alloys containing niobium, tantalum and zirconium are also being developed [32–35]. The addition of *β*-stabilizing elements in titanium should mitigate some stress-shielding effects [36] to further modify a porous structure's osseointegration potential. Many of these novel alloys

have not yet been implemented in porous structures for testing in pre-clinical trials. Almost all of the AM implant materials studied *in vivo* in this review were commercially pure titanium (44%) or Ti-6Al-4V (53%), with materials such as tantalum or iron-manganese composing the remaining 3%. Other materials including NiTi [37,38], polyamide [39], and stainless steel [40] have been used for porous implants, but not using metallic AM.

Another common observation of as-fabricated parts is the anisotropic response that has been documented thoroughly by Kok et al. for additively manufactured materials [41]. Factors such as build orientation and thermal cycling prominently influence the grain structure and mechanical properties, causing heterogeneity in parts produced through powder bed and directed energy deposition processes. However, anisotropy as related to biological response is substantially harder to evaluate and will not be included in this review.

Types of Porous Implant Structures

A diverse range of lattice geometries can be designed for implant structures. In this work, these are categorized based on their topology/structure into reticulated, stochastic, functionally-graded, or other forms (Fig. 1). While the reticulated form is most commonly observed in the literature due to their simple design, there is a growing number of studies that also investigate more complex stochastic lattice geometries. The precise deformation behaviour and mechanical characteristics are dependent on this base structure, where most cellular solids display a simplified three-stage progression of linear elasticity, stress plateauing, and densification [42].

Reticulated lattices describe a unit cell geometry that repeats precisely through the entirety of the structure. Frequently termed 'regular' or 'repeated' lattices, these structures offer tunable isotropic properties. These are the most common form of lattice in the literature for bone implants and include several geometries such as tetrahedral, octahedral, dodecahedral, or cubic [43]. Since implant stiffness has a geometric dependency, the unit cell strut orientation and porosity have a great impact on mechanical response. Diamond and rhombic dodecahedral lattices, for example, have been shown to have a lower stiffness than other simple cellular structures but are not able to withstand as much compressive load [44].

Triply-periodic minimal surface (TPMS) unit cells are a subset of reticulated lattices that are becoming increasingly common in the literature. Skeletal or sheet TPMS cells are free from self-intersections and locally minimize surface area by implementing zero mean curvature within the unit cell [45]. Cell migration by durotaxis and the permeable nature of a TPMS geometry suggests that cell migration occurs easier on lattices formed with this zero-mean curvature [46]. In terms of mechanical characterization, TPMS geometries display adequate fatigue properties [47] and have low stiffness while maintaining reasonable peak stress values [48]. Common TPMS geometries include Schwarz diamond, Schwarz primitive, Schwarz gyroid, and Schoen's wrapped package (I-WP) surface (Fig. 2). TPMS geometries are in the early stages of exploration for *in vivo* implant applications, where Schwarz primitive structures have been modified to become functionally graded and have been successfully implanted in pigs [49].

Stochastic lattices, also termed 'irregular' or 'trabecular' lattices, have no defined unit cell that repeats through the structure of the lattice. Stochastic lattices typically used biomimicry-derived principles to simulate a trabecular bone structure within the implant geometry. One production method is to analytically-derive struts from a three-dimensional Voronoi tessellation where the porosity and strut thickness can be controlled by the number of seeds and scaling factor [51]. A stochastic lattice geometry can be generated using the Voronoi technique that follows the natural pattern of trabecular bone [52]. Interestingly, the effect of structure on mechanical properties of these trabecular lattices mimics what is seen in trabecular bone [53,127]. A reduction in strut frequency has a much greater effect on mechanical properties than a comparable
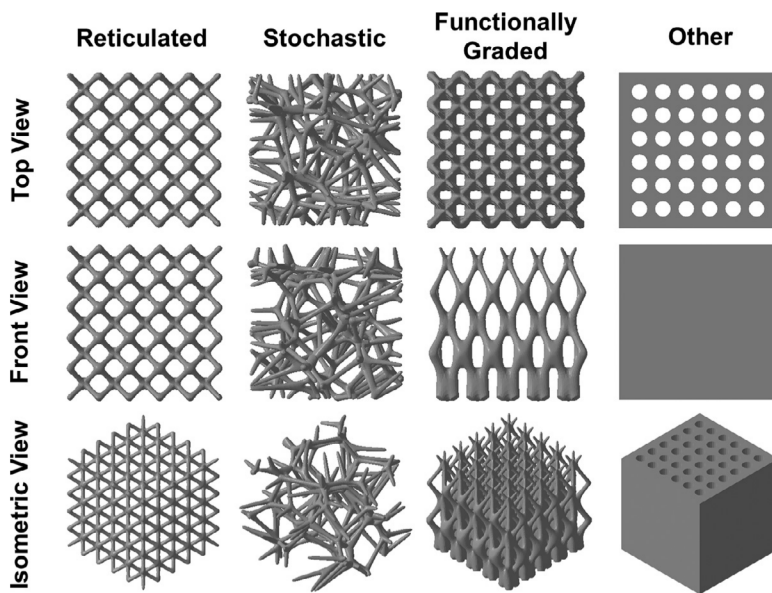
Fig. 1. Examples of reticulated, stochastic, functionally-graded, and other porous lattice structures over a short range of unit cells. Reticulated structures have a repeating structure in three directions. Stochastic geometries have no repeating short-order geometry. Functionally-graded and other porous lattices usually have an ordered structure in at least one-direction but have varying properties in one or more directions.
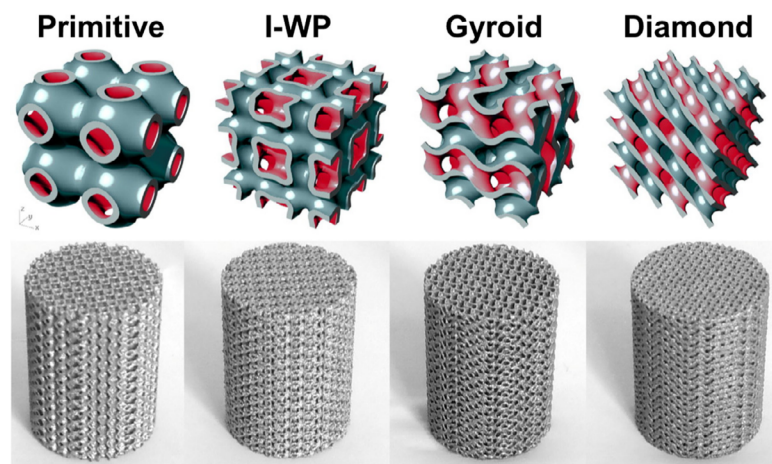
Fig. 2. Examples of primitive, I-WP, gyroid, and diamond TPMS lattice structures. These fall under the subset of reticulated lattice. Only recently have TPMS lattices been studied for in vivo bone applications. Adapted from reference [50] with permission from Elsevier (Copyright 2017).

porosity increase by reduction of strut thickness [53], where buckling of individual struts in transverse loading becomes more likely as the distance between strut intersections increases. In addition, when designing these lattices, it is important to consider the seed density and three-dimensional isotropy of the base polyhedra to account for bending stresses *in vivo*. Stochastic lattices may have much more unpredictable short-order response *in vivo* compared to reticulated lattice structures but the random directional properties for a truly stochastic lattice should average out for larger implants.

Porous foams can also be classified as stochastic lattices due to their lack of regular patterning in the interior of highly porous open-cell specimens. While technically a form of traditional powder metallurgy rather than AM [54], it is also important to briefly consider the response of stochastic foam-like geometries for osseointegration and osteoconduction due to their similarity to other stochastic implants. Due to the rearrangement of the space holder particles during fabrication, these stochastic foams typically have an anisotropic mechanical response [55]. The investigation and processing of porous forms as implant materials is a vast field, and readers interested in this topic are referred elsewhere for more information [56–58].

The problem with classification into reticulated and stochastic structures is the subset of implants that does not fall into either category. Implants with a spatial variation in some property, such as material composition, microstructure, or pore size, constitute an important class

known as functionally-graded materials. Functional grading is easily implemented into additive manufacturing processes by modifying the geometry of the CAD model [59], changing processing parameters at different layers during a build, or by changing the composition of the feedstock powder over the course of a build [60]. Since their properties are not the same in the three principal directions but they still have a consistent repeating component, they cannot be classified as either reticulated or stochastic architectures. The weakest point in a functionally-graded material, typically the region with the highest porosity [61], in uniform mechanical loading ultimately dictates the strength of the entire structure. When adapted to complex loads in the body, these emergent types of porous implants may offer the potential to mitigate stress shielding, offer selective bioactivity, and adapt to changes in macroscale bone geometry [62].

Other forms of porous architecture cannot be classified into reticulated or stochastic structures. Micromachined porous channels, for example, lack the 3D repeatability and true randomness of reticulated and stochastic structures, respectively. This type of geometry is often seen in early investigations of porous materials for osteoconduction [63] but are becoming less common as additive manufacturing technologies advance. These other forms of additively manufactured lattice structure (Fig. 1, last column) are inclusive to any geometry that cannot be classified as reticulated, stochastic, or functionally-graded.
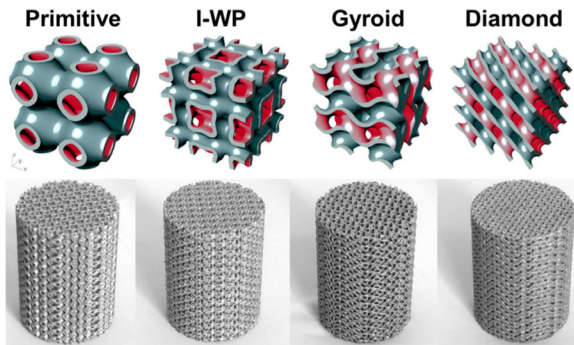
Fig. 3. Influence of unit cell size and strut size on pore size and porosity for a reticulated lattice structure. Increasing unit cell size with a constant strut size results in a more porous structure with larger pores. Increasing strut size with a constant unit cell size results in a denser structure with smaller pores.

Unit Cell Modulation

Many geometric adaptations of porous implants are possible. Two factors that govern the pore distribution through the implant are the strut thickness and the size of the representative unit cell, for which progressive variations are shown in Fig. 3 for a reticulated lattice. With a constant unit cell size, increasing the strut size results in a smaller final pore size (all columns, Fig. 3). However, increasing the unit cell size while keeping strut size constant results in a larger pore size (all rows, Fig. 3). The appearance of pore shape is also dependent on these factors, where pores can appear more rounded in some instances (e.g. the bottom row, middle column, Fig. 3).

Models to predict the global mechanical response of some porous implant structures and their associated manufacturing consistency have been systematically investigated [64] to create a design space for tailoring mechanical properties based on the adjustment of strut size and pore size. This information will prove valuable for adjusting design parameters to best match a given anatomical site as more histomorphometric measurements are collected for different pore structures. Where variation in AM processing parameters can also affect the mechanical properties of the implant [65], it may indeed be difficult to isolate mechanical contributions from processing parameters and topological design in process-structure-property relationships. Currently, the precise correlation between strut size, pore size, *in vivo* histology, and *in vivo* histomorphometry has not been defined to definitively declare 'optimum' design parameters for any given clinical or pre-clinical anatomical site. In the papers reviewed in this work, this variability is clear where pore sizes ranged from 50 μm [63] to 1200 μm [66], strut thickness varied from 120 μm [67] to 800 μm [68], and percent porosity ranged from 30% [69] to 83.5% [70].

Geometric factors in a lattice including pore size, net porosity, and strut size can also contribute significantly to the microfluidics for implants in an *in vivo* environment. Bone has a naturally porous network for molecular transport of waste, oxygen, and nutrients [71]. Impairment of this vascular network in bone tissue has been shown to decrease both bone volume fractions and the presence of osteogenic markers [72]. A comparable transport pathway exists as the interconnected pore network of some metallic implants. Work from Warnke et al., for example, has found that *in vitro* culture of osteoblasts can occlude a 450 μm pore

after just three weeks of culture. Yet it is important to highlight that *in vitro* culture is not always a predictor of *in vivo* performance [73].The design of the scaffold unit cell in a porous structure is therefore important in ways other than just long-term mechanical consideration. The influence of pore architecture on microfluidics in early-stage osteogenesis and angiogenesis for bone tissue repair should be considered for implant design, especially where predictive tools have been developed in the literature [74]. As will become evident later in this review, certain pore structures can become occluded on their periphery as a result of their topology.

***In Vivo* Response to AM Metallic Implants**

Commonly Used Animal Models

Due to differences in animal physiology and biomechanics, accurate comparison of *in vivo* osseointegration can be difficult. Threshold strains for periosteal osteogenesis have been shown to differ within a similar anatomical location in a murine model [75], and careful surgical procedures and post-operative management is requisite for intraspecies comparisons of osteogenic data [76]. Critical-sized defects (CSDs) have been standardized as a metric for evaluating *in vivo* osseointegration and are defined as the size of an intraosseous wound that will not spontaneously heal over the lifetime of the animal [77]. CSDs for murine, leporine, canine, caprine, and ovine models have been standardized for some select anatomical locations and observation periods in ASTM F2721, but there is much debate on appropriate sizing for CSDs [78]. For murine femora, the CSD ranges from 5–10 mm with typical study endpoints between 8–24 weeks [79]. Ulnar and radial CSDs in leporine bone are defined at 20 mm, with an endpoint of 8–12 weeks [79]. CSDs in canine radii, ulnae, and femora are slightly larger at 21–25 mm with a longer recommended endpoint of 12–24 weeks [79]. CSDs in the tibia of caprine bone should be 26–35 mm, or 25–50 mm in the tibia and metatarsus of ovine bone [79]. For these two models, endpoints should be set at 26 weeks or 16–24 weeks, respectively [79].

Reviews covering the benefits and bone structure of murine, leporine, porcine, and ovine pre-clinical models [80] along with the appropriate defect sizes for several anatomical sites in each model have been done previously [81]. The animal model governs the implant size, which can be especially important in porous AM materials as observation of bone growth into the depth of the implant is reliant on sampling of several sites throughout a single implant. Implants for smaller mammals will naturally contain fewer pores due to the fabrication limits of most AM processes, making systematic sampling more limited. An implant with a pore size of 500 μm and strut size of 250 μm in a critical-sized rat tibial defect, for example, may only have ten pores across its maximum diameter. Where the goal of pre-clinical studies is to predict how implants might behave in humans, measurements of bone homogeneity, penetration depth, and maturity in a porous implant are limited in their translational capability when considering larger implant sizes in humans.

The selection of pre-clinical animal model is important when considering osseointegration and early osteoconduction since the microscopic bone structure is species-dependent [80] and can therefore differ considerably at different time points. Herein, we will comment on the effect of various lattice structures on the extent of both osseointegration and bone maturity in several pre-clinical models, including the rabbit tibia, rabbit femur, rabbit cranium, goat/sheep metatarsus, pig cranium, and canine dorsal muscle. It is important to note that because of the aforementioned biological differences, a direct comparison of quantitative histomorphometry between species is not suitable.

Observations from Histological Evaluations

At the tissue level, early bone apposition resembles woven bone, where randomly oriented collagen fibrils form during rapid bone mod-

eling [82]. It is also possible to form fibrolamellar bone under rapid growth conditions in fast-growing mammals, birds, or sauropods, where bone is subjected to substantial load [83,84]. This fibrolamellar bone has a unidirectional collagenous orientation but is still mechanically weak relative to more mature, remodelled bone. Finally, after remodelling, lamellar bone has a fixed structure of alternating lamellae, where the orientation of the lamellae alternates between sublayers [85]. This results in a mechanically mature form of bone *in vivo*. The transition from nascent to mature bone typically has both a strain-dependency [86] and time-dependency as cytokines are expressed differently throughout the remodeling stages [87,88].

Most bone implants are evaluated by histological analyses. Various stains enable an understanding of the biological response to an implant, including the inflammatory response and most importantly the quality of the bone apposition around and within the scaffold. Here, we address some common histological interpretations of bone quality with respect to lattice structures, including fibrous encapsulation, the strain-dependency of osseointegration, bone formation within scaffold pores, and bone maturation.

A common unwanted histological observation following *in vivo* implantation can be the formation of fibrous tissue surrounding or within the scaffold interior. Optimal early-stage *in vivo* conditions for osseointegration includes a fine provisional network of inflammatory tissue for cell signalling [89], mechanical anchorage [89], and neovascularization in the granulation tissue [90] but bulk formation of fibrous tissue through a porous implant can affect physiological loading of bone at the implant surface [91]. Ideally, the fibrous tissue that forms during the initial stage of wound healing as part of the inflammatory response is replaced by bone tissue during osteogenesis [92]. Since osteogenic cells stop migrating after bone matrix secretion has started, the initial fibrin structure is important to allow cells to have a migratory pathway through porous structures [92]. The thickness of the inflammatory fibrous tissue layer is also dictated by the topology of the implant surface [93] in the host response to foreign bodies. Penetration of early fibrovascular tissue into AM titanium lattice interiors has been seen for additively manufactured implants in leporine [94], ovine [39], and caprine [95] bone tissue irrespective of lattice type. In all three of these studies, the net porosity exceeded 60% and fibrovascular tissue was frequently observed at a pore size near 600 μm. This is in agreement with trends in porous bioceramics, where vasculature increases as the minimum pore size increases with a similar net porosity (to a maximum investigated diameter of 700 μm) [96].

AM lattice structures, which often have high surface area to volume ratios due to microscale topography, can be especially prone to fibrosis. A study of porous Ti-6Al-4V in porcine crania has shown that the fibrous encapsulation has only allowed for scarce bone-implant contact at the exterior of the implant despite healthy trabecular regeneration in the implant interior, limiting the implant's stability [97]. Unfavourable fibrous encapsulation has been seen to also limit bone-implant contact in a titanium scaffold implanted in an ovine model [39] and murine model [67]. In cases where layers of fibrous tissue prevent bone from anchoring directly to the implant, the long-term integrity of the bone-implant interface is compromised. In terms of novel materials, an iron-manganese porous implant exhibited strong bone-implant contact after four weeks in a murine model [98].

Fibrous tissue formation is not always requisite for *de novo* bone formation [37]. In lattice structures, isolated pockets of new bone can form on the scaffold interior in a strain-dependent relationship, where mechanically flexible scaffolds tend to have higher rates of net bone formation on regions within the resected volume [39]. The structure of this bone is also shown to be strain-dependent in the literature, where woven bone readily forms in sham models, but a strain threshold tends to exist for lamellar bone formation in bone defects [86]. Specifically, Claes and Heigele have supposed that there is a certain strain threshold (< 5% strain) for intramembranous ossification to take place during general fracture healing [99]. This strain threshold is an important consid-

eration for lattice optimization, where overly compliant scaffolds may see delayed osteoconduction, but overly stiff scaffolds may see increased stress-shielding.

The typical bone remodeling process forms woven bone during the early stages of osseointegration and gradually replaces it with lamellar bone [100]. However, bone maturation in lattice structures tends to be a more complicated issue. For leporine models, lamellar bone was not observed to form until at least 8 weeks, with woven bone commonly distributed through the lattices as early as 4 weeks [69,94,101,102]. Lattices with higher porosity (herein described as greater than 75%) were also observed to delay bone maturation in leporine models, where the structure of bone through the lattice was predominantly woven bone after 8 weeks and lamellar bone was not visible until at least 16 weeks [103]. Overall, formation of lamellar bone in larger mammals will tend to be slower than in smaller mammals within the scaffold interior as the remodelling process as a whole is shorter in small mammals [104]. While insufficient data exists to validate the relationship between maturation rate and porosity in canine, ovine, and caprine models, there are benchmarks set for each in the present literature. In canine models, woven bone dominates the structure of highly porous metallic implants after 8 weeks and shows signs of maturation at 16 weeks [105]. For low-porosity implants in caprine models, limited woven bone is present after 12 weeks with a greater amount of woven bone present after 26 weeks [95]. The woven to lamellar transition in this caprine study was between the 26-week and 52-week timepoints [95]. Titanium scaffolds in an ovine model displayed predominantly woven bone after 6 weeks, but similar polyamide control scaffolds showed regions of woven bone sandwiched between lamellar bone [39]. At the cellular level, Shah et al. have noted a net increase in ovine osteocyte density at the interface of EBM porous constructs compared to fully dense specimens [68]. This may be attributed to a high rate of initial osteoblast adhesion to the implant surface, or to high turnover rates to create an apparent 'less-aged' bone structure at the interface of the pores [68]. Raman spectroscopy had indicated in this study that there was increased maturity at the interface of the porous structure by comparing the CO_3^{2-}/PO_4^{3-} peak ratio [68].

In general, however, it is important to note that bone maturation depends strongly on the implant location and animal model, rather than the AM scaffold design or implant chemistry. Despite limitations in implant comparison from study to study, the interplay of design criteria such as pore size and porosity were shown to influence intraspecies bone maturation and quantity of fibrovascular tissue at early stages of implantation. Implants with a target pore geometry of roughly 600 μm and porosity of 75% should provide an adequate balance between these two simultaneous processes during bone regeneration, although much of this conclusion stems from leporine histology data.

Defining Common Histomorphometric Parameters

The most common quantitative factors extracted from histomorphometry to characterize osseointegration are bone volume per total volume, bone area and bone-implant contact. Bone volume density (BV/TV) is a common way of quantifying osseointegration by measuring the ratio of bone tissue volume to total volume using micro-computed tomography [106]. Bone area (BA) is an equivalent 2D measurement that measures the area of new bone growth over the total area available for bone ingrowth within a region of interest surrounding or inside a scaffold [106]. Similarly, bone-implant contact (BIC) measures the length of direct bone contact along an implant, usually presented as a percentage of the total length available. Implant stability in pre-clinical models can be evaluated by measuring the BIC, and correlating this to mechanical testing methods, including pull-out force, push-out force, or removal torque. Pull-out and push-out tests measure the required force to remove an implanted structure, although the results between the two are not always directly comparable [107]. Lastly, removal torque tests are an alternative way to measure bone-implant anchorage by evaluating the

Table 1

Trends in osseointegration with pore size for various pre-clinical animal models. Bone-implant contact (BIC), bone area (BA), bone volume fraction (BV/TV), pull-out force, or push-out force serve as the most common techniques for quantifying osseointegration of lattice geometries. In all cases, increasing implantation time shows an increased value in at least one of these metrics.

Pore Size (µm)	Pre-Clinical Model	Implantation Time/Type	BIC (%)	BA (%)	BV/TV (%)	Pull-Out Force (N)	Push-Out Force (N) or Push-Out Stress (MPa)	Reference
100–200	Leporine	8 wk^{CPT-S}	-	26, 30	-	-	-	[69]
200–300	Leporine	2 wk^{CPT-R}	-	-	-	38	-	[94]
		4 wk^{CPT-R}	-	-	-	126	-	[94]
		8 wk$^{CPT-R/S}$	47	29, 36	-	115	-	[69,94,112]
300–400	Leporine	4 wk^{CPT-R}	-	30	-	-	-	[113]
		8 wk^{CPT-R}	35	32	-	-	-	[112]
	Caprine	12.5 wk^{Ti64-R}	-	1	-	-	-	[95]
		25.5 wk^{Ti64-R}	-	17	-	-	-	[95]
		51 wk^{Ti64-R}	-	25	-	-	-	[95]
400–500	Leporine	2 wk$^{R/S}$	-	12, 27, 23, 24	-	-	140, 221, 181, 219	[114]
		4 wk$^{CPT/Ti64-R/S}$	-	20, 30, 32, 34, 34	-	-	2.8 [MPa], 362, 372, 419, 434	[113–115]
		7 wk$^{R/S}$	-	24, 33, 36, 37	-	-	401, 419, 473, 492	[114]
		12 wk^{Ti64-R}	-	-	-	-	3.6 [MPa]	[115]
	Porcine	2 wk^{Ti64-R}	0.5	-	5.6	-	-	[97]
		4 wk^{Ti64-R}	4.1	-	13.8	-	-	[97]
		8.5 wk^{Ti64-R}	6.0	-	34.2	-	-	[97]
500–600	Leporine	2 wk^{CPT-R}	-	-	-	68	-	[94]
		4 wk^{CPT-R}	-	-	-	147	-	[94]
		8 wk^{CPT-R}	39	31	19	157	-	[70,94,112]
	Canine	16 wk^{CPT-O}	-	8	-	-	-	[66]
		26 wk^{CPT-O}	-	18	-	-	-	[66]
		52 wk^{CPT-O}	-	25	-	-	-	[66]
600–700	Leporine	4 wk^{Ti64-R}	-	-	-	-	3.2 [MPa]	[115]
		8 wk^{CPT-R}	37, 50	28, 30	15, 25	-	-	[70,112]
		12 wk^{Ti64-R}	-	-	-	-	4.3 [MPa]	[115]
	Canine	16 wk^{CPT-O}	-	8	-	-	-	[66]
		26 wk^{CPT-O}	-	14	-	-	-	[66]
		52 wk^{CPT-O}	-	19	-	-	-	[66]
800–900	Leporine	2 wk^{CPT-R}	-	-	-	33	-	[94]
		3 wk^{CPT-R}	23	-	18	-	-	[116]
		4 wk$^{CPT/Ti64-R}$	-	52	-	127	2.9 [MPa]	[94,113,115]
		8 wk^{CPT-R}	31	-	14	131	-	[94,116]
		12 wk^{Ti64-R}	-	-	-	-	3.9 [MPa]	[115]
900–1000	Canine	16 wk^{CPT-O}	-	3	-	-	-	[66]
		26 wk^{CPT-O}	-	5	-	-	-	[66]
		52 wk^{CPT-O}	-	12	-	-	-	[66]
> 1000	Leporine	3 wk^{CPT-R}	38	-	24	-	-	[116]
		4 wk^{CPT-R}	-	39	-	-	-	[113]
		8 wk^{CPT-R}	30	-	10	-	-	[116]
	Canine	16 wk^{CPT-O}	-	2	-	-	-	[66]
		26 wk^{CPT-O}	-	4	-	-	-	[66]
		52 wk^{CPT-O}	-	7	-	-	-	[66]

$^{-}$ Data not available; ^{CPT} Commercially-pure titanium; ^{Ti64} Ti-6Al-4V; ^{R} Reticulated; ^{S} Stochastic; ^{O} Other

required torque to remove a threaded screw from its implant site. While other histomorphometric parameters exist for specific applications, the ones listed above are most abundant in the literature.

However, in AM, due to the lack of bone ubiquity through most lattice structures, it has become increasingly common practice to segment the implant into distinct regions for histomorphometry, since bone volume tends to be higher at the scaffold exterior. Therefore, histomorphometric measurements at the early stage of bone ingrowth in AM lattices are regularly supplemented by segmenting into distinct inner/outer lattice regions, but consistency in this volumetric segmentation is lacking across the literature. For example, Palmquist et al. separate 2D subregions into three vertical 'zones' and three horizontal 'levels' for calculation of BV/TV and BIC [108]. Alternatively, Reznikov et al. assigned a scoring system to define bone-implant contact for evenly-spaced micro-computed tomography slices from the periosteal surface inwards, with a manually-defined boundary between the scaffold interior and exterior [39]. Where most *in vivo* trials have been performed in small mammals, such as rats and rabbits, the problem of bone nucleation on a scaffold

interior may amplify when scaling up for clinical application in larger mammals, and this would represent a decrease in measured BIC or BA, which are often related to osteoconduction. For example, existing pre-clinical models in larger mammals, such as ovine, have shown slower osteoconduction through the porous structures, where bone area on the interior third of the scaffold is approximately half of the outer third [108]. In addition, where porous networks for larger implants may have the same lattice structures as their smaller counterparts, the bulk BV/TV ratio may decrease if the bone penetration stagnates or slows for a specific geometry, defect size, or animal model.

Understanding the interplay between unit cell structure, implant stiffness, and resulting osseointegration is important for *in vivo* success. Where a wealth of *in vitro* and compression data exists for various lattice designs [48,109–111], there is little information describing these relationships quantitatively and systematically during *in vivo* studies. Due to variability in experimental techniques (e.g. animal type, anatomical location, surgical methods, implantation time, implant size, pore morphology, pore size, etc.), only qualitative observations can be critically

Table 2
Select histomorphometric observations with respect to % porosity and pre-clinical model for implanted AM lattices. Bone-implant contact (BIC), bone area (BA), bone volume fraction (BV/TV), pull-out force, or push-out force serve as the most common techniques for quantifying osseointegration of lattice geometries.

Porosity (%)	Pre-Clinical Model	Implantation Time/Type	BIC (%)	BA (%)	BV/TV (%)	Pull-Out Force (N)	Push-Out Force (N) or Push-Out Stress (MPa)	Reference
30–40	Leporine	8 wk$^{CPT\text{-}S}$	-	26, 29	-	-	-	[69]
	Caprine	12.5 wk$^{Ti64\text{-}R}$	-	1	-	-	-	[95]
		25.5 wk$^{Ti64\text{-}R}$	-	7	-	-	-	[95]
		51 wk$^{Ti64\text{-}R}$	-	25	-	-	-	[95]
40–50	Leporine	4 wk$^{Ti64\text{-}R}$	-	-	-	-	2.8 [MPa]	[115]
		8 wk$^{CPT\text{-}S}$	-	30	-	-	-	[69]
		12 wk$^{Ti64\text{-}R}$	-	-	-	-	3.6 [MPa]	[115]
50–60	Leporine	3 wk$^{CPT\text{-}R}$	38	-	24	-	-	[116]
		4 wk$^{Ti64\text{-}R}$	-	-	-	-	2.9 [MPa]	[115]
		8 wk$^{CPT\text{-}R}$	30	-	10	-	-	[116]
		12 wk$^{Ti64\text{-}R}$	-	-	-	-	3.9 [MPa], 4.3 [MPa]	[115]
	Ovine	12 wk^{O}	-	-	20, 43	-	-	[117]
60–70	Leporine	2 wk$^{CPT\text{-}R/S}$	-	12, 23, 24, 27	-	33, 38, 68	140, 181, 219, 221	[114]
		3 wk$^{CPT\text{-}R}$	23	-	18	-	-	[116]
		4 wk$^{CPT\text{-}R/S}$	-	20, 30, 34, 34	-	126, 127, 147	362, 372, 419, 434	[94,114]
		7 wk$^{R/S}$	-	24, 33, 37	-	-	401, 419, 473	[114]
		8 wk$^{CPT\text{-}R}$	31	-	14	115, 131, 157	-	[94,116]
	Porcine	2 wk$^{Ti64\text{-}R}$	0.47	-	5.6	-	-	[97]
		4 wk$^{Ti64\text{-}R}$	4.14	-	13.8	-	-	[97]
		8.5 wk$^{Ti64\text{-}R}$	5.96	-	34.2	-	-	[97]
	Ovine	6 wk$^{CPT\text{-}R}$	-	-	6.9	-	-	[39]
70–80	Leporine	8 wk$^{CPT\text{-}R}$	35, 37, 47	30, 32, 36	-	-	-	[112]
80–90	Leporine	8 wk$^{CPT\text{-}R}$	39, 50	28, 31	15, 19, 25	-	-	[70,112]
	Ovine	6 wk$^{CPT\text{-}S}$	-	-	9.4	-	-	[39]

⁻ Data not available; ^{CPT} Commercially-pure titanium; ^{Ti64} Ti-6Al-4V; ^{R} Reticulated; ^{S} Stochastic; ^{O} Other

analyzed from study to study. For this reason, we have little information about the 'ideal' lattice structure for osseointegration and osteoconduction. Table 1 and Table 2 attempt to sort the histomorphometric and mechanical findings in the literature by the predominant governing geometrical parameters: pore size and percent porosity, respectively.

Observations from Histomorphometric Evaluations

In general, porous AM implants have been observed to outperform solid controls in various forms of bone histomorphometry [101,112,114,117], but determining which lattice geometries perform is still ongoing. Wang et al. have proven that the unit cell structure of a reticulated lattice can influence bone growth kinetics, where diamond-based lattice structures caused higher bone area fractions than tetrahedral lattice structures [114].Wieding et al. have similarly modified a porous structure to find that a simple reticulated cubic lattice showed less bone ingrowth than a hollow cage structure with angled struts [118]. In contrast, de Wild et al. have observed that osseointegration and osteoconduction occur independent of unit cell architecture [112]. By changing the strut thickness or unit cell dimensions of any lattice structure, there is a change in local stiffness through the implant. Since nascent bone tends to be locally strained depending on implant stiffness, further *in vivo* investigation into lattice geometry is necessary to evaluate the optimal lattice structure and perhaps appropriate functional grading for bone implants. As a reference, the implanted scaffolds summarized in this work have an apparent modulus that varies from 0.6–38 GPa, with the vast majority having a modulus under 10 GPa.

The pore size in a lattice structure appears to be a dominant factor affecting osseointegration and *in vivo* mechanical stability. Table 1 summarizes quantitative findings for bone ingrowth and stability for porous

implants depending on pore size for several pre-clinical models. Optimal pore size for orthopaedic applications was first documented to range from 50–400 μm for maximum fixation strength [119]. While a pore size in this range may be correlated to good mechanical anchorage, it is important to note that there may be no minimum pore size for the onset of osseointegration within the current manufacturing limitations of additive manufacturing. Itälä et al., for example, monitored osseointegration into 50 μm machined cylindrical holes and found secondary osteonal structures present in a leporine model [102]. Defining an upper bound for pore size is more difficult. Fukuda et al. has noted that square pores with a diagonal length of 500 μm outperformed larger pores (600 μm, 900 μm, and 1200 μm) in terms of bone penetration depth and BA for a canine model [66]. In contrast to this, cylindrical pores with a diameter of 900 μm in an AM structure displayed greater bone volumes than pores with diameters of 500 μm and 700 μm in a canine model [115]. This canine study, however, had also shown that trabeculae thickness in the new bone was highest for the 500 μm grouping [115], reiterating that sometimes not only bone quantity but quality are important predictors of implant success. In a study that examined porous metallic structures with smaller pores, it was found that increasing pore size to the largest size (300 μm) resulted in a higher interfacial bone fraction [69]. A recent work has attempted to investigate the effect of systematically modifying both strut size and strut spacing in rabbit crania [113]. This study finds statistically higher BA percentages for a strut spacing of 800 μm compared to alternate spacings of 500 μm and 1800 μm after four weeks of implantation, but indeterminate results in terms of bone bridging and histomorphometry associated with strut diameter. As a whole, trends in the literature reveal that osseointegration and osteoconduction are most favourable in the pore size range of 300–500 μm, but contrasting studies implicate that this size range could be marginally higher based on un-

known confounding factors or experimental design of pre-clinical trials. The translation from pre-clinical to clinical model should also consider the rate of bone apposition in humans relative to any given pre-clinical model if pore occlusion effects are to be considered significant.

The other factor greatly affecting osseointegration is the percent (%) porosity. Table 2 expresses bone formation and implant stability with respect to porosity. There is a distinct lack of information about correlating implant stability to net porosity in highly porous (> 75% porosity) metallic implants in a quantitative regard, as few systematic trials have been conducted to evaluate the percent porosity by keeping a constant pore size. Li et al., for example, evaluated *in vitro* response with respect to pore size (300–400 μm, 400–500 μm, 500–700 μm) in their specimens by keeping the same porosity [95], but did not do correlative *in vivo* experiments on two of the study groups. Meanwhile, de Wild's work on highly porous scaffolds (70–90% porosity) show remarkably high values of bone-implant contact compared to other porosity values and therefore excellent potential for osteoconduction [112]. The interplay between unit cell size, pore size, and porosity in the geometric design of scaffolds makes it difficult to isolate the *in vivo* response to a particular geometric variable, but instead highlights the importance of considering all three simultaneously for lattice design. In terms of novel materials, tantalum scaffolds have shown better bone-implant contact than titanium, with a higher fraction of early osteoid and a lack of early interfacial gaps at the bone-implant interface [120]. In general, implants of any type with a percent porosity in the range of 50–70% showed reasonable osseointegration, where lower measurements of BIC, BA, or BV/TV were observed outside of this range.

Conclusions

As additive manufacturing has become more commonplace in the field of metallic implant production, it is increasingly important to evaluate the performance of complex geometries in pre-clinical *in vivo* models. This review surveyed existing studies to make general conclusions about the *in vivo* performance of AM metallic lattice structures based on histological and histomorphometric data. For lattice structures, geometric considerations such as strut thickness and unit cell size dictate the resulting pore size and percent porosity of the implant. This review notes a clear lack of systematic evaluation of AM implant designs in the present literature to identify an optimum pore architecture and size for osseointegration in critical-sized bone defects. However, we find that the most common form of porous AM implant studied *in vivo* tends to have a reticulated lattice structure, with a pore size ranging from 400–500 μm and percent porosity ranging between 60–70%. Most of these implants have been made of titanium alloys and are produced by selective laser melting. There have been few studies to systematically evaluate the effects of other pore structures, such as stochastic/trabecular architectures, and therefore, we cannot speculate if any given reticulated structure with this pore structure is best, or simply the most widely investigated. From the studies evaluated in this review, porosity seems to correlate strongly to bone maturity (where porosity between 50–70% trended towards larger amounts of lamellar bone in the pore network), while pore size may be more closely related to the mechanical stability of the implant (where increased values of BIC, pull-out force, and push-out force were correlated to pore sizes between 300–500 μm). Early onset of woven-to-lamellar transition and formation of favourable precursory fibrovascular tissue is most common in implants with a pore size of 600 μm and a porosity of 75%.

Lastly, where many publications modify lattice geometry from a mechanical perspective to lower implant stiffness, it is our opinion that future work should perhaps shift to developing strategies for improved integration of high-quality bone tissue throughout the interior of the implant. For example, in almost all cases reported in this review, complete penetration of bone throughout the lattice interior was lacking. While this review did not broach the topic of surface modification for AM due to a lack of publications reporting *in vivo* performance, considerable lit-erature citing *in vitro* methods for modifying implant pore chemistry and topography is available, including acid etching [70], sandblasting [70], micro-arc oxidation [121], dip coating [122], or other methods [123]. Surface modification approaches to regulate osteoconduction, which are widely effective on conventionally cast porous and non-porous metallic implants [124–126], should receive more attention, especially in a systematic manner to compare their efficacy when applied to the interior of a porous implant.

Declaration of Competing Interest

The authors declare no conflict of interest.

CRediT authorship contribution statement

Joseph Deering: Conceptualization, Data curation, Formal analysis, Writing - original draft, Writing - review & editing. **Kathryn Grandfield:** Conceptualization, Funding acquisition, Supervision, Writing - review & editing.

Acknowledgements

References

[1] Albrektsson T, Johansson C. Osteoinduction, osteoconduction and osseointegration. Eur Spine J 2001;10(Suppl 2):S96–101.

[2] Huiskes R, Weinans H, van Rietbergen B. The relationship between stress shielding and bone resorption around total hip stems and the effects of flexible materials. Clin Orthop Relat R 1992;274:124–34 NA;.

[3] Ashby MF, Medalist RFM. The mechanical properties of cellular solids. Metall Trans 1983;14(9):1755–69.

[4] Choren JA, Heinrich SM. Silver-Thorn MB. Young's modulus and volume porosity relationships for additive manufacturing applications. J Mater Sci 2013;48(15):5103–12.

[5] Hao Y-L, Li S-J, Yang R. Biomedical titanium alloys and their additive manufacturing. Rare Metals 2016;35(9):661–71.

[6] Karre R, Niranjan MK, Dey SR. First principles theoretical investigations of low Young's modulus beta Ti–Nb and Ti–Nb–Zr alloys compositions for biomedical applications. Mater Sci Eng C 2015;50:52–8.

[7] Luo JP, Sun JF, Huang YJ, Zhang JH, Zhang YD, Zhao DP, Yan M. Low-modulus biomedical Ti–30Nb–5Ta–3Zr additively manufactured by selective laser melting and its biocompatibility. Mater Sci Eng C 2018;97:275–84 (Mater. Sci. Eng. R 47 3 2004).

[8] Yilmazer H, Niinomi M, Nakai M, Cho K, Hieda J, Todaka Y, Miyazaki T. Mechanical properties of a medical *β*-type titanium alloy with specific microstructural evolution through high-pressure torsion. Mater Sci Eng C 2013;33(5):2499–507.

[9] Niinomi M, Nakai M, Hieda J. Development of new metallic alloys for biomedical applications. Acta Biomater 2012;8(11):3888–903.

[10] Schulze C, Weinmann M, Schweigel C, Keßler O, Bader R. Mechanical Properties of a Newly Additive Manufactured Implant Material Based on Ti-42Nb. Materials 2018;11(1):124.

[11] Krishna BV, Bose S, Bandyopadhyay A. Low stiffness porous Ti structures for load-bearing implants. Acta Biomater 2007;3(6):997–1006.

[12] Xin XZ, Xiang N, Chen J, Wei B. In vitro biocompatibility of Co–Cr alloy fabricated by selective laser melting or traditional casting techniques. Mater Lett 2012;88:101–3.

[13] Hazlehurst K, Wang CJ, Stanford M. Evaluation of the stiffness characteristics of square pore CoCrMo cellular structures manufactured using laser melting technology for potential orthopaedic applications. Mater Design 2013;51:949–55.

[14] Sing SL, An J, Yeong WY, Wiria FE. Laser and electron-beam powder-bed additive manufacturing of metallic implants: a review on processes, materials and designs. J Orthopaed Res 2015;34(3):369–85.

[15] Li Y, Jahr H, Zhou J, Zadpoor AA. Additively manufactured biodegradable porous metals. Acta Biomater 2020;115:29–50.

[16] Wang Z, Wang C, Li C, Qin Y, Zhong L, Chen B, Li Z, Liu H, Chang F, Wang J. Analysis of factors influencing bone ingrowth into three-dimensional printed porous metal scaffolds: a review. J Alloy Compd 2017;717:271–85.

[17] Wang X, Xu S, Zhou S, Xu W, Leary M, Choong P, Qian M, Brandt M, Xie YM. Topological design and additive manufacturing of porous metals for bone scaffolds and orthopaedic implants: a review. Biomaterials 2016;83:127–41.

[18] Zok FW. Integrating lattice materials science into the traditional processing–structure–properties paradigm. Mrs Commun 2019;9(4):1284–91.

[19] Weber FE. Reconsidering Osteoconduction in the era of additive manufacturing. Tissue Eng Part B Rev 2019;25(5):375–86.

[20] Frazier WE. Metal additive manufacturing: a review. J Mater Eng Perform 2014;23(6):1917–28.

[21] Wong KV, Hernandez A. A review of additive manufacturing. Isrn Mech Eng 2012;2012:1–10.

[22] Bikas H, Stavropoulos P, Chryssolouris G. Additive manufacturing methods and modelling approaches: a critical review. Int J Adv Manuf Technol 2016;83(1–4):389–405.

[23] Mullen L, Stamp RC, Brooks WK, Jones E, Sutcliffe CJ. Selective Laser Melting: a regular unit cell approach for the manufacture of porous, titanium, bone in-growth constructs, suitable for orthopedic applications. J Biomed Mater Res Part B Appl Biomater 2009;89B(2):325–34.

[24] Guo Q, Zhao C, Qu M, Xiong L, Escano LI, Hojjatzadeh SMH, Parab ND, Fezzaa K, Everhart W, Sun T, Chen L. In-situ characterization and quantification of melt pool variation under constant input energy density in laser powder-bed fusion additive manufacturing process. Addit Manuf 2019;28:600–9.

[25] Qiu C, Yue S, Adkins NJE, Ward M, Hassanin H, Lee PD, Withers PJ, Attallah MM. Influence of processing conditions on strut structure and compressive properties of cellular lattice structures fabricated by selective laser melting. Mater Sci Eng 2015;628:188–97 (Prog. Mater. Sci. 46 2001).

[26] Liu Y, Yang Y, Mai S, Wang D, Song C. Investigation into spatter behavior during selective laser melting of AISI 316L stainless steel powder. Mater Design 2015;87:797–806.

[27] Ghouse S, Babu S, Arkel RJV, Nai K, Hooper PA, Jeffers JRT. The influence of laser parameters and scanning strategies on the mechanical properties of a stochastic porous material. mater design. 2017;131 (J. Biomed. Mater. Res. B Appl. Biomater. 89B 2 2009):498–508.

[28] Weißmann V, Drescher P, Bader R, Seitz H, Hansmann H, Laufer N. Comparison of Single Ti6Al4V struts made using selective laser melting and electron beam melting subject to part orientation. Metals-basel 2017;7(3):91.

[29] Wang L, Felicelli SD, Pratt P. Residual stresses in LENS-deposited AISI 410 stainless steel plates. Mater Sci Eng 2008;496(1–2):234–41.

[30] Rangaswamy P, Holden TM, Rogge RB, Griffith ML. Residual stresses in components formed by the laserengineered net shaping (LENS®) process. J Strain Analysis Eng Des 2003;38(6):519–27.

[31] Yuan L, Ding S, Wen C. Additive manufacturing technology for porous metal implant applications and triple minimal surface structures: a review. Bioact Mater 2019;4(1):56–70.

[32] Kreitcberg A, Brailovski V, Prokoshkin S. New biocompatible near-beta Ti-Zr-Nb alloy processed by laser powder bed fusion: process optimization. J Mater Process Tech 2018;252:821–9.

[33] Mehjabeen A, Song T, Xu W, Tang HP, Qian M. Zirconium alloys for orthopaedic and dental applications. Adv Eng Mater 2018;20(9):1800207.

[34] Niinomi M, Liu Y, Nakai M, Liu H, Li H. Biomedical titanium alloys with Young's moduli close to that of cortical bone. Regen Biomater 2016;3(3):173–85.

[35] Ozan S, Lin J, Li Y, Wen C. New Ti-Ta-Zr-Nb alloys with ultrahigh strength for potential orthopedic implant applications. J Mech Behav Biomed 2017;75:119–27.

[36] Long M, Rack HJ. Titanium alloys in total joint replacement—a materials science perspective. Biomaterials 1998;19(18):1621–39.

[37] Kujala S, Ryhänen J, Danilov A, Tuukkanen J. Effect of porosity on the osteointegration and bone ingrowth of a weight-bearing nickel–titanium bone graft substitute. Biomaterials 2003;24(25):4691–7.

[38] Ayers RA, Simske SJ, Bateman TA, Petkus A, Sachdeva RLC, Gyunter VE. Effect of nitinol implant porosity on cranial bone ingrowth and apposition after 6 weeks. J Biomed Mater Res 1999;45(1):42–7.

[39] Reznikov N, Boughton OR, Ghouse S, Weston AE, Collinson L, Blunn GW, Jeffers J, Cobb JP, Stevens MM. Individual response variations in scaffold-guided bone regeneration are determined by independent strain- and injury-induced mechanisms. Biomaterials 2018;194:183–94 (J. Bone Joint Surg. Am. 89 Suppl 3 2007).

[40] Alvarez K, Hyun S-K, Nakano T, Umakoshi Y, Nakajima H. In vivo osteocompatibility of lotus-type porous nickel-free stainless steel in rats. Mater Sci Eng C 2009;29(4):1182–90.

[41] Kok Y, Tan XP, Wang P, Nai MLS, Loh NH, Liu E, Tor SB. Anisotropy and heterogeneity of microstructure and mechanical properties in metal additive manufacturing: a critical review. Mater Design 2018;139:565–86.

[42] Gibson LJ. Biomechanics of cellular solids. J Biomech 2005;38(3):377–99.

[43] Mahmoud D, Elbestawi MA. Lattice structures and functionally graded materials applications in additive manufacturing of orthopedic implants: a review. J Manuf Mater Process 2017;1(2):13.

[44] Ahmadi SM, Yavari SA, Wauthle R, Pouran B, Schrooten J, Weinans H, Zadpoor AA. Additively manufactured open-cell porous biomaterials made from six different space-filling unit cells: the mechanical and morphological properties. Materials 2015;8(4):1871–96.

[45] Kapfer SC, Hyde ST, Mecke K, Arns CH, Schröder-Turk GE. Minimal surface scaffold designs for tissue engineering. Biomaterials 2011;32(29):6875–82.

[46] Rajagopalan S, Robb RA. Schwarz meets Schwann: design and fabrication of biomorphic and durataxic tissue engineering scaffolds. Med Image Anal 2006;10(5):693–712.

[47] Kelly CN, Francovich J, Julmi S, Safranski D, Guldberg RE, Maier HJ, Gall K. Fatigue Behavior of As-Built Selective Laser Melted Titanium Scaffolds with Sheet-based Gyroid Microarchitecture for Bone Tissue Engineering. Acta Biomater 2019;94:610–26.

[48] Al-Ketan O, Rowshan R, RKA Al-Rub. Topology-mechanical property relationship of 3D printed strut, skeletal, and sheet based periodic metallic cellular materials. Addit Manuf 2018;19:167–83 (Acta Biomater. 4 2008).

[49] Li L, Shi J, Zhang K, Yang L, Yu F, Zhu L, Liang H, Wang X, Jiang Q. Early osteointegration evaluation of porous Ti6Al4V scaffolds designed based on triply periodic minimal surface models. J Orthop Transl 2019 (BMC Muscoskelet Disord 18 2017).

[50] Bobbert FSL, Lietaert K, Eftekhari AA, Pouran B, Ahmadi SM, Weinans H, Zadpoor AA. Additively manufactured metallic porous biomaterials based on minimal surfaces: a unique combination of topological, mechanical, and mass transport properties. Acta Biomater 2017;53:572–84 (J. Biomech. 45 6 2012).

[51] Fantini M, Curto M, Crescenzio FD. A method to design biomimetic scaffolds for bone tissue engineering based on Voronoi lattices. Virtual Phys Prototyp 2016;11(2):77–90.

[52] Liang H, Yang Y, Xie D, Li L, Mao N, Wang C, Tian Z, Jiang Q, Shen L. Trabecular-like Ti-6Al-4V scaffolds for orthopedic: fabrication by selective laser melting and in vitro biocompatibility. J Mater Sci Technol 2019;35:1284–97 (Der Unfallchirurg 109 2006).

[53] Silva MJ, Gibson LJ. Modeling the mechanical behavior of vertebral trabecular bone: effects of age-related changes in microstructure. Bone 1997;21(2):191–9.

[54] Ryan G, Pandit A, Apatsidis DP. Fabrication methods of porous metals for use in orthopaedic applications. Biomaterials 2006;27(13):2651–70.

[55] Imwinkelried T. Mechanical properties of open-pore titanium foam. J Biomed Mater Res A 2007;81A(4):964–70.

[56] Yu C-J, Eifert HH, Banhart J, Baumeister J. Metal foaming by a powder metallurgy method: Production, properties and applications. Mater Res Innov 1998;2(3):181–8.

[57] Singh S, Bhatnagar N. A survey of fabrication and application of metallic foams (1925–2017). J Porous Mat 2018;25(2):537–54.

[58] Wen CE, Yamada Y, Shimojima K, Chino Y, Asahina T, Mabuchi M. Processing and mechanical properties of autogenous titanium implant materials. J Mater Sci Mater Med 2002;13(4):397–401.

[59] Mahmoud D, Elbestawi MA, Yu B. Process–structure–property relationships in selective laser melting of porosity graded gyroids. J Med Dev 2019;13(3):031005.

[60] Shishkovsky I, Missemer F, Smurov I. Direct metal deposition of functional graded structures in Ti- Al system. Physcs Proc 2012;39:382–91.

[61] Fousová M, Vojtěch D, Kubásek J, Jablonská E, Fojt J. Promising characteristics of gradient porosity Ti-6Al-4V alloy prepared by SLM process. J Mech Behav Biomed 2017;69:368–76.

[62] Sola A, Bellucci D, Cannillo V. Functionally graded materials for orthopedic applications – an update on design and manufacturing. Biotechnol Adv 2016;34(5):504–31.

[63] Itälä AI, Ylänen HO, Ekholm C, Karlsson KH, Aro HT. Pore diameter of more than 100 μm is not requisite for bone ingrowth in rabbits. J Biomed Mater Res 2001;58(6):679–83.

[64] Melancon D, Bagheri ZS, Johnston RB, Liu L, Tanzer M, Pasini D. Mechanical characterization of structurally porous biomaterials built via additive manufacturing: experiments, predictive models, and design maps for load-bearing bone replacement implants. Acta Biomater 2017;63:350–68.

[65] Tsopanos S, Mines RAW, McKown S, Shen Y, Cantwell WJ, Brooks W, Sutcliffe CJ. The influence of processing parameters on the mechanical properties of selectively laser melted stainless steel microlattice structures. J Manuf Sci Eng 2010;132(4):041011.

[66] Fukuda A, Takemoto M, Saito T, Fujibayashi S, Neo M, Pattanayak DK, Matsushita T, Sasaki K, Nishida N, Kokubo T, Nakamura T. Osteoinduction of porous Ti implants with a channel structure fabricated by selective laser melting. Acta Biomater 2011;7(5):2327–36.

[67] Stok JV der, Jagt OPV der, Yavari SA, Haas MFPD, Waarsing JH, Jahr H, Lieshout EMMV, Patka P, Verhaar JAN, Zadpoor AA, Weinans H. Selective laser melting-produced porous titanium scaffolds regenerate bone in critical size cortical bone defects. J Orthopaed Res 2013;31(5):792–9.

[68] Shah FA, Snis A, Matic A, Thomsen P, Palmquist A. 3D printed Ti6Al4V implant surface promotes bone maturation and retains a higher density of less aged osteocytes at the bone-implant interface. Acta Biomater 2016;30:357–67 (Biomaterials 27 2006).

[69] de Vasconcellos LMR, Leite DO, Oliveira FN de, Carvalho YR, Cairo CAA. Evaluation of bone ingrowth into porous titanium implant: histomorphometric analysis in rabbits. Braz Oral Res 2010;24(4):399–405.

[70] de Wild M, Schumacher R, Mayer K, Schkommodau E, Thoma D, Bredell M, Gujer AK, Grätz KW, Weber FE. Bone Regeneration by the Osteoconductivity of Porous Titanium Implants Manufactured by Selective Laser Melting: a histological and micro computed tomography study in the rabbit. Tissue Eng Pt A 2013;19(23–24):2645–54.

[71] Hollister SJ. Porous scaffold design for tissue engineering. Nat Mater 2005;4(7):518–24.

[72] Ramasamy SK, Kusumbe AP, Schiller M, Zeuschner D, Bixel MG, Milia C, Gamrekelashvili J, Limbourg A, Medvinsky A, Santoro MM, Limbourg FP, Adams RH. Blood flow controls bone vascular function and osteogenesis. Nat Commun 2016;7(1):13601.

[73] Azeem A, English A, Kumar P, Satyam A, Biggs M, Jones E, Tripathi B, Basu N, Henkel J, Vaquette C, Rooney N, Riley G, O'Riordan A, Cross G, Ivanovski S, Hutmacher D, Pandit A, Zeugolis D. The influence of anisotropic nano- to micro-topography on in vitro and in vivo osteogenesis. Nanomedicine-uk 2015;10(5):693–711.

[74] Mehdizadeh H, Sumo S, Bayrak ES, Brey EM, Cinar A. Three-dimensional modeling of angiogenesis in porous biomaterial scaffolds. Biomaterials 2013;34(12):2875–87.

[75] Hsieh Y-F, Robling AG, Ambrosius WT, Burr DB, Turner CH. Mechanical loading of diaphyseal bone in vivo: the strain threshold for an osteogenic response varies with location. J Bone Miner Res 2001;16(12):2291–7.

[76] Mapara M, Thomas BS, Bhat K. Rabbit as an animal model for experimental research. Dent Res J 2012;9(1):111.

[77] Schmitz JP, Hollinger JO. The Critical size defect as an experimental model for craniomandibulofacial nonunions. Clin Orthop Relat R 1986(205) NA299???308.

[78] Schemitsch EH. Size matters: defining critical in bone defect size. J Orthop Trauma 2017;31:S20–2 NA;.

[79] F04 AC Guide for Pre-clinical in vivo Evaluation in Critical Size Segmental Bone Defects; 2014.

[80] Pearce A, Richards R, Milz S, Schneider E, Pearce S. Animal models for implant biomaterial research in bone: a review. Eur Cells Mater 2007;13:1–10.

[81] Li Y, Chen S-K, Li L, Qin L, Wang X-L, Lai Y-X. Bone defect animal models for testing efficacy of bone substitute biomaterials. J Orthop Transl 2015;3(3):95–104.

[82] Clarke B. Normal bone anatomy and physiology. Clin J Am Soc Nephro 2008;3:S131–9 Supplement 3.

[83] Magal RA, Reznikov N, Shahar R, Weiner S. Three-dimensional structure of minipig fibrolamellar bone: adaptation to axial loading. J Struct Biol 2014;186(2):253–64.

[84] Barrera JW, Cabec AL, Barak MM. The orthotropic elastic properties of fibrolamellar bone tissue in juvenile white-tailed deer femora. J Anat 2016;229(4):568–76.

[85] Weiner S, Traub W, Wagner HD. Lamellar bone: structure–function relations. J Struct Biol 1999;126(3):241–55.

[86] Turner CH, Forwood MR, Rho J-Y, Yoshikawa T. Mechanical loading thresholds for lamellar and woven bone formation. J Bone Miner Res 2009;9(1):87–97.

[87] Marsell R, Einhorn TA. The biology of fracture healing. Inj 2011;42(6):551–5.

[88] AI-Aql ZS, Alagl AS, Graves DT, Gerstenfeld LC, Einhorn TA. Molecular Mechanisms Controlling Bone Formation during Fracture Healing and Distraction Osteogenesis. J Dent Res 2008;87(2):107–18.

[89] Corradetti B. The Immune Response to Implanted Materials and Devices; 2017.

[90] Tonnesen MG, Feng X, Clark RAF. Angiogenesis in wound healing. J Invest Derm Symp P 2000;5(1):40–6.

[91] Esposito M, Hirsch J, Lekholm U, Thomsen P. Biological factors contributing to failures of osseointegrated oral implants, (I). Success criteria and epidemiology. Eur J Oral Sci 1998;106(1):527–51.

[92] Davies JE. Mechanisms of endosseous integration. Int J Prosthodont 1998;11(5):391–401.

[93] Anderson JM. Inflammatory response to implants. Asaio J 1988;34(2):101–7.

[94] Taniguchi N, Fujibayashi S, Takemoto M, Sasaki K, Otsuki B, Nakamura T, Matsushita T, Kokubo T, Matsuda S. Effect of pore size on bone ingrowth into porous titanium implants fabricated by additive manufacturing: an in vivo experiment. Mater Sci Eng C 2016;59:690–701.

[95] Li G, Wang L, Pan W, Yang F, Jiang W, Wu X, Kong X, Dai K, Hao Y. In vitro and in vivo study of additive manufactured porous Ti6Al4V scaffolds for repairing bone defects. Sci Rep-uk 2016;6(1):34072.

[96] Bai F, Wang Z, Lu J, Liu J, Chen G, Lv R, Wang J, Lin K, Zhang J, Huang X. The correlation between the internal structure and vascularization of controllable porous bioceramic materials in vivo: a quantitative study. Tissue Eng Pt A 2010;16(12):3791–803.

[97] Ponader S, von Wilmowsky C, Widenmayer M, Lutz R, Heinl P, Körner C, Singer RF, Nkenke E, Neukam FW, Schlegel KA. In vivo performance of selective electron beam-melted Ti-6Al-4V structures. J Biomed Mater Res A 2010;92A(1):56–62.

[98] Carluccio D, Xu C, Venezuela J, Cao Y, Kent D, Bermingham M, Demir AG, Previtali B, Ye Q, Dargusch M. Additively manufactured iron-manganese for biodegradable porous load-bearing bone scaffold applications. Acta Biomater 2020;103:346–60.

[99] Claes LE, Heigele CA. Magnitudes of local stress and strain along bony surfaces predict the course and type of fracture healing. J Biomech 1999;32(3):255–66.

[100] Bosshardt DD, Chappuis V, Buser D. Osseointegration of titanium, titanium alloy and zirconia dental implants: current knowledge and open questions. Periodontol 2000 2017;73(1):22–40.

[101] Chang JZ-C, Tsai P-I, Kuo MY-P, Sun J-S, Chen S-Y, Shen H-H. Augmentation of DMLS biomimetic dental implants with weight-bearing strut to balance of biologic and mechanical demands: from bench to. Anima. Mater. 2019;12(1):164.

[102] Itälä AI, Ylänen HO, Ekholm C, Karlsson KH, Aro HT. Pore diameter of more than 100 μm is not requisite for bone ingrowth in rabbits. J Biomed Mater Res 2001;58(6):679–83.

[103] Ilea A, Vrabie O-G, Băbțan A-M, Miclăuş V, Ruxanda F, Sárközi M, Barbu-Tudoran L, Mager V, Berce C, Boşca BA, Petrescu NB, Cadar O, Câmpian RS, Barabás R. Osseointegration of titanium scaffolds manufactured by selective laser melting in rabbit femur defect model. J Mater Sci Mater Medicine 2019;30(2):26.

[104] Reinwald S, Burr D. Review of nonprimate, large animal models for osteoporosis research. J Bone Miner Res 2008;23(9):1353–68.

[105] Faria PEP, Carvalho AL, Felipucci DNB, Wen C, Sennerby L, Salata LA. Bone formation following implantation of titanium sponge rods into humeral osteotomies in dogs: a histological and histometrical study. Clin Implant Dent R 2010;12(1):72–9.

[106] Recker RR, Kimmel DB, Dempster D, Weinstein RS, Wronski TJ, Burr DB. Issues in modern bone histomorphometry. Bone 2011;49(5):955–64.

[107] Seong W, Grami S, Jeong SC, Conrad HJ, Hodges JS. Comparison of push-in versus pull-out tests on bone-implant interfaces of rabbit Tibia dental implant healing model. Clin Implant Dent R 2013;15(3):460–9.

[108] Palmquist A, Snis A, Emanuelsson L, Browne M, Thomsen P. Long-term biocompatibility and osseointegration of electron beam melted, free-form–fabricated solid and porous titanium alloy: Experimental studies in sheep. J Biomater Appl 2013;27(8):1003–16.

[109] Liu F, Mao Z, Zhang P, Zhang DZ, Jiang J, Ma Z. Functionally graded porous scaffolds in multiple patterns: New design method, physical and mechanical properties. Mater Design 2018;160:849–60 (Biomaterials 23 2002).

[110] Arabnejad S, Johnston RB, Pura JA, Singh B, Tanzer M, Pasini D. High-strength porous biomaterials for bone replacement: a strategy to assess the interplay between cell morphology, mechanical properties, bone ingrowth and manufacturing constraints. Acta Biomater 2016;30:345–56.

[111] Lee J, Cha HD, Shim J, Jung JW, Kim JY, Cho D. Effect of pore architecture and stacking direction on mechanical properties of solid freeform fabrication-based scaffold for bone tissue engineering. J Biomed Mater Res A 2012;100A(7):1846–53.

[112] de Wild M, Zimmermann S, Rüegg J, Schumacher R, Fleischmann T, Ghayor C, Weber FE. Influence of microarchitecture on osteoconduction and mechanics of porous titanium scaffolds generated by selective laser melting. 3d Print Addit Manuf 2016;3(3):142–51.

[113] de Wild M, Ghayor C, Zimmermann S, Rüegg J, Nicholls F, Schuler F, Chen T-H, Weber FE. Osteoconductive Lattice Microarchitecture for Optimized Bone Regeneration. 3d Print Addit Manuf 2019;6(1):40–9.

[114] Wang H, Su K, Su L, Liang P, Ji P, Wang C. The effect of 3D-printed Ti6Al4V scaffolds with various macropore structures on osteointegration and osteogenesis: a biomechanical evaluation. J Mech Behav Biomed 2018;88:488–96 (J. Mech. Behav. Biomed. Mater. 34 2014).

[115] Ran Q, Yang W, Hu Y, Shen X, Yu Y, Xiang Y, Cai K. Osteogenesis of 3D printed porous Ti6Al4V implants with different pore sizes. J Mech Behav Biomed 2018;84:1–11 (Crit. Rev. Biomed. Eng. 40 2012).

[116] Lopez-Heredia MA, Goyenvalle E, Aguado E, Pilet P, Leroux C, Dorget M, Weiss P, Layrolle P. Bone growth in rapid prototyped porous titanium implants. J Biomed Mater Res A 2008;85A(3):664–73.

[117] Schouman T, Schmitt M, Adam C, Dubois G, Rouch P. Influence of the overall stiffness of a load-bearing porous titanium implant on bone ingrowth in critical-size mandibular bone defects in sheep. J Mech Behav Biomed 2016;59:484–96.

[118] Wieding J, Lindner T, Bergschmidt P, Bader R. Biomechanical stability of novel mechanically adapted open-porous titanium scaffolds in metatarsal bone defects of sheep. Biomaterials 2015;46:35–47.

[119] Bobyn JD, Pilliar RM, Cameron HU, Weatherly GC. The optimum pore size for the fixation of porous-surfaced metal implants by the ingrowth of bone. Clin Orthop Relat R 1980(150):263–70 NA;.

[120] Bandyopadhyay A, Mitra I, Shivaram A, Dasgupta N, Bose S. Direct comparison of additively manufactured porous Titanium and Tantalum implants towards in vivo osseointegration. Addit Manuf 2019;28:259–66.

[121] Xiu P, Jia Z, Lv J, Yin C, Cheng Y, Zhang K, Song C, Leng H, Zheng Y, Cai H, Liu Z. Tailored Surface Treatment of 3D Printed Porous Ti6Al4V by Microarc Oxidation for Enhanced Osseointegration via Optimized Bone In-Growth Patterns and Interlocked Bone/Implant Interface. Acs Appl Mater Inter 2016;8(28):17964–75.

[122] Deering J, Clifford A, D'Elia A, Zhitomirsky I, Grandfield K. Composite Dip Coating Improves Biocompatibility of Porous Metallic Scaffolds. Mater Lett 2020;274:128057.

[123] Liu X, Chu PK, Ding C. Surface modification of titanium, titanium alloys, and related materials for biomedical applications. Mater Sci Eng R Reports 2004;47(3–4):49–121.

[124] Wang J, Tang J, Zhang P, Li Y, Wang J, Lai Y, Qin L. Surface modification of magnesium alloys developed for bioabsorbable orthopedic implants: a general review. J Biomed Mater Res Part B Appl Biomaterials 2012;100B(6):1691–701.

[125] Asri RIM, Harun WSW, Samykano M, Lah NAC, Ghani SAC, Tarlochan F, Raza MR. Corrosion and surface modification on biocompatible metals: a review. Mater Sci Eng C 2017;77:1261–74.

[126] Chouirfa H, Bouloussa H, Migonney V, Falentin-Daudré C. Review of titanium surface modification techniques and coatings for antibacterial applications. Acta Biomater 2018;83:37–54.

[127] Deering J, Dowling KI, DiCecco L-A, McLean GD, Yu B, Grandfield K. Selective Voronoi tessellation as a method to design anisotropic and biomimetic implants. Journal of the Mechanical Behavior of Biomedical Materials 2021. doi:10.1016/j.jmbbm.2021.104361.

Appendix 2: Composite Dip Coating Improves Biocompatibility of Porous Metallic Scaffolds

While most conventional surface modification processes focus on solid implant materials, it is important to establish their efficacy for coating the intricacy of interconnected pore networks. This work assesses the efficacy of a dip coating technique for use in porous metals. Nanoceramic titania particles embedded within a polymethylmethacrylate coating matrix are present on both the exterior and interior of the scaffold, meaning that the coating technique is applicable to porous metals. The coated and uncoated stainless steel scaffolds both encourage an increase in metabolic activity in Saos-2 cells across a 7-day span, whereas the solid stainless steel cylinders do not. This study complements the solvent casting coating synthesis technique presented in Chapter 4, proving that other forms of biomedical coating can deliver biofunctionalized materials to the scaffold interior in addition to the scaffold exterior to help sustain osseointegration.

Contents lists available at ScienceDirect

Materials Letters

journal homepage: www.elsevier.com/locate/mlblue

Composite dip coating improves biocompatibility of porous metallic scaffolds

Joseph Deering [a], Amanda Clifford [a], Andrew D'Elia [a], Igor Zhitomirsky [a,b], Kathryn Grandfield [a,b,*]

[a] Department of Materials Science and Engineering, McMaster University, Hamilton, ON, Canada
[b] School of Biomedical Engineering, McMaster University, Hamilton, ON, Canada

ABSTRACT

Porous materials are becoming more common for bone implants, and it is increasingly important to find surface modification strategies that affect both the implant exterior and porous interior. In this study, selective laser melting (SLM) was used to create porous stainless steel implants 8 mm in diameter, which were subsequently dip coated with a composite polymethylmethacrylate-alumina (PMMA-Al_2O_3) film. Imaging with electron microscopy found evidence of the films at a depth of 2.2 mm into the porous implants, with dual-scale topography created by the native SLM stainless steel substrate and alumina nanoparticles. Energy dispersive X-ray spectroscopy confirmed the presence of the coating along the periphery of interior pores. In vitro tests with osteoblast-like cells showed greater cell metabolism on composite-coated samples compared to uncoated dense samples after seven days of culture.

© 2020 Elsevier B.V. All rights reserved.

1. Introduction

Porous metallic implant materials are becoming increasingly common for usage in bone and joint replacement due to their ability to mitigate stress-shielding effects [1]. The use of additive manufacturing enables effective scaffold design in bone implants by creating tunable mechanical performance [2] and channels for mass transport [3] by implementing porosity.

To encourage bone ingrowth, implants have been coated with composite materials, which can contain bioceramic particles such as calcium phosphate [4], rutile [5], and alumina [6]. One key limitation of conventional coating techniques, such as plasma spraying, is their line-of-sight processing [7], which prevents uniform coating deposition in the interior of porous structures, and their high-temperature processing. Changing the surface composition and topography in the interior of porous specimens is possible by electrochemical methods, such as micro-arc oxidation [8,9], where oxides of the base metal, calcium, or phosphorus are added to the surface. Composite materials have also been developed as a feedstock for additive manufacturing processes as a means of modifying the interior of porous structures compared to structures produced by traditional titanium feedstocks [10]. Recently, immersion techniques [11] and electrophoretic deposition [12] have been

effective for depositing bioactive and organic coating materials on the interior of porous structures. Where alumina-based ceramic materials have been traditionally used for bulk implant components due to their excellent biocompatibility in bone applications [13], their integration in nanoparticle form on the interior of porous constructs has not been evaluated. Polymethylmethacrylate (PMMA), commonly known as a primary constituent in some bone cements, has recently been shown to have favourable osteogenic effects as an implant coating [14]. The potential for PMMA-Al_2O_3 organic composite material to coat the interior of porous metallic scaffolds remains unexplored.

The objective of this work was the development of a facile dip coating method to deposit a composite PMMA-Al_2O_3 coating on the interior of an additively manufactured porous scaffold. Scanning electron microscopy (SEM) was used to confirm deposition, and the potential for improving osseointegration was explored with an in vitro cell metabolism assay.

2. Methods

2.1. Scaffold production

Cylinders (h = 8 mm, ø = 8 mm) were designed in Autodesk Netfabb and hollowed to create body-centred cubic lattice struts rotated 45° about the X and Y axes. Fully dense implants as well as porous implants with strut diameters of 450 μm with a unit cell

* Corresponding author.
  E-mail address: kgrandfield@mcmaster.ca (K. Grandfield).

spacing of 1.2 mm, and therefore pores with an approximate throat diameter of 275 μm were formed. Scaffolds were built using 304L stainless-steel powder (<45 μm, Carpenter Additive) using the selective laser melting (SLM) process (EOSINT M280, Germany). Laser power was set to 200 W, scan speed 800 mm/s, hatch spacing 80 μm, and layer thickness 40 μm during fabrication. Metal scaffolds were cleaned with ethanol and deionized water in an ultrasonic bath for 20 min. Scaffolds were either kept whole or sectioned longitudinally for subsequent coating.

2.2. Coating deposition and characterization

Polymethylmethacrylate (MW ~ 120,000, Millipore Sigma) and alumina (0.13 μm, Al_2O_3, Baikowski) particles were obtained. Under continuous stirring, 10 g L^{-1} PMMA was added to a mixed solvent containing 20% deionized water and 80% isopropanol (Millipore Sigma) and heated to 55 °C, at which point the PMMA fully dissolved, only marginally increasing the viscosity. The PMMA solution was cooled back to room temperature, and Al_2O_3 particles were added to a concentration of 10 g L^{-1}. Metallic scaffolds were coated whole to produce specimens for cell viability assays or in halves for easier investigation of the midplane with electron microscopy. Scaffolds were attached to copper tape (see Fig. S1), immersed into the PMMA-Al_2O_3 suspension under sonication for one minute, removed, and air dried at room temperature for 24 h to evaporate solvent.

The mid-plane of the scaffold was sputter coated with carbon for conductivity, mounted to a SEM stub with silver paint and analyzed by SEM imaging (FEI Magellan 400) and energy dispersive X-ray spectroscopy (EDS) using an accelerating voltage of 10 kV.

2.3. Cell viability

Saos-2 osteosarcoma cells (ATCC) were seeded on additively manufactured solid implants, porous implants, and PMMA-Al_2O_3 coated porous implants at a density of 10,000 cells/cm^2 in McCoy's Modified 5A media. Cells were cultured at 37 °C in an atmosphere of 5% CO_2 for seven days. After one, three, and seven days, a solution of 5% alamarBlue reagent in media (Life Technologies Inc.) was added to wells for 60 min. The dye was pipetted into a separate plate and fluorescence was measured at an excitation-emission wavelength of 540–580 nm. Statistical significance was determined using a two-way ANOVA in R with Tukey's HSD test and $p < 0.05$.

3. Results and discussion

3.1. Coating deposition

Dip coating with the PMMA-Al_2O_3 composite produced a coating on both the exterior and interior of the scaffolds. Where PMMA bonds to the substrate may be governed by bidentate ligands, the mechanical strength of the composite coating on the stainless steel substrate is possibly increased compared to other coatings with monodentate bonding coordination. Higher magnification images of a representative pore (Fig. 1A) illustrate the presence of the
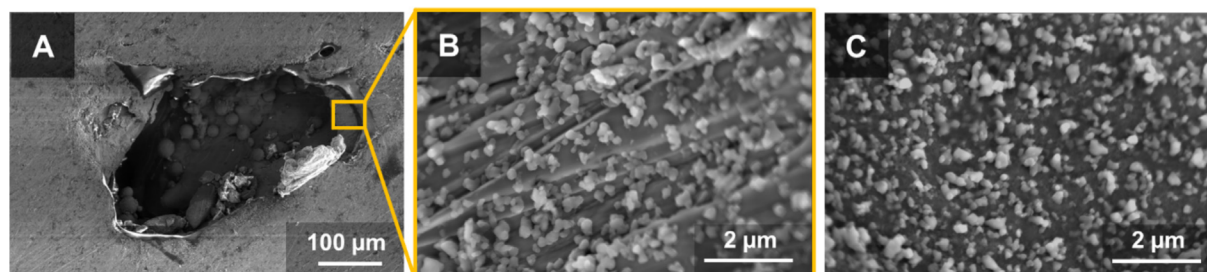
Fig. 1. (A) Image of a representative pore on the interior of the scaffold. Thickness of PMMA-Al_2O_3 around the pore periphery is not constant. (B) Surface topography of PMMA-Al_2O_3 composite coating at the scaffold interior. (C) Surface topography of the PMMA-Al_2O_3 composite coating at the scaffold exterior. The Al_2O_3 distribution is comparable at scaffold exterior and interior sites.
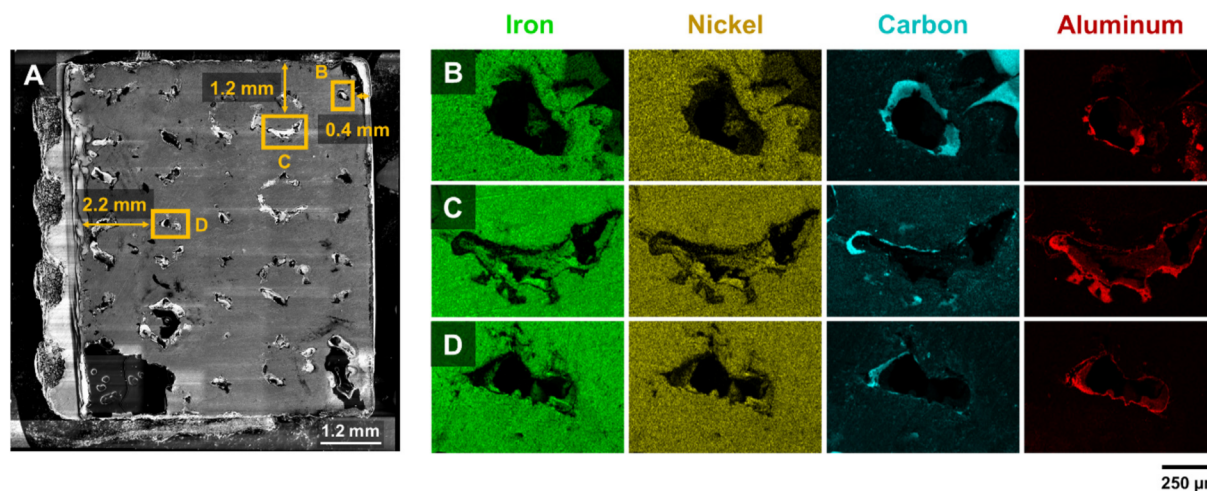
Fig. 2. (A) Cross-sectional SEM image with bright regions representative of the coating. Sampling sites at various distances to exterior correspond to EDS maps at depths of 0.4 mm (Row B), 1.2 mm (Row C) and 2.2 mm (row D). Increased intensity of aluminum and carbon at the pore periphery indicates complete penetration of the coating into the interior pores.

Fig. 3. Saos-2 cell viability on solid, porous, and coated porous AM parts. Porous implants coated with the PMMA-Al_2O_3 composite coating showed significantly higher cell proliferation after seven days compared to solid components, while all porous implants showed significantly more cell proliferation after seven days.

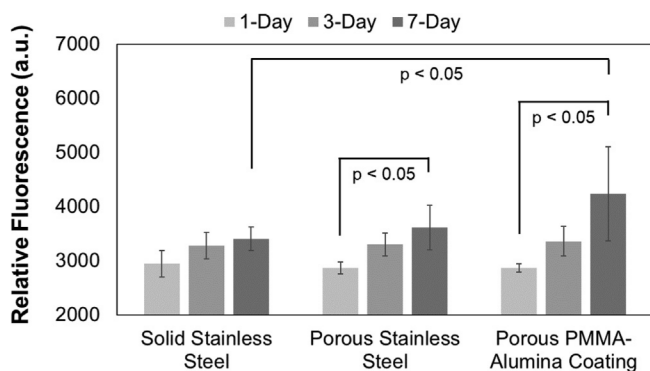composite coating at an interior site, where non-uniform thickness is observed around the periphery of the pore. There is also evidence of sintered stainless steel particles on the lattice struts within the pores, adding elements of microscale topography on both interior and exterior lattice sites. Nanoparticles of Al_2O_3 were observed to be uniformly distributed through the PMMA matrix without aggregation (Fig. 1B) at interior sites of the scaffolds. These nanoparticles, in conjunction with inherent striations in the PMMA matrix, add elements of nanoscale topography to interior and exterior sites in the scaffold, which can be favourable for osseointegration [15]. Coating deposition on the interior appears consistent with the exterior (Fig. 1C), where Al_2O_3 is evenly distributed through the PMMA.

EDS maps at interior scaffold sites (Fig. 2A) on the cross-section are shown in Fig. 2B, 2C, and 2D. Each site has a different distance to the scaffold exterior. Elemental signals characteristic to the uncoated stainless-steel (Fe, Ni) were uniform on the cross-sectional surface, while signals characteristic to the composite coating (C, Al) displayed higher intensity directly around the pore periphery at depths of 0.4 mm, 1.2 mm, and 2.2 mm.

3.2. Cell viability

The results of cell viability assays on the solid implants, porous implants, and PMMA-Al_2O_3 coated porous implants are shown in Fig. 3. After seven days of culture, the PMMA-Al_2O_3 coated scaffolds significantly outperformed dense stainless-steel samples, confirming what has been shown previously on two-dimensional substrates [14]. Statistically higher cell metabolism was also observed from day one to day seven on both the porous implants without coating and PMMA-Al_2O_3 coated porous implants. These results suggest that the addition of an interconnected porosity network with a diameter of 275 μm allows for rapid cellular proliferation through the porous interior of the scaffold relative to the control. The addition of PMMA-Al_2O_3 composite coatings on porous scaffolds further improves osseointegration potential relative to uncoated implants. By coating the SLM implant surface, surface topography, chemistry, and wettability are modified, and it is probable that metallic particle release is impeded. All of these factors can change the dynamics of cell-surface interaction, contributing to the resulting increase in cell viability seen here.

4. Conclusions

PMMA-Al_2O_3 composite films were successfully deposited on the porous interior of SLM stainless steel implants using a facile dip coating method. SEM and EDS maps confirmed that the coating

penetrated at least 2.2 mm into the scaffold interior, indicating that this immersion technique is suitable for coating the complete interior of porous metallic implants with a biomedical composite material. The alumina nanoparticles also contributed to a nanoscale topography around the pore periphery. *In vitro* characterization of the coated scaffolds with Saos-2 cells showed statistically higher rates of cell metabolism when compared to fully dense structures with the same geometry. Therefore, the dip coating method is a promising approach for creating composite coatings on porous implants to improve the potential osteoconductivity of their interior pores. The successful demonstration of Al_2O_3 nanoparticles, PMMA, and stainless steel scaffolds as pilot materials should lead to investigation of other additives and substrates, such as titanium alloys, for polymer-composite coatings on porous SLM implants. Future work should also evaluate the limits of PMMA-Al_2O_3 integration in larger-sized implants.

CRediT authorship contribution statement

Joseph Deering: Conceptualization, Investigation, Formal analysis, Writing - original draft. **Amanda Clifford:** Investigation, Methodology, Writing - review & editing. **Andrew D'Elia:** Investigation, Methodology, Writing - review & editing. **Igor Zhitomirsky:** Conceptualization, Supervision, Funding acquisition, Writing - review & editing. **Kathryn Grandfield:** Conceptualization, Supervision, Funding acquisition, Writing - review & editing.

Declaration of Competing Interest

The authors declare that they have no known competing financial interests or personal relationships that could have appeared to influence the work reported in this paper.

Acknowledgements

Appendix A. Supplementary data

Supplementary data to this article can be found online at https://doi.org/10.1016/j.matlet.2020.128057.

References

[1] S. Arabnejad, B. Johnston, M. Tanzer, D. Pasini, Fully porous 3D printed titanium femoral stem to reduce stress-shielding following total hip arthroplasty, J. Orthopaed. Res. 35 (8) (2017) 1774–1783.

[2] X. Wang, S. Xu, S. Zhou, W. Xu, M. Leary, P. Choong, et al., Topological design and additive manufacturing of porous metals for bone scaffolds and orthopaedic implants: a review, Biomaterials 83 (2016) 127–141.

[3] A.A. Zadpoor, Additively manufactured porous metallic biomaterials, J. Mater. Chem. B 7 (26) (2019) 4088–4117.

[4] N. Eliaz, N. Metoki, Calcium phosphate bioceramics: a review of their history, structure, properties, coating technologies and biomedical applications, Materials 10 (4) (2017) 334.

[5] A. Clifford, B.E.J. Lee, K. Grandfield, Zhitomirsky I. Biomimetic modification of poly-l-lysine and electrodeposition of nanocomposite coatings for orthopaedic applications, Colloids Surfaces B Biointerfaces 176 (2018) (Polym. (United Kingdom). 121 2017):115–21.

[6] A.J. McManus, R.H. Doremus, R.W. Siegel, R. Bizios, Evaluation of cytocompatibility and bending modulus of nanoceramic/polymer composites, J. Biomed. Mater. Res. A 72A (1) (2005) 98–106.

[7] E. Munting, The contributions and limitations of hydroxyapatite coatings to implant fixation, Int. Orthop. 20 (1) (1996) 1–6.

[8] P. Xiu, Z. Jia, J. Lv, C. Yin, Y. Cheng, K. Zhang, et al., Tailored surface treatment of 3D printed porous Ti6Al4V by microarc oxidation for enhanced osseointegration via optimized bone in-growth patterns and interlocked bone/implant interface, Acs Appl. Mater Inter. 8 (28) (2016) 17964–17975.

[9] Z. Chen, X. Yan, Y. Chang, S. Xie, W. Ma, G. Zhao, et al., Effect of polarization voltage on the surface componentization and biocompatibility of micro-arc oxidation modified selective laser melted Ti6Al4V, Mater. Res. Express 6 (8) (2019) 086425.

[10] H. Attar, S. Ehtemam-Haghighi, N. Soro, D. Kent, M.S. Dargusch, Additive manufacturing of low-cost porous titanium-based composites for biomedical applications: advantages, challenges and opinion for future development, J. Alloy. Compd. 827 (2020) 154263.

[11] C. Domínguez-Trujillo, E. Peón, E. Chicardi, H. Pérez, J.A. Rodríguez-Ortiz, J.J. Pavón, et al., Sol-gel deposition of hydroxyapatite coatings on porous titanium for biomedical applications, Surf Coatings Technol. 333 (2018) 158–162.

[12] V.O. Kollath, Q. Chen, S. Mullens, J. Luyten, K. Traina, A.R. Boccaccini, et al., Electrophoretic deposition of hydroxyapatite and hydroxyapatite–alginate on rapid prototyped 3D Ti6Al4V scaffolds, J. Mater. Sci. 51 (5) (2016) 2338–2346.

[13] P. Zeng, Biocompatible alumina ceramic for total hip replacements, Mater. Sci. Tech. Ser. 24 (5) (2013) 505–516.

[14] A. D'Elia, J. Deering, A. Clifford, B.E.J. Lee, K. Grandfield, I. Zhitomirsky, Electrophoretic deposition of polymethylmethacrylate and composites for biomedical applications, Colloids Surf. B Biointerfaces 188 (2019) 110763.

[15] O. Omar, D. Karazisis, A. Ballo, S. Petronis, H. Agheli, L. Emanuelsson, et al., The role of well-defined nanotopography of titanium implants on osseointegration: cellular and molecular events in vivo, Int. J. Nanomed. 11 (2016) 1367–1382.

Appendix 3: Ellipsoidal Mesoscale Mineralization Pattern in Human Cortical Bone Revealed in 3D by Plasma Focused Ion Beam Serial Sectioning

This work provides insight into the application of plasma focused ion beam microscopy for the assessment of mesostructural features in mature human cortical bone. The application of PFIB-SEM and image processing techniques to mineral ellipsoids and the LCN in human bone allow for spatial characterization of the mature tissue in the absence of any implant. Characterization of the spatial characteristics of mineral ellipsoids especially complement the themes of ellipsoidal packing arrangements and disorder presented in the peri-implant bone tissue in Chapter 6.

Permission for reprint has been provided by Elsevier, with the full article available at https://doi.org/10.1016/j.jsb.2020.107615.

Ellipsoidal mesoscale mineralization pattern in human cortical bone revealed in 3D by plasma focused ion beam serial sectioning

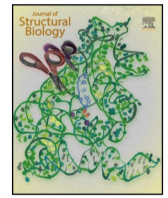Dakota M. Binkley[a,d], Joseph Deering[b], Hui Yuan[c], Aurélien Gourrier[d,e], Kathryn Grandfield[a,b,*]

[a] School of Biomedical Engineering, McMaster University, Hamilton, Canada
[b] Department of Materials Science and Engineering, McMaster University, Hamilton, Canada
[c] Canadian Centre for Electron Microscopy, McMaster University, Hamilton, Canada
[d] Univ. Grenoble Alpes, LIPHY, F-38000 Grenoble, France
[e] CNRS, LIPHY, F-38000 Grenoble, France

ABSTRACT

Visualizing bone mineralization and collagen fibril organization at intermediate scales between the nanometer and the hundreds of microns range, is still an important challenge. Similarly, visualizing cellular components which locally affect the tissue structure requires a precision of a few tens of nanometers at maximum while spanning several tens of micrometers. In the last decade, gallium focused ion beam (FIB) equipped with a scanning electron microscope (SEM) proved to be an extremely valuable structural tool to meet those ends. In this study, we assess the capability of a recent plasma FIB-SEM technology which provides a potential increase in measurement speed over gallium FIB-SEM, thus paving the way to larger volume analysis. Nanometer-scale layers of demineralized and mineralized unstained human femoral lamellar bone were sequentially sectioned over volumes of 6–16,000 μm³. Analysis of mineralized tissue revealed prolate ellipsoidal mineral clusters measuring approximately 1.1 μm in length by 700 nm at their maximum diameter. Those features, suggested by others in high resolution studies, appear here as a ubiquitous motif in mineralized lamellar bone over thousands of microns cubed, suggesting a heterogeneous and yet regular pattern of mineral deposition past the single collagen fibril level. This large scale view retained sufficient resolution to visualize the collagen fibrils while also partly visualizing the lacuno-canalicular network in three-dimensions. These findings are strong evidence for suitability of PFIB as a bone analysis tool and the need to revisit bone mineralization over multi-length scales with mineralized tissue.

1. Introduction

Bone's remarkable mechanical properties are essentially determined by its macro-to-microarchitecture and tissue properties (Currey, 2002). Mineralized collagen fibrils with typical diameters of 100 nm are considered to be the fundamental building block of this multiscale structural hierarchy and tissue mechanics is primarily determined by fibril orientation and mineral density (Granke et al., 2013; Wagermaier et al., 2006; Weiner et al., 1999). Thus, the precise organization of collagen fibrils and of the mineral phase in healthy and pathological bone tissue is still an active area of research.

In addition to the intrinsic fibrillar organization pattern in a 1–10 μm range, resulting from tight biological control and self-assembly mechanisms, periodic modulations can be observed over distances up to 100 μm in lamellar bone of many species. This characteristic length scale corresponds to the presence of vascular channels in human cortical bone around which the mineralized collagen fibrils are organized with high symmetrical regularity (Giraud-Guille, 1988; Wagermaier et al., 2006; Weiner et al., 1999). It also corresponds to the typical thickness of trabecular bone which is mostly found in the epiphyses of long bones, between the two surfaces of flat bones and also within irregular bones, such as vertebrae and the sacrum. This high degree of organization up to the microscopic scale is, however, partly perturbed by dendritic osteocytes embedded in the tissue, whose cell bodies are usually spaced apart by ∼25 μm on average, depending on the tissue organization (Hannah et al., 2010; Kollmannsberger et al., 2017; Repp et al., 2017). This dense, highly interconnected cellular network is a key player for bone functions (Bonewald, 2011) and potentially constitutes a source of local tissue disorganization with respect to higher levels of symmetry. It is therefore becoming evident that analyzing the sub-microscopic structure of bone tissue also requires visualizing the lacuno-canalicular porosity network (LCN) hosting the

osteocytes (Kerschnitzki et al., 2011) as well as the cellular details.

While a plethora of characterization tools exist for bone (Georgiadis et al., 2016) visualizing ultrastructural details with sufficient resolution to distinguish 100 nm diameter mineralized collagen fibrils while probing sufficiently large volumes with representative LCN organizations (in the 100 μm range) is still an important technical challenge.

A subset of ultrastructural characterization tools allows exploration of collagen-mineral arrangement with electron microscopy, chiefly transmission electron microscopy (TEM) as well as electron tomography (Grandfield et al., 2018; Landis et al., 1996; McNally et al., 2012; Reznikov et al., 2018; Weiner and Traub, 1992). These methods allow visualization of small volumes of up to 200 nm thick with subnanometer to angstrom resolution. Although TEM techniques have been central to defining collagen-mineral arrangement and mineral platelet morphology, even electron tomography is limited by geometrical restrictions and specimen thickness requirements, leading to missing wedge artifacts (Wang et al., 2017) which conflate reconstructions and therefore, some conclusions made via this method. Recently, another electron microscopy approach has surfaced as a highly complementary tool of TEM in bone hierarchical investigations, namely, focused ion beam (FIB) scanning electron microscopy (SEM), usually abbreviated to FIB-SEM, but also called FIB-SEM serial sectioning or FIB-SEM tomography. In this method, a heavy ion (in most cases from a liquid metal ion source, such as gallium (Ga^+)) beam is used to sequentially mill material, the block-face of which is then imaged with a coincident electron beam. FIB-SEM enables visualization of larger volumes (approximately $10 \times 10 \times 10 - 20 \times 20 \times 20$ μm^3) than TEM which partly compensates for the loss in resolution to a few nanometers. Indeed, FIB-SEM serial-sectioning has been demonstrated on embedded or cryogenically preserved tissues including, mineralized turkey tendon (Zou et al., 2019), human, pig and rat lamellar bone (Reznikov et al., 2014a, 2014b, 2013), human trabecular bone (Reznikov et al., 2014a), mandibular bone of the minipig (Maria et al., 2019), zebrafish larvae (Akiva et al., 2019; Silvent et al., 2017), embryonic chicken bone (Kerschnitzki et al., 2016) and the interface of cementum and periodontal ligament (Hirashima et al., 2020b, 2020a) to name a few. Nearly all studies utilize demineralized bone and were therefore focused on the collagen fibrils. Very few studies capture large sections of the LCN, which were therefore performed with a much lower spatial resolution than technically possible, to acquire larger fields of view on mineralized bone tissue (Schneider et al., 2011). Therefore, so far, FIB-SEM studies of bone were designed to focus on either the collagen organization or the LCN and could not allow for investigation of both or the mineral within bone.

A relatively new technology, plasma focused ion beam (PFIB-SEM) presents many advantages for capturing large scale volumes with high resolution. A PFIB is a dual beam FIB-SEM instrument that uses an inductively coupled Xenon (Xe^+) plasma ion source. The more massive Xe^+ ion generally leads to higher material removal rates for the same ion beam current as Ga^+-based FIB-SEM technology, for example material sputtering rates range from ~ 10–30% to upwards of ~300% higher for the same current and duration (Burnett et al., 2016). Conservative estimates therefore state that PFIB-SEM is 20 – 60x faster for 3D acquisition than Ga^+-based FIB-SEM (Altmann and Young, 2014; Burnett et al., 2016). Not only the ion source, but also the ion optics of the two systems vary. The PFIB is capable of much higher ion beam currents (few pA to > 1 μA) compared to Ga-FIB (few pA to 100 nA), and retains a focused spot size unlike Ga^+ at high ion beam currents to enable thin slicing (Smith et al., 2006). The PFIB also maintains a quality surface for imaging, with the amount of surface amorphization decreased by 20–40% on silicon compared to Ga^+-FIB (Kelley et al., 2013), and the surface roughness reduced by an order of magnitude (from 400 to 50 nm RMS on interconnects) when using a rocking polish (Altmann and Young, 2014). These potential benefits translate for biological imaging in 3D, ultimately offering possibility for larger, smoother, and less damaged volumes to be acquired by the PFIB in
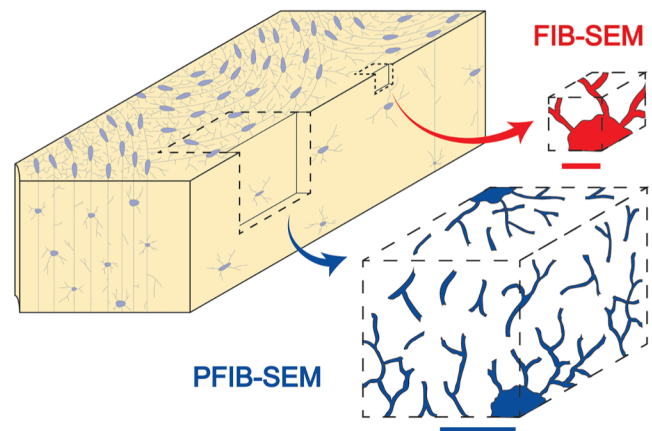

Fig. 1. Comparative accessible bone volumes with FIB vs PFIB-SEM with respect to LCN features. Size restrictions in conventional FIB-SEM techniques (red) essentially allow imaging a single osteocyte lacuna in bone tissue due to their inherently small volumes. The PFIB-SEM technique (blue) is able to probe volumes that are an order of magnitude larger than conventional FIB-SEM methods, allowing for high-resolution 3D reconstruction of a larger proportion of lacunae and canaliculi, thus theoretically providing a broader visualization of the LCN network characteristics. Red scale bar: 10 μm. Blue scale bar: 50 μm. (For interpretation of the references to colour in this figure legend, the reader is referred to the web version of this article.)

shorter times with the same nanoscale resolution as images afforded by the Ga^+ FIB-SEM (Bassim et al., 2014; Burnett et al., 2016). As outlined in Fig. 1, this 3D imaging allows a portion the osteocyte lacuno-canalicular network and the tissue to be probed simultaneously. To our knowledge, PFIB-SEM has yet to be employed in the investigation of bone ultrastructure to microscale structure (also referred to as mesoscale structure), despite its success in characterizing other materials with porous features, including concrete (Burnett et al., 2016) and hydroxyapatite coatings on biomedical alloys (Hu et al., 2017).

In this work, we apply PFIB-SEM serial sectioning to human bone for the first time. We highlight substantial contrast differences between demineralized and mineralized human femoral lamellar bone following widely reported staining and embedding sample preparation protocols. We show that, without having to go through the burdensome procedure of demineralizing and staining, similar or better imaging performances can be achieved on mineralized bone. This offers new perspectives which we explore to probe the mesoscale organization of mineralized collagen fibrils in human bone. We highlight the presence of ellipsoidal mineral clusters, a potentially underestimated intermediate level of organization between collagen fibrils and lamellae in human osteonal bone. We also show that the extent of the probed volume allows visualization of a large portion of the LCN while retaining sufficient spatial resolution to observe collagen features.

2. Materials and methods

Specimen A fresh-frozen human femur of a 68-year-old male, with no known bone disease, was obtained with institutional ethical approval (HIREB No. 12–085-T) and immediately upon thawing, fixed in a 4% glutaraldehyde (Sigma Aldrich, Missouri, US) solution in a 0.1 M cacodylate buffer for 7 days. The bone was sectioned using a slow speed diamond saw (Buehler Isomet, Illinois, US) under hydrated conditions. A longitudinal section, approximately 2 mm thick, was cut along the length of the femur for demineralization. It was imaged normal to the cutting plane. A transverse section, also 2 mm thick, was extracted for immediate dehydration and embedding, remaining in its naturally mineralized state. This section was imaged normal to the cutting plane. A schematic detailing sample orientation is shown in Fig. S1.

Demineralization and Staining Protocols In preparation for

demineralization, the longitudinally sectioned bone was polished to approximately 200 μm in thickness with 400, 800, 1200, and 2400 grit emery paper and finally a 50 nm diamond suspension on a polishing cloth (Buehler, Illinois, US). The sample was demineralized by immersion in a solution of 5% ethylenediaminetetraacetic acid (EDTA) (Sigma Aldrich, Missouri, US) and 2% paraformaldehyde (PFA; Sigma Aldrich, Missouri, US) in cacodylate buffer, pH 7 until the sample was visibly transparent (approximately 72 h). The demineralized bone was rinsed 10 times with deionized water prior to staining. The sample was then pre-stained with Alcian blue using a modified version of a previously published protocol (Reznikov et al., 2014b). The sample was placed in 5% Alcian blue in an aqueous solution was heated to 30 °C and cooled to room temperature on a hot plate for a total of 10 cycles to increase the uptake of the dye and decrease aggregation. The demineralized bone was rinsed 5 times with deionized water prior to subsequent staining. The sample was then stained by successive treatments with osmium tetroxide and thiocarbohydrazide (OTOTO) according to previously described methods (Reznikov et al., 2013).

Mineralized Sample Preparation Unlike the demineralized sample, the mineralized sample was neither demineralized nor stained. The fixed 2 mm thick transverse section directly underwent the dehydration and embedding protocol below.

Dehydration and Embedding Protocols for Demineralized and Mineralized Samples Both the demineralized and mineralized tissue were dehydrated in a graded series of ethanol (70%, 80%, 90%, 95%, 100%) for 12 h each, and further dehydrated in 100% propylene oxide (Sigma Aldrich, Missouri, US). The tissues were gradually infiltrated (25%, 50%, 75%, 100%) with EMbed812 resin (Electron Microscopy Sciences, USA) in propylene oxide (Sigma Aldrich, Missouri, USA). The embedded blocks were then cured in an oven at 60 °C. The top surface and adjacent cross-section of the embedded bone were polished with 400, 800, 1200, and 2400 grit emery paper, and a 50 nm diamond suspension on a polishing cloth (Buehler, Illinois, US) to expose the bone in the resin.

Sample Coating The polished demineralized and mineralized bone was placed on standard SEM stubs using silver paint. Both the exposed top face and cross-section intended for PFIB-SEM slicing were coated with 5 nm of gold using a Precision Etching Coating System (PECS II) coater (Gatan Inc., CA, USA) to minimize charging effects.

PFIB-SEM Serial Sectioning: Demineralized Tissue A Xenon-sourced PFIB microscope (Helios G4 UXe, Thermo Scientific, Hillsboro, USA) equipped with a Schottky field-emission gun SEM was employed. To protect the region of interest, a $63 \times 47 \times 5\ \mu m^3$ Pt capping layer was deposited on the top surface using a 20nA and 12 keV ion beam. Brief capping layer experiments (see Supplementary Data and Figures, which includes Tables S1 and S2, and Fig. S2) were completed to determine suitable protective layer compositions to minimize curtaining artifacts attributed to ion channeling and preferential milling. Suitable protective layer compositions for demineralized and mineralized tissues were qualitatively determined to be platinum (Pt) and carbon (C), respectively.

Trenches adjacent to the area of interest were milled in order to expose the cross-section and reduce shadowing to detectors and the redeposition of material. An X-shaped fiducial was milled into the exposed cross-section to allow for post-processing data alignment though translational registration. The electron beam was focused on the exposed cross-section at 2 keV and 1.6nA under 'immersion mode', with a working distance of 5.9 mm, pixel width of 20 nm, a 500 ns dwell time with 2 frame integrations. Imaging was completed with a retractable concentric backscattered detector (CBS). Sequential milling and images were collected using Auto Slice and View software (Thermo Scientific, OR, USA), with a 4nA ion current, 30 keV accelerating voltage, 20 nm slice thickness, and a 4° stage rocking angle, which has been demonstrated to minimize curtaining artifacts (Loeber et al., 2017). A full workflow is visualized in Fig. S3. The final cropped volume of the demineralized bone was $45.8 \times 40.9 \times 8.7\ \mu m^3$.

PFIB-SEM Serial Sectioning: Mineralized Tissue Similarly to the demineralized dataset, a protective capping layer 50 μm × 50 μm × 8 μm of C was deposited on the area of interest using ion beam deposition at 60nA and 12 keV. An X-shaped fiducial was milled into the exposed cross-section to allow for post-processing data alignment. The electron beam was focused on the exposed cross-section at 1.5 keV and 0.8nA, with a working distance of 2.7 mm, pixel width of 12.5 nm, a 500 ns dwell time, with 8 frame integrations. Imaging was completed with an in-lens detector under backscatter mode. Tomography data was collected using Auto Slice and View software (Thermo Scientific, OR, USA), with 1nA ion current, 30 keV accelerating voltage, 25 nm slice thickness, and a 7° stage rocking angle. The final cropped tomogram of the mineralized bone was 28.6 μm × 25.6 μm × 8.7 μm.

PFIB Data Reconstruction and Visualization The tomographic datasets were processed using Dragonfly 4.1 (Objects Research Systems, QC, Canada). Datasets were aligned using a cross-correlation approach and curtain artifacts were removed using the image processing toolbox available in Dragonfly. Shadowing effects from the SEM image aligning fiducial were removed on the demineralized images by changing the shading compensation, applying a histogram balance, and also by applying a contrast limited adaptive histogram equalization to the mineralized images. The images were reconstructed, and the osteocyte network was segmented using a U-Net classifier trained with 15 manually segmented images. Segmentations were inspected against the original datasets and minor corrections were implemented manually, including some denoising and selection of missed canaliculi on 2D slices. The machine learning outputs and revised datasets were transformed to a thickness mesh to calculate the canalicular diameter (Fig. S4). Cellular organelles and the cell body were segmented manually. Small volumes were extracted from the mineralized dataset to view the mineral morphology, where a Gaussian filter (σ = 0.5) was applied to reduce noise. Orthogonal slices, two-dimensional, and three-dimensional volumes were extracted from these smaller datasets.

It is important to note some geometrical information and the assignment of planes and directions. In our volumes, the XY plane always represents the milling and image plane during acquisition while the YZ and XZ planes are reconstructed after slice registration. By this convention, Z is always the thickness of the serial sectioning dataset. A clarification of the sample geometries from the bulk tissue are clarified in Fig. S1.

3. Results and discussion

3.1. PFIB on mineralized versus demineralized bone tissue

PFIB-SEM was conducted on both demineralized and mineralized bone. A section of demineralized and stained lamellar bone was reconstructed into a volume measuring $45.8 \times 40.9 \times 8.7\ \mu m^3$ with an isotropic voxel size of 20 nm, while a slightly smaller 3D volume measuring $28.6 \times 25.6 \times 8.7\ \mu m^3$ with an anisotropic voxel size of $12.5 \times 12.5 \times 25$ nm was obtained on the mineralized sample. A side-by-side comparison of similar regions, neighboring an osteocyte lacuna, and measuring the same size of approximately 6 μm × 7 μm is shown in Fig. 2. What is immediately apparent between the two specimens is the drastic change in contrast when mineral is present. This contrast must logically be associated to mineralization fluctuations in the tissue. Upon closer inspection of the mineralized data, this contrast takes the form of regular bright patches scattered throughout the imaged volume surrounded by a darker border with dimensions in the micron range. In the demineralized sample, only slight, ill-defined change in contrast is detected which could be due to preferential staining of regions previously mineralized, or to remnant mineral still causing electron beam scattering. Both preparation methods enabled the detection of canaliculi, apparent as circular or linear black voids (mineralized sample), or black voids with a brightly stained periphery (demineralized stained sample).
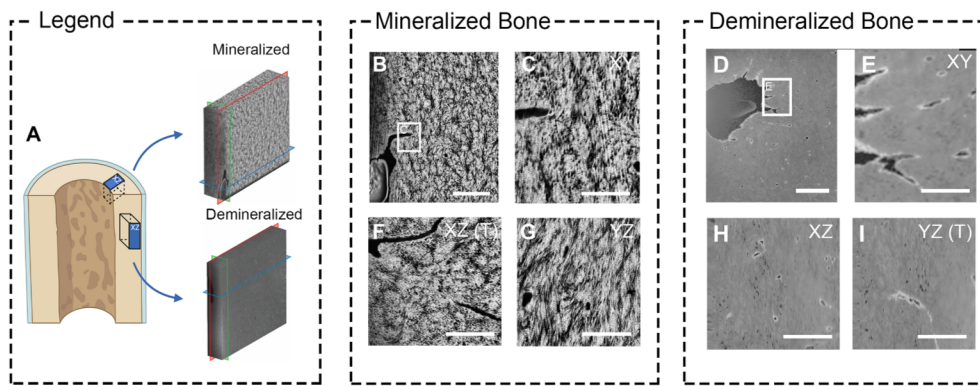
Fig. 2. Comparison of mineralized and demineralized bone analyzed by FIB-SEM. (A) A schematic demonstrating that the mineralized and demineralized samples were sectioned in the transverse and longitudinal directions, respectively. Sub-volumes between the mineralized and demineralized bone were selected in regions near the osteocyte lacuna (B,D) and canaliculi (C,E) for comparison along orthogonal planes. In the mineralized sample, marquises are evident on the (B) XY and (G) YZ planes, while rosettes are revealed in the (F) XZ plane, which is the anatomically transverse section of the bone, denoted by "(T)". In the demineralized sample, very faint outlines of marquise-like shapes are noted in the (H) XZ plane and faint rosettes on (I) the YZ plane, which corresponds to the anatomically transverse section of the bone. Scale bars: (B,D) 5 μm, remainder 2 μm. Figure A was created using BioRender.com.

While FIB-SEM serial sectioning has been widely used on a combination of demineralized and mineralized bone tissue from a variety of species (a summary of previous studies is presented in Table 1), these works have focused on investigating other aspects of human bone than mineral. For example, a mineralized volume of murine bone focused on elucidating the LCN network connections (Schneider et al., 2011), while a mineralized and heavily stained sample of chick embryonic calvaria showed the collagen arrangement during ossification (Hashimoto et al., 2017). Mineralized zebrafish larvae were also investigated (Silvent et al., 2017) and showed pathways for ion transport through blood vessels (Akiva et al., 2019), but no similar mineral clusters to size and shape of those noted herein were highlighted. A major finding of this work is therefore the ability to visualize previously unnoticed distinct mineral clusters by FIB-SEM within human cortical bone when using mineralized and unstained sections of bone.

3.2. Evidence of ubiquitous ellipsoidal microscopic mineral clusters in bone tissue

Closer inspection of the full mineralized data in 3D and along orthogonal directions is shown in Fig. 3. The mineral clusters appear more circular in the transverse direction (Fig. 3D) and more elongated longitudinally (Fig. 3B). To analyze the mineral clusters, five sub-volumes (cubes with side length of 3 μm) were selected along a random diagonal direction (Fig. 4 and Fig. S4). These highlight more clearly the shape and orientation of those mineral clusters: they appear more circular in the XZ plane (transverse to osteon), irrespective of the ROI location in the sample and are more elongated in the orthogonal planes, especially YZ where the smallest features have dimensions compatible with mineralized collagen fibrils aligned in the longitudinal plane. Extracting one representative mineral cluster and showing all its orthogonal planes and as a 3D reconstruction (Fig. 5), the shape of these structures in 3D more closely resembles a prolate ellipsoid, than a perfect sphere, the elongation direction being the osteonal axis. Several more of these clusters were segmented (Fig. S5) and dimensions extracted, measuring on average 700 ± 164.4 nm in diameter at their maximum midpoint and 1.14 ± 0.26 μm in length (Table S3). The circular-like shape is shown across the whole XZ plane in Supplementary Movie 1 and the true ellipsoidal nature of these in more detail in Supplementary Movie 2.

Similar mineral clusters have been identified on the floor of osteocyte lacunae (Shah et al., 2016) and more recently, at the apex of rat calvarial sutures (Shah et al., 2020) by exposing bone to deproteinization protocols. In Shah et al. the shape has been identified as a marquise, which is not uniform throughout bone, but rather changes to a less organized marquise moving away from the bone mineralization front, suggesting that this shape is a transient early form of mineral deposit (Shah et al., 2020). The same general shapes, identified as

prolate ellipsoids, have been shown in the turkey tendon (Zou et al., 2019), and over small sections of human bone, e.g. Movie S1 in Reznikov et al. (Reznikov et al., 2018).

We note that this structure is ubiquitous throughout an entire 45 μm section of lamellar bone and represents a hierarchical level of mineral organization above the single collagen fibril level of 100 nm in diameter and below the typical dimensions of an osteon lamella of 5–7 μm. It also shows that this structure is not a member of the "disorganized" sub-lamella motif (Reznikov et al., 2013) associated with canaliculi. The two earlier papers citing ellipsoidal mineral shapes have also postulated that the presence of a cross-collagen fibril mineralization motif may be possible (Reznikov et al., 2018; Zou et al., 2019). Our findings on the microscale, depicting mineral clusters that span roughly 700 nm in width and just over 1 μm in length over a distance of 45 μm clearly indicate that mineral is indeed associated with more than one collagen fibril, confirming earlier hypotheses that tissue mineralization occurs in patterns regularly spaced over large distances past the single collagen fibril level.

Seminal works focusing on early bone formation by Bonucci *et al.* and Bernard and Pease outline similar spherical shapes as "calcification loci" or "round bodies" between collagen fibrils in osteoid (Bernard and Pease, 1969; Bonucci, 1971). These are thought to elongate, firstly unrelated to collagen banding, then lastly become associated with the fibril interior, or to coarsen from calcification loci to bone nodules which coalesce to form all mineralized tissue (Bernard and Pease, 1969; Bonucci, 1971). These findings are supported by cryo electron microscopy studies, which observe the accumulation of mineral on the exterior of the fibril in *in vitro* conditions (Nudelman et al., 2013). Similar spherical particles 'calcospherulites' have been postulated to be related to the mineralization front only (Midura et al., 2008) and early bone mineralization from *in vitro* culture of MC3T3-E1 osteoblast cells show comparable spherical particles (mineralization foci), and also notes these in mouse calvarial bone with osteopontin closely associated with their margin (Addison et al., 2015). It remains to be determined if the ellipsoidal shapes uncovered herein once began as spherical clusters, as so predominantly noted in early bone formation literature.

3.3. The mineral: linking to the nanoscale

Viewing the mineral clusters in the transverse (XZ) plane, means that we view a section perpendicular to the long axis of the osteon, closely aligned along the femur axis in our case and, presumably, of the collagen fibrils. In such an orientation the circular shape is fully consistent with previously observed features in high-resolution TEM (Fig. 6) in human bone, termed "rosettes" (Grandfield et al., 2018), "lacy" pattern (Reznikov et al., 2018) or otherwise unnamed in the alveolar bone of minipigs (Maria et al., 2019). Dispersed between some rosettes are clear black circular or linear voids marking the canaliculi,

Table 1

Partial summary of FIB-SEM serial sectioning on various mineralized tissues When not available, slice thickness (Z) is given in place of voxel size, and total thickness of tomogram (Z_T) is given in place of all tomogram dimensions in X, Y, Z.

| Tissue	Preparation	Tomogram Size	Voxel Size	Volume (um^3)	Reference
Human Bone					
Cortical bone	Demineralized	45.8 × 40.9 × 8.7 μm	20 × 20 × 20 nm	16 297	Present work
Cortical bone	Mineralized	28.6 × 25.6 × 8.7 μm	12.5 × 12.5 × 25 nm	6 370	Present work
Cortical bone	Demineralized	N/A	10 × 10 × 10 nm	N/A	(Reznikov et al., 2018)
Cortical bone	Demineralized	$Z_T = 6 – 9$ μm	10 × 10 × 10 nm to 12.5 × 2.5 × 12.5 nm	N/A	(Reznikov et al., 2014b)
Trabecular bone	Demineralized	$Z_T = 6 – 9$ μm	10 × 10 × 10 nm to 12.5 × 12.5 × 12.5 nm	N/A	(Reznikov et al., 2014a)
Other Mammalian Bone					
Minipig alveolar bone	Demineralized	$Z_T = 10 – 15$ μm	10 × 10 × 10 nm to 12.5 × 12.5 × 12.5 nm	N/A	(Maria et al., 2019)
Minipig fibrolamellar bone	Demineralized	$X = 10.24$ μm $Y = 8.6$ μm	10 × 10 × 10 nm	N/A	(Almany Magal et al., 2014)
Murine trabecular bone	Demineralized	25 × 20 × 20 μm	$Z = 50$ nm	10 000	(Hasegawa et al., 2018)
Murine proximal tibial metaphysis	Demineralized	40 × 40 × 40 μm	20 × 20 × 20 nm	64 000	(Robles et al., 2019)
Murine femur	Mineralized	19 × 14 × 11 μm	18 × 18 × 29.5 nm	2 926	(Schneider et al., 2011)
Murine bone-osteoblastic processes	Demineralized	30 × 20 × 17.5 μm	$Z = 50$ nm	10 500	(Hasegawa et al., 2017)
Rat lamellar bone	Demineralized	10 × 10 × 2 – 10 μm	$Z = 10$ nm	200–1 000	(Reznikov et al., 2013)
Embryonic Avian Bone					
Long bones	Demineralized	N/A	N/A	N/A	(Kerschnitzki et al., 2016)
Calvaria bone	Mineralized	25 × 25 × 25 μm	25 × 25 × 25 nm	15 625	(Hashimoto et al., 2017)
Tendon					
Turkey	Mineralized Demineralized	N/A	12 × 12 × 24 nm 6 × 6 × 8.7 nm	N/A	(Zou et al., 2019)
Rat	Demineralized	$Z_T = 260$ μm	$Z = 60$ nm	N/A	(Kanazawa et al., 2014)
Dental Materials					
Mice cementum	Demineralized	73 × 63 um × 8 μm	36 × 36 × 100 nm	36 792	(Hirashima et al., 2020b)
Rat dentin	Demineralized	73 × 63.6 × 4.2 μm	36 × 36 × 100 nm	19 500	(Tanoue et al., 2018)
Zebrafish					
Zebrafish larvae	Demineralized and mineralized	26 × 22 × 12 um	26 × 26 × 26 nm	6 864	(Silvent et al., 2017)
Zebrafish larvae	Mineralized, cryo-FIB-SEM	30 × 23 × 12 um 40 × 23 × 24.5 um	10 × 10 × 20 nm 20 × 20 × 40 nm	8 280 22 540	(Akiva et al., 2019)
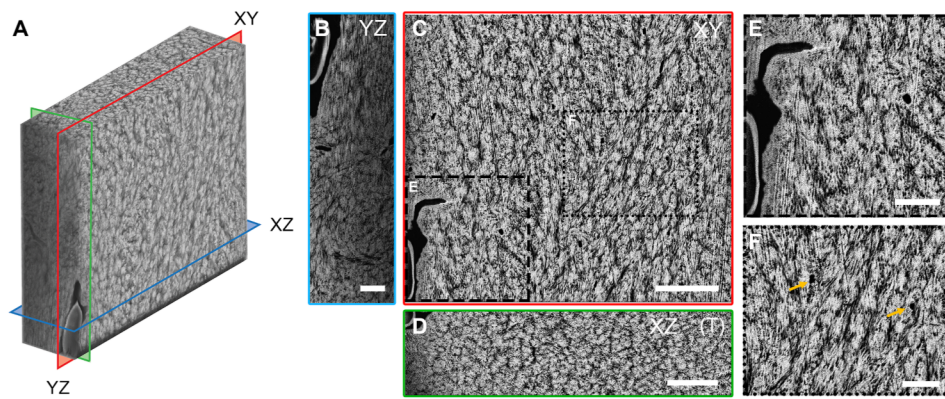
Fig. 3. PFIB-SEM of mineralized lamellar bone (A) 3D reconstruction of mineralized bone with an isotropic voxel size of 25 nm and total volume measuring 28.6 μm × 25.6 μm × 8.7 μm. YZ (green), XY (red), and XZ (blue) orthogonal planes are annotated to show the location of the images in B, C, and D, respectively. Mineral appears light grey/white, while canalicular networks, porosity and collagen all share black contrast. (B) An image extracted from the YZ plane of the reconstructed volume, note an osteocyte in the top left corner and dark canaliculi traversing the view on oblique angles. Scale bar: 2 μm. (C) An image of the XY plane. In this view, the mineral component of bone appears bright, while canaliculi appear as black round circles (inset F). An osteocyte is present in the bottom left (inset E). Scale bar: 5 μm. (D) An image extracted from the XZ plane of the reconstructed volume, corresponding to the transverse anatomical plane. Scale bar: 3 μm. (E) Inset of (C), with osteocyte (bottom left) showing a clear membrane (light grey) and the LCN, which appears black. Cell processes were not visible within canaliculi extending from this osteocyte. Mineral appears finer near the canaliculi periphery, but may be due to shadowing. Scale bar: 2 μm. (F) Inset of (C), where white arrows point to circular canaliculi. Note that due to the absence of staining, the canaliculi in this case appear black. Scale bar: 2 μm. (For interpretation of the references to colour in this figure legend, the reader is referred to the web version of this article.)

and a substantial portion of black volume surrounds each rosette. Upon closer inspection of Fig. 6B, a unique feature of each rosette is its mineral-dense center (Supplementary Movie S3).

The rosette features noted by (Grandfield et al., 2018) in large TEM sections, are reproduced in higher resolution images in Fig. 6C and D for comparison. With the higher resolution and compositional contrast afforded by high angle annular dark field scanning transmission electron microscopy (HADDF STEM), we begin to make sense of the black regions surrounding the rosettes as viewed in PFIB-SEM. The features are outside of the resolution limit of the PFIB-SEM, but with the STEM images, we can see individual mineral plates exist in this space, and are clearly resolved, wrapping around perfectly circular black volumes. Since these black regions correspond to low density regions in the SEM, we postulate that these are one of two features; sub-cellular or sub-micron level porosity within the extracellular matrix itself or collagen viewed in cross-section, or possibly a combination of both.

While many comprehensive reviews cover the hierarchical levels of bone mineralization (Reznikov et al., 2014c; Weiner and Traub, 1992), we should draw attention to some of the competing views on collagen-mineral arrangement, chief of which is the concept of intra versus interfibrillar mineralization, referring to mineral either occupying (mainly the gap zone of) the collagen fibril, or external to the fibril/between fibrils. This conflicting view essentially stems from convincing results reported over decades supporting both observations. For example, X-ray or neutron diffraction peaks can readily be observed at small angles with the same 67 nm periodicity as is exhibited by non-mineralized collagen fibrils of bone or tendon, pointing to intrafibrillar mineralization in the collagen fibril gap zone (Bigi et al., 1988), as confirmed by TEM (Weiner and Traub, 1989). More recent STEM results

obtained with FIB-SEM prepared ultrathin samples suggest, on the contrary, that mineral nanoparticles are quasi-exclusively extrafibrillar (McNally et al., 2012; Schwarcz, 2015). Recent STEM tomography suggests a motif of cross-fibrillar mineralization, both intra-and inter-fibrillar (Reznikov et al., 2018). However, Landis *et al.* clearly reported electron microscopy evidence for the presence of both intra and extrafibrillar mineral in turkey tendon more than three decades ago (Landis et al., 1991) which is likely confirmed by our STEM observations of rosettes with a potential mix of inter and intrafibrillar mineralization.

Nevertheless, how this occurs or what this looks like remains elusive. Our images over large volumes with 12.5 nm resolution in X and Y and 25 nm resolution in Z, complemented by those from Grandfield *et al.* (Grandfield et al., 2018), suggest the potential for a combination of intra and interfibrillar mineralization. Since the black circular regions on the periphery of the mineral cluster make up such a large fraction of the sample, it is highly unlikely they are all vacant of any material and therefore may not only represent sub-micron porosity. Hence, at least a part likely represent collagen fibrils in cross-section and the bright mineral encircling them therefore, represents interfibrillar mineralization between each collagen fibril. Collagen, as a light element, will not scatter electrons well in the PFIB-SEM or TEM when unstained as in the case of the mineralized sample herein, meaning that it likely will always appear black in cross-section. The presence of collagen in these cross-sectional dark regions has been confirmed in TEM sections using elemental analysis (Lee et al., 2019). On the other hand, the central area of the rosettes, viewed in our PFIB and the complementary STEM (Fig. 6 B,C,D), suggests that the central portion may be much more densely infiltrated with mineral. A close up slice-by-
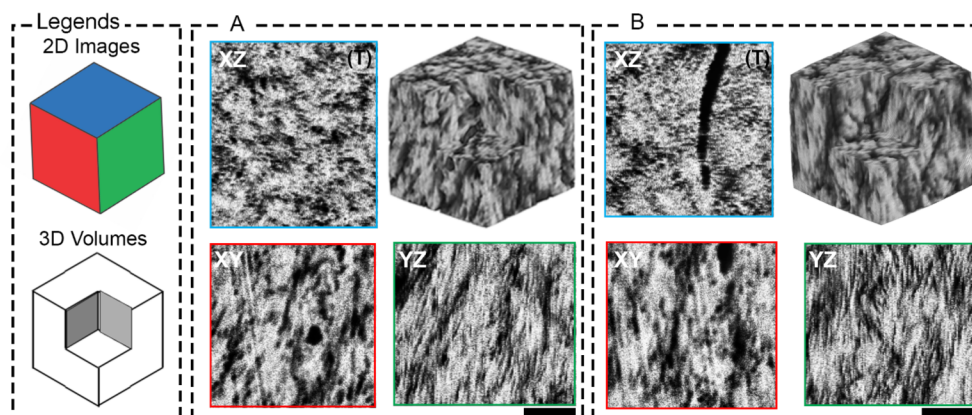

Fig. 4. Exploring mineral and collagen orientation in 3D. The PFIB volume is cropped into smaller volumes (A,B) measuring 3 μm each side to explore the orientation of mineral and collagen fibrils. The transverse planes (XZ) show clear rosette shapes, while the YZ plane along the long axis of the femur, shows collagen fibrils in plane, denoted by their characteristic banding pattern. XY planes show the faint outline of diamond, or marquise shapes.
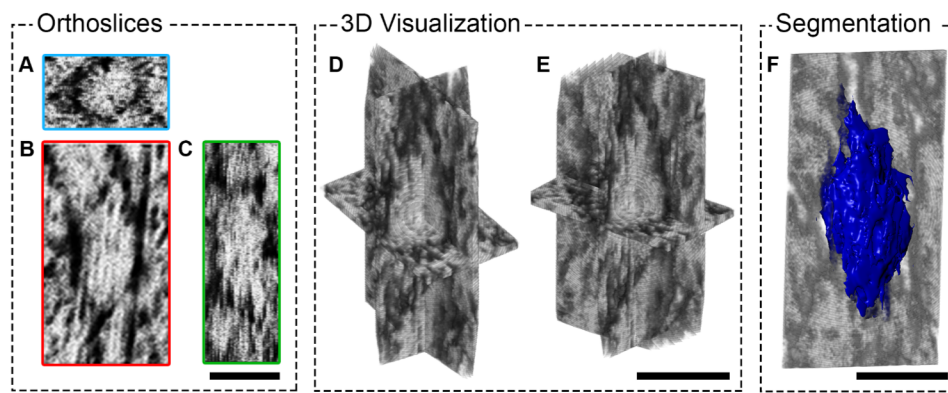
Fig. 5. Mineral cluster morphology in 3D. A representative mineral cluster from PFIB-SEM of the mineralized sample has been isolated to probe its shape both by separated (A,B,C) and intersecting orthogonal planes (D,E). In (A) the transverse slice, perpendicular to the long axis of the femur, is given by plane XZ. Here, a clear rosette shape is visible also discernible from the top-down tilted view in (E). Segmentation of the 3D shape in (F) confirms its likely shape as a prolate ellipsoid. All scale bars: 1 μm.

slice view of one mineral cluster is highlighted in Movie S3, where the bright mineral is concentrated in the central region and more sparsely on the periphery. Yet, even in these densely mineralized regions, there are still signs of discrete particles albeit less well defined than at the rosette periphery. While PFIB-SEM is still in its infancy, optimization of the voxel size and slice thickness will enable probing this hypothesis in the future. Indeed, with the addition of elemental information by energy dispersive X-ray spectroscopy (EDX) mineral transport in other species has been shown on single slices of a block-face (Kerschnitzki et al., 2016b). Multi-spectral tomography or serial sectioning, i.e. collection of both images and EDX spectra slice-by-slice, could confirm both nanoscale structures and mineral locations in the future.

3.4. PFIB-SEM for the visualization of the LCN

One other potential advantage of PFIB-SEM serial sectioning is the large volumes quickly accessible with high resolution which enable exploration of the osteocyte and the LCN. Here we begin by assessing demineralized and stained bone, the usual sample preparation method for FIB-SEM. The demineralized reconstructed section is shown alongside three orthogonal planes (Fig. 7B,C,D), where key features are the osteocyte in the top-left and its surrounding lacuna and canalicular extensions. While a boundary between the osteocyte and the lacuna is indistinguishable, perhaps due to a lack of high pressure freezing sample preparation, some distinct membrane-bound cellular organelles were present and segmented of which, the nucleus is most prominent (Fig. 7E). In all slices, the canaliculi are clearly resolvable, primarily as relatively circular features with a bright boundary, due to osmium

tetroxide staining, in the XY plane (arrows Fig. 7F) or as oblong, branch-like features in YZ and XZ (Fig. 7B, D). While a separate slice in Fig. 2G highlights the capability to image the distinct collagen banding patterns also with PFIB-SEM which is a hallmark of most FIB-SEM serial sectioning performed on demineralized bone focused on fibril orientation (Reznikov et al., 2014b, 2013).

The segmentation of the LCN from this demineralized dataset is shown in Fig. 8A and B, with segmented cellular organelles in C and D. Here, the canaliculi appear to extend outwards from the osteocyte lacuna in all directions, with many connections also observed extending up from the bottom right-hand side of Fig. 8A. Indeed, another osteocyte was located just outside of the volume captured in the tomogram, but visualized during set-up (shown in Fig. S6). Therefore, the center of the volume approximately represents the meeting zone of the canaliculi from at least two osteocytes. The canalicular diameter in this segmentation was 346 ± 146 nm (Fig. 8E). The volume and segmented LCN of the demineralized sample are available in Supplementary Movie 4.

A slightly smaller 3D volume of the mineralized set is shown in Fig. 3A. Similarly, the reconstructed volume is shown alongside its orthogonal planes (Fig. 3B,C,D), where the XY plane was acquired during imaging, and the YZ and XZ planes created after image registration. While PFIB can mill extremely large volumes, the precise control of slice thickness well-resolved features in all planes. By avoiding laborious demineralization and staining processes, the resultant volumes and cross-sections show much different contrast. The bright white to light-grey contrast is representative of heavy matter, in this case the mineral, while any empty space, canaliculus, or light elements, like collagen, appear black. An osteocyte with its outer
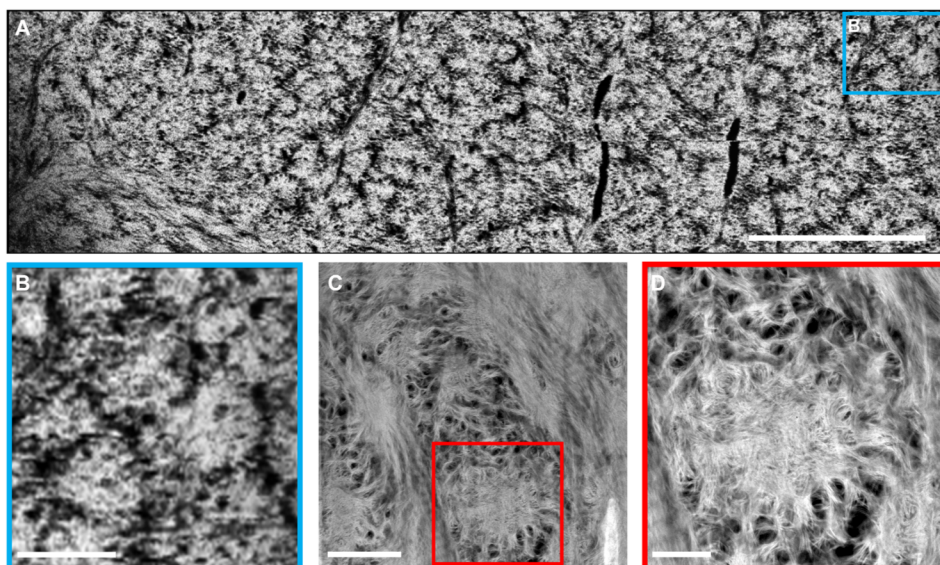

Fig. 6. Mineral clusters linked to the nanoscale. A transverse slice (perpendicular to the long axis of the femur) from the mineralized PFIB-SEM volume is shown in (A) with higher resolution inset in (B). Scale bars: 5 μm and 1 μm, respectively. The mineral appears in rosette shapes across the entirety of the section. Black space surrounds the clusters, or takes the form of black lines representing the canalicular network running through the section. A lacuna is located near the bottom left corner, but not shown on this slice. A side-by-side comparison with HAADF STEM images of human femoral bone (C) with higher magnification inset (D), reprinted with permission from (Grandfield et al., 2018), shows that the black space in PFIB surrounding the rosettes is comprised of mineral plates, wrapping around circular volumes, likely representing collagen, while the central portion remains densely mineralized. Scale bars: 500 nm and 200 nm, respectively.
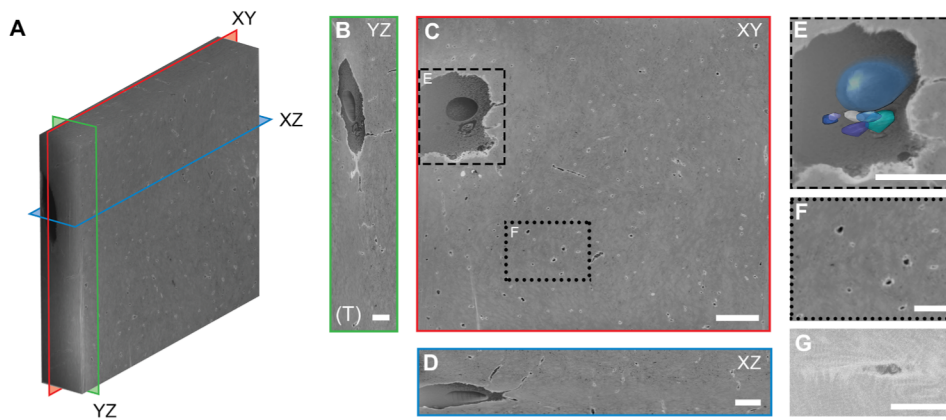
Fig. 7. PFIB-SEM of demineralized lamellar bone. (A) 3D reconstruction of demineralized bone with an isotropic voxel size of 20 nm and total volume measuring 45.8 μm × 40.9 μm × 8.7 μm. YZ (green), XY (red), and XZ (blue) orthogonal planes are annotated to show the location of the images in B, C, and D, respectively. (B) An image extracted from the YZ plane of the reconstructed volume, with osteocyte visible. Scale bar: 2 μm. (C) An image of the XY plane. In this view, canaliculi appear as bright circles (inset F). An osteocyte is resolved within the dataset (inset E). Scale bar: 5 μm. (D) An image extracted from the XZ plane of the reconstructed volume. Scale bar: 3 μm. (E) Inset of (C), showing the osteocyte within its lacuna with higher magnification, segmented cellular organelles are overlaid on the image. Scale bar: 5 μm. (F) Inset of (C), where white arrows point to canaliculi in cross-section. Due to staining, their circular periphery appears bright white. Scale bar: 2 μm. (G) A higher magnification image from another demineralized area, showing characteristic collagen banding around a canaliculi. Scale bar: 1 μm. (For interpretation of the references to colour in this figure legend, the reader is referred to the web version of this article.)

membrane in its lacuna is visible in the bottom left of the section (Fig. 3E), although cellular processes are not. These cellular features have been well characterized using traditional FIB-SEM of osteocytes in trabecular bone (Hasegawa et al., 2018; 2017) and near atomic resolution using TEM tomography (Kamioka et al., 2012). Canaliculi are visible as black circles (arrows Fig. 3F) in the XY plane and appear as oblong shapes or tubular features (Fig. 3B, D) that span the entirety of the YZ and XZ plane.

The segmentation of the LCN from this mineralized dataset is shown in Fig. 9A and B, with what appears to be the cellular membrane, and not the lightly scattering osteopontin-rich hypocalcified lamina limitans that also exists around osteocytes (McKee and Nanci, 1996), segmented in C and D. However, we do note that for investigation of cellular structures, different sample preparation methods and analysis, including cryo-FIB would be more suitable. Most of the canaliculi appear co-aligned in the Z-direction (Fig. 9B) within this volume, with minimal branching across the volume. It is well known the canalicular density can vary strongly within different regions of a bone sample. Also, in osteons, osteocytes are flattened in the tangential plane (in the lamellar plane) with the highest density of canaliculi oriented radially. Recall, that the samples were cut in orthogonal directions and planes were assigned such that the XY plane was the milling and image plane in PFIB-SEM (Fig. S1). Based on the images of segmented canaliculi, it is most likely that the demineralized XY plane falls radially with respect to an osteon, while the mineralized XY plane likely falls tangentially with respect to an osteon. The average canalicular diameter in the mineralized bone was 284 ± 82 nm (Fig. 9E), still in line with values reported by other techniques but a narrower range in comparison to the diameters reported for the demineralized bone above (346 ± 146 nm). This difference could either be explained by a loss of mineral at the canalicular surface during demineralization, or to the difficulty to precisely define this interface due to a relative diffuse staining at the canaliculi surface of demineralized bone. Interestingly, 33% of the values fall in a relatively narrow range of 300–400 nm for the demineralized sample while 58% of the canaliculi diameters are slightly more broadly distributed within 250–450 nm. For the mineralized sample, 50% are between 300 and 400 nm and 73% between 250 and 450 nm. It is important to note, however, that a precise quantification of canaliculi diameter strongly depends on the segmentation procedure. Fig. S7 highlights differences in segmentation, when meticulously corrected manually (shown in Figs. 8 and 9), or when segmentation is completely relaxed and automated. The volume and segmented LCN of the
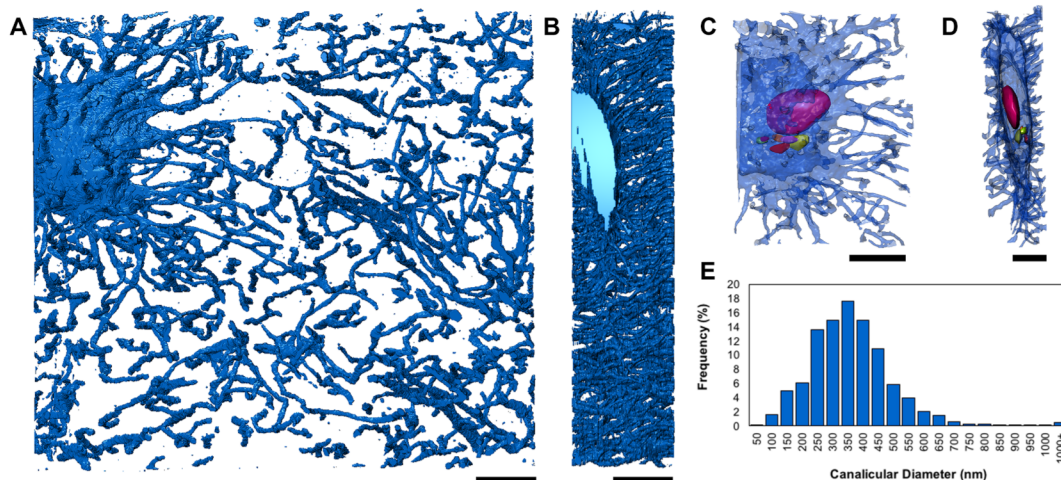

Fig. 8. LCN network in demineralized lamellar bone. (A) XY projection of the segmented LCN where canalicular extensions span the volume. More canaliculi appear near the osteocyte cell in the top left corner, and near the bottom right corner of the volume, which is confirmed to be proximal to a second osteocyte that was not captured in the PFIB-SEM dataset (Fig. S5). Scale bar: 10 μm. (B) The segmented LCN from the YZ projection, which shows connections spanning the depth of the reconstruction. Scale bar: 5 μm. (C) A segmentation of the osteocyte and nearby extending canaliculi with resolvable cellular organelles segmented (multi-coloured) in 3D. Scale bar: 5 μm. (D) The cell from the YZ plane showing the 3D distribution of cellular organelles. Scale bar: 3 μm. (E) A frequency histogram of canalicular diameter from the segmentation. The average canalicular diameter is 346 ± 146 nm.
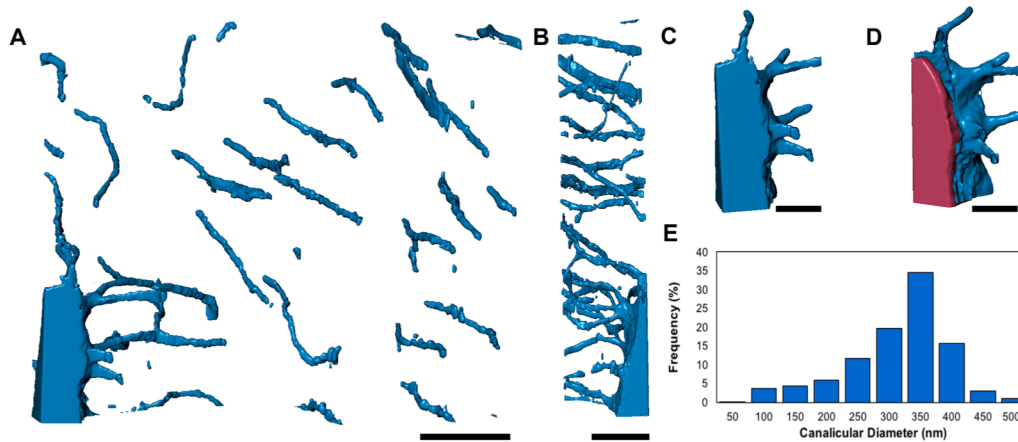
Fig. 9. LCN network in mineralized lamellar bone. (A) XY projection of the segmented LCN where long canalicular connections appear to extend primarily along the Z-direction of the re-construction. This corresponds to along the XZ or transverse plane, therefore likely part of a network that would span osteonal layers. Part of an osteo-cyte is present in the bottom left corner of the segmentation. Scale bar: 5 μm. (B) The segmented LCN from the YZ view, which shows co-aligned connec-tions spanning the depth of the re-construction, with most being aligned in this direction. Scale bar: 5 μm. (C) A segmentation of the lacunae and ex-tending space that (D) the osteocyte cell (pink) resides in. Scale bar 2 μm. (E) A frequency histogram of canalicular diameter from the segmentation. The average canalicular diameter is 285 ± 82 nm. (For interpretation of the references to colour in this figure legend, the reader is referred to the web version of this article.)

mineralized sample are available in Supplementary Movie S5.

Osteocytes or LCN have been studied with a variety of techniques. Functional studies mostly rely on optical microscopy, due to the large variety of available fluorescent dyes that allow targeting specific cel-lular components and biomarkers (Ciani et al., 2009; Sano et al., 2015). Confocal and non-linear two-and three-photon microscopy have also been used to study the LCN characteristics and have the additional advantage of allowing large fields of views (Genthial et al., 2017; Kerschnitzki et al., 2011; Repp et al., 2017). However, all these methods suffer the classical diffraction limitation and the spatial re-solution is typically limited to ∼200 nm laterally and ∼500 nm axially, such that the smallest canaliculi are out of reach, thus complicating network connectivity analysis. Higher resolution afforded by SEM was used to report canaliculi diameters in a range of 259 ± 129 nm on 2D sections of mice humeri (You et al., 2004). Similarly, atomic force microscopy (AFM) studies report canaliculi diameters of 426 ± 118 nm on 2D sections of cortical bovine tibia (Lin and Xu, 2011).

To overcome the limits of dimensional quantification on 2D ob-servations, pseudo-3D visualization is often performed with SEM using resin-embedded and acid-etched bone replica (Bonewald, 2011; Shah and Palmquist, 2017). In 3D, two partial osteocyte lacunae and their junctions in murine bone were probed by traditional FIB-SEM (Schneider et al., 2011). However, the roughly 20 μm wide view did not capture a full lacuna, nor an osteocyte maintained within. While os-teocytes and individual organelles were not classified in this work, as was not the aim, the feasibility to probe cellular organelle structures opens a potential avenue for further PFIB-SEM applications.

X-ray tomography is also frequently used to assess various char-acteristics of the LCN. However, reaching sufficient resolutions to capture the smallest canaliculi still remains a challenge. Canaliculi with diameters of 320–390 ± 120 nm were reported for human cortical femurs analyzed by X-ray phase contrast synchrotron nanotomography (SR-nanoCT) (Varga et al., 2015), but such measurements currently provide typical resolutions of 100–200 nm in the best cases (Varga et al., 2016). These works characterize the osteocyte network and LCN of mineralized bone tissue, and reveal some texture that is attributed to the collagen banding pattern (Peyrin et al., 2014). However, while a larger volume is obtained, even using a synchrotron source, voxel sizes ranged from 50 to 130 nm (Wittig et al., 2019) to 280 nm (Peyrin et al., 2012), double to a full order of magnitude larger than the 25 nm ob-tained herein. Conversely, the advancements in image processing for X-ray data are significantly more developed than the nascent field of PFIB, and reconstructed and denoised to reveal fine details of bone structure (Dong et al., 2014; Pacureanu et al., 2013; 2012). Future PFIB-SEM evaluation of bone structure and LCN should focus on further

optimization of acquisition parameters as well image processing tech-niques to reveal the structural and biological linkage in bone. Ulti-mately, PFIB-SEM could advantageously provide accurate quantifica-tion of local regions of the LCN if coupled with other less resolved methods which provide a visualization of larger portions of the net-work.

3.5. Study limitations

While this paper provides an exciting proof-of-concept for using PFIB-SEM serial sectioning to analyze bone, we are aware that there are some limitations to our study design. Firstly, we recognize that the demineralized and mineralized datasets represent a single data point and from different orientations in bone – along and transverse to the long axis of the femur. Nevertheless, the findings presented in a single dataset are representative of volumes larger than several datasets of traditional FIB-SEM. Of course, our future work will probe a wider range of samples, both anatomical location and species. We do note that specimens were prepared by dehydration and embedding, rather than cryogenic FIB-SEM. Future possibilities for cryo-PFIB-SEM exist. Nevertheless, our findings are in line with structures shown in cryo-genic-FIB-SEM, and embedded FIB-SEM published by others (Table 1). The volumes probed in this study, while comparable to the largest FIB-SEM datasets on bone, are still on the small scale for what is possible with PFIB-SEM. Larger volumes, capturing several osteocytes and their connections, will indeed be interesting to probe in the future, bringing PFIB-SEM to the level of investigations carried out with X-ray techni-ques. Lastly, in our work, we've analyzed a skeletally mature bone specimen, though it is true that the age of the osteon and specific la-mella probed is unknown. While we anticipate the prolate ellipsoid or marquise structure is not associated only with mineralization fronts, future work comparing primary and secondary osteons would be in-teresting to shed light on whether this is a permanent or transient structure in lamellar bone.

4. Conclusion

PFIB-SEM is a promising technique to probe both the nano and microscale hierarchy of bone. Herein, we demonstrate that PFIB-SEM serial sectioning can achieve volumes of thousands of microns cubed, while maintaining resolution of collagen fibrils on demineralized bone. The large volume and fast milling capabilities of this technique enabled an approach to begin probing the LCN and mineralized fibrils si-multaneously. Moreover, this work demonstrates that analyzing mi-neralized bone, as opposed to demineralized bone, is essential for making claims on collagen-mineral arrangement and bone hierarchical

structure in general. As suggested by others in human bone (Reznikov et al., 2018), rat bone (Shah et al., 2020) and turkey tendon (Zou et al., 2019), we confirm that the mineral in cortical human bone takes on a prolate ellipsoidal shape. Our large scale imaging confirms that these clusters are indeed densely packed across lamellar bone and not isolated events. The central cross-section of these ellipsoids represents the "rosette" features described previously (Grandfield et al., 2018). It is therefore clear that the organization of mineral is not solely restricted to its inter- versus intrafibrillar arrangement with collagen, but depends on coordination across several collagen fibrils. We suggest that the presence of inter-fibrillar mineral is likely on the exterior of these clusters, while intrafibrillar mineral appears to be a possibility in the interior. Further work is needed to probe this hypothesis and investigate how this arrangement changes across osteons, and of course, in other types of bone.

5. Funding sources

CRediT authorship contribution statement

Dakota Marie Binkley: Conceptualization, Methodology, Data curation, Formal analysis, Writing - original draft, Writing - review & editing. **Joseph Deering:** Data curation, Formal analysis, Writing - review & editing. **Hui Yuan:** Methodology, Writing - review & editing. **Aurélien Gourrier:** Conceptualization, Funding acquisition, Supervision, Writing - original draft, Writing - review & editing. **Kathryn Grandfield:** Conceptualization, Funding acquisition, Supervision, Writing - original draft, Writing - review & editing.

Declaration of Competing Interest

The authors declare that they have no known competing financial interests or personal relationships that could have appeared to influence the work reported in this paper.

Acknowledgements

Appendix A. Supplementary data

Supplementary data to this article can be found online at https://doi.org/10.1016/j.jsb.2020.107615.

References

Addison, W.N., Nelea, V., Chicatun, F., Chien, Y.-C., Tran-Khanh, N., Buschmann, M.D., Nazhat, S.N., Kaartinen, M.T., Vali, H., Tecklenburg, M.M., Franceschi, R.T., McKee, M.D., 2015. Extracellular matrix mineralization in murine MC3T3-E1 osteoblast cultures: an ultrastructural, compositional and comparative analysis with mouse bone. Bone 71, 244–256. https://doi.org/10.1016/j.bone.2014.11.003.

Akiva, A., Nelkenbaum, O.r., Schertel, A., Yaniv, K., Weiner, S., Addadi, L., 2019. Intercellular pathways from the vasculature to the forming bone in the zebrafish larval caudal fin: Possible role in bone formation. J. Struct. Biol. 206 (2), 139–148. https://doi.org/10.1016/j.jsb.2019.02.011.

Altmann, F., Young, R.J., 2014. Site-specific metrology, inspection, and failure analysis of three-dimensional interconnects using focused ion beam technology. J. Micro/Nanolith. MEMS MOEMS 13 (1), 011202. https://doi.org/10.1117/1.JMM.13.1.011202.

Bassim, N., Scott, K., Giannuzzi, L.A., 2014. Recent advances in focused ion beam technology and applications. MRS Bull. 39 (4), 317–325. https://doi.org/10.1557/mrs.2014.52.

Bernard, G.W., Pease, D.C., 1969. An electron microscopic study of initial intramembranous osteogenesis. Am. J. Anat. 125 (3), 271–290.

Bigi, A., Ripamonti, A., Koch, M.H.J., Roveri, N., 1988. Calcified turkey leg tendon as structural model for bone mineralization. Int. J. Biol. Macromol. 10 (5), 282–286.

Bonewald, L.F., 2011. The amazing osteocyte. J. Bone Miner. Res. 26 (2), 229–238.

Bonucci, E., 1971. The locus of initial calcification in cartilage. Clin. Orthop. Relat. R. 78, 108–139. https://doi.org/10.1097/00003086-197107000-00010.

Burnett, T.L., Kelley, R., Winiarski, B., Contreras, L., Daly, M., Gholinia, A., Burke, M.G., Withers, P.J., 2016. Large volume serial section tomography by Xe Plasma FIB dual beam microscopy. Ultramicroscopy 161, 119–129. https://doi.org/10.1016/j.ultramic.2015.11.001.

Ciani, C., Doty, S.B., Fritton, S.P., 2009. An effective histological staining process to visualize bone interstitial fluid space using confocal microscopy. Bone 44 (5), 1015–1017.

Currey, J.D., 2002. Bones: Structure and Mechanics. Princeton University Press.

Dong, P., Haupert, S., Hesse, B., Langer, M., Gouttenoire, P.-J., Bousson, V., Peyrin, F., 2014. 3D osteocyte lacunar morphometric properties and distributions in human femoral cortical bone using synchrotron radiation micro-CT images. Bone 60, 172–185.

Genthial, R., Beaurepaire, E., Schanne-Klein, M.-C., Peyrin, F., Farlay, D., Olivier, C., Bala, Y., Boivin, G., Vial, J.-C., Débarre, D., Gourrier, A., 2017. Label-free imaging of bone multiscale porosity and interfaces using third-harmonic generation microscopy. Sci. Rep. 7 (1).

Georgiadis, M., Müller, R., Schneider, P., 2016. Techniques to assess bone ultrastructure organization: orientation and arrangement of mineralized collagen fibrils. J. R. Soc. Interface 13 (119), 20160088. https://doi.org/10.1098/rsif.2016.0088.

Giraud-Guille, M.M., 1988. Twisted plywood architecture of collagen fibrils in human compact bone osteons. Calcif. Tissue Int. 42 (3), 167–180.

Grandfield, K., Vuong, V., Schwarcz, H.P., 2018. Ultrastructure of bone: hierarchical features from nanometer to micrometer scale revealed in focused ion beam sections in the TEM. Calcif. Tissue Int. 103 (6), 606–616.

Granke, M., Gourrier, A., Rupin, F., Raum, K., Peyrin, F., Burghammer, M., Saïed, A., Laugier, P., 2013. Microfibril orientation dominates the microelastic properties of human bone tissue at the lamellar length scale. Plos One 8, e58043. doi: 10.1371/journal.pone.0058043.

Hannah, K.M., Thomas, C.D.L., Clement, J.G., De Carlo, F., Peele, A.G., 2010. Bimodal distribution of osteocyte lacunar size in the human femoral cortex as revealed by micro-CT. Bone 47 (5), 866–871.

Hasegawa, T., Endo, T., Tsuchiya, E., Kudo, A.i., Shen, Z., Moritani, Y., Abe, M., Yamamoto, T., Hongo, H., Tsuboi, K., Yoshida, T., Nagai, T., Khadiza, N., Yokoyama, A., Luiz de Freitas, P.H., Li, M., Amizuka, N., 2017. Biological application of focus ion beam-scanning electron microscopy (FIB-SEM) to the imaging of cartilaginous fibrils and osteoblastic cytoplasmic processes. J. Oral Biosci. 59 (1), 55–62. https://doi.org/10.1016/j.job.2016.11.004.

Hasegawa, T., Yamamoto, T., Hongo, H., Qiu, Z., Abe, M., Kanesaki, T., Tanaka, K., Endo, T., de Freitas, P.H.L., Li, M., Amizuka, N., 2018. Three-dimensional ultrastructure of osteocytes assessed by focused ion beam-scanning electron microscopy (FIB-SEM). Histochem. Cell Biol. 149 (4), 423–432. https://doi.org/10.1007/s00418-018-1645-1.

Hashimoto, M., Nagaoka, N., Tabata, K., Tanaka, T., Osumi, R., Odagaki, N., Hara, T., Kamioka, H., 2017. Three-dimensional morphometry of collagen fibrils in membranous bone. Integr. Biol. 9 (11), 868–875. https://doi.org/10.1039/c7ib00073a.

Hirashima, S., Kanazawa, T., Ohta, K., Nakamura, K.-I., 2020a. Three-dimensional ultrastructural imaging and quantitative analysis of the periodontal ligament. Anat Sci Int 95 (1), 1–11. https://doi.org/10.1007/s12565-019-00502-5.

Hirashima, S., Ohta, K., Kanazawa, T., Togo, A., Tsuneyoshi, R., Kusukawa, J., Nakamura, K., 2020b. Cellular network across cementum and periodontal ligament elucidated by FIB/SEM tomography. Microscopy 69, 53–58. doi: 10.1093/jmicro/dfz117.

Hu, C., Aindow, M., Wei, M., 2017. Focused ion beam sectioning studies of biomimetic hydroxyapatite coatings on Ti-6Al-4V substrates. Surf Coatings Technology 313, 255–262. doi: 10.1016/j.surfcoat.2017.01.103.

Kamioka, H., Kameo, Y., Imai, Y., Bakker, A.D., Bacabac, R.G., Yamada, N., Takaoka, A., Yamashiro, T., Adachi, T., Klein-Nulend, J., 2012. Microscale fluid flow analysis in a human osteocyte canaliculus using a realistic high-resolution image-based three-dimensional model. Integr Biol 4, 1198–1206. doi: 10.1039/c2ib20092a.

Kanazawa, T., Gotoh, M., Ohta, K., Shiba, N., Nakamura, K.-I., 2014. Novel characteristics of normal supraspinatus insertion in rats: an ultrastructural analysis using three-dimensional reconstruction using focused ion beam/scanning electron microscope tomography. Muscles Ligaments Tendons 4, 182–7. doi: 10.11138/mltj/2014.4.2.182.

Kelley, R.D., Song, K., Van Leer, B., Wall, D., Kwakman, L., 2013. Xe+ FIB milling and measurement of amorphous silicon damage. Microsc Microanal 19 (S2), 862–863. https://doi.org/10.1017/s1431927613006302.

Kerschnitzki, M., Akiva, A., Ben Shoham, A., Asscher, Y., Wagermaier, W., Fratzl, P.,

Addadi, L., Weiner, S., 2016a. Bone mineralization pathways during the rapid growth of embryonic chicken long bones. J. Struct. Biol. 195 (1), 82–92. https://doi.org/10.1016/j.jsb.2016.04.011.

Kerschnitzki, M., Akiva, A., Shoham, A.B., Koifman, N., Shimoni, E., Rechav, K., Arraf, A.A., Schultheiss, T.M., Talmon, Y., Zelzer, E., Weiner, S., Addadi, L., 2016b. Transport of membrane-bound mineral particles in blood vessels during chicken embryonic bone development. Bone 83, 65–72. https://doi.org/10.1016/j.bone.2015.10.009.

Kerschnitzki, M., Wagermaier, W., Roschger, P., Seto, J., Shahar, R., Duda, G.N., Mundlos, S., Fratzl, P., 2011. The organization of the osteocyte network mirrors the extracellular matrix orientation in bone. J. Struct. Biol. 173 (2), 303–311.

Kollmannsberger, P., Kerschnitzki, M., Repp, F., Wagermaier, W., Weinkamer, R., Fratzl, P., 2017. The small world of osteocytes: connectomics of the lacuno-canalicular network in bone. New J. Phys. 19, 073019–073019.

Landis, W.J., Hodgens, K.J., Arena, J., Song, M.J., McEwen, B.F., 1996. Structural relations between collagen and mineral in bone as determined by high voltage electron microscopic tomography. Microsc. Res. Tech. 33 (2), 192–202.

Landis, W.J., Moradian-oldak, J., Weiner, S., 1991. Topographic imaging of mineral and collagen in the calcifying turkey tendon. Connect. Tissue Res. 25 (3-4), 181–196.

Lee, B.E.J., Luo, L., Grandfield, K., Andrei, C.M., Schwarcz, H.P., 2019. Identification of collagen fibrils in cross sections of bone by electron energy loss spectroscopy (EELS). Micron 124, 102706. https://doi.org/10.1016/j.micron.2019.102706.

Lin, Y., Xu, S., 2010. AFM analysis of the lacunar-canalicular network in demineralized compact bone. J. Microscopy 241, 291–302.

Loeber, T.H., Laegel, B., Wolff, S., Schuff, S., Balle, F., Beck, T., Eifler, D., Fitschen, J.H., Steidl, G., 2017. Reducing curtaining effects in FIB/SEM applications by a goniometer stage and an image processing method. J. Vacuum Sci. Technol. B Nanotechnol. Microelectron. Mater. Process. Meas. Phenom. 35 (6), 06GK01. https://doi.org/10.1116/1.4991638.

Almany Magal, R., Reznikov, N., Shahar, R., Weiner, S., 2014. Three-dimensional structure of minipig fibrolamellar bone: adaptation to axial loading. J. Struct. Biol. 186 (2), 253–264. https://doi.org/10.1016/j.jsb.2014.03.007.

Maria, R., Ben-Zvi, Y., Rechav, K., Klein, E., Shahar, R., Weiner, S., 2019. An unusual disordered alveolar bone material in the upper furcation region of minipig mandibles: a 3D hierarchical structural study. J. Struct. Biol. 206 (1), 128–137. https://doi.org/10.1016/j.jsb.2019.02.010.

McKee, M.D., Nanci, A., 1996. Osteopontin at mineralized tissue interfaces in bone, teeth, and osseointegrated implants: ultrastructural distribution and implications for mineralized tissue formation, turnover, and repair. Microsc Res Techniq 33, 141–164. https://doi.org/10.1002/(sici)1097-0029(19960201)33:2<141::aid-jemt5>3.0.co;2-w.

McNally, E.A., Schwarcz, H.P., Botton, G.A., Arsenault, A.L., 2012. A model for the ultrastructure of bone based on electron microscopy of ion-milled sections. Plos One 7, e29258. doi: 10.1371/journal.pone.0029258.

Midura, R.J., Vasanji, A., Su, X., Midura, S.B., Gorski, J.P., 2008. Isolation of Calcospherulites from the Mineralization Front of Bone. Cells Tissues Organs 189, 75–79. doi: 10.1159/000152914.

Nudelman, F., Lausch, A.J., Sommerdijk, N.A.J.M., Sone, E.D., 2013. In vitro models of collagen biomineralization. J. Struct. Biol. 183 (2), 258–269. https://doi.org/10.1016/j.jsb.2013.04.003.

Pacureanu, A., Langer, M., Boller, E., Tafforeau, P., Peyrin, F., 2012. Nanoscale imaging of the bone cell network with synchrotron X-ray tomography: optimization of acquisition setup: Synchrotron x-ray tomography reveals the bone cell network. Med. Phys. 39 (4), 2229–2238.

Pacureanu, A., Larrue, A., Langer, M., Olivier, C., Muller, C., Lafage-Proust, M.-H., Peyrin, F., 2013. Adaptive filtering for enhancement of the osteocyte cell network in 3D microtomography images. IRBM 34 (1), 48–52. https://doi.org/10.1016/j.irbm.2012.12.013.

Peyrin, F., Dong, P., Pacureanu, A., Langer, M., 2014. Micro- and nano-CT for the study of bone ultrastructure. Curr. Osteoporos. Rep. 12 (4), 465–474. https://doi.org/10.1007/s11914-014-0233-0.

Peyrin, F., Pacureanu, A., Zuluaga, M.A., Dong, P., Langer, M., 2012. 3D X-Ray CT imaging of the bone lacuno-canalicular network. 2012 9th IEEE Intl Symposium Biomedical Imaging (ISBI) 1, 1788–1791. doi: 10.1109/isbi.2012.6235929.

Repp, F., Kollmannsberger, P., Roschger, A., Kerschnitzki, M., Berzlanovich, A., Gruber, G.M., Roschger, P., Wagermaier, W., Weinkamer, R., 2017. Spatial heterogeneity in the canalicular density of the osteocyte network in human osteons. Bone Reports 6, 101–108.

Reznikov, N., Almany-Magal, R., Shahar, R., Weiner, S., 2013. Three-dimensional imaging of collagen fibril organization in rat circumferential lamellar bone using a dual beam electron microscope reveals ordered and disordered sub-lamellar structures. Bone 52 (2), 676–683.

Reznikov, N., Bilton, M., Lari, L., Stevens, M.M., Kröger, R., 2018. Fractal-like hierarchical organization of bone begins at the nanoscale. Science 360 (6388), eaao2189.

https://doi.org/10.1126/science:aao2189.

Reznikov, N., Chase, H., Brumfeld, V., Shahar, R., Weiner, S., 2015a. The 3D structure of the collagen fibril network in human trabecular bone: Relation to trabecular organization. Bone 71, 189–195. https://doi.org/10.1016/j.bone.2014.10.017.

Reznikov, N., Shahar, R., Weiner, S., 2014b. Three-dimensional structure of human lamellar bone: the presence of two different materials and new insights into the hierarchical organization. Bone 59, 93–104. https://doi.org/10.1016/j.bone.2013.10.023.

Reznikov, N., Shahar, R., Weiner, S., 2014c. Bone hierarchical structure in three dimensions. Acta Biomater. 10 (9), 3815–3826. https://doi.org/10.1016/j.actbio.2014.05.024.

Robles, H., Park, SungJae, Joens, M.S., Fitzpatrick, J.A.J., Craft, C.S., Scheller, E.L., 2019. Characterization of the bone marrow adipocyte niche with three-dimensional electron microscopy. Bone 118, 89–98. https://doi.org/10.1016/j.bone.2018.01.020.

Sano, H., Kikuta, J., Furuya, M., Kondo, N., Endo, N., Ishii, M., 2015. Intravital bone imaging by two-photon excitation microscopy to identify osteocytic osteolysis in vivo. Bone 74, 134–139.

Schneider, P., Meier, M., Wepf, R., Müller, R., 2011. Serial FIB/SEM imaging for quantitative 3D assessment of the osteocyte lacuno-canalicular network. Bone 49 (2), 304–311. https://doi.org/10.1016/j.bone.2011.04.005.

Schwarcz, H.P., 2015. The ultrastructure of bone as revealed in electron microscopy of ion-milled sections. Semin. Cell Dev. Biol. 46, 44–50. https://doi.org/10.1016/j.semcdb.2015.06.008.

Shah, F.A., Palmquist, A., 2017. Evidence that osteocytes in autogenous bone fragments can repair disrupted canalicular networks and connect with osteocytes in de novo formed bone on the fragment surface. Calcif Tissue Int 101 (3), 321–327. https://doi.org/10.1007/s00223-017-0283-2.

Shah, F.A., Ruscsák, K., Palmquist, A., 2020. Transformation of bone mineral morphology: From discrete marquise-shaped motifs to a continuous interwoven mesh. Bone Reports 13, 100283. https://doi.org/10.1016/j.bonr.2020.100283.

Shah, F.A., Zanghellini, E., Matic, A., Thomsen, P., Palmquist, A., 2016. The orientation of nanoscale apatite platelets in relation to osteoblastic–osteocyte lacunae on trabecular bone surface. Calcif Tissue Int 98 (2), 193–205. https://doi.org/10.1007/s00223-015-0072-8.

Silvent, J., Akiva, A., Brumfeld, V., Reznikov, N., Rechav, K., Yaniv, K., Addadi, L., Weiner, S., 2017. Zebrafish skeleton development: High resolution micro-CT and FIB-SEM block surface serial imaging for phenotype identification. Plos One 12, e0177731. doi: 10.1371/journal.pone.0177731.

Smith, N.S., Skoczylas, W.P., Kellogg, S.M., Kinion, D.E., Tesch, P.P., Sutherland, O., Aanesland, A., Boswell, R.W., 2006. High brightness inductively coupled plasma source for high current focused ion beam applications. J. Vac. Sci. Technol. B 24 (6), 2902. https://doi.org/10.1116/1.2366617.

Tanoue, R., Ohta, K., Miyazono, Y., Iwanaga, J., Koba, A., Natori, T., Iwamoto, O., Nakamura, K.-I., Kusukawa, J., 2018. Three-dimensional ultrastructural analysis of the interface between an implanted demineralised dentin matrix and the surrounding newly formed bone. Sci. Rep. 8 (1). https://doi.org/10.1038/s41598-018-21291-3.

Varga, P., Hesse, B., Langer, M., Schrof, S., Männicke, N., Suhonen, H., Pacureanu, A., Pahr, D., Peyrin, F., Raum, K., 2015. Synchrotron X-ray phase nano-tomography-based analysis of the lacunar–canalicular network morphology and its relation to the strains experienced by osteocytes in situ as predicted by case-specific finite element analysis. Biomech. Model Mechanobiol. 14 (2), 267–282.

Varga, P., Weber, L., Hesse, B., Langer, M., 2016. X-ray and Neutron Techniques for Nanomaterials Characterization 1–42. doi: 10.1007/978-3-662-48606-1_1.

Wagermaier, W., S. Gupta, H., Gourrier, A., Burghammer, M., Roschger, P., Fratzl, P., 2006. Spiral twisting of fiber orientation inside bone lamellae. Biointerphases 1 (1), 1–5.

Wang, X., Shah, F.A., Palmquist, A., Grandfield, K., 2017. 3D Characterization of Human Nano-osseointegration by On-Axis Electron Tomography without the Missing Wedge. ACS Biomater. Sci. Eng. 3 (1), 49–55.

Weiner, S., Traub, W., 1992. Bone structure: from angstroms to microns. FASEB 6, 879–885. https://doi.org/10.1096/fasebj.6.3.1740237.

Weiner, S., Traub, W., 1989. Crystal size and organization in bone. Connect. Tissue Res. 21 (1-4), 259–265.

Weiner, S., Traub, W., Wagner, H.D., 1999. Lamellar bone: structure–function relations. J. Struct. Biol. 126 (3), 241–255.

Wittig, N.K., Laugesen, M., Birkbak, M.E., Bach-Gansmo, F.L., Pacureanu, A., Bruns, S., Wendelboe, M.H., Brüel, A., Sørensen, H.O., Thomsen, J.S., Birkedal, H., 2019. Canalicular junctions in the osteocyte lacuno-canalicular network of cortical bone. ACS Nano 13 (6), 6421–6430.

You, L.-D., Weinbaum, S., Cowin, S.C., Schaffler, M.B., 2004. Ultrastructure of the osteocyte process and its pericellular matrix. Anat. Rec. 278A (2), 505–513.

Zou, Z., Tang, T., Macías-Sánchez, E., Sviben, S., Landis, W.J., Bertinetti, L., Fratzl, P., 2019. Three-dimensional Structural Interrelations between Cells, Extracellular Matrix and Mineral in Vertebrate Mineralization. BioRxiv 803007. doi: 10.1101/803007.